

Dissertation

Mechanical characterization of individual trabeculae

carried out for the purpose of obtaining the degree of Doctor technicae (Dr. techn.),
submitted at TU Wien, Faculty of Mechanical and Industrial Engineering, by

Dipl.-Ing. Martin Frank, BSc

Mat.Nr.: 1126091

under the supervision of

Univ.Prof. Dipl.-Ing. Dr.sc.nat. Philipp J. Thurner

Univ.Prof. Dipl.-Ing. Dr.techn. Dieter H. Pahr

Institute of Lightweight Design and Structural Biomechanics, E317

Vienna, February 2021

reviewed by

Prof. Dr. Ralph Müller

Prof. DI Dr. techn. Christian Hellmich

Institute for Biomechanics,

Institute for Mechanics of Materials

ETH Zürich, Switzerland

and Structures, TU Wien, Austria



Die approbierte gedruckte Originalversion dieser Dissertation ist an der TU Wien Bibliothek verfügbar.
The approved original version of this doctoral thesis is available in print at TU Wien Bibliothek.

This work was not supported by any funding agency.

I confirm, that going to press of this thesis needs the confirmation of the examination committee.

Affidavit

I declare in lieu of oath, that I wrote this thesis and performed the associated research myself, using only literature cited in this volume. If text passages from sources are used literally, they are marked as such.

I confirm that this work is original and has not been submitted elsewhere for any examination, nor is it currently under consideration for a thesis elsewhere.

I acknowledge that the submitted work will be checked electronically-technically using suitable and state-of-the-art means (plagiarism detection software). On the one hand, this ensures that the submitted work was prepared according to the high-quality standards within the applicable rules to ensure good scientific practice "Code of Conduct" at the TU Wien. On the other hand, a comparison with other student theses avoids violations of my personal copyright.

Vienna, 1st March, 2021



Martin Frank



Die approbierte gedruckte Originalversion dieser Dissertation ist an der TU Wien Bibliothek verfügbar.
The approved original version of this doctoral thesis is available in print at TU Wien Bibliothek.

Acknowledgements

My deepest gratitude goes to all the people who supported me during the last six years. First of all, I want to thank my two supervisors, Prof. Philipp Thurner and Prof. Dieter Pahr. Philipp, I have always esteemed your great mixture of having clear, interesting project ideas, but still giving me a lot of autonomy and flexibility. Dieter, I want to thank you for always keeping an eye on the big picture and also for your detailed approach in technical issues. Besides your professional support, I want to thank both of you for a really relaxed and balanced work environment in both biomechanics groups. A special thanks also goes to my two examiners, Prof. Ralph Müller and Prof. Christian Hellmich, not only for the consent to review my thesis, but also for the constructive feedback in the course of conferences.

Further, I want to highlight the support and help from all my project and master students, Seyedmasoud Chehrehrazi, Celestine Didier, Julia Fischer, Andreas Grabos, Omar Kabbani and Patrick Karner. Thanks a lot for our great collaboration and your numerous remarks and suggestions for the experiments; this really increased my (and hopefully also your) motivation for scientific working. Particularly, I want to thank Julia and Andy; both of you did such a great job that we were even able to write publications together. Working with you in the lab was always fun, not only talking about our experiments, but also having lots of nice private chats. I want to thank Dorothee Marx for the preliminary work of the test set-up and a cordial welcome during my first PhD months. Andreas Reisinger, I want to thank you for a great collaboration, the development of the rheological model and for your inspiring ideas for future work.

In general, I want to thank all of my colleagues from the Institute of Light Weight Design and Structural Biomechanics, not only for the great professional support, but also for the nice lunch breaks at Naschmarkt and for a good time together besides work (especially for introducing the great sport of bouldering to me). Particularly, I want to thank my colleagues from the numerical biomechanics group, Tobias Haftner, Andrea Lorenz, Anastasiia Starikova, Lukas Steiner, Monika Stipsitz, and Alexander Synek. Alex, many thanks for our countless (not only scientific) discussions and our actually not too seldom morning chats. The same thanks goes to all my colleagues from the experimental biomechanics group, Orestis Andriotis, Caitlyn Collins, Martin (the hot) Handelshausner, Katja Haslinger, Matthis Nalbach, Vedran Nedelkovski, and Andreas Rohatschek. Moreover, I want to thank Robert Exler for the technical support with the test set-up, Maria Steininger for the organizational support, Gerhard Schneider for the IT support (which was, despite of initial complaints, always fast and reliable), and Helmut Böhm for showing how teaching can be really fun.

Last but not least I want to thank my parents, my family, and my friends for their great support, also in hard times. Because of you I could always relax besides work. My greatest thanks goes to Lina Bittner, my partner through thick and thin. Lina, you were and are my greatest support; you did not only show a lot of tolerance for the really intensive time, but you also make me always happy with your lovely kind.

Danksagung

Meine größte Dankbarkeit geht an Alle, die mich im Laufe der letzten sechs Jahre unterstützt haben. Als allererstes möchte ich meinen beiden Betreuern, Prof. Philipp Thurner und Prof. Dieter Pahr danken. Philipp, ich habe es sehr zu schätzen gelernt, dass du ein guten Mix aus klaren, interessanten Projektideen hattest und mir gleichzeitig sehr viel Eigenverantwortung und Flexibilität ermöglicht hast. Dieter, dir möchte ich dafür danken, dass du immer „das Große Ganze“ im Auge hattest und mich auch bei technischen Problemen mit tollen Lösungsvorschlägen unterstützt hast. Neben der beruflichen Unterstützung möchte ich euch beiden für ein sehr entspanntes und ausgeglichenes Klima in beiden Biomechanikgruppen danken. Einen besonderen Dank richte ich hier auch an meine beiden Prüfer, Prof. Ralph Müller und Prof. Christian Hellmich, nicht nur für die Einwilligung zur Beurteilung meiner Arbeit, sondern auch für die konstruktiven Anmerkungen auf Konferenzen.

Hervorheben möchte ich insbesondere die Unterstützung und Hilfe von allen meinen Projekt- und MasterstudentInnen, Seyedmasoud Chehrehrazi, Celestine Didier, Julia Fischer, Andreas Grabos, Omar Kabbani und Patrick Karner. Vielen Dank für die tolle Zusammenarbeit und eure zahlreichen Anmerkungen und Anregungen bei den Versuchen, die meine (und hoffentlich auch eure) Motivation für das wissenschaftliche Arbeiten gestärkt haben. Ganz besonders möchte ich dabei Julia und Andy danken, ihr beide habt eine so hervorragende Arbeit geleistet, dass wir sogar gemeinsame Publikationen schreiben konnten. Gerade im Labor hat es mir immer viel Spaß gemacht mit euch nicht nur über die Versuche, sondern auch privat zu plaudern und verdanke euch dort eine sehr schöne Zeit. Ich danke auch Dorothee

Marx für die tolle Vorarbeit zur Entwicklung des ursprünglichen Versuchsaufbaus und einen herzlichen Einstieg in meine ersten PhD-Monate. Andreas Reisinger, dir möchte ich für die tolle Zusammenarbeit danken, die Entwicklung des rheologischen Modells und für deine anregenden Ideen zur weiteren Forschung.

Generell danke ich allen meinen KollegInnen vom Institut für Leichtbau und Struktur-Biomechanik nicht nur für die tolle berufliche Unterstützung, sondern auch für die netten Mittagspausen am Naschmarkt und abseits für eine lustige Zeit zusammen (speziell auch dafür, mir das Bouldern schmackhaft gemacht zu haben). Besonders möchte ich mich bei meinen KollegInnen der numerischen Biomechanik bedanken, Tobias Haftner, Andrea Lorenz, Anastasiia Starikova, Lukas Steiner, Monika Stipsitz, und Alexander Synek. Alex, vielen Dank für unsere zahlreichen (nicht nur wissenschaftlichen) Diskussionen und die doch nicht zu seltenen morgendlichen Plaudereien. Derselbe Dank gilt auch meinen KollegInnen der experimentellen Biomechanik, Orestis Andriotis, Caitlyn Collins, Martin (the hot) Handelshäuser, Katja Haslinger, Matthis Nalbach, Vedran Nedelkovski, und Andreas Rohatschek. Außerdem möchte ich mich bei Robert Exler für die technische Unterstützung beim Versuchsaufbau, bei Maria Steininger für die organisatorische Hilfe, bei Gerhard Schneider für die IT-Hilfe (die trotz anfänglicher Beanstandung immer schnell und zuverlässig erfolgt ist) und bei Helmut Böhm dafür, mir zu zeigen, wie viel Spaß Unterrichten machen kann, bedanken.

Zu guter Letzt möchte ich mich bei meinen Eltern, meiner Familie und meinen Freunden für die tolle Unterstützung auch in schwierigen Zeiten bedanken. Dank euch habe ich abseits meiner Arbeit einen schönen Ausgleich gefunden und so immer wieder mal abschalten können. Mein allergrößter Dank gilt Lina Bittner, meiner Partnerin durch dick und dünn. Lina, du warst und bist immer meine wichtigste Stütze und hast nicht nur sehr viel Toleranz für die doch sehr intensive Zeit gehabt, sondern mich auch immer wieder mit deiner liebevollen Art glücklich gemacht.

Contents

Contents	ix
Abstract	xiii
Kurzfassung	xv
List of Figures	xvii
List of Tables	xxi
1 Introduction	1
1.1 Motivation	1
1.2 Aims	4
1.3 Structure of thesis	6
1.4 Paper contributions and declaration of contributions	7
2 Background	9
2.1 Hierarchical structure of trabecular bone	9
2.2 Advanced glycation end-products (AGEs)	11
2.3 Microdamage	14
2.4 Bone remodeling	15
2.5 Osteoporosis	18
2.6 Osteoporosis treatment	22
2.7 Mechanical characterization of trabecular bone tissue	25
3 Methods development and data analysis approaches	35
	ix

3.1	Tensile tests of individual trabeculae	36
3.2	Cyclic tensile testing of individual trabeculae	61
3.3	Elasto-visco-plastic rheological modeling of trabecular bone tissue	65
3.4	Microdamage formation in individual trabeculae during fatigue tests	70
4	Dehydration causes transition from ductile to quasi-brittle failure mode	89
4.1	Related publications and declaration of contributions	89
4.2	Introduction	90
4.3	Material and methods	92
4.4	Results	96
4.5	Discussion	104
4.6	Conclusions	109
5	Osteoporosis affects mainly morphometry not material properties in femoral head	111
5.1	Related publications and declaration of contributions	111
5.2	Introduction	112
5.3	Material and methods	113
5.4	Results	118
5.5	Discussion	132
5.6	Conclusions	140
6	Changes of material properties with anti-resorptive treatment	143
6.1	Related publications and declaration of contributions	143
6.2	Introduction	144
6.3	Material and methods	145
6.4	Results	150
6.5	Discussion	152
6.6	Conclusions	161
7	Influence of non-enzymatic glycation on the material properties	163
7.1	Related works and declaration of contributions	163
7.2	Introduction	164

7.3	Material and methods	165
7.4	Results	169
7.5	Discussion	170
7.6	Conclusions	173
8	Synthesis and outlook	175
8.1	Conclusion	177
8.2	Outlook	178
	Bibliography	181
	Appendix A: List of publications and co-supervisions	223
	Appendix B: Compression tests of individual trabeculae	227
	Appendix C: Three-point bending tests of individual trabeculae	231
	Curriculum Vitae	232



Die approbierte gedruckte Originalversion dieser Dissertation ist an der TU Wien Bibliothek verfügbar.
The approved original version of this doctoral thesis is available in print at TU Wien Bibliothek.

Abstract

Osteoporosis is the most common bone disease, however, only 60 % of patients with an increased fracture risk are correctly identified. Hereby, a major limitation is that mainly bone quantity (bone mass) is used for osteoporosis classification, whereas bone quality (bone architecture and material properties) is usually neglected. While bone architecture has already been shown to be deteriorated in aging and osteoporosis, much less is known about potential changes of the material properties of trabecular bone tissue (individual trabeculae). Similarly, anti-resorptive drugs, used for osteoporosis treatment, have been shown to improve the mechanical properties of whole bones, but their effect on the material properties remains elusive. Further, a few previous studies supposed that glycation of trabecular bone (occurring naturally with aging or in diabetes) causes a decrease of tissue toughness, but the found effects were weak. In general, previous studies on micro-mechanical experiments of individual trabeculae were limited by testing only a small number of samples in different, not well-defined loading scenarios mainly in air, which cannot reflect the physiological tissue behavior. Taken together, there is a strong need to perform a thorough mechanical characterization of individual trabeculae.

In the first part of this thesis a novel test set-up was developed to characterize individual trabeculae in defined monotonic, cyclic, and fatigue tensile tests in a wet environment at a high throughput rate. Further, a rheological model was applied to gain elastic, viscous, plastic, and failure properties of individual trabeculae in one single experiment.

In the second part, these procedures were used to determine the effects of hydration, osteoporosis, anti-resorptive treatment, and glycation on the apparent mechanical and material properties. A key finding of the cyclic loading experiments was that

trabecular bone tissue cannot be modeled properly as a linear-elastic material, as it demonstrates an elasto-visco-plastic behavior. Dehydration of individual bovine trabeculae indicated a 2-fold increase of tensile modulus and strength, accompanied with 3-fold decrease of toughness. As a consequence, previously determined material properties in air, that considered trabecular bone tissue as linear-elastic, are not reliable. Interestingly, apparent mechanical and material properties of individual human trabeculae from the femoral head were not significantly affected by osteoporosis or aging. In contrast, trabecular architecture was deteriorated in both conditions. Therefore, there is currently no need for computer simulations, such as Finite Element (FE) analysis, to adapt the input material properties due to aging or osteoporosis to predict fracture risk, at least in the femoral head. In contrast, anti-resorptive treatment of beagle dogs with alendronate (a bisphosphonate) resulted in a significantly larger tensile modulus and ultimate stress, associated with a significantly larger Tissue Mineral Density (TMD). Further, anti-resorptive treatment with raloxifene (a selective estrogen receptor modulator) caused a significantly larger toughness. Hence, improved whole bone mechanics is partially related to enhanced material properties, but the underlying mechanisms are distinct between different drugs. *In vitro* glycation of individual bovine trabeculae indicated an increased dynamic modulus and secant modulus. However, because of a limited sample size (15 in total), no final conclusions could be drawn so far.

In conclusion, this thesis highlighted that trabecular bone tissue has to be modeled as an elasto-visco-plastic material. Hereby, the results reported in this thesis suggest that modeling of trabecular bone tissue in the human femoral head can be performed independently from aging or osteoporosis, such as in FE analysis for prediction of fracture risk. The improved whole bone mechanics after anti-resorptive treatment is at least partly caused by improved material properties. The presented findings will contribute to a better fracture risk prediction and a more profound understanding of the influence of bone quality on whole bone mechanics.

Kurzfassung

Osteoporose ist die häufigste Knochenerkrankung, allerdings werden nur 60 % der PatientInnen mit einem erhöhten Frakturrisiko korrekt identifiziert. Ein Hindernis ist, dass hauptsächlich die Knochenmenge (Knochenmasse) in die Osteoporoseklassifizierung einbezogen wird, während die Knochenqualität (Architektur und Materialeigenschaften) nicht berücksichtigt wird. Bei Alterung und Osteoporose kommt es zu einer Verschlechterung der Knochenarchitektur, während wenig über deren Effekt auf die Materialeigenschaften von trabekulären Knochen (Einzeltrabekel) bekannt ist. Zudem wurde gezeigt, dass antiresorptive Medikamente, die zur Osteoporosebehandlung verwendet werden, die mechanischen Eigenschaften von ganzen Knochen verbessern, aber deren Effekt auf die Materialeigenschaften ist unklar. Des Weiteren haben wenige frühere Studien vermuten lassen, dass Glykierung von trabekulärem Gewebe (welche natürlich bei Alterung und Diabetes vorkommt) eine Reduzierung der Gewebestärke verursacht, wobei die Resultate wenig aussagekräftig waren. Generell waren vorherige Studien über die mikromechanischen Eigenschaften von Einzeltrabekeln aufgrund einer kleinen Probenanzahl und verschiedenen, nicht genau definierten Lastfällen und Tests in Luft, die das physiologische Verhalten nicht widerspiegeln können, limitiert. Folglich besteht ein großer Bedarf an einer gründlichen mechanischen Charakterisierung von Einzeltrabekeln.

Im ersten Teil dieser Arbeit wurde ein neuartiger Testaufbau entwickelt, um Trabekel in definierten monotonen, zyklischen, und Ermüdungsversuchen unter Zug, in feuchter Umgebung und mit hoher Durchsatzrate zu testen. Weiters wurde ein rheologisches Modell angewandt, um die elastischen, viskosen, plastischen und Versagensmerkmale von Trabekeln in einem einzelnen Experiment zu bestimmen.

Im zweiten Teil der Arbeit wurden diese Methoden verwendet um die Effekte von Hydrierung, Osteoporose, antiresorptiver Behandlung und Glykierung auf die apparenten mechanischen und Materialeigenschaften zu bestimmen. Ein zentrales Ergebnis der zyklischen Tests war, dass trabekuläres Knochengewebe nicht adäquat als linear-elastisch beschrieben werden kann, sondern ein elastisch-viskoses-plastisches Material ist. Dehydrierung von Rindertrabekeln führte zu einer 2-fachen Erhöhung des Zugmoduls und der Festigkeit, sowie zu einer 3-fachen Abnahme der Zähigkeit. Infolgedessen sind zuvor bestimmte Materialeigenschaften in Luft, die trabekuläres Knochengewebe als linear-elastisch annahmen, nicht zuverlässig. Unerwartet war, dass die mechanischen und Materialeigenschaften menschlicher Trabekel nicht signifikant von Osteoporose oder Alterung betroffen sind. Allerdings war die Knochenarchitektur unter beiden Bedingungen verschlechtert. Daher gibt es momentan keinen Grund bei Computersimulationen, wie FE Analysen, eine Anpassung der verwendeten Materialeigenschaften aufgrund von Alterung oder Osteoporose vorzunehmen, um das Frakturrisiko im Femurkopf zu berechnen. Im Gegensatz dazu zeigte die Behandlung von Hunden mit Alendronat eine signifikante Erhöhung von Zugmodul und Festigkeit, verbunden mit einer signifikant erhöhten Mineralisierungsdichte. Außerdem resultierte die Behandlung mit Raloxifen in einer signifikant erhöhten Zähigkeit. Somit kann die verbesserte Mechanik von ganzen Knochen teilweise auf verbesserte Materialeigenschaften zurückgeführt werden, wobei hier verschiedene Mechanismen zwischen den Medikamenten verantwortlich sind. *In vitro* Glykierung von Rindertrabekeln zeigte einen erhöhten dynamischen Zug- und Sekanten-Modul. Jedoch konnten aufgrund der begrenzten Stichprobengröße (15 Proben gesamt) noch keine endgültigen Schlussfolgerungen gezogen werden. Zusammenfassend wurde in dieser Arbeit hervorgehoben, dass trabekulärer Knochen als elastisch-viskoses-plastisches Material beschrieben werden muss. Die Modellierung von trabekulärem Knochengewebe des humanen Femurkopfes kann unabhängig von Alterung oder Osteoporose erfolgen, wie z.B. in FE Analysen zur Vorhersage des Frakturrisikos. Die verbesserten mechanischen Eigenschaften von ganzen Knochen nach antiresorptiver Behandlung sind zumindest zum Teil auf verbesserte Materialeigenschaften zurückzuführen. Die präsentierten Ergebnisse werden sowohl zu einer besseren Vorhersage des Frakturrisikos, als auch zu einem tieferen Verständnis des Einflusses der Knochenqualität auf die gesamte Knochenmechanik beitragen.

List of Figures

1.1	Graphical abstract	5
2.1	Hierarchical structure of trabecular bone	12
2.2	Formation of Advanced Glycation End-products (AGEs)	13
2.3	Different types of microdamage stained with basic fuchsin	16
2.4	Basic multicellular unit (BMU), bone remodeling; terminal differentia- tion of osteoblasts and osteoclastogenesis	17
2.5	Dual X-ray absorptiometry	20
2.6	Scanning Electron Microscopy (SEM) image of normal and osteoporotic bone	21
2.7	Mechanical characterization of trabecular bone tissue	26
2.8	Scanning acoustic microscopy (SAM)	28
2.9	Mean values of elastic tissue modulus determined with different tech- niques	34
3.1	Bone dissection	40
3.2	Specimen preparation	42
3.3	Digital Image Correlation (DIC)	49
3.4	Strain tracking, alignment and FE-modeling	50
3.5	Determination of cross-sectional area	52
3.6	Estimation of tilt influence on stiffness and strength with a simple FE-model	55
3.7	Stress-strain curves of tensile experiments of individual trabeculae close to a physiologic environment	57
3.8	Cyclic loading profiles	63
3.9	Determination of tensile modulus evolution in cyclic tensile testing	64

3.10	Determination of apparent mechanical properties by curve-fitting on the envelope curve	65
3.11	2-layer rheological model	70
3.12	Loading profile and stress-strain determination with the 2-layer rheological model	71
3.13	Effects of neglecting different elements of the 2-layer model	72
3.14	Stress-strain diagram for fatigue loading	76
3.15	Determination of damage area	78
3.16	Microdamage formation shown for different cycle numbers	80
3.17	Microdamage density, dependent on the number of fatigue cycles	81
3.18	Confocal images of microdamage in 2D and 3D images	86
3.19	Adjustment of displacement in fatigue tests	87
3.20	Constant holding ahead of testing in fatigue tests	87
4.1	Operation chart for whitening detection in speckle-patterned trabeculae	95
4.2	True stress-strain curves for wet and dry trabeculae	97
4.3	Apparent mechanical properties of wet and dry trabeculae	98
4.4	Full field strain maps of a selected dry and wet trabecula	100
4.5	Whitening of a selected wet and dry trabecula	102
4.6	Correlation of strain at whitening onset with apparent yield strain	103
4.7	Fracture surface analysis of dry and wet trabeculae	103
5.1	Operation chart osteoporosis	119
5.2	Clinical data of osteoporotic and control patients	120
5.3	Tensile modulus evolution of osteoporotic and control trabeculae	121
5.4	Material parameters determined with the rheological model and apparent mechanical properties determined with curve fitting of osteoporotic and control trabeculae, based on the fracture criterion	123
5.5	Material parameters determined with the rheological model and apparent mechanical properties determined with curve fitting of osteoporotic and control trabeculae, based on the T-score	124
5.6	TMD distributions of individual trabeculae	127
5.7	TMD histograms of individual trabeculae	128

5.8	Correlation plots of mean TMD with apparent mechanical and material properties	128
5.9	μ CT-derived bone morphometry, based on the fracture criterion . . .	130
5.10	μ CT-derived bone morphometry, based on the T-score	131
5.11	Representative cross-sectional slices of bone spheres, used for μ CT-derived bone morphometry	131
5.12	Correlation of μ CT-derived bone morphometry and material properties with age	132
5.13	Effect of holding period on unloading modulus	133
6.1	Determination of whitening as stop criterion shown for a selected sample	148
6.2	Selected stress-strain curves of alendronate, control and raloxifene treated specimens	152
6.3	Boxplots of material properties determined with the rheological model and apparent mechanical properties, determined with curve fitting, of alendronate, control and raloxifene treated specimens	153
6.4	Tissue mineral density and its correlation with dynamic modulus of alendronate, control and raloxifene treated specimens	154
6.5	Selected microscopy images stained with basic fuchsin for microdamage and boxplot of damage density of alendronate, control and raloxifene treated specimens	154
7.1	Induction of Non-Enzymatic Glycation (NEG) with ribose	168
7.2	Selected stress-strain curves of control and glycation treated trabeculae	171
7.3	Stress-strain curve and cyclic tensile modulus after glycation	171
B1	Compression tests of individual trabeculae - with x-y table	228
B2	Compression tests of individual trabeculae - without x-y table	229
C1	Three-point bending set-up for testing individual trabeculae	231



Die approbierte gedruckte Originalversion dieser Dissertation ist an der TU Wien Bibliothek verfügbar.
The approved original version of this doctoral thesis is available in print at TU Wien Bibliothek.

List of Tables

3.1	Influence of chosen cross-sectional area on apparent mechanical parameters	58
4.1	Apparent mechanical properties of dry and wet trabeculae	99
5.1	Baseline clinical characteristics of osteoporotic and control patients .	120
5.2	Tensile loading and unloading modulus of the first three cycles of osteoporotic and control trabeculae	121
5.3	Material properties determined with the rheological model and apparent mechanical properties determined with curve fitting on the envelope curve of osteoporotic and control trabeculae	122
5.4	Material properties determined with the rheological model and apparent mechanical properties determined with curve fitting on the envelope curve of transversal and longitudinal trabeculae	126
5.5	TMD of osteoporotic and control trabeculae	126
5.6	μ CT-derived bone morphometry of osteoporotic and control trabeculae	129
6.1	Material properties determined with the rheological model and apparent mechanical properties determined with curve fitting on the envelope curve of alendronate, control, and raloxifene treated specimens	155
6.2	Mean TMD obtained with μ CT and variables obtained with micro-damage assessment for alendronate, control, and raloxifene treated specimens	155
7.1	Components of glycation and control treatment solution	168

7.2	Material properties determined with the rheological model and apparent mechanical properties determined with curve fitting on the envelope curve of control and glycated trabeculae	170
-----	-----------------------------------------------------------------------------------------------------------------------------------------------------------------------------------------------	-----

List of Abbreviations and Symbols

- 2D** Two-dimensional
- 3D** Three-dimensional
- aBMD** areal Bone Mineral Density
- AGEs** Advanced Glycation End-products
- BP** Bisphosphonate
- CLSM** Confocal Laser Scanning Microscopy
- CV** Coefficient of Variation
- CT** Computed Tomography
- DEXA** Dual Energy X-ray Absorptiometry
- DIC** Digital Image Correlation
- FE** Finite Element
- FRAX** Fracture Risk Assessment Tool
- HBSS** Hanks Balanced Salt Solution
- IQR** Inter Quartile Range
- K.W.** Kruskal-Wallis-test
- NCPs** Non Collagenous Proteins
- NEG** Non-Enzymatic Glycation
- NoC** Number of Cycles
- qBEI** quantitative Back-scattered Electron Imaging

RMSE Root Mean Square Error

ROI Region of Interest

SAM Scanning Acoustic Microscopy

SEM Scanning Electron Microscopy

SERM Selective Estrogen Receptor Modulator

SNR Signal to Noise Ratio

TMD Tissue Mineral Density

Bone Histomorphometry

BS Bone surface

BV/TV Bone volume to total volume

DA Degree of anisotropy

Tb.N Trabecular number

Tb.Sp Trabecular separation

Tb.Th Trabecular thickness

Bone Microdamage

BA Bone area

Cr.Dn Linear microcrack density

Cr.N Linear microcrack number

Df.Ar Diffuse area

Df.Dx.Dn Diffuse damage density

Dx.Ar Damage area

Dx.Dn Damage density

Apparent mechanical properties

\hat{E} Apparent elastic modulus

$\hat{\epsilon}_y$ Apparent yield strain

$\hat{\epsilon}_{y0.2}$ Apparent yield strain at 0.2 % offset

$\hat{\epsilon}_u$ Apparent ultimate strain

$\hat{\sigma}_h$ Apparent hardening stress

$\hat{\sigma}_y$ Apparent yield stress

$\hat{\sigma}_{y0.2}$ Apparent yield stress at 0.2 % offset

$\hat{\sigma}_u$ Apparent ultimate stress

\hat{p} Apparent hardening coefficient

\hat{W}_{el} Apparent elastic work

\hat{W}_{py} Apparent post-yield work

Material properties

$E_{pr} \equiv E_{\infty}$ Prandtl-layer/Long-term elastic modulus

E_{mx} Maxwell-layer/Dynamic elastic modulus

E_0 Instantaneous elastic modulus

σ_y Yield stress

p Hardening coefficient

σ_u Ultimate stress

η Viscosity

$\tan(\delta)$ Loss tangent



Die approbierte gedruckte Originalversion dieser Dissertation ist an der TU Wien Bibliothek verfügbar.
The approved original version of this doctoral thesis is available in print at TU Wien Bibliothek.

CHAPTER 1

Introduction

“In nature there is no difference between design, engineering and fabrication; the bone does it all.”

Neri Oxman

1.1 Motivation

Osteoporosis is the most common bone disease with an estimated lifetime risk of (30 to 40) %, close to that of coronary heart disease [1]. In our aging society the demographic shift is expected to even increase the numbers of osteoporotic fractures further. For instance the amount of annual fractures has been projected to increase by 68 %, the costs even by 74 %, in the United States by 2040 [2]. Currently, osteoporosis is under-diagnosed and under-treated [3], although early intervention is essential in preventing disease progression [4]. One major limitation is that diagnosis is mainly based on determination of bone mass (quantity) [5, 6], which only identifies 60 % of patients needed to treat correctly [1]. Sequentially, also bone quality parameters, such as bone structure/architecture and material/tissue properties should be considered as additional indicators in determination of an increased fracture risk. In more detail it is essential to identify and quantify bone quality parameters that might be affected by osteoporosis. Regions rich in trabecular bone are predominantly effected by osteoporotic fractures, like the femoral neck and the

vertebrae [7], and thus, especially trabecular bone quality should be investigated. At the structural level, trabecular bone consists of a Three-dimensional (3D) network of millimeter sized struts and plates, so called trabeculae [8]. These trabeculae are the building blocks of trabecular bone and are referred as the tissue level, including the material properties (see section 2.1 for further details).

So far, trabecular bone quality has been mainly investigated at the structural level in aging and osteoporosis and indicated a deterioration of bone architecture [9]. In contrast, changes of the material properties have been reported controversially [10]. Previous studies determined mainly the elastic properties of individual trabeculae in several non-uniform test procedures, whereby reported values varied over one order of magnitude [11]. Thus, a direct comparison of values obtained from different studies is almost impossible. Possible reasons for this large deviations are difficulties in handling of microscopic samples, undefined test conditions, and different test procedures [12]. Particularly, a small sample size, accompanied with a large biological variation [13, 14], and testing at non-physiologic, dry conditions [15–17] contribute to discrepancies in the reported material properties.

As a consequence, a defined test procedure in a wet, physiologic environment is needed at a high throughput to determine, if clinically relevant changes of material properties occur in osteoporosis. Further, material properties should not be limited solely to the elastic behavior, as trabecular bone tissue has been shown to own a pronounced post-yield phase [18], and a strain-rate dependent, viscous behavior [19, 20]. Hereby, characterization of the material behavior at physiological loading scenarios, such as impact and fatigue, is important, in addition to monotonic tests [21]. If material properties change significantly in osteoporosis, this knowledge should be incorporated in an improved diagnosis of fracture risk. On the other hand, if material properties remain unaffected, then prediction of fracture risk can be performed with current computer simulations, such as FE analysis, without the necessity to adapt the material properties between healthy and osteoporotic patients. These simulations are able to predict patient specific strength of bones, such as the distal radius [22] or vertebrae [23] better than imaging modalities alone [24].

Identified patients with a high fracture risk are conventionally treated with so-called anti-resorptive drugs [25]. Hereby, the increase of bone mass (quantity) after treatment was demonstrated to be mainly responsible for the decrease of the fracture risk in the most commonly used drugs, namely Bisphosphonate (BP) [26]. However, treatment with a novel drug, raloxifene, resulted in a similar decrease of fracture risk, but merely increased bone mass [27]. Sequentially, changes at the material/tissue level, rather than bone quantity, are likely responsible for the beneficial whole bone mechanics after treatment. However, the effects of especially bisphosphonates on the material properties of individual trabeculae have only been determined in one single study [28] (where no change was reported) and thus the effect of anti-resorptive treatment on the material properties of trabecular bone tissue remains unclear [29].

Recently, also diabetes in the elderly has been associated with an increased fracture risk [30]. Hereby, increased levels of sugars cause the formation of so-called AGEs, which are thought to make bone more brittle and as such, more likely to fracture [31]. Besides diabetes, an accumulation of AGEs occurs naturally with aging [32], in osteoporosis [33], and after bisphosphonate treatment [34]. Analysis of the effect of increased levels of AGEs on the material properties of individual trabeculae has only been performed in two previous studies [35,36] and the effect was found to be only moderate. Hence, more studies are necessary to investigate if there is a clinically relevant effect of AGEs on the material properties of trabecular bone tissue.

Taken together, there is a strong need of a thorough characterization of the material properties of trabecular bone tissue in aging, osteoporosis, treatment, and glycation. A profound knowledge of the material properties will enable a better diagnosis and determination of treatment success.

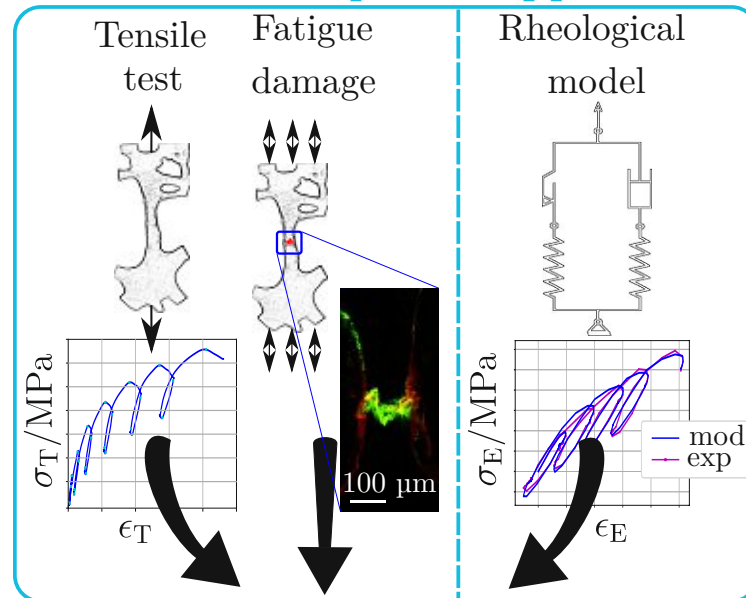
1.2 Aims

The primary goal of this thesis was to thoroughly characterize the mechanical behavior of individual trabeculae. As such, the first goal was to develop a reliable test set-up that enables testing of individual trabeculae in a wet environment at a high throughput. Second, this test set-up should be used to determine if there are clinically relevant effects of hydration, aging, osteoporosis, glycation, or anti-resorptive treatment on the material properties of trabecular bone tissue (see figure 1.1).

1. Establishment of mechanical characterization procedures
 - a) Development of a tensile test set-up for mechanical characterization of individual trabeculae close to a physiologic, wet environment at a high sample throughput
 - b) Application of a rheological model to evaluate the material properties of individual trabeculae (elastic modulus, viscosity, yield point, post-yield hardening, and failure properties)
 - c) Development of a fatigue test for microdamage induction in individual trabeculae
2. Investigation of clinically relevant research hypotheses:
 - a) Dehydration of individual trabeculae causes a transition towards a brittle mechanical behavior
 - b) Deterioration of trabecular bone architecture in osteoporosis and aging is associated with altered material properties of individual trabeculae
 - c) Improved whole bone mechanics after anti-resorptive treatment of osteoporosis is caused by improved material properties of individual trabeculae
 - d) Accumulation of AGEs causes a stiffening of individual trabeculae together with a reduced toughness

Mechanical characterization of individual trabeculae

Methods developed & applied



Determined effects of

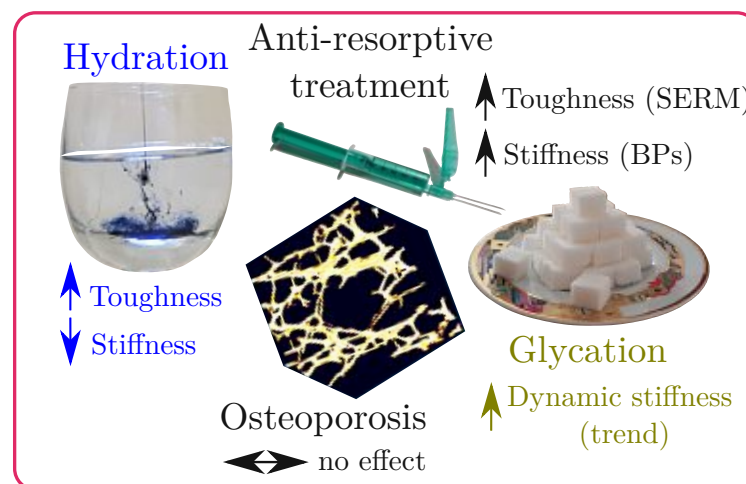


Figure 1.1: Graphical abstract. Mechanical characterization of individual trabeculae was performed by a novel tensile test, in combination with a rheological model. Hereby, cyclic loading was used to extract comprehensive material properties. Further, a fatigue damage test was developed to induce microdamage. These methodological approaches were used to determine the effects of hydration, glycation, osteoporosis, and anti-resorptive treatment on the apparent mechanical and material properties. In short, hydration increased tissue toughness, but decreased tissue stiffness. Osteoporosis indicated no significant effect. Anti-resorptive treatment caused an increase of stiffness for alendronate (a BP) and an increase of toughness for raloxifene (a SERM). Glycation showed a trend of increased dynamic stiffness.

1.3 Structure of thesis

Chapter 2 provides an overview about the background of the current thesis. Following topics are outlined: The hierarchical structure of trabecular bone (section 2.1), advanced glycation end-products (AGEs) (section 2.2), microdamage (section 2.3), bone remodeling (section 2.4), osteoporosis (section 2.5), osteoporosis treatment (section 2.6), and the mechanical characterization of trabecular bone tissue (section 2.7).

Chapter 3 describes the methods developed and applied in this thesis. Section 3.1 presents the developed tensile test set-up and the determination and evaluation of the obtained stress-strain curves. Section 3.2 describes cyclic tensile tests for a more comprehensive material characterization. Section 3.3 illustrates the refined evaluation of the mechanical experiments, based on a rheological model developed in a joint project by Andreas Reisinger. Next, section 3.4 explains the developed fatigue test for microdamage formation and the applied staining procedure for microdamage visualization.

Chapter 4 addresses the effects of dehydration on the material properties of bovine individual trabeculae, with an emphasis on the damage and fracture behavior. Further, **Chapter 5** presents the alterations of human trabecular bone structure and tissue in osteoporosis and aging. **Chapter 6** illustrates changes in the apparent mechanical and material properties, and microdamage accumulation in beagle dogs treated with anti-resorptive drugs. Finally, **Chapter 7** shows the effects of accumulation of AGEs on the mechanical behavior of bovine trabecular bone tissue.

Chapter 8 synthesizes the obtained results of the previous chapters regarding the mechanical characterization of individual trabeculae and the effects of hydration, aging, osteoporosis, treatment, and glycation on the material properties. Finally, an outlook highlights the importance of the obtained results and possible future research questions that should be addressed.

1.4 Paper contributions and declaration of contributions

This thesis is based on the following publications. In publications I-III the author of the current thesis contributed to the study design, performed the methodology, the formal analysis, the investigation, and wrote the manuscript.

- I M. Frank, D. Marx, D. H. Pahr, and P. J. Thurner. Mechanical properties of individual trabeculae in a physiological environment. *Proceedings of the 13th IASTED International Conference on Biomedical Engineering, BioMed 2017*, pages 141–146, 2017.
- II M. Frank, D. Marx, V. Nedelkovski, J. T. Fischer, D. H. Pahr, and P. J. Thurner. Dehydration of individual bovine trabeculae causes transition from ductile to quasi-brittle failure mode. *Journal of the Mechanical Behavior of Biomedical Materials*, 87(July):296–305, 2018.
- III M. Frank, A. G. Reisinger, D. H. Pahr, and P. J. Thurner. Effects of osteoporosis on bone morphometry and material properties of individual human trabeculae in the femoral head. Conditionally accepted in *Journal of Bone and Mineral Research - Plus*.

In publications IV-V (* joint first author) the author of the current thesis contributed to the study design, performed the formal analysis, the data curation, and wrote the manuscript. The joint first authors, *J.-T. Fischer* (paper IV) and *A. Grabos* (paper V) performed the investigation, the methodology, and the validation, respectively. Further, the author of the current thesis co-supervised their work in course of their diploma thesis. A more detailed description about the contributions of each author is always given at the beginning of the corresponding chapters.

- IV M. Frank*, J.-T. Fischer*, and P. J. Thurner. Microdamage formation in individual bovine trabeculae during fatigue testing. *Journal of Biomechanics*, 2021 Jan 22;115:110131

1. INTRODUCTION

V M. Frank*, A. Grabos*, A. G. Reisinger, D. B. Burr, D. H. Pahr, M. R. Allen, and P. J. Thurner. Effects of anti-resorptive treatment on the material properties of individual canine trabeculae in cyclic tensile tests. Conditionally accepted in *Bone*

Further, the author of the current thesis provided the experimental data for publication VI. The first author of that paper, *A. G. Reisinger* developed the rheological model, which was applied in course of the present thesis (and related publications) to gain the material properties of individual trabeculae from cyclic loading experiments.

VI A. G. Reisinger, M. Frank, P. J. Thurner, and D. H. Pahr. A two-layer elasto-visco-plastic rheological model for the material parameter identification of bone tissue. *Biomechanics and Modeling in Mechanobiology*, 19, 2149–2162 (2020)

CHAPTER 2

Background

“Somehow, we have the erroneous belief that we are all but flesh, blood, and bones and that’s all. So we direct our values to material things”

Maya Angelou

2.1 Hierarchical structure of trabecular bone

Bone is a fascinating organ that demonstrates remarkable mechanical properties, which are mainly attributed to the hierarchical structure of bone tissue [37]. A profound knowledge of this hierarchy and its functions is essential to be able to perform mechanical tests at different levels. Four major levels can be distinguished, namely whole bone, macroscale, microscale, and nanoscale [38], as seen in figure 2.1. Weiner and Wagner [39] and Rho et al. [40] even specified seven different hierarchical levels, by adding the sub-micro-structure, an additional level at the nano-structure (consisting now of two nano-levels), and the sub-nano-structure.

At the *macroscale* bone is composed of trabecular and cortical bone, which both are built from lamellar bone, the most abundant type in mammals, including humans [41]. Cortical bone is a very dense, compact material that serves mainly as a load bearing structure, like in the middle of long bones (diaphysis) or as a shell surrounding trabecular bone, like at the end of long bones (epiphysis),

in flat bones (e.g. skull), and irregular bones (e.g. vertebrae) [42]. In contrast, trabecular bone is a highly porous material, built up by tiny struts and plates, so called trabeculae [8]. These structures are aligned along trajectories of principal stress to transmit forces between the ends of long bones and the diaphysis [43,44].

At the *microscale* individual trabeculae are formed by trabecular bone packets, which are separated by cement lines [45]. These packets are formed during the remodeling process, similar to osteons in cortical bone [42]. Thus, individual bone packets show a different mineralization, whereby outer packets have a lower mineralization compared to central ones (see figure 2.1-D), since remodeling occurs on the trabecular surface [46]. As trabecular bone is subjected to a higher bone turnover rate than cortical bone [42], metabolic diseases, like osteoporosis, affect more regions with high trabecular bone content, such as vertebrae, hip, and distal radius [47] (see section 2.5).

At the *sub-microscale* bone packets are built from individual lamellae, which are (3 to 5) μm thick [37]. The lamellae are composed of sublayers, built of arrays of aligned mineralized collagen fibrils (see figure 2.1-F). The orientation of these plywood-like structures differs with respect to the collagen fibril axis and crystal planes.

At this scale bone cells become visible, which are responsible for bone remodeling [48] (see section 2.4). Hereby, four different cell types are distinguished: osteoblasts, which deposit new bone matrix; bone lining cells, essential in the transitions of bone remodeling and the involved signaling processes; osteocytes, responsible for mechanical load and damage sensing, and osteoclasts, which remove bone matrix [49]. Microdamage, occurring between or inside individual lamellae [50], is usually caused by repetitive loading [51] and acts as a stimulus for bone remodeling [52]. Anti-resorptive treatments, such as bisphosphonates, decrease bone resorption and were demonstrated to increase the amount of microdamage [53], which in extreme cases can lead to atypical fractures [54] (see section 2.6).

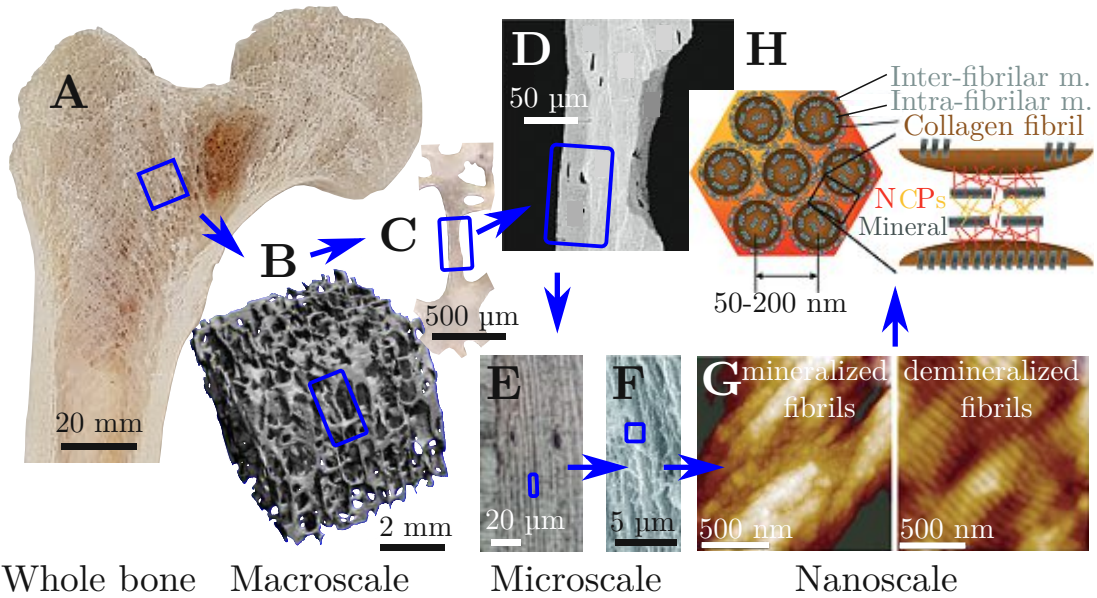
At the *nanoscale*, fibril arrays are formed by mineralized collagen fibrils [55]. First, collagen type I molecules self-assemble in a typical staggered fashion into

fibrils. Then, hydroxyapatite crystals fill the gap regions within the fibrils (intra-fibrillar mineral) [56] and cover the entire fibril surface (extra-fibrillar mineral) [57] to perform tissue mineralization. Non Collagenous Proteins (NCPs) control the size and shape of extra-fibrillar mineral crystals, most likely facilitate the attachment of these with the fibrils, and build the interface between adjacent mineralized fibrils [58]. Moreover, NCPs were demonstrated to facilitate self-healing of rejoined trabecular fracture surfaces based on ion-mediated bonds [59]. At this scale the formation of AGEs between individual collagen molecules and other proteins occurs, which is caused by an accumulation of sugars e.g. with increasing age [32], and in diabetes [60] (see section 2.2). These cross-links were reported to decrease bone toughness at the scale of individual trabeculae [36], however, correlations were weak ($r^2 = 0.09$) and no final conclusions could be drawn yet. Further, the origin of microdamage is also at this scale, in particular inside the collagen fiber-matrix and the mineral-collagen aggregate [61].

At the *sub-nanoscale* trabecular bone consists of vol. 27% water, compared to vol. 23% in cortical bone [62, 63], besides the protein and mineral phase. As bone is a living material, also the relative composition of its substitutes can change with age, disease, and treatment [64]. Especially, the hydration state of bone is essential, since dehydration has been shown to change both the structure and the mechanical properties of trabecular bone [65]. Further, changes at the lamellar level [16] and at the level of individual trabeculae [66] have been associated with dehydration. Thus, reliable mechanical characterization has to be always carried out in a physiologic, wet environment (see section 2.7).

2.2 Advanced glycation end-products (AGEs)

For a long time post-translational modification of proteins by Non-Enzymatic Glycation (NEG) was thought to only occur in slow turnover tissue, such as cartilage and tendon [60, 69]. However, during the last two decades it was demonstrated that bone does not turn over uniformly, showing areas with slow turnover that sequentially also become susceptible to post-translational modification by NEG [70]. Hereby, NEG causes the formation of AGEs, which were demonstrated to increase



Whole bone Macroscale Microscale Nanoscale

Figure 2.1: Hierarchical structure of trabecular bone, based on Georgiadis et al. [67]. At the macroscale trabecular bone is built of a network of struts and plates, the trabeculae. At the microscale, these individual trabeculae, composed of trabecular bone packets, which are formed by several lamellae, can be observed. At the nanoscale, bone is composed of mineralized collagen fibrils, non-collagenous proteins, and water. **A**: Human femur cut in half. **B**: Trabecular network, imaged with μ Computed Tomography (CT). **C**: Individual rod-shaped trabecula, imaged with phase contrast microscopy. **D**: Individual trabecular bone packets are shown at different gray levels, separated by bright cement lines, imaged with quantitative Back-scattered Electron Imaging (qBEI); modified from Fratzl et al. [45]. **E**: Magnified region of polished trabecular bone surface illustrating individual lamellae and lacunae, imaged with bright field microscopy. **F** Mineralized collagen fibrils, imaged with SEM in secondary imaging mode; reprinted from Thurner et al. [59]. **G**: Mineralized collagen fibrils (left) and demineralized fibrils (right), imaged with atomic force microscopy (AFM); reprinted from Kindt et al. [68]. **H**: Nanoscale model of bone, indicating collagen fibrils, mineral, and NCPs; reprinted from Thurner et al. [58].

with age and diabetes [71], but also in osteoporosis [33]. In more detail, AGEs are formed in the presence of sugars by condensation with free amino groups such as lysine and arginine [31] (see figure 2.2). Hereby, specific types of AGEs, like the formation of pentosidine, requires a sequential oxidation reaction, whereas other types of AGEs form in non-oxidative reactions [72].

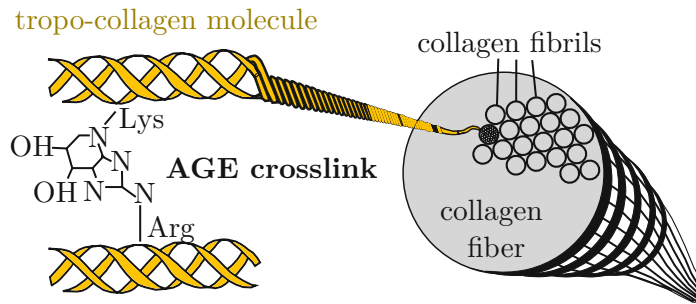


Figure 2.2: Formation of AGEs between collagen molecules by condensation with free amino groups of lysine (Lys) and arginine (Arg) (modified from Gautieri et al. [73]).

NEG of bone occurs both in collagenous and non-collagenous matrix proteins, however, due to the abundance of type I collagen in bone, AGEs are reported in terms of collagen [70]. AGEs are a representation of several inter-molecular crosslinks [74], whereby only two, pentosidine and carboxymethyl-lysine (CML), have been quantified in bone [31]. Hereby, CML concentration is 40–100 times greater than pentosidine [75]. Although pentosidine shows a significant correlation with total AGEs in bone, its accumulation is different between cancellous and cortical bone (of the same apparent volume) [76]. Nevertheless, pentosidine has been demonstrated as a reliable biomarker for bone loss in aging, showing an exponential increase of its plasma concentration with age [32].

Besides NEG, also enzymatically-mediated collagen cross-links increase with age, but these make the bone stiffer and stronger [77]. In contrast, there is evidence for AGEs to make cortical bone more brittle and more likely to fracture [31, 78], and to cause a reduced toughness of individual trabeculae [36]. However, only weak correlations ($R^2 = 0.09$) were determined, and thus, more research is needed for

confirmation. Further, a reduction in the degree of mineralization and an excessive formation of pentosidine in the femoral neck were considered as potential sources of poor bone quality in osteoporosis [79]. Osteoporosis is conventionally treated with bisphosphonates (see section 2.6), which slows down bone remodeling and thus might cause an accumulation of AGEs. Indeed, Tang et al. showed that one-year treatment of dogs with risedronate or alendronate (but only at doses $5\times$ higher as used in clinics) resulted in a significant accumulation of AGEs in the cortical tibia, associated with a reduction of post-yield work-to-fracture [80]. Further, artificial glycation of cancellous bone cores resulted in a reduction of damage fraction, accompanied by a stiffness loss [35] and loss of toughness [36] of individual trabeculae, also suggesting a weakening of bone at the tissue level. However, this previous data was not conclusive, since selected trabeculae showed a non-homogeneous geometry, associated with a large deviation, and only weakly significant differences were reported in a few mechanical properties (ultimate strain and secant stiffness at point of failure). Thus, only a comprehensive mechanical characterization of trabecular bone tissue will shed light on potential changes with accumulation of AGEs.

At the bone cellular level AGEs were shown to promote apoptosis of osteoblastic cells and further contribute to deficient bone formation [81]. Another effect of AGEs is the stiffening of collagen by cross-links, hindering fibrillar sliding, which is essential for plastic deformation in bone [78]. In aged bone this effect might cause increased microcracking at larger scales to compensate for this reduction in toughness.

2.3 Microdamage

The term microdamage is used to describe microscopic cracks that are formed during daily activities, such as walking, by fatigue loading of bone [50]. Three distinct types of microdamage can be distinguished (see figure 2.3): Two different patterns of microcracks, namely linear and cross-hatching, and diffuse damage [82, 83].

Linear microcracks have a preferential orientation and are typically $50\ \mu\text{m}$ [84] to $90\ \mu\text{m}$ [85] long, whereas their thickness is only a few micrometer. In cortical

bone, linear microcracks have been shown to be preferentially formed along the lamellar interfaces, which have been loaded in compression [86]. Linear microcracks trigger bone remodeling [87] (see section 2.4), which essentially causes removal of the damaged bone site and replacement with new bone.

In contrast, *diffuse damage* is repaired by different mechanisms that do not involve the bone remodeling process [88, 89]. Diffuse damage is formed by sub-microscopic cracks inside lamellae and has been shown to be dominant in tensile loaded regions [90]. Morphologically, diffuse damage can be classified as damage that has no preferential orientation in any direction [50].

Cross-hatching shows a typical pattern (see figure 2.3) and was less frequently observed than linear microcracks, in human vertebrae [83]. Similar to linear microcracks, cross-hatching was reported to be present in compressive areas, such as vertical trabeculae in vertebrae. However, cross-hatching seems to be only present close to the trabecular surface, in contrast to linear microcracks.

Aging has been reported to be associated with an accumulation of microdamage, even exponentially after the age of 40 [61]. One possible explanation for this accumulation might be a slow down of repair mechanism in the aging body [50], which might even result in extreme cases in stress fractures [91], as suggested by a mathematical model [92].

2.4 Bone remodeling

Bone is a living tissue, which is able to self-repair [94] and to adapt to mechanical loading [95]. This feature is attributed to cells located within bone and known as bone remodeling [48]. Hereby, the average rate of bone turnover is 3.6 % per year in healthy adults and might be doubled in children [96]. The most important cells involved in bone remodeling are osteocytes, osteoblasts, osteoclasts, and bone lining cells [49] (see figure 2.4).

Osteoblasts originate from perivascular mesenchymal stem cells (MSCs) and are

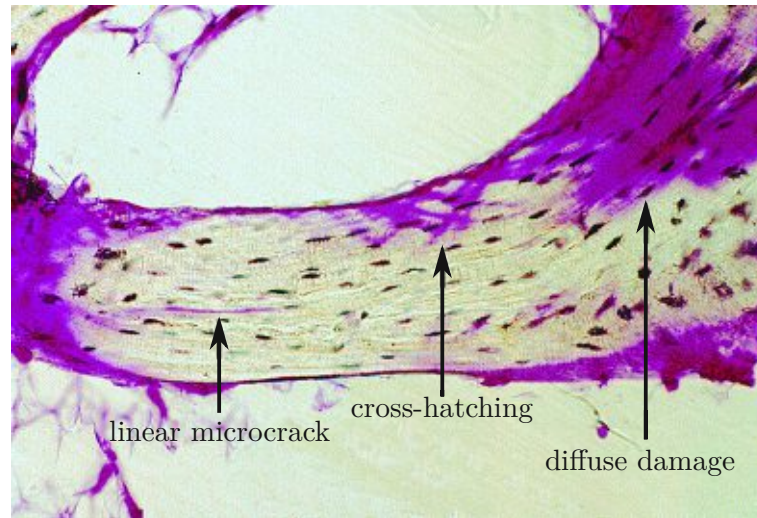


Figure 2.3: Different types of microdamage stained with basic fuchsin. Left: linear microcrack, middle: cross-hatching and right: diffuse damage (image modified from Fazzalari et al. [93]).

recruited from blood vessels during bone remodeling [97]. These cells are essential in building the basic multicellular unit (BMU, see figure 2.4-A) in the bone remodeling compartment (BRC) in cortical and trabecular bone. Hereby, the major role of osteoblasts is the production of bone matrix proteins and bone mineralization [98], promoting bone formation. Mature osteoblasts are cuboidal-shaped cells and further undergo apoptosis, or differentiate into osteocytes or bone-lining cells [99](see figure 2.4-B).

Osteocytes are the most abundant cell type in bone, accounting for approximately 95 % of all cells [100]. These cells originate from osteoblasts, which come incorporated in the bone matrix during protein deposition [100]. Osteocytes are able to sense mechanical loads [101] and trigger bone remodeling by adaptation of protein expression [102].

Bone-lining cells also emerge from osteoblasts and cover the bone surface in regions where no bone remodeling occurs (see figure 2.4-A). These cells are flat-shaped and important in protecting the bone matrix from resorption by osteoclasts and in formation of the BMU [49].

Osteoclasts originate from hematopoietic stem cells and are responsible for removal of the mineralized bone matrix during bone remodeling [103]. These cells are stimulated by macrophage colony stimulating factor (M-CSF) to differentiate into osteoclast precursors, which further fuse into multinucleated osteoclasts, by binding of the receptor activator of NF- κ B ligand (RANKL) to RANK [104] (see figure 2.4-C). These events are triggered by osteoblasts, which are also able to inhibit osteoclastogenesis by secretion of osteoprotegerin (OPG), which binds to RANKL and hence, protects bone from excessive resorption [105].

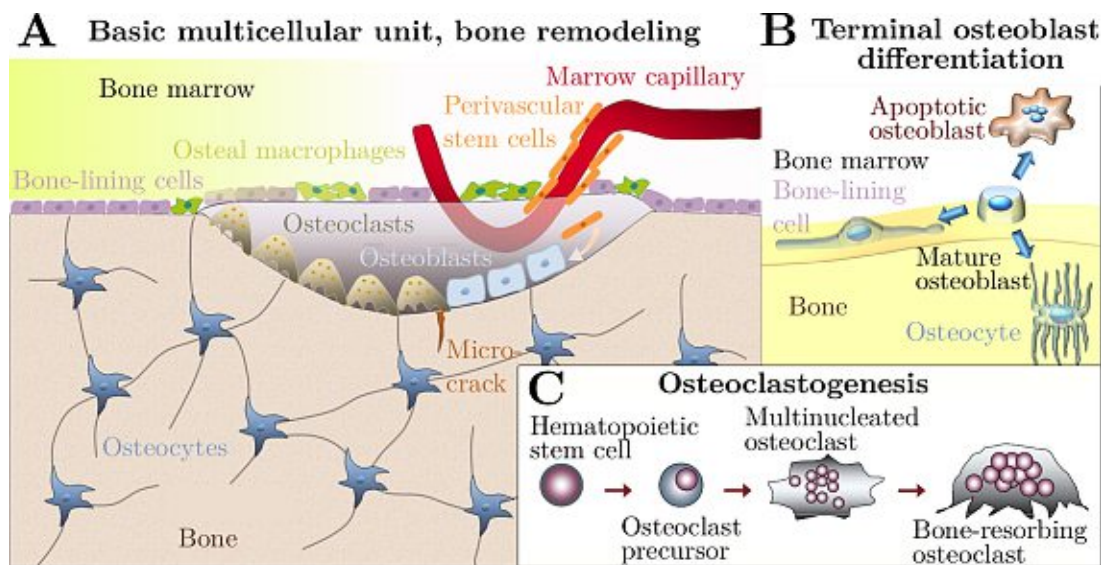


Figure 2.4: **A:** Basic multicellular unit (BMU) within the bone remodeling compartment (BRC). The scheme illustrates the key cells involved in bone remodeling (image modified from Khosla et al. [97]). Apoptosis of *osteocytes*, often caused by fatigue *microcracks*, initiates recruitment of *osteoclasts* (pre-cursor cells), essential in bone resorption. Moreover, *perivascular stem cells* are recruited from the *marrow capillary* (inside the bone marrow) and differentiate into *osteoblasts*, which deposit and mineralize bone matrix. *Bone-lining cells* and *osteal macrophages* cover the endosteal surface and further border the BRC. **B:** Terminal differentiation of osteoblasts (modified from Capulli et al. [99]). **C:** Osteoclastogenesis (modified from Lee et al. [104]).

Bone remodeling is performed by clusters of all these mentioned cells, arranged

within a temporary anatomical structure, the BMU (see figure 2.4-A). The leading front is responsible for bone resorption (rich in osteoclasts), whereas the tail region is responsible for bone formation (rich in osteoblasts). Five sequential phases of bone remodeling are distinguished: activation, resorption, reversal, formation, and termination. In brief, a stimulus, such as microdamage, limb immobilization or hormone (parathyroid hormone) release triggers the *activation phase*. Sequentially, osteoblasts react on signals generated by osteocytes and recruit osteoclast precursors to the remodeling site in the *resorption phase*. Multinucleated osteoclasts are formed and start to secrete matrix metalloproteinases (MMPs) to degrade the unmineralized organic matrix (osteoid). Further, hydrogen ions are pumped into these resorption cavities to dissolve the mineralized matrix. In the *reversal phase* remaining collagen remnants are removed by reversal cells (osteoblast-lineage cells, which also secrete MMPs [106]) to prepare the bone surface for sequential osteoblast-mediated bone formation. In the *formation phase* osteoblast progenitors are attracted to the resorption site, differentiate and secrete molecules, such as collagen type I and NCPs, essential in bone formation. Moreover, hydroxyapatite is incorporated into the newly formed osteoid. The resorption phase takes approximately two weeks [107], the reversal phase about four to five weeks [108] and the formation phase approximately four months in duration [109]. Finally, when an equal quantity of resorbed bone has been replaced, the remodeling cycle is stopped in the *termination phase*. [103]

2.5 Osteoporosis

Osteoporosis is listed as one of ten diseases causing the largest burden of disease [1] and affects approximately 200 million people worldwide [110]. Osteoporosis is defined as a decrease in total bone mass, determined by measuring the areal Bone Mineral Density (aBMD) [5]. Conventionally, this is performed with Dual Energy X-ray Absorptiometry (DEXA) scans [6]; X-ray images are taken at two different defined energies to discriminate bone from soft tissue. Images are taken at the lumbar spine and/or the femoral neck, as these two sites are the most common regions affected by osteoporotic fractures [7] (see figure 2.5). Osteoporotic fractures have been further described as low trauma fractures, such as a fall from

standing [111]. According to WHO, osteoporosis is defined as a aBMD value below 2.5 standard deviations, compared to a healthy cohort, more commonly known as the T-score [1,5]. If the T-score lies between -2.5 and -1.0 then the patient suffers from *osteopenia*. The DEXA based determination of osteoporosis has a sensitivity (correct identification of diseased patients) of only 60% [1]. Sequentially, around 40% remain undetected and will not get adequate treatment, although early intervention is essential in preventing progress of this disease [4]. Thus, the WHO recommends to include more patient specific data in osteoporosis screening, based on a questionnaire. Information about age, BMI, fracture history, cortisol treatment, epidemiologic information, and other factors are used to calculate a 10-year fracture risk probability, the FRAX score [112]. This enabled a broader screening for osteoporosis [113], however no significant improvement in the discriminatory value of FRAX (with aBMD) in comparison to aBMD alone was found in early post-menopausal women [114]. Thus, other factors, such as microdamage and material composition, have been suggested to be affected by osteoporosis [61].

Microdamage has been shown to accumulate with increasing age, and has been suggested to be related to the increased fracture risk especially in elderly women [61]. However, no conclusion has been drawn so far on the relation to osteoporotic stress fractures. A possible explanation is that there is a superposition of microdamage accumulation, insufficient bone repair, and reduced bone mass, adding up to fragility. Although osteoporosis is known to be caused at the cellular level, no agreement has been reached so far on its effects on the tissue bone matrix. Conflicting results have been reported about the TMD. A decrease of TMD has been described in osteoporosis [116–118], while other studies determined an increase [119–121]. Also no effect of osteoporosis on TMD at all has been mentioned [122]. However, in that study an increased heterogeneity of TMD was observed in osteoporosis, as also reported previously [119]. As TMD is usually correlated to tissue elastic modulus, also controversial results have been described regarding tissue elastic modulus [119–121]. A decrease of elastic modulus in osteoporosis was observed [119], whereas other studies found increased values [120, 121].

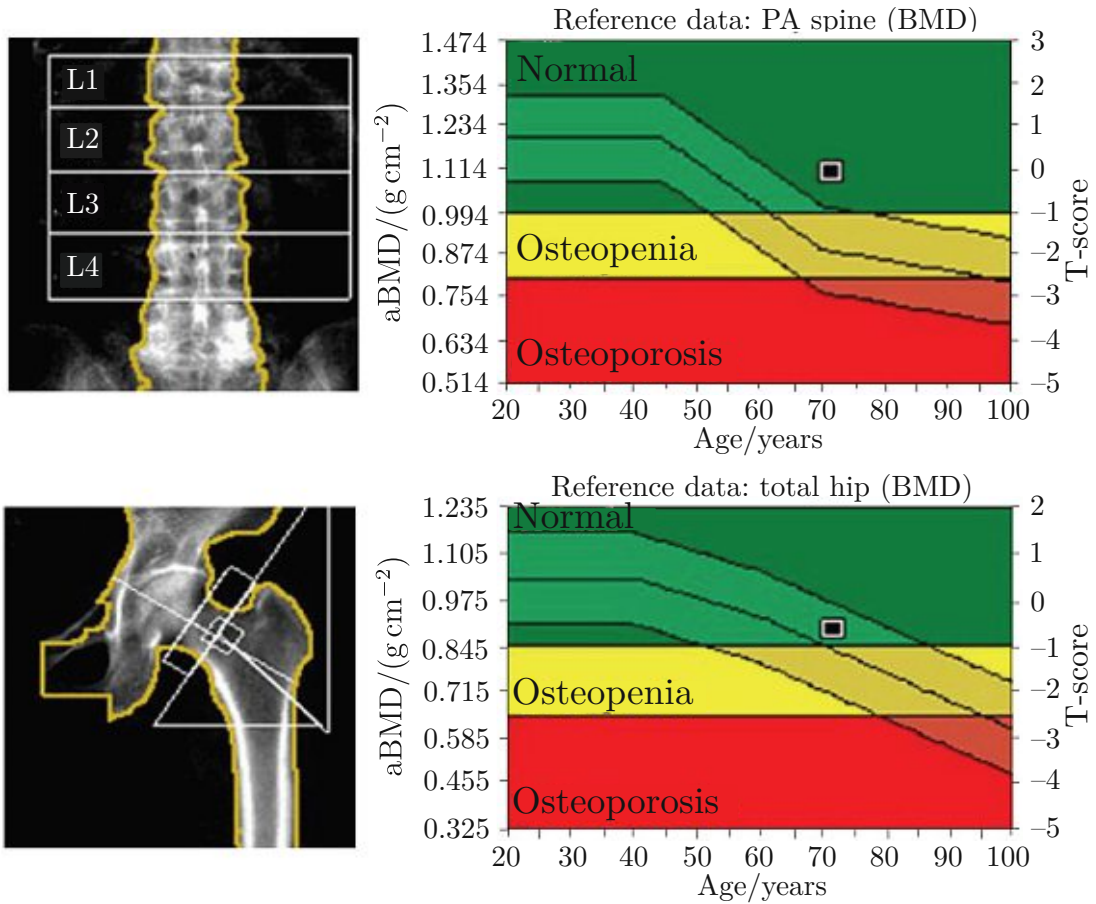


Figure 2.5: Dual X-ray absorptiometry of lumbar spine (top) and the femoral neck (bottom) with corresponding diagrams with indicated reference lines for normal mean \pm standard deviation BMD and T-score with respect to age. The actual patient aBMD-value/T-score is shown as \blacksquare in the diagram. Image modified from Li et al. [115].

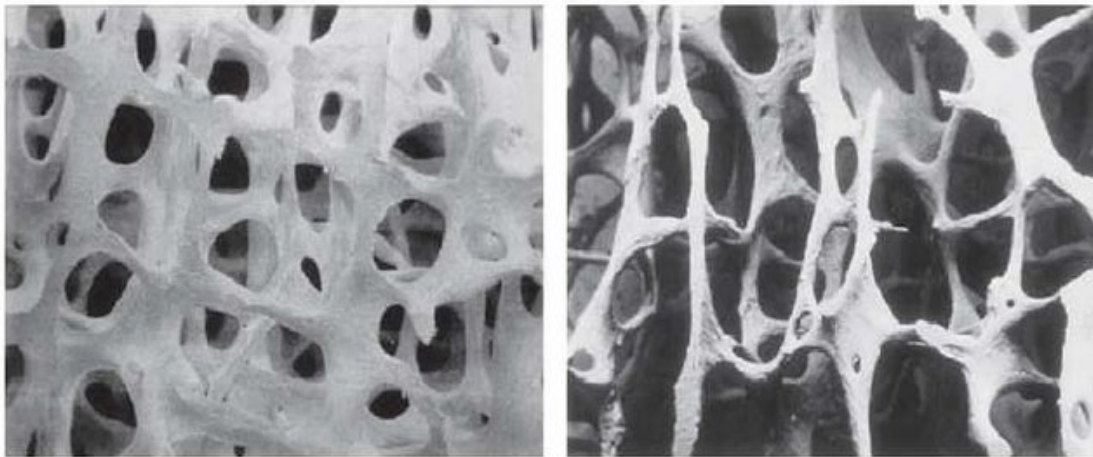


Figure 2.6: SEM image of normal (left) and osteoporotic (right) bone; image reprinted from Chhipa et al. [123].

At the morphological level there is a consensus that the observed decrease of aBMD in osteoporosis is caused by an increase of trabecular bone porosity (see figure 2.6). In more detail, especially the trabecular bone morphology is altered, reflected by a decrease of bone volume to total volume (BV/TV), trabecular number (Tb.N), and an increase of trabecular separation (Tb.Sp).

Osteoporosis is classified into a primary and a secondary type [124]. In principle, primary osteoporosis is a disease of the elderly, related to menopausal estrogen loss and aging. Riggs et al. further specified the post-menopausal form as type I osteoporosis, associated with trabecular bone loss, and the senile form as type II, associated with trabecular and cortical bone loss in men and women [125]. Accordingly, type I osteoporosis is directly linked to a lack of endogenous estrogen, whereas composite influences of long-term remodeling inefficiency, adequacy of dietary calcium and vitamin D, intestinal mineral absorption, renal mineral handling, and parathyroid hormone secretion are observed in type II [124]. Secondary osteoporosis is caused from a variety of possible chronic conditions, resulting in acceleration of bone loss. Examples are long-term glucocorticoid therapy, hyperparathyroidism, malignancies, gastrointestinal diseases, and renal failure [126].

No clear description of the difference between normal aging and senile osteo-

porosis has been made so far [127]. In contrast, post-menopausal osteoporosis (type I), the most common type, is known to be associated with an increase of osteoclast activity and accompanied with a decrease of osteoblasts [128]. In more detail, Damien et al. showed that the estrogen receptor is involved in the osteoblasts adaptive response to mechanical strain [129]. Sequentially, the reduced ability of bone remodeling after the menopause might be caused by a down-regulation of the estrogen receptor, because of absence of estrogen. Further, it has been shown that estrogen withdrawal is associated with osteocyte apoptosis [130]. Similarly, also glucocorticoid excess, mechanical disuse, and aging have been linked to osteocyte apoptosis [131–133], whereas physiological levels of mechanical stimulation facilitated osteocyte viability [131]. In post-menopausal women, osteoporosis can be further divided into normal turnover (NT) and high turnover (HT), whereby HT is less frequent, representing only 30 % of the cases [134]. Interestingly, bone mineral content (BMC) does not differ between HT and NT, although HT osteoporosis demonstrated an increased osteoclast number, accompanied with an increased bone formation at a reduced duration [135].

Bone turnover can be determined by so called bone turnover markers (BTM). These BTMs can be used in osteoporosis screening, but are not routinely used in clinics because of their degree of variability. Recently, BTMs have been suggested to be used before starting anti-resorptive treatment, eg. as baseline measurements and in subsequent treatment monitoring [136]. Here, one marker of bone resorption (CTX) and one of formation (P1NP) is recommended to standardize monitoring.

2.6 Osteoporosis treatment

Treatment of osteoporosis usually starts with non-pharmacological interventions, such as adequate intake of calcium and vitamin D, regular exercise, measures to prevent falls or to minimize their impact, smoking cessation, and moderation of alcohol intake [4]. According to the “Clinician’s Guide to Prevention and Treatment of Osteoporosis” pharmacological treatment should start in patients with hip or vertebrae fractures, T-score ≤ -2.5 , in post-menopausal women and men aged ≥ 50 with osteopenia, and a 10-year hip fracture probability $\geq 3\%$ [137]. Recom-

mended drugs are bisphosphonates (BPs), calcitonin, selective estrogen receptor modulators (SERMs), estrogens, and/or hormone therapy, parathyroid hormone fragment, and receptor activator of nuclear factor kappa-B (RANK) ligand inhibitor.

Initial pharmacological treatment of osteoporosis in post-menopausal women at high risk for osteoporotic fractures is the oral administration of bisphosphonates, according to the “European Society of Endocrinology” [25]. As alternative initial treatment, Denosumab is suggested, an antibody that binds with high affinity to RANKL and sequentially inhibits the interaction with RANK. If the risk for osteoporotic fractures is very high, such as those with severe or multiple vertebral fractures, then administration of parathyroid hormone fragment is advised. Patients, where administration of the before mentioned medications is not appropriate, should be treated with Selective Estrogen Receptor Modulator (SERM)s, such as raloxifene. If none of the aforementioned medications is appropriate or tolerated, then calcitonin should be administered. Further, treated patients should be monitored every (1 to 3) years with DEXA scans to assess the response to treatment. Alternatively, bone turnover markers should be monitored to identify non-responders or non-adherence.

The overall goal of treatment of osteoporosis is fracture prevention [138]. Hereby, the majority of drugs (BPs, estrogen, SERMs and denosumab) can be summarized as anti-resorptive medicine [139]. They reduce the number, activity, and lifespan of osteoclasts [140] and thus decrease bone resorption, resulting in an increase of bone mass, which further reduces the probability of osteoporotic fractures [139].

Bisphosphonate treatment is currently the first line medication in osteoporosis [25]. For example alendronate has been shown to reduce bone remodeling and increase aBMD significantly (by almost 22 %), after a 12 month treatment period [141]. In a further study the aBMD increase was determined to be dose-dependent, at least in the low dose regimen ((1 to 5) mg) [142]. Also clinically apparent vertebral fractures were reduced by almost 50 % after alendronate treatment [143]. However, long-term treatment was demonstrated to cause severely suppressed bone turnover in some patients, and might result in delayed healing of non-spinal fractures [144].

High dose treatment of dogs with BPs resulted in an accumulation of microdamage, associated with a reduction of bone toughness [145]. This effect might be linked to the two most severe side effects in patients, osteonecrosis of the jaw (ONJ) and atypical femur fractures (AFF) [139]. ONJ is characterized as the “presence of exposed bone in the maxillofacial region that did not heal within 8 wk after identification by a health care provider” [146]. Its incidence was estimated to be as low as between 1 in 10.000 and < 1 in 100.000 patient-treatment years. On the contrary, in intravenous treatment ONJ occurs in the range of 1–10 per 100 patients [146]. AFFs are stress fractures located in the sub-trochanteric region and diaphysis of the femur. BP treatment causes an incidence of AFF of 3.2 to 50 cases per 100.000 person-treatment years [147], but increases to ~ 100 per 100.000 person-treatment years in long-term treatment [147]. Hereby, a localization of bisphosphonates in areas of developing stress fractures was recognized.

SERM treatment, such as with raloxifene, has the big advantage of estrogen-like effects on bone, while acting as an estrogen antagonist on breast and endometrium tissue [139]. Raloxifene treatment was demonstrated to increase aBMD by 2.7 % in the vertebrae and to decrease vertebral fractures by (30 to 50) % in treatment for three years, without affecting other fracture locations [148]. As raloxifene also acts as an antagonist on breast tissue, a 72 % reduction in the risk of invasive breast cancer has been reported [149]. However, raloxifene causes hot-flushes, an three-fold increased incidence of thrombo-embolic disease, and an increased risk of stroke [150]. Sequentially, raloxifene is recommended in post-menopausal women with spinal osteoporosis and with an increased risk of breast cancer [139].

Siegmund et al. developed a non-linear model to discriminate different effects, such as matrix constituents, microcrack characteristics, and trabecular architecture on the fracture resistance of bone from dogs treated with anti-resorptive medication [151]. They predicted that BP treatment is associated with brittle fracture and an accumulation of microcracks, whereas SERM treatment leads to a more ductile fracture and a smaller increase in microcrack density. It was concluded that bisphosphonates are more effective in low aBMD patients, but SERMs are recommended in milder osteoporotic cases.

2.7 Mechanical characterization of trabecular bone tissue

The previous sections outlined that bone changes at several hierarchical levels, because of load adaptation, aging, disease, and treatment. Usually, fracture risk is described at the whole bone scale. However, engineering materials highlighted that a crack grown at the material level might develop into a full-scale failure. Hence, material characterization is also essential at the tissue level in bone for fracture prediction. Further, any level on the hierarchy might be changed because of adaptations and hence, all levels should ideally be characterized properly. As outlined previously, the mechanical testing of bone must be performed in a physiologic, wet environment, since material properties change at several levels with dehydration [16, 65, 66]. Mechanical properties of whole bones can be determined by standard mechanical tests and thus the variability in obtained results is mainly caused by biological variation, such as anatomic site, bone shape (of whole bones), age, and disease [152]. At the macroscale mechanical testing becomes already more difficult, especially because of non standardized test procedures, inaccurate strain measurement, and end-artifacts [153]. Nevertheless, a large amount of studies have been performed at this scale, providing a rather good understanding of the mechanical behavior at this scale [63]; however, only under the assumption of a linear-elastic behavior, yet. Mechanical characterization of trabecular bone at the tissue level (individual trabeculae) is more challenging because of the microscopic sample size, irregular geometry of trabeculae, and a difficult definition of test procedures (for a comprehensive review see Luchinetti et al. [12]). Sequentially, only a few studies have been conducted at this level yet, compared to larger scales. Further, reported values for material and mechanical properties vary tremendously (e.g. elastic modulus varies from (1 to 15) GPa [12]). So far, most studies focused only on determination of the putative elastic behavior of trabecular bone tissue. Wu et al. summarized determined values for elastic modulus in a recent review [11] and highlighted the most important approaches for mechanical characterization, namely nanoindentation, ultrasonic testing, macro-mechanical testing, and micro-mechanical testing [11] (see figure 2.7). These different techniques, their advantages, limitations, and values of determined material properties (mean values of healthy

tissue) are discussed in the following sections.

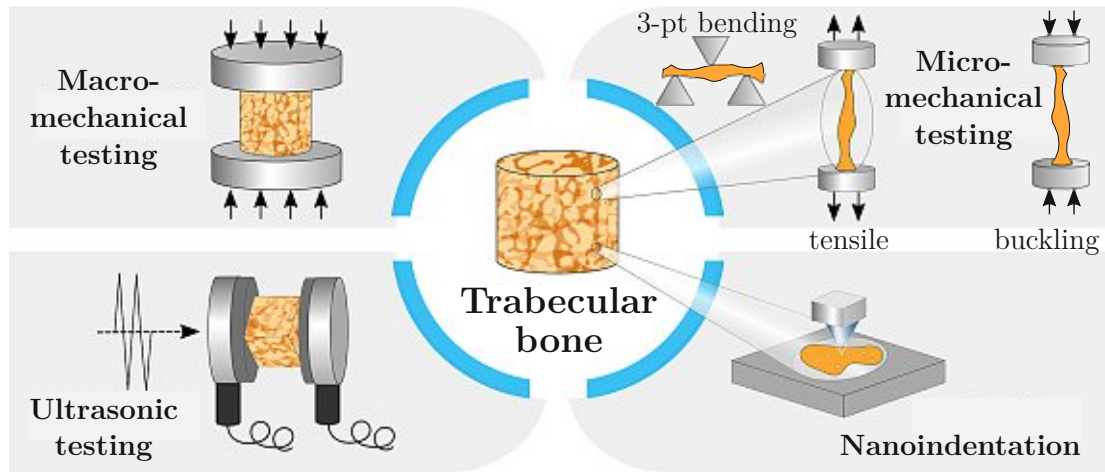


Figure 2.7: Mechanical characterization of trabecular bone tissue, image modified from Wu et al. [11]. Macro-mechanical testing, paired with FE analysis, is used to back-calculate tissue elasticity. Ultrasonic testing enables determination of elasticity, as speed of sound is dependent on tissue elastic properties. Micro-mechanical testing determines tissue properties directly from an experiment, such as a tensile, buckling or three point-bending test. Nanoindentation is used to measure elastic properties at the scale of individual lamellae.

2.7.1 Macro-mechanical testing

Macro-mechanical testing can be combined with micro Finite Element analysis (μ FEA) to back-calculate an average tissue elastic modulus of trabecular bone via an assumed constitutive material behavior, as first described by van Rietbergen et al. [154]. In principle, trabecular bone cores are imaged with μ CT to obtain the geometric structure. These bone cubes (or bone cylinders) typically have a side length of (5 to 8) mm and are mechanically tested in compression. The determined apparent stiffness in the numerical simulation is compared to the one obtained experimentally and sequentially, an averaged tissue elastic modulus can be back-calculated. Reported tissue elastic moduli ranged from (5.6 to 20) GPa [11]. Possible causes for this variation are differences in the selection of the segmentation threshold [155] (associated with partial volume effects [156]), the dependency on the voxel resolution [157] (coarsening with a factor of six resulted in a reduction

of elastic modulus by (60 to 80) % [158]), and different meshing techniques [159]. The main limitations of this technique are attributed to its two main assumptions: bone is linear-elastic and homogeneous [11]. It is still unclear if trabecular bone tissue (individual trabeculae) behaves linear-elastic at small strains. Further, tissue mineralization has been shown to be heterogeneous, as trabecular bone packets on the surface are less mineralized than the ones close to the core [45].

2.7.2 Ultrasonic testing

Ultrasonic testing can be performed on trabecular bone cores or cubes, but the large void fractions in trabecular bone cause wave attenuations [160], resulting in a mixture of structural and material properties. Evaluation of the actual bone tissue elasticity is possible on thin slices (in the range of a few 100 μm) with Scanning Acoustic Microscopy (SAM), as first described by Hasegawa et al. [161]. This a non-destructive technique to determine the tissue elastic modulus, based on the relation of elastic properties to the velocity of wave propagation, similar to conventional ultrasonic measurements [162] (see figure 2.8). However, the resolution of Scanning Acoustic Microscopy (SAM) is about 60 μm [161], compared to measurements of whole trabeculae [162] or even trabecular networks [163] in the range of several milli meters. Determined tissue elastic modulus was reported ranging from (10.0 ± 1.3) GPa [164] (conventional pulse-transmission transit in trabecular bone cubes, 20 mm side-length) to (17.5 ± 1.5) GPa [165] (in SAM). The major limitation of all ultrasonic measurements are the high frequency sound waves, in comparison with quasi-static mechanical tests [12]. However, the effects of strain rate on the mechanical properties are still reported contrarily [166, 167].

2.7.3 Micro-mechanical testing

Micro-mechanical testing is done at quasi-static conditions on individual trabeculae and has been reviewed comprehensively in [11, 12, 170]. Different test approaches were applied, mostly three-point bending [18, 119, 171–176], and tensile tests [18, 36, 162, 171, 177–179]. There are only two studies that performed buckling tests on individual trabeculae [66, 180], one that used four-point bending [181] and one that did compression tests on machined bone tissue cubes [182]. All techniques

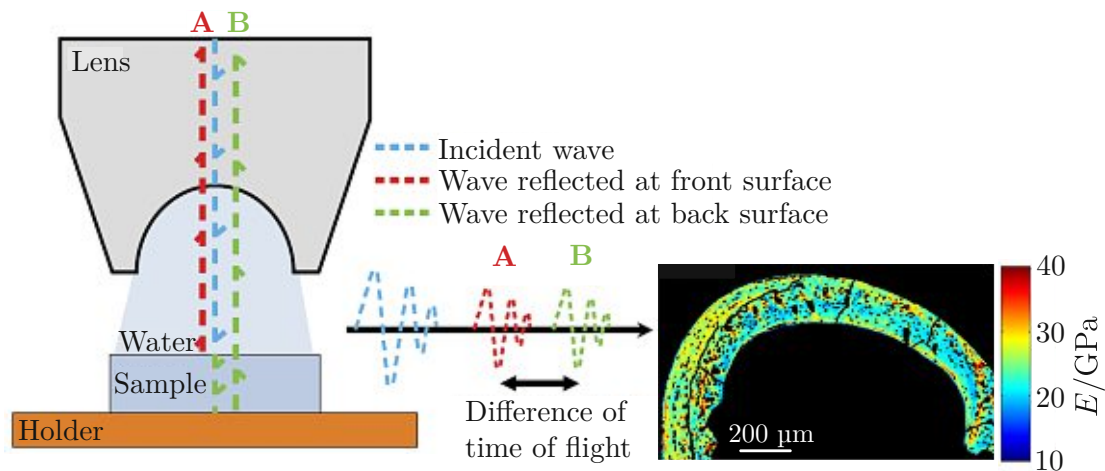


Figure 2.8: Scanning acoustic microscopy (SAM) of bone (image modified from Blouin et al. [168]). An ultrasonic **incident wave** is partly **reflected at the front surface (A)**, travels through the sample and is **reflected at the back surface (B)**. The difference in the time of flight (ΔTOF) is used to calculate the sound velocity via sample thickness and sequentially the elastic modulus (E). An exemplary mapping of E of a cross section of a mouse femur is shown on the right (modified from Blouin et al. [169]).

have their advantages and limitations and are reviewed in the following paragraphs.

Buckling tests were performed in first studies on individual trabeculae [66, 180] and reported mean elastic moduli ranged from (11.4 to 14.1) GPa. After dissection trabeculae were glued with epoxy onto ceramic rods and subjected to compression [66]. Although buckling might be a reasonable physiological load [183], experimental implementation and determination of mechanical properties is challenging because of undefined boundary effects, sample alignment, superposition of shear, and irregular trabecular geometry. Further, inelastic buckling had to be assumed, because of the low slenderness ratio [66]. Exemplary compression/buckling tests in two different test configurations, which were carried out in course of the present thesis, can be found in Appendix B.

Three-point bending is less difficult to implement, as individual trabeculae only have to be excised from the trabecular network and placed onto the support (see Appendix C for a manufactured three-point bending sample holder in course of the

present thesis). However, three-point bending tests likely give erroneous results, as the cross-sectional area of trabeculae is inhomogeneous, leading to undefined stress states. To overcome this issue trabeculae have been milled to homogeneous rectangular beams and tested in four point bending [181], providing a homogeneous stress state between the supports. Nevertheless, uneven contact [181], local stress accumulation next to the support and loading point [162], a small aspect ratio (smaller than 10), and usage of Bernoulli beam theory [119, 181] are still limitations to be considered. As trabeculae typically have an aspect ratio of 3 to 10, Timoshenko beam theory was also used to account for shear deformation [167]. An accurate measurement of specimen length is still crucial, as the calculated elastic modulus depends on the length to the power of three. Elastic moduli were reported ranging from (2.0 to 11.4) GPa.

Tensile tests are the most commonly used experiments for material characterization because of the homogeneous stress state, provided regular specimen geometry, and material isotropy. Individual trabeculae do not hold these assumptions, but can be approached as elliptical cylinders and considered as transverse isotropic along the longitudinal trabecular axis [12]. Reported values for trabecular tissue elastic modulus range from (0.75 to 15.6) GPa. The most challenging issues of tensile tests are sample mounting and accurate displacement measurement [12]. For mounting, trabeculae have to be embedded in resin, like epoxy or cyanoacrylate glue. Hereby, sample alignment is very crucial, since misalignment leads to shear stress. Displacement determination has been done with recording of platen displacement [36, 162, 178], usage of optical methods [18, 171, 177, 179], and with a laser Michelson interferometer [184]. Platen displacement will underestimate true displacements, since epoxy and cyanoacrylate glue is less stiff than trabecular bone tissue and will deform more, resulting in a combined monitored displacement. Thus, optical methods, such as Digital Image Correlation (DIC), are preferable [18, 171].

As outlined in the previous paragraphs, several different micro-mechanical tests have been used to determine trabecular tissue elastic modulus. Interestingly, determined mechanical properties with three-point bending and tensile tests have been reported to differ significantly, even when performed in the same studies [18, 171].

Here, three-point bending experiments resulted in a significant lower tissue elastic modulus, which might be caused by an overestimation of bending strain, because of local deformations of the specimen at the supports. Further, measurement of displacement might also be erroneous, depending on the used measurement technique (optical or machine displacement). Sequentially, no true material parameters could be determined, as elastic modulus is a material constant, which is, by definition, independent from the used test approach or the applied strain rate. However, there is an ongoing debate whether bone tissue is an elastic material, or if it exhibits elasto-plastic hardening, which can be displayed using loading/unloading experiments [185,186]. According to this, it would be favorable to study also the viscosity, plasticity, and failure mechanisms of trabecular bone tissue. So far, most studies focused on the elastic behavior and only a few studies determined the yield [18,119,171] or post-yield properties [18,36,119,171].

Limitations of all micro-mechanical tests are especially attributed to the tiny size of individual trabeculae. Thus, substantial loss of samples [184], accompanied with a large biological variation of tissue properties [13,14] requires a high test throughput [12]. The small size of trabeculae and difficulties in sample clamping require embedding of samples. Sequentially, strain tracking has to be performed optically, to determinate actual strain on the trabecular shaft. Of course, also optical strain determination might be erroneous, especially in the small strain regimen. Further, determined material and apparent mechanical properties indicate a critical dependency on stress determination. The irregular shape of individual trabeculae makes it difficult to estimate a representative cross-sectional area. Thus, a combination with FE analysis has been performed in previous studies [18,171]. However, assumptions in the numerical model, especially selection of appropriate boundary conditions, is crucial. Elastic modulus showed to be significantly correlated with trabecular thickness [119], caused by a stronger influence of lacunae and microcracks for thinner trabeculae [12,187]. In contrast, Yamada et al. found no significant dependency of elastic modulus on size, orientation or shape in cantilever bending experiments [188]. Taken together, mechanical properties determined from micro-mechanical experiments possibly always involve a structural influence, which might also explain, beside the large biological variation, the huge range of

reported values. Only one study used machined bone cubes of trabecular tissue (of 300 μm side length) to overcome this issue [182]. Elastic modulus and Poisson ratio were determined in compression in three orthogonal directions. Elastic modulus in longitudinal direction ($E_1 = (3.47 \pm 0.41)$ GPa) was significantly higher than that of the transverse directions ($E_2 = (2.57 \pm 0.28)$ GPa and $E_3 = (2.54 \pm 0.22)$ GPa). However, a verification of reported values and the effect of milling on the mechanical properties of trabeculae was missing.

2.7.4 Nanoindentation

All of the aforementioned techniques determined the homogenized material properties of trabecular bone tissue. Thus, these properties involve bone packets, different lamellar orientations, boundary effects between those phases and local defects [11]. In contrast, nanoindentation is used to determine tissue elastic properties at the scale of one to several individual lamellae (for comprehensive reviews see [58, 189]). Despite its wide usage, reported values for elastic modulus varies from (1.3 to 22.3) GPa, which may be attributed to differences in preparation and testing protocols [11], heterogeneity of tissue, and different testing environments (wet vs. dry) [58]. In brief, samples have to be embedded in poly methyl methacrylate (PMMA) or epoxy resin and polished to ensure a flat surface. Different material properties of this resin caused no change in the measured bone elastic modulus, but a change in the tissue hardness [190]. Tissue elastic modulus and hardness are calculated from the unloading curve using the Oliver–Pharr method (OPM) [191] in most cases, which assumes purely elastic behavior during the first part of the unloading process. For calculations, bone tissue is assumed to be isotropic with a Poisson’s ratio of 0.3 [189], whereby varying the Poisson’s ratio from 0.2 to 0.4 caused relative errors between (9.9 to -8.2) % [192]. Further, trabecular bone tissue is transverse isotropic [12], whereby apparent elastic modulus in indentation is a function of the axis of indentation and the full elasticity tensor [189].

Besides different preparation protocols, the high variation of reported elastic moduli may also result from different indentation sites within individual trabeculae.

In more detail, Mulder et al. proved that not only mineralization, but also elastic modulus is higher in the core region of trabeculae, compared to the surface [193]. However, indentation is mostly performed in the higher mineralized core to avoid embedding artifacts [194]. This fact might explain the trend of higher reported elastic moduli in nanoindentation, compared to micro-mechanical tests (see figure 2.9). Another factor may be hydration state. Nanoindentation is commonly performed on dried specimens (compare Thurner et al. [58]) because of easier experimental handling. But, elastic modulus in hydrated trabecular human vertebrae was 29 % lower than in dried specimens, in nanoindentation experiments [17].

Correlation of elastic modulus determined with nanoindentation and macroscopic experiments have been reported controversy. Silva et al. found no significant correlation between elastic modulus obtained with nanoindentation and three-point-bending tests of whole bones [195], whereas Hengsberger et al. reported a good agreement between nanoindentation and macroscopic tests [196]. Similarly, Turner et al. determined almost identical values for trabecular elastic modulus with nanoindentation (18.1 ± 1.7 GPa) and SAM (17.5 ± 1.1 GPa). A comparison of obtained values for tissue elastic modulus with different testing approaches is given in the following section.

2.7.5 Comparison of testing approaches

Figure 2.9 summarizes obtained values for trabecular tissue elastic modulus determined with macro-mechanical, micro-mechanical, ultrasonic, and nanoindentation experiments (based on a recent review from Wu et al. [11]). For bovine bone, reported values range from (6.5 to 18.7) GPa for FE analysis [157, 197], from (10.9 to 13.1) GPa for ultrasonic measurements [163, 198], from (2.0 to 9.1) GPa for bending tests [171, 172, 188], from (0.75 to 15.6) GPa for tensile tests [171, 178, 179] and from (18.9 to 20.0) GPa for nanoindentation [199, 200]. For human bone, reported values range from (5.7 to 18.0) GPa for FE analysis [201–204], from (10.0 to 17.5) GPa for ultrasonic measurements [162–165], from (2.1 to 10.1) GPa for bending tests [18, 119, 173, 181, 205], from (9.2 to 16.2) GPa for tensile tests [18, 162, 177] and from (5.1 to 22.3) GPa for nanoindentation [14, 17, 165, 177, 192, 206–212]. In

bovine and human specimens ultrasonic measurements and nanoindentation studies reported higher elastic moduli compared to median values of all measurement techniques. This systematic deviation, likely caused by higher strain rates in ultrasonic measurements and local material properties at a smaller scale, have already been discussed in the previous sections. Similarly, micro-mechanical experiments tend to report lower elastic moduli, compared to overall median values. Reasons might be the incorporation of local effects between trabecular packets, bone lamellae, microcracks, and lacunae. Interestingly, moduli back-calculated from FE analysis are close to overall median values, possibly because of homogenization of lower levels, and influence of the trabecular structure.

Elastic moduli determined in wet conditions always tend to be lower than in dry state (except three-point bending of human bone, where only a small amount of data was available, seen figure 2.9). Thus, it is important to keep in mind that the hydration state has a substantial influence on reported material and apparent mechanical properties, independent from the used measurement technique. In dry conditions, elastic moduli determined in tensile experiments of individual trabeculae were close to overall median values. So far, only one study has performed tensile tests in an almost wet condition (specimen preparation was done wet and tests were conducted immediately after removal) [178]. Hence, there is a clear need to better characterize individual trabeculae in tension in a wet environment. Further, tensile tests give the homogeneous mechanical behavior at the tissue level, which is essential for computer simulations, such as FE analysis. At this level, the mechanical behavior is influenced by the micro-scale (bone packets, lamellar orientation, microcracks, and porosity) and sequentially obtained material parameters represent homogenized values at the tissue scale. If performed properly (reliable boundary conditions, sample alignment, test environment, and strain measurement) tensile tests enable a defined mechanical material characterization of trabecular bone tissue. In conclusion, tensile tests were chosen to be the most reliable test method, and used for determination of mechanical behavior of individual trabeculae in this thesis.

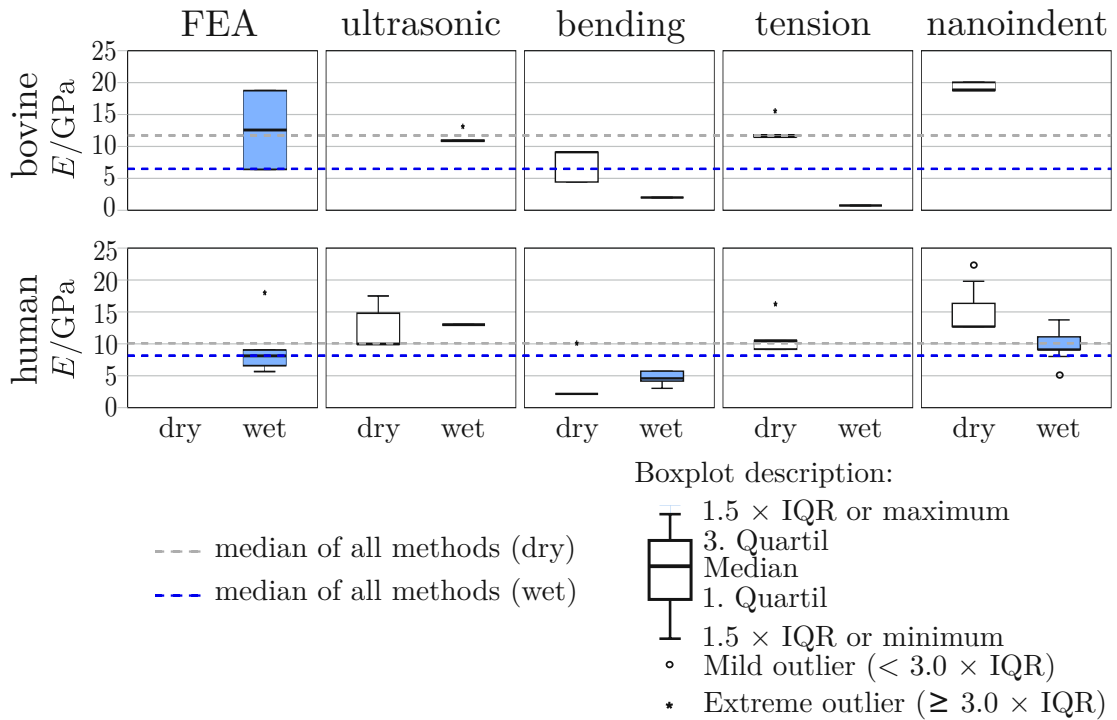


Figure 2.9: Mean values of elastic tissue modulus (E) determined with different techniques (FEA: FE analysis). Values are reported for bovine (top) and human (bottom) specimens tested in a dry (white) and wet (blue) environment. Taken elastic moduli are based on the studies reviewed in Wu et al. [11]. Studies, where no mean values were reported, test environment was not properly defined, or nanoindentation was explicitly done in transverse direction where excluded. Values were weighted by the number of tested specimens. The blue and gray lines represent the median elastic moduli of all combined experiments, to indicate the relation of the individual test approaches to that value. Note that data is often skewed because of the small number of data points and the weighting of used values by the number of tested samples per study, causing that median and 1. or 3. quartile are often almost identical.

CHAPTER 3

Methods development and data analysis approaches

“Find something you love to do. Work it to the bone. And you’ll be successful.”

John Schnatter

This chapter presents the developed and applied methods of the current thesis. First, a novel test set-up for tensile testing of individual trabeculae, close to a physiologic, wet environment, is described (see section 3.1). This set-up was further used to perform cyclic tensile tests to enable a more comprehensive material characterization (see section 3.2). Next, section 3.3 demonstrates a rheological model, which was developed by *Andreas G. Reisinger* in a joint project. This model was applied to identify elastic, viscous, plastic, and post-yield tissue properties of individual trabeculae from cyclic tensile tests. Finally, section 3.4 illustrates the development of a fatigue test set-up to induce and visualize microdamage in individual trabeculae at a defined tensile stress state. The fatigue test is based on the tensile test set-up described in section 3.1. The methodological implementation of the fatigue test and establishment of the microdamage labeling procedure was done by *Julia-Theresa Fischer* in course of her Master thesis and the author of the current thesis, *Martin Frank*, co-supervised the project, took part in the

optimization process, and performed the evaluation and interpretation of obtained results.

3.1 Tensile tests of individual trabeculae

3.1.1 Related publications and declaration of contributions

Partial results of the presented work (text, tables and figures) have been *published* in “Proceedings of the IASTED International Conference Biomedical Engineering (BioMed 2017)” in 2017, entitled “Mechanical Properties of Individual Trabeculae in a Physiologic Environment” and co-authored by Dorothee Marx, Dieter H. Pahr and Philipp J. Thurner. Partial results of the tensile test set-up and the data evaluation (see sections 3.1.3 “Sample preparation” to 3.1.3 “Determination of apparent mechanical parameters”) have been *published* in the “Journal of the Mechanical Behavior of Biomedical Materials” in 2018, entitled “Dehydration of individual bovine trabeculae causes transition from ductile to quasi-brittle failure mode” and co-authored by Dorothee Marx, Vedran Nedelkovski, Julia-Theresa Fischer, Dieter H. Pahr and Philipp J. Thurner.

Author contributions: In both publications, the first author and author of the current thesis, *Martin Frank*, took part in the study design, performed the development and refinement of the test set-up, all mechanical tests, data processing, data interpretation, and wrote the manuscripts. *Dorothee Marx* developed the original test set-up (water-bath and the concept of silicone chambers for specimen preparation), which was used for tensile tests of cortical bone. This set-up was modified by *Martin Frank* (specimen preparation, mounting, and clamping) to enable tensile testing of individual trabeculae at a high throughput. *Vedran Nedelkovski* took the electron microscopy images for fracture surface analysis and assisted in data interpretation of fracture surfaces. *Julia-Theresa Fischer* contributed in optimization of the test set-up and sample preparation. *Dieter H. Pahr* and *Philipp J. Thurner* designed the studies, supervised the work of *Martin Frank* and supported the interpretation of the results.

3.1.2 Introduction

Characterization of the mechanical behavior of trabecular bone can be done with a variety of different methods (see section 2.7). As already outlined all approaches have advantages and limitations. However, a defined tensile test enables a direct measurement of the whole mechanical behavior of individual trabeculae, from elastic to failure properties. Nevertheless, several issues have to be addressed in micro-mechanical tensile experiments: Sample mounting (including alignment), accurate strain measurement, determination of a reliable cross-sectional area and a physiologic test environment.

In first tensile experiments individual trabeculae were directly clamped with screws [178]. Reported tissue elastic modulus was 1 GPa, much lower than values determined in later studies (~ 10 GPa) [18, 162, 171, 177, 179]. This discrepancy might result from shear forces in clamped samples, as sample slipping was excluded in that study [178]. Later studies used different resins, like epoxy [177], cyanoacrylate [120, 162, 179] or poly methyl methacrylate (PMMA) [18, 171, 184] for specimen fixation. This enabled an easier sample handling, accompanied with a better defined sample alignment and lower shear forces.

Nevertheless, strain recording was done very differently. Some studies used platen displacement [120, 162], a laser Michelson interferometer [184] or optical methods [179], including digital image correlation (DIC) [18, 171, 177]. Platen displacement will overestimate specimen strain (because of deformation of the glue) and the measured strain has to be corrected for this effect [120]. A direct determination of tissue strain using DIC is more favorable, since it enables a direct, local determination of deformations. Moreover, DIC can also be used to determine full field strain maps of specimens to monitor local damage formation and failure.

The cross-sectional area of individual trabeculae has also been determined in several different ways. First studies simply assumed a circular cross-sectional area and only measured the trabecular diameter [162, 178] for area calculation. Later, Jirousek et al. measured the cross-sectional area with a microscope, at the point

of fracture [177] and Yamada et al. determined an average cross-sectional area using μ CT [179]. To overcome the limitation of the irregular shape of individual trabeculae, McNamara et al. [120,121] and Carretta et al. [18,171] used FE analysis to back-calculate material parameters in an inverse approach. However, definition of reliable boundary conditions and assumptions, such as linear-elastic material behavior and small strains, are still limitations.

Last but not least, the test environment has a substantial influence on the mechanical material behavior, as already mentioned in section 2.7.5. Townsend et al. showed that dehydration causes a transition from ductile to quasi-brittle behavior, in buckling tests of individual trabeculae [66]. Further, also at the scale of lamallae dehydration caused a significant increase in elastic modulus, in nanoindentation experiments [16,17]. Unfortunately, no tensile tests on individual trabeculae have been performed so far in a physiologic, wet environment.

Goal of this study was to develop a defined tensile test approach for individual trabeculae in a wet, physiologic environment, at a large throughput. As such, tissue strain had to be recorded optically, using a DIC algorithm. In addition, specimen fixation was done with resin and sample alignment had to be ensured microscopically. Further, different ways of determination of cross-sectional area were investigated, and compared to back-calculated material properties from FE analysis, for a reliable stress determination. The high sample throughput was especially necessary because of the expected large biological variation.

3.1.3 Materials and methods

The second phalanx of a 16-month-old bull was obtained from a local butcher (Fleischerei Hödl, Vienna, Austria). All soft tissue was removed mechanically with scalpels and tweezers and the bone was frozen at $-18\text{ }^{\circ}\text{C}$ until further manipulation (see figure 3.1-A). All preparation steps, including mechanical testing, were performed in Hanks Balanced Salt Solution (HBSS) at $\text{pH} = 7.4$, at room temperature ($23\text{ }^{\circ}\text{C}$).

The following sections describe the final, optimized methods that were used in chapters 7, 5 and 6. The initial set-up was used in the dehydration study (chapter 4) and optimized during the course of the present thesis. However, only slight modifications were performed, involving a better sample fixation, faster and tighter embedding, optimization of machine tuning parameters and optimization of strain tracking. The final, presented methods represent the latest, recommended methods. Moreover, hints for a reliable sample preparation and testing are provided.

Sample preparation

The head of the second phalanx was cut transversally into 2 mm thick slices, using a bandsaw (300 CP – Diamond Bandsaw, Exakt, Germany; see figure 3.1-B). Next, bone slices were put into distilled water and a oral water jet (OralB, Germany) was used to remove bone marrow (see figure 3.1-C). Bone slices were further cut into half with a precision saw (Isomet Low Speed Saw, Buehler GmbH, Germany), for easier sample handling. Specimens were placed in 9 cm Petri dishes, filled with HBSS. Identification of individual trabeculae was done with a stereo microscope (SZX10, Olympus Corporation, Japan). Following selection criteria were chosen: Trabeculae had to appear transparent (because of the small diameter) and to have a length of approximately 500 μm , with an aspect ratio close to three. Further, enough residual bone at the top and bottom of the trabeculae had to be present, to enable glue attachment. Selected specimens were milled out under the microscope using a hand held miller (Dremel 400, Dremel Europe, The Netherlands), equipped with a 1 mm conical dental miller (MF Dental, Germany; see figure 3.1-D & E). A rectangular PVC template with $(3 \times 1 \times 1) \text{ mm}^3$ cross-sectional area was used for positioning of milling spots. This template was pressed down with tweezers to avoid slipping of the template and the bone slice. The rectangular shape was then carefully scratched onto the surface of the bone with the miller. This first milling step was only intended to provide a guide gouge for the actual milling. After some experience, this pre-milling could be performed without the template. Then, the actual milling was performed in the order as shown in figure 3.1-D. The first milling line ① was cut parallel to the longitudinal trabecular axis. Then, a perpendicular, short edge ② was milled (L-shape). Next, the remaining long edge ③ was milled

3. METHODS DEVELOPMENT AND DATA ANALYSIS APPROACHES

to get an U-shape. At this stage the sample was inspected for potential bone parts (which mask the trabecular strut), or for bridges (which connect the top and bottom part across the trabecular strut). These parts had to be milled out. Finally, after verifying that the U-shape was milled out completely trough the bone, the last short edge ④ was removed. Here, special care had to be taken, since any rapid movement would have destroyed the sample. The dissected specimens were then inspected again for potential bone parts that might mask the trabecular strut. These bone parts could be removed with the miller, but this resulted in damage induction or even fracture in some samples. As an improvement, surgical scissors were used to carefully remove interfering bone parts. Hereby, cutting had to be done very slowly and carefully to avoid shear stress induction.

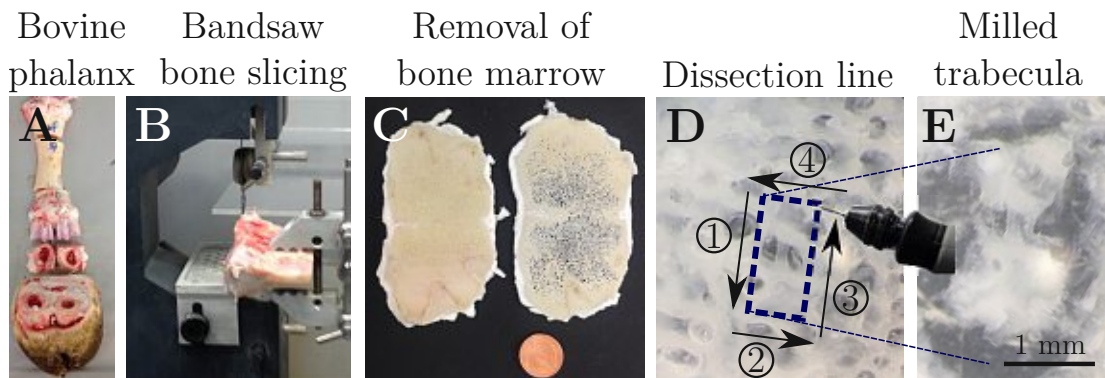


Figure 3.1: Bone dissection. **A:** Bovine toe: Hoof, cartilage and second phalanx, soft tissue removed. **B:** Bone slicing with the bandsaw. **C:** Bone slices with bone marrow (left) and after removal (right). **D:** Dissection of individual trabecula, including residual bone for embedding, using a hand-held miller. The cutting order is shown with arrows and marked as ① to ④. **E:** Dissected trabecular specimen.

Dissected individual trabeculae were scanned with a μ CT for geometry determination (see section 3.1.3 “Micro computed tomography (μ CT) and image processing” and figure 3.2-A). Then, specimens were put into custom-made silicone chambers for embedding (see figure 3.2-B). These chambers are 2 mm in depth and consist of a rectangular central region with flaps (separated by 1 mm) to hold specimens in position. Circular end pieces allow embedding of trabeculae in epoxy resin. Sample alignment is very crucial, as determined mechanical properties are highly dependent on a defined tensile stress state. Hence, shear and bending forces can

be minimized if samples are embedded properly. First, individual trabeculae were roughly positioned inside the silicone chambers using sharp tweezers and a needle, under the stereo microscope. Then, centering and longitudinal alignment was verified from the top with a light microscope (Zeiss Axio Imager, Carl Zeiss AG, Germany; see figure 3.2-B). Silicone chambers were designed to be also accessible from the side. Thus, trabecular alignment could also be verified from an orthogonal view, either with a 45° mirror or by tilting the chambers by 90°. If trabeculae were misaligned, alignment was corrected with the sharp tweezers under the stereo microscope, which enables a native view, in contrast to the light microscope, where the view is inverted. After appropriate alignment, trabeculae were held in position using modeling clay, which also avoided trickling of epoxy glue onto the trabecular strut. Modeling clay was positioned using a needle and gently compressed to ensure leak-proofness (see figure 3.2-C). In more detail, adding the modeling clay was performed similar to building a wall. Small pieces of clay were rolled to form thin, long cylinders. One of these pieces was put underneath the trabecular strut and pressed into the corner between the ground and the flaps of the silicone. Then, a second cylinder was added on top of the former piece and also pressed against the vertical silicone. Hereby, the needle is used similar to a spatula to evenly distribute the clay, to smooth it and hence, to close gaps between individual pieces.

Sample alignment was verified again in both orthogonal planes, to ensure that manipulation did not cause any trabecular movement. Next, a two-component epoxy glue (UHU Endfest 300, UHU, Germany) was mixed at a volumetric 1:1 ratio. A droplet of black paint (R&G universal-color paste deep black 250G, Modellbau Lindinger, Austria) was added to better distinguish epoxy from modeling clay and bone. After mixing, epoxy was put into a vacuum desiccator for 5 min to remove air bubbles. Epoxy was put into the circular end pieces of the silicone chambers with a needle and complete filling of the chambers (up to the edge) was ensured under the stereo microscope. Specimens were left at ambient conditions for 16 h in air for epoxy hardening.

Hardening of epoxy was checked using a needle. If epoxy was hardened properly,

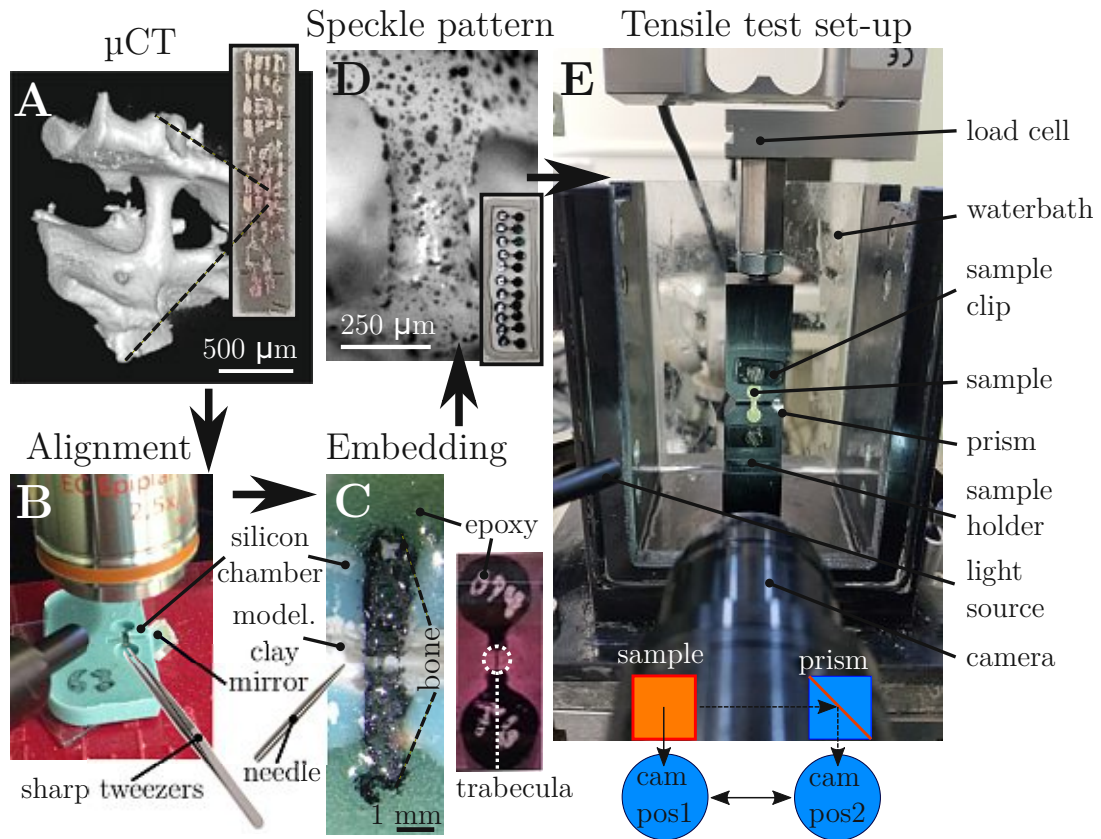


Figure 3.2: Specimen preparation. **A:** μ CT of individual trabecula, for geometry and TMD determination; inset shows parallel scanning of multiple trabeculae on a sample holder. **B:** Alignment of trabecula in the silicone chamber, using sharp tweezers; alignment is verified from top and with a mirror (or by tilting the chamber by 90°) from an orthogonal plane. **C:** Embedding of bone with epoxy glue (here already speckled with black paint for better visibility); modeling clay is put with a needle around the bone to seal the trabecula from epoxy. Inset illustrates the final embedded sample with epoxy stained in black. **D:** Trabecula with applied black speckle pattern for optical strain determination; inset indicates parallel spraying of several samples on a microscopy slide. **E:** Tensile test set-up, including water bath, filled with HBSS, load cell, sample holders with sample clips (to avoid horizontal sample movement), light source, camera and prism. Inset shows that the camera can be moved from position 1 (frontal view on **sample**) to position 2 (view on **prism** to view the sample from the side).

samples were re-hydrated with HBSS. Then, the sharp tweezers and the needle were used to expand the silicone chambers next to the epoxy, in perpendicular direction. This procedure enabled, together with the added HBSS, a better separation of the whole sample from the silicone. Sequentially, specimens could be removed by placing a finger or rod underneath the longitudinal direction of the chamber and by bending the chamber perpendicular to that axis. Proper expanding ahead is crucial to perform sample demolding without damaging it. A direct removal of the sample from the chamber might result in fracture of the trabecular strut and should be avoided.

Then, a speckle pattern had to be applied to enable optical strain tracking. Trabeculae were dried, using small pieces of paper tissue. Samples were placed on microscopy slides and put into a plastic box to apply the speckle pattern. The microscopy slide was placed at one end of the box, closed with the lid and placed in a laminar flow. A black water-soluble spray paint (RAL9005, Dupli-Color, Motip dupli, Germany) was used to speckle the samples. The paint was sprayed for (4 to 5) s into the opposite edge of the box to avoid direct spraying onto the trabeculae. Then the lid was closed for 2 min to allow the dust of speckle particles to settle down onto the samples. This procedure was repeated 5 to 8 times and resulted in a rather uniform pattern of fine black dots (see figure 3.2-D). Verification of appropriate speckle pattern quality was checked with the stereo microscope.

Micro computed tomography (μ CT) and image processing

Prior to sample embedding individual trabeculae were mounted with modeling clay on a PVC plate (see inset in figure 3.2-A), put in the 9 mm sized sample holder of the μ CT100 (Scanco Medical AG, Switzerland), covered with HBSS and scanned at room temperature (37 °C). Trabeculae were scanned at 55 kVp, 145 μ A, integration time 200 ms, average data 3, 1500 projections, nominal resolution of 3.3 μ m and aluminum filter 0.5 mm, to obtain the geometry (see figure 3.2-A) and mineral density. For human samples, tube voltage was increased to 70 kVp (see section 5), since that value was reported in literature more frequently for human trabeculae. All other parameters were kept the same.

Image processing of μ CT data was performed with medtool (v4.3, Dr. Pahr Ingenieure e.U., Austria), whereas 3D-visualization was performed with 3Dslicer (v4.1.0r19886, Slicer Community). Since 3D-visualization of μ CT data required a large amount of memory, all 3D images were re-scaled by a factor of 3, after each performed step in medtool. The actual operations were thus always performed on the original images (to obtain the final aligned and cropped image at high resolution) and on the re-scaled images (to display alignment and cropping of all necessary steps in 3Dslicer). Following steps were performed with individual medtool imaging converter (mic) scripts and custom written python scripts (except tasks explicitly mentioned with *3Dslicer*):

- μ CT data (.ISQ-files) was converted to .mhd-files
- .mhd-files were loaded in *3Dslicer* and the boundary box was adjusted to the size of each trabeculae and exported as .asv files
- .mhd-files were cropped to the boundaries obtained from the .asv files in medtool
- the initial frames from side and frontal video recordings were converted to .mhd-files
- the offsets of these .mhd-files were determined with a custom written python script, to center them at the trabecular strut
- the .mhd-files from the side and frontal recording were loaded with the re-scaled, cropped .mhd-file of the μ CT image in *3Dslicer*
- the μ CT images were manually registered onto the two orthogonal Two-dimensional (2D) images, using the transform panel in *3Dslicer*
- the obtained rotation matrices were saved as .txt files and used to rotate the μ CT images in medtool
- a custom written python script was applied to remove the offset in the .mhd files, caused by the rotation

- the rotated, re-scaled μ CT images were loaded with the frontal, initial video recording in *3Dslicer*
- the boundary box of the μ CT images was set to the upper and lower mean tracking particle positions in *3Dslicer* and saved as .asv files (see figure 3.4)
- the original μ CT image were cropped, using the obtained boundary box from the .asv files in medtool
- the cropped trabecular struts were filtered with a 5×5 median filter in medtool
- the filtered trabecular struts were segmented using the iterative selection method of Ridler and Calvard [213] to find a single level threshold at the minimum between the background and bone distribution; unconnected bone was removed with the FAST approach in medtool
- segmentation quality was verified with overlay plots of mid-plane images from the binary, segmented images and the original, cropped ones in medtool

Determination of Tissue Mineral Density (TMD)

TMD was determined from μ CT scans of a density calibrated μ CT100 (Scanco Medical AG, Switzerland), which were performed as described in the previous section. Calibration was done using five 6 mm diameter hydroxyapatite cylinders of known density (0, 100, 200, 400, 800; whereby 800 is measured weekly as control to ensure actual validity of the calibration). The original .ISQ-files, containing the scaled Linear Attenuation Coefficients (μ_{scale}) at each voxel, were re-scaled to the physical Linear Attenuation Coefficients (μ , in cm^{-1}) according to [214]:

$$\mu = \frac{\mu_{\text{scale}}}{4096} \quad (3.1)$$

Next, the image was converted from the physical Linear Attenuation Coefficients to *TMD* (in mg cm^{-3} of calcium hydroxyapatite (HA)), according to:

$$TMD = \mu k_{\text{cal}} + d_{\text{cal}} \quad (3.2)$$

, where k_{cal} is the slope and d_{cal} the intercept of the TMD calibration and was taken from the .aim-files of the corresponding .ISQ files. These values correspond to the original calibration of the μCT ($k_{\text{cal}} = 370.175 \text{ mg cm}^{-3} \text{ HA}$, $d_{\text{cal}} = -191.025 \text{ mg cm}^{-3} \text{ HA}$).

The conversations described above were performed using medtool (v4.3, Dr. Pahr Ingenieure e.U., Austria), with the *mic* plugin, as follows:

- μCT data (.ISQ-files) was converted to .mhd-files
- .mhd-files were cropped to contain the trabecular strut only
- .mhd-files were re-scaled from the scaled Linear Attenuation Coefficients (μ_{scale}) to *TMD* as described in equations 3.1 and 3.2
- obtained images were filtered with a Gauss-filter ($\sigma = 1$, support = 1) and segmented at a single level threshold of $490 \text{ mg cm}^{-3} \text{ HA}$
- the obtained images were converted to a binary mask and used to determine the TMD histogram of the trabecular (masked) volume of the TMD converted images
- a custom written python script was used to calculate average TMD (TMD_{avg}), standard deviation of TMD (TMD_{std}) and median TMD (TMD_{med})

TMD_{avg} and TMD_{std} are reported for the used studies described in this thesis. TMD_{med} was calculated to verify that TMD distribution was not skewed ($TMD_{\text{med}} \sim TMD_{\text{avg}}$).

Tensile test

Samples were re-hydrated for at least 2 h before testing. In the first test, an epoxy template was used to check alignment and uniform movement during the tensile test, before mounting the actual samples. Figure 3.2-E illustrates the tensile test set-up. This set-up is mounted in a servo-electric load frame (SELmini-001, Thelkin

AG, Switzerland), with a nominal step size of 1 μm . Load was recorded with a 10 N load cell (HBM-S2M, Germany, relative error of 0.02 % at full scale output). Samples were placed in the sample holder with the sharp tweezers. Then, a pre-load of 0.08 N was applied to align the sample and to ensure contact between the holder and the sample. The sample clips were carefully turned over the circular end pieces of the epoxy and gently screwed on. Hereby, care has to be taken to do not fasten the screws too tight, as this would induce shear forces in the trabecula. The actual value of the load cell should be monitored during fastening and forces above 0.2 N should be avoided. After fastening both screws, the frontal plastic part is used to close the water-bath. The four clamps are used to seal the bath and the eccentric screw on the bottom is also fastened. Then, HBSS is poured into the water-bath to cover the sample entirely. Finally, the pre-load is again set to 0.08 N and the actual experiment can be started.

Displacement and strain determination

Sample displacement was recorded optically with a video camera (UI-3250CP-M-GL, IDS GmbH, Germany), at 10 Hz, equipped with a KITO-D zoom objective (mounted on a KITO-ADP-0.5 adapter, Kitotec GmbH, Germany). Figure 3.2-E illustrates that the camera was set to position 1 for frontal plane recording. For alignment verification the camera was moved to position 2. Here, an orthogonal view of the sample could be imaged using a prism. This side alignment check was only performed at the beginning and at the end of the tensile experiment. Pre-trials ensured that this procedure allowed a sufficient accurate alignment verification, without the need of a continuous recording from the side. Images were recorded using the software $\mu\text{EyeCockpit}$ (IDS Imaging Development Systems GmbH, Germany). The recorded image was centered at the trabecular strut and the image size was set to 600 pixel \times 800 pixel to only contain the trabecula.

After video recording images were processed with ImageJ (1.45 s, National Institutes of Health, USA). First, images were cropped to the region, which only contains the trabecular strut. Next, the plugin StackReg [215] was used to remove translational rigid body movement of the whole trabecula. Then, a point tracking

algorithm (*trackpy* v.0.3.2 [216], based on the study of Crocker and Grier [217]) was used to determine trajectories of individual particles throughout the image sequence. Figure 3.3 displays the major steps in strain determination. First, the algorithm identifies black dots on bright background (see figure 3.3-A) and links them to trajectories in all frames (see figure 3.3-B). Hereby, dots are assumed as Gaussian blobs, having a pre-defined *particle size*. The set particle size has to be in the range from 9 to 19 to give reliable results for trabeculae and has to be uneven. Small numbers result in a larger number of recognized particles, but likely give a decreased Signal to Noise Ratio (SNR), since more data points (and thus noise) are assumed as potential particles. In contrast, large particle sizes have a larger SNR, but a smaller number of particles is identified. The best results were obtained with a particle size of 15. Figure 3.3-C displays the histogram of the identified particles. In order to remove low intensity particles, that would result in a lower SNR, a *minimum mass* (cut-off) can be specified (usually 500 in the present thesis).

Additionally, settings for computation of the trajectories have to be done. The *search range* describes the number of pixels that a blob is allowed to move from one frame to another to be considered as the same particle (3 in the present studies). Further, the algorithm is capable to consider a particle, which is lost from one frame to another, but appears again later on, as the same particle. The variable *memory* depicts the number of frames a particle is remembered and considered as the same one (5 in the present studies). The *trackpy* algorithm uses sub-pixel resolution, since the centroid (brightness weighted average position) of each blob is used for tracking. A quick estimation of accurate sub-pixel resolution can be done by checking if the decimal parts of the x and y positions are evenly distributed (see figure 3.3-D). If the chosen particle size is too small, then the histogram shows a dip in the middle (U-shape of the histogram). More precisely, the median uncertainty of particle location can be estimated from the radius of gyration, the mask size and the signal-to-noise ratio, according to Savin and Doyle [218]. In the dehydration study (see chapter 4) the uncertainty was calculated as $0.40\ \mu\text{m}$.

A custom written python script was used to calculate average displacement and

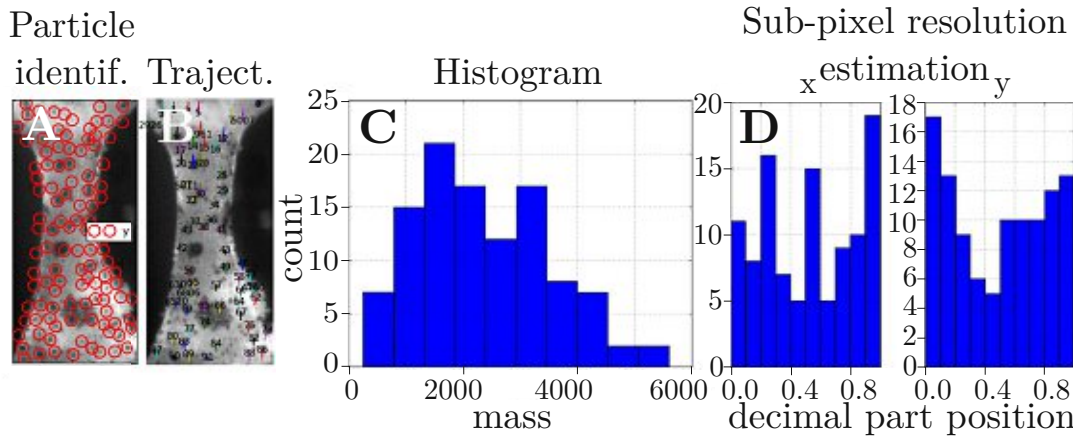


Figure 3.3: Digital Image Correlation (DIC). **A**: Particle identification of black dots (encircled in red) on the trabecular strut. **B**: Computation of particle trajectories over time frames, for each particle, shown in the middle frame. **C**: Histogram of particle intensity (mass, in first frame), used to select the threshold of minimum intensity. **D**: Estimation of sub-pixel resolution using the histogram of the decimal parts of the x and y positions.

strain, based on the identified particle locations from the *trackpy* algorithm. Individual particle-pairs between the top and bottom of individual trabeculae were automatically selected, based on two parameters: x - and y -length-factor. The y -length-factor describes the minimum distance, with respect to the largest y -distance between all particles, two particles have to be separated vertically to be considered as a particle-pair. Additionally, the x -length-factor is the maximum value in horizontal direction that two potential particles for pairing are allowed to be separated. Usage of 0.1 for the x -length-factor and 0.7 for the y -length-factor resulted in pairs of particles which are almost above each other, without much horizontal deviation (see figure 3.4-A). Reliable results were obtained if the number of particle pairs was greater than 10.

The vertical lengths between all selected particle pairs was determined in all frames and averaged. This vertical length in the first frame was the initial length (l_0 , see figure 3.4-B). The change in vertical length (Δl) was determined in all subsequent frames (see figure 3.4-C). The vertical engineering strain was calculated as:

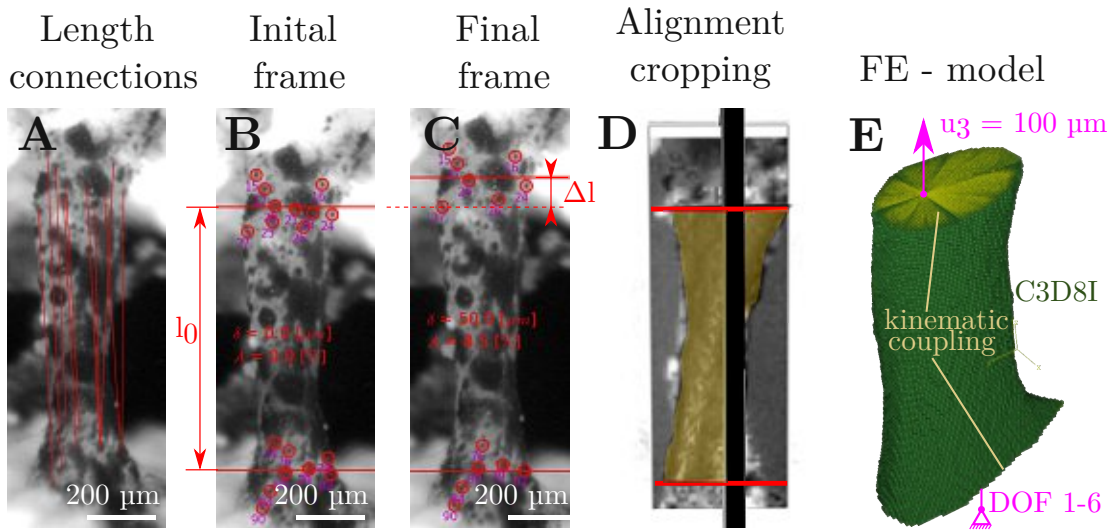


Figure 3.4: Strain tracking, alignment and FE-modeling. **A**: Length connections between particles at the top and bottom region of the trabecula. **B**: Visualization of average length in the initial frame (l_0). **C**: Display of length change (Δl) in the final frame. **D**: μCT images were aligned to the initial frontal and side image, which were recorded with the camera during the experiment. Then, the μCT images were cropped to the initial trabecular length (l_0) from the initial frame. **E**: FE-modeling was done with a voxel to element (C3D8I) conversion from μCT images. All nodes and the top and bottom plane were connected to a reference node, respectively. The top reference node was moved by 100 μm (all other DOFs locked), whereas the bottom one was constrained in all DOFs.

$$\epsilon_E = \frac{\Delta l}{l_0} \quad (3.3)$$

Sequentially, an average engineering strain was calculated. In the present study, engineering strain (ϵ_E) and stress (σ_E) were used. However, as determined ultimate vertical strains ranged from (3 to 12) %, engineering strain was converted to true, logarithmic strain (ϵ_T) [219], in subsequent studies:

$$\epsilon_T = \ln(1 + \epsilon_E) \quad (3.4)$$

Force and stress determination

As outlined in section 3.1.2 usage of a representative cross-sectional area is crucial for determination of material and apparent mechanical properties. In the current thesis, volumetric geometry was determined with a μ CT (see section 3.1.3 “Micro computed tomography (μ CT) and image processing”). Although care was taken to align trabeculae along the vertical axis during μ CT scanning (see inset in figure 3.2-A), precise digital alignment according to the initial video sequence of each experiment was still necessary (see figure 3.4-D). Digital alignment was done using 3DSlicer (v4.1.0r19886, Slicer Community). The μ CT image was re-scaled by a factor 3 and converted to a .mhd-file. Further, the initial frame from the frontal plane and the first image from the side view were converted to .mhd-files. The offsets of the .mhd files were modified such that all images were centered at the trabecular strut. Hereby, the frontal and side image were rotated to be oriented orthogonal. Then, the μ CT image was transformed to be aligned on both images from the experiment (see section 3.1.3 “Micro computed tomography (μ CT) and image processing”). After that, the μ CT image was cropped to the determined upper and lower mean particle position from the strain tracking (see figure 3.4-D).

The representative cross-sectional area (A_{ref}) was then determined in three different ways (see figure 3.5). First, the volume of the cropped, segmented μ CT image (yellow in figure 3.5-A) was divided by its length (the initial length l_0), giving a mean cross-sectional area A_{mean} . Second, the segmented slice in the middle position between the top and bottom of the cropped trabeculae was used to determine the cross-sectional area A_{mid} (red in figure 3.5-A). Third, the same slice was used to measure the elliptical major a and minor axis b (see figure 3.5-C) to calculate the elliptical area A_{ellip} as:

$$A_{\text{ellip}} = \frac{\pi a b}{4} \quad (3.5)$$

The engineering stress σ_E , based on the force measured with the load cell during the experiment (F_{exp}), was then calculated as:

$$\sigma_E = \frac{F_{\text{exp}}}{A_{\text{ref}}} \quad (3.6)$$

As true, logarithmic strain was used in subsequent studies, engineering stress was converted to true stress as [219]:

$$\sigma_T = \sigma_E (1 + \epsilon_E) \quad (3.7)$$

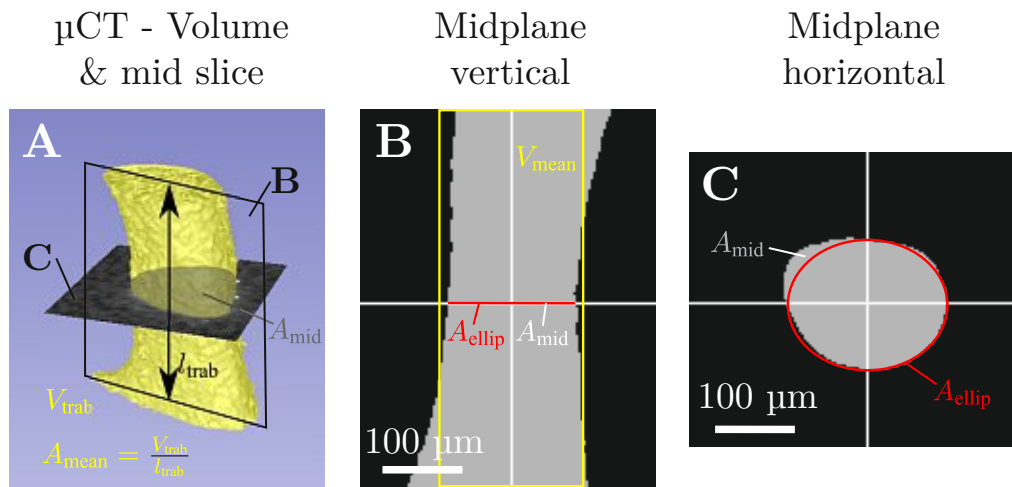


Figure 3.5: Determination of cross-sectional area. **A**: The volume of the trabecula (V_{trab}) was determined in μCT images and divided by its length (l_{trab}) to get the mean cross-sectional area (A_{mean}). The mid-slice (in the center) was used to determine the mid-area (A_{mid}). **B**: Mid-plane in vertical direction, indicating mean virtual volume (V_{mean}). **C**: Mid-plane in horizontal direction, indicating elliptical area A_{ellip} and A_{mid} .

Determination of apparent mechanical parameters

Load and displacement signals were manually synchronized by detecting the point of failure in both signals. As suggested by Carretta et al. [171] a simple isotropic Voce model [220] was used to describe the mechanical behavior of trabecular bone tissue in the elastic and post-yield region. Since the mechanical properties of whole trabeculae were determined by curve-fitting, these properties still inherit a structural influence and are thus described as *apparent mechanical* properties (denoted with a \wedge). In contrast, variables determined with the rheological model

are described as *material* properties. In the linear region, the constitutive behavior is given by Hooke's law:

$$\sigma_E = \hat{E} \epsilon_E \quad , \text{ if: } \quad \epsilon_E \leq \hat{\epsilon}_y \quad (3.8)$$

Hereby, apparent elastic modulus \hat{E} is determined as the slope of a linear regression. A custom-written python script evaluated the slope, as well as the yield point, whereby this idea was based on a previous study of Synek et al. [221]. In principle, the R^2 value is determined as a function of the window size of used data points. The center of the window is in the center of the expected linear region (the first third of the curve). Increasing the number of used data points in the linear region results in a decrease of the residuals and a larger R^2 value. However, if the data window is enlarged in the non-linear region, then the residuals increase and lower the R^2 value. This approach was done first towards lower strains from the center (to find the linear start point). Then, the window was enlarged towards larger strain values until the maximum R^2 value was found. This value was taken as the apparent yield point, since the stress-strain curve showed a non-linear behavior afterwards.

In the post-yield region the constitutive behavior was given by:

$$\sigma_E = \hat{\sigma}_y + \hat{\sigma}_h (1 - e^{-\hat{B} \epsilon_{pl}}) \quad , \text{ if: } \quad \epsilon_E > \hat{\epsilon}_y \quad (3.9)$$

Hereby, $\hat{\sigma}_y$ denotes the apparent yield stress, $\hat{\sigma}_h$ the apparent hardening stress, which is the difference between the apparent stress at failure $\hat{\sigma}_u$ and $\hat{\sigma}_y$. Plastic strain (ϵ_{pl}) is the difference between engineering strain (ϵ_E) and apparent yield strain ($\hat{\epsilon}_y$). The apparent hardening coefficient (\hat{B}) was determined in SciPy (V 0.18.0, The Scipy community) using an exponential data fit. The point of failure was simply defined as the last recorded point before sample fracture. Apparent elastic (\hat{W}_{el}) and post-yield work (\hat{W}_{py}) were determined with numerical integration of the stress-strain curve from zero strain to the apparent yield strain ($\hat{\epsilon}_y$) and from $\hat{\epsilon}_y$ to $\hat{\epsilon}_u$, respectively, using the trapz function of numpy (V 0.18.0, The Scipy community).

FE analysis

Pre-processing for FE analysis was done in medtool (v4.3, Dr. Pahr Ingenieure e.U., Austria). A voxel-to-element conversion was performed to get hexahedral C3D8I elements from voxel images of cropped, aligned trabecular struts (see figure 3.4-D). Further, a template script was used to define the boundary conditions (BC) according to figure 3.4-E. A kinematic coupling of all nodes of the bottom plane to a reference node at the center of gravity (COG) in that plane was done. The same procedure was done for the nodes at the top plane. The bottom reference node was constrained at all degrees of freedom (DOF). The top reference node was moved by 100 μm in vertical direction (u_3), whereas all other DOFs were constrained.

The actual FE analysis was performed in Abaqus (V6.14, Simulia, Dassault Systèmes, France). Medtool was used to capture the reaction force of the bottom reference node in vertical direction (F_3) from the output database. This value was divided by the applied 100 μm displacement (u_3) to calculate the apparent stiffness and compared to the apparent stiffness from the actual experiment. The relative error between these two values was calculated and used to correct the used elastic modulus of 10 GPa to the actual sample specific value.

Influence of trabecular tilt angle on determined stiffness and strength

The influence of the tilt angle of the longitudinal trabecular axis on the determined mechanical properties was estimated with a simple FE-model. A single linear quadratic beam element with a circular cross section was used to estimate the influence of different inclinations (0° , 5° , and 10°) on the determined apparent stiffness and strength. Hereby, an elasto-plastic material with perfect isotropic hardening was chosen. Different boundary conditions were investigated, like complete constraint of both beam ends, constraint of translation, but not of rotation, and constraint of one end, while the other one was free to move. Constraint of both ends (all rotational and translational DOFs) resulted in a moderate decrease of 10 % of stiffness and only of 1.4 % of strength at 10° inclination. Free rotation of one end (while still both ends were constrained in translation) yielded similar results. In contrast, constraint of only one end, with no constraint of the second end, resulted

in a different load-displacement behavior (see figure 3.6). Here, apparent stiffness decreased by almost 50 % if the sample was tilted by 10°. However, strength was only decreased by 2%. Taken together, sample alignment is very crucial to avoid underestimation of stiffness. Moreover, it is essential to provide a consistent, symmetric fixation to avoid bending of samples.

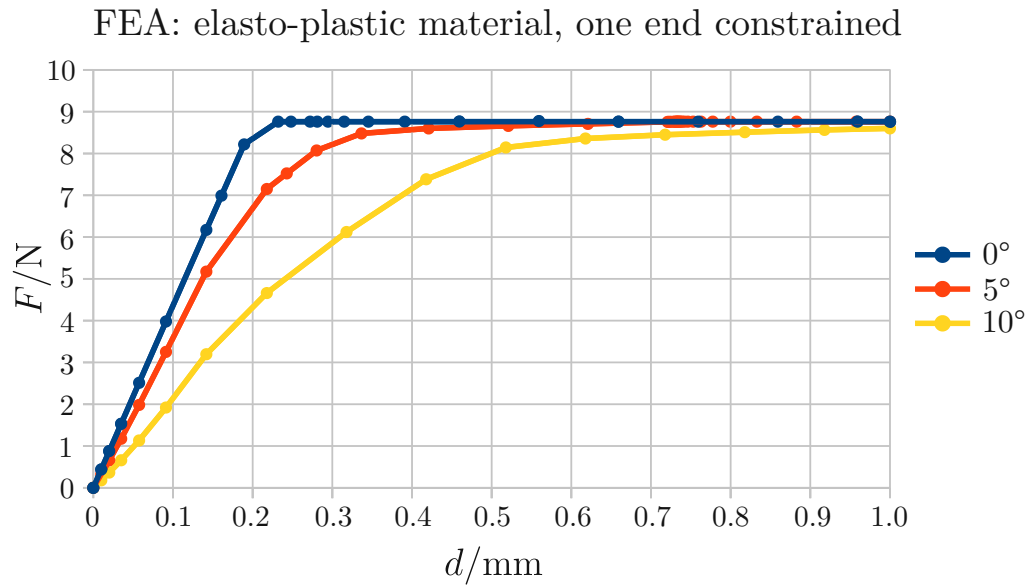


Figure 3.6: Estimation of tilt influence on stiffness and strength with a simple FE-model. A single linear quadratic beam element was tilted by 0°, 5°, and 10° and an elasto-plastic material with perfect isotropic hardening was used. The bottom end was constrained in all DOFs, while the top end was displaced by 1 mm.

Validation of tensile test set-up

The validation of the tensile test set-up was done with PVC samples with a known elastic modulus of 3.2 GPa. Eight dog-bone shaped samples were CNC milled (PFK-0203-PX – CNC Router, BZT Maschinenbau GmbH, Germany) from a 1 mm thick PVC plate to a width of 0.5 mm. Samples were aligned and embedded in epoxy in silicone chambers in the same way as described for bone samples (see section 3.1.3 “Sample preparation”). Determination of mean cross sectional area (A_{mean}), stress and strain, and apparent elastic modulus was done in the same way

as for bone samples (see sections 3.1.3 “Micro computed tomography (μ CT) and image processing” to 3.1.3 “Determination of apparent mechanical parameters”. The determined average elastic modulus of the PVC samples was (2.9 ± 0.3) GPa. Accuracy was calculated as 16 % and determined as the ratio of the root-mean-square deviation to the mean. Precision was 12 % and determined as the Coefficient of Variation (CV equals the ratio of the standard deviation to the mean). Giving the high sample throughput, the obtained accuracy and precision indicates a reliable measurement set-up. Further, CNC milling resulted in local deviations of the assumed geometry, which has probably also contributed to deviations of obtained values of elastic modulus in comparison to the true value.

Statistical analysis

Statistical analysis was performed with R (Version 3.3.2, The R Foundation) [222]. Data was first inspected with histograms, Q-Q plots and then checked for outliers. As data did not show outliers, the comparison of mechanical parameters was done with a one-way ANOVA and Tukey honest significant difference (HSD) was used as a post hoc test. Values below a significance level α of 0.05 were considered as significant.

3.1.4 Results

Ten individual trabecular specimens were successfully prepared and tested. One specimen was discarded as it experienced misalignment. Figure 3.7 illustrates the determined engineering stress-strain curves of all samples, based on the elliptical area (A_{ellip}). The calculated average stress strain-strain curve is shown in bold and was calculated with an assumed Voce-model (according to the formulas displayed in the figure). The mean values (\pm standard deviation) for the elliptical area, mean area and the FE analysis are shown in table 3.1. The determined elastic modulus was significantly different between all three methods. Mean elastic modulus was (9.9 ± 3.4) GPa for elliptical area, (7.6 ± 2.4) GPa for mean area and (8.2 ± 2.4) GPa for FE analysis. As expected, FE analysis results in larger stress values than those of an assumed elliptical cross-sectional area, but in lower values than those obtained from an assumed mean area.

As only a linear-elastic FE analysis was used, no further material properties were obtained with that approach. Tissue strain determined with an elliptical or mean area were the same, as only stresses and works depend on the cross-sectional area (see table 3.1). Mean yield strain (ϵ_y) was $(0.8 \pm 0.4) \%$, mean ultimate strain (ϵ_u) was $(9.8 \pm 3.8) \%$ for both approaches. Yield stress, ultimate stress and post-yield work were significantly larger in the elliptical area based approach, compared to the mean area one. A direct comparison between the calculated elliptical cross-sectional area (A_{ellip}) with the actual cross-sectional area at the median slice (A_{mid}) showed that there is no significant difference ($p = 0.614$).

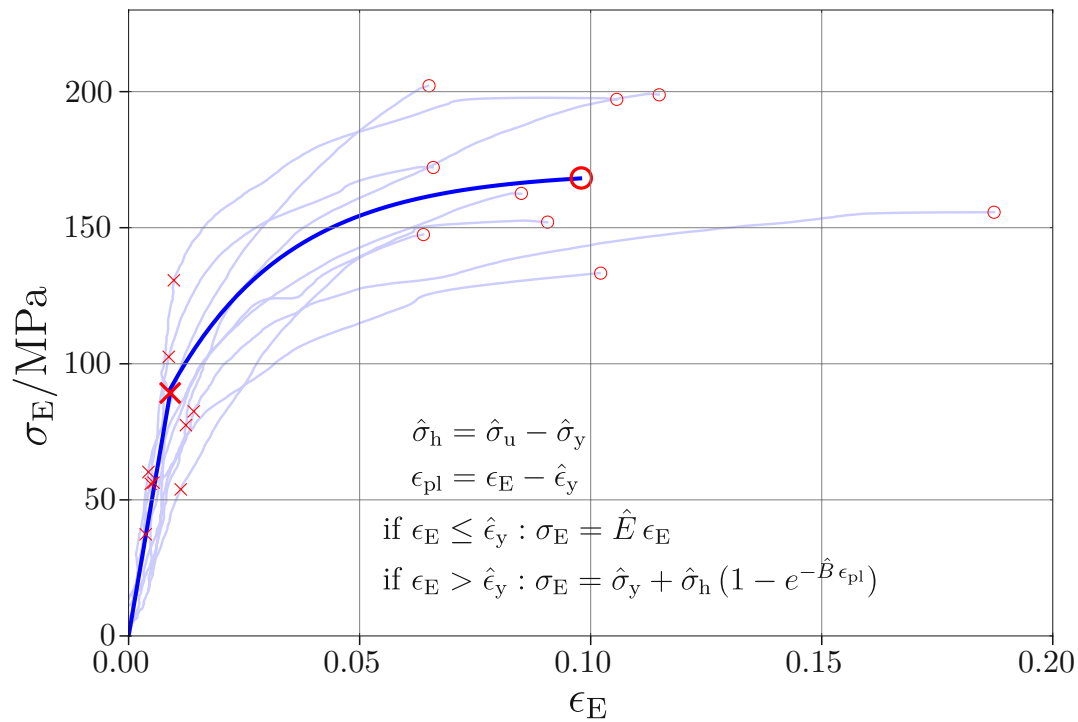


Figure 3.7: Stress-strain curves of tensile experiments of individual trabeculae close to a physiologic environment. Experimental curves are shown bright, the calculated average curve is shown **bold**. Equations denote the used Voce-model for determination of the apparent mechanical parameters (with \wedge for discrimination of material parameters obtained with the rheological model, see section 3.3 in subsequent studies). \times denotes yield points, \circ points of failure.

Parameter	Elliptical	Mean	FE
\hat{E}/GPa	9.9 ± 3.4	7.6 ± 2.4^a	8.2 ± 2.4^{ab}
$\hat{\sigma}_y/\text{MPa}$	73 ± 29	59 ± 25^a	
$\hat{\epsilon}_y/\%$	0.8 ± 0.4	0.8 ± 0.4	
$\hat{\sigma}_u/\text{MPa}$	169 ± 25	138 ± 24^a	
$\hat{\epsilon}_u/\%$	9.8 ± 3.9	9.8 ± 3.9	
\hat{B}	39 ± 13	39 ± 13	
$\hat{\sigma}_h/\text{MPa}$	96 ± 28	79 ± 22	
$\hat{W}_{py}/(\text{MJ m}^{-3})$	12.8 ± 5.6	10.3 ± 5.9^a	
$\hat{W}_{el}/(\text{MJ m}^{-3})$	0.3 ± 0.2	0.3 ± 0.2	

Table 3.1: Influence of chosen cross-sectional area apparent mechanical parameters. Mean \pm standard deviation are reported. ^a significant difference to Elliptical, $p = 0.001$. ^b significant to Mean, $p = 0.001$.

3.1.5 Discussion

This is the first study that successfully performed tensile experiments of individual trabeculae close to a physiologic, wet environment. Tensile tests were performed in HBSS ($\text{pH} = 7.4$) to mimic a realistic physiologic environment for bone tissue. Previously, only four studies carried out tensile experiments of individual trabeculae up to fracture [18, 36, 120, 171]. However, three of those studies [18, 120, 171] tested in air, meaning that trabeculae were dried out. Only in the study from Hernandez et al. [36] droplets of HBSS were added onto the samples to stay them hydrated. The only mechanical property of human trabeculae determined in that study was ultimate strain as $(8.8 \pm 3.7) \%$. In the present study ultimate strain was determined as $(9.8 \pm 3.8) \%$ for bovine trabeculae, similar to these previous values. In contrast, reported ultimate strain values for dried young bovine trabeculae was $(5.1 \pm 2.2) \%$ [171], $(5.1 \pm 2.4) \%$ [18] for dried human trabeculae and $(5.6 \pm 6.2) \%$ for dried 54 week old rat trabeculae [120] (no treatment group). Sequentially, determined ultimate strain in a wet, physiologic environment is approximately doubled, compared to dehydrated trabeculae, irrespective of species. Ultimate strain can be seen as a failure property, which is linked to the ductility, describing if a loaded trabecula fractures or not [223]. Accordingly, hydrated trabeculae are able to absorb much more energy, because of the larger deformation, compared to

dried specimens.

Besides failure properties, dehydration of trabecular bone tissue was reported to cause significant changes of the elastic modulus (E). For example, Townsend et al. determined that dehydration causes a transition from a ductile behavior of hydrated trabeculae ($E = 11.4$ GPa) to a brittle one ($E = 14.1$ GPa) in dried specimens. Similarly, Hengsberger et al. [196] and Wolfram et al. [17] found a significant difference between the elastic modulus of hydrated and dried trabecular bone tissue in nanoindentation. These findings highlight the necessity to perform micro-mechanical experiments in a hydrated state.

In addition, the influence of the cross-sectional area, which was determined with different approaches, on apparent mechanical properties was performed. So far, it has only been mentioned that there is a structural influence on obtained material and apparent mechanical properties [18, 120, 171] but no direct comparison has been performed yet. Here, three different approaches were compared: Cross-sectional area was assumed to be elliptical (determined at the mid slice), calculated as the mean area (volume divided by its length) and a FE analysis was performed to back-calculate tissue elastic modulus. A significant ($p = 0.001$) difference in the determined tissue elastic modulus was found between all approaches (see table 3.1). These findings highlight that there is a structural influence of the geometric shape of individual trabeculae on the material and apparent mechanical properties.

McNamara et al. [120] and Carretta et al. [18, 171] already suggested to use FE analysis in tensile experiments to overcome this issue. Elastic modulus was reported as (2.8 ± 2.1) GPa for 54 week untreated rat trabeculae [120], (16.2 ± 2.5) GPa for healthy human trabeculae [18] and (11.8 ± 2.6) GPa for young bovine trabeculae [171]. Thus, the determined value of (8.2 ± 2.4) GPa in the present study is comparable to those determined by Carretta et al. for young bovine specimens [171]. But, there is apparently a large difference in the elastic modulus between different species.

First studies assumed a circular cross-sectional area [162, 178], and later Jirousek

et al. used an elliptical area [177], whereas Bini et al. assumed a rectangular one [184]. Reported values for elastic modulus, using an assumed regular geometric area, ranged from 1 GPa [178] to 10.4 GPa [162]. In the present study elastic modulus was determined as (9.9 ± 3.4) GPa, assuming an elliptical area. This value is close to the reported (10.4 ± 3.5) GPa from Rho et al. [162], where a circular cross-sectional area was assumed and (9.2 ± 1.3) GPa from Jirousek et al. [177], where an elliptical cross-sectional area was assumed. However, other studies reported much lower values: Bini et al. reported (1.4 to 1.9) GPa [184] and Ryan et al. 1 GPa [178] for elastic modulus. In a later study, Yamada et al. determined an average cross-sectional area using μ CT [179]. That study reported (11.5 ± 5.0) GPa for tissue elastic modulus, compared to (7.6 ± 2.4) GPa, based on the mean area, in the present study.

Taken together, determined elastic moduli are comparable to values reported in literature but there is a tremendous variation of those values, even when the same approach was used to determine the cross sectional area (compare 1 GPa [178] to 10.4 GPa [162] for an assumed circular cross-sectional area). Sequentially, differences in the test procedure and the strain recording might play an important role. Nevertheless, the current study could clearly highlight that there is a significant difference in reported material/mechanical properties, if different approaches are used to determine a representative cross-sectional area in the same test procedure. FE analysis is probably the most reliable method to minimize the structural influence of the trabecular shape. However, FE analysis also inherits the limitation to assume bone as a linear-elastic and homogeneous material. Further, FE analysis requires modeling and computational resources, resulting in a more sophisticated and time-consuming evaluation, compared to geometrically determined representative cross-sectional areas. An assumed elliptical area in the mid plane gives significantly lower stresses (ultimate stress and yield stress) and post-yield work, compared to stresses based on an average mean area. Interestingly, the back-calculated tissue elastic modulus from FE analysis is almost the average value of the values based on the mean and elliptical area. Thus, an estimation of back-calculated stress values can be done by taking the average cross-sectional area from the mean and mid area approach. Moreover, stress values obtained from the mid area approach can

be considered as a upper estimation of actual stress values, whereas those from the mean approach as a lower boundary.

Limitations of the current study are that trabeculae were obtained from a young bull. Carretta et al. showed that elastic modulus, yield stress and ultimate stress change significantly in old bulls [171]. Further, a comparison to literature indicates that there might be a difference in elastic moduli between different species, when using FE analysis. Thus, it remains to be shown that back-calculated values from FE analysis are also close to the average value of mean and mid area based values in mature bulls and, more importantly, in humans. Only one animal was used in the current study. Thus, more donors should be used in future studies to verify the found differences in a larger population. Moreover, a direct comparison of wet and dry trabeculae in the current test set-up would shed more light on the effect of dehydration on the mechanical behavior of individual trabeculae. Last but not least FE analysis inherits the limitation of an assumed linear-elastic, homogeneous material behavior. Implementation of a non-linear material model, like the Voce model, would enable the back-calculation of further mechanical properties, such as yield and post-yield properties. However, information about viscosity and damage would be still lacking. Hence, cyclic experiments with holding periods would enable a more thorough mechanical characterization of trabecular bone tissue.

3.2 Cyclic tensile testing of individual trabeculae

As mentioned in the previous section, monotonic tensile experiments are lacking the possibility to discriminate viscous, plastic and damage properties. Conventionally, different experiments are needed to determine these additional material properties. For example, hold-relaxation experiments enable determination of viscous properties. Loading/unloading experiments can discriminate elastic material behavior from plastic, damage or viscous contributions. Given that sample preparation and handling is quite difficult with individual trabeculae (see section 2.7.3) it was decided to use a loading protocol which enables a comprehensive material character-

ization of all these properties in a single experiment. Further, the modulus can be obtained in each loading and unloading cycle to determine potential changes, like a decrease of modulus because of damage accumulation. Determination of modulus in the first unloading cycle (before sample yielding) also enables calculation of the true elastic behavior, without contributions from viscosity, damage or plasticity.

Since trabeculae differ in size and geometry, a sample specific loading protocol would be favorable. The cross sectional area was always determined with μ CT measurements ahead of mechanical testing (see section 3.1.3 “Micro computed tomography (μ CT) and image processing”). Thus, a force controlled loading profile could theoretically be used for engineering stress controlled profiles. However, three major limitations were encountered with that approach. First, the used servo-electric load frame (SELmini-001, Thelkin AG, Switzerland) could not perform well in load control mode, irrespective of the used tuning parameters. Second, the load protocol would be also influenced by potential errors made during stress determination. Additionally, the throughput is lower, if the loading protocol has to be adjusted for each experiment separately. On the contrary, a displacement controlled experiment is more straight forward to implement. The protocol is always the same, but the sample geometry has to be almost constant to provide similar stress-strain responses between individual samples. Further, machine control is much more efficient and accurate (in case of the used servo-electric load frame). Taken together, it was decided to use a displacement based loading protocol. As shown in figure 3.8 two different protocols were used in the current thesis. In samples that were tested until failure fewer cycles were necessary as in those for microdamage induction (see figure 3.8-A). Here, the holding time in the first loading and unloading cycle was set to 100s to ensure almost complete relaxation. In subsequent cycles the holding time was set to 10s, to determine incomplete relaxation. This loading protocol was used in the studies “Elasto-visco-plastic rheological modeling of trabecular bone tissue” (section 3.3), “Osteoporosis affects mainly morphometry not material properties in femoral head” (chapter 5) and “Influence of non-enzymatic glycation on the material properties” (chapter 7). In contrast, in the study “Changes of material properties with anti-resorptive treatment” (section 6) it was intended to induce microdamage in a reasonable amount of test cycles. Sequentially, only short

holding times (10 s) were used and the number of test cycles was increased to 14 (see figure 3.8-B). It has to be noted that these samples had to be displaced much more, as they showed a much lower modulus than previous specimens.

Loading profiles - controlled by machine displacement (d)

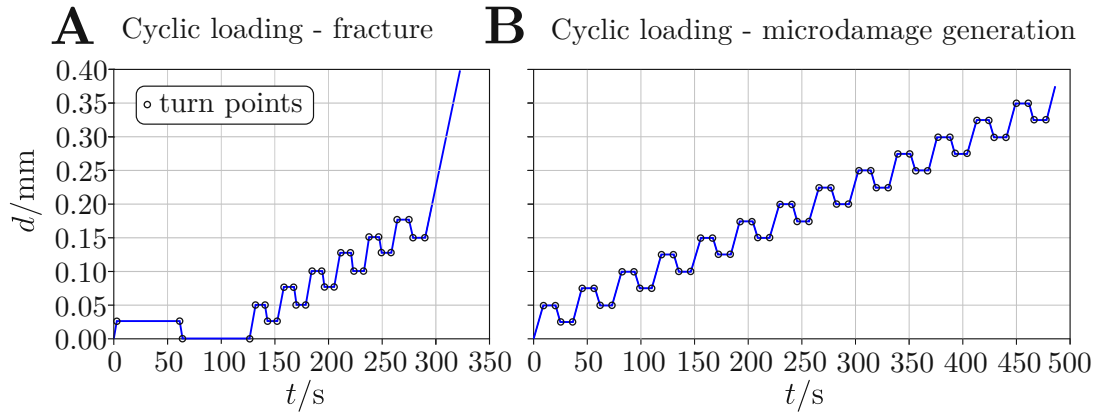


Figure 3.8: Cyclic loading profiles, controlled by machine displacement (d). **A**: Loading profile for experiments up to fracture. **B**: Loading profile for microdamage generation. \circ denotes the turn points (used for curve segmentation).

3.2.1 Cyclic testing - tensile modulus evolution

Obtained stress-strain curves were segmented into individual cycles (containing loading, holding and unloading phases), as this information is known from the used displacement profile (turn-points between loading and holding phases are marked as “o” in figure 3.8). A custom-made python script was used to obtain exponential fits ($f(x)$) for each loading ($f(x) = a(1 - e^{-\frac{x}{b}} + c)$) and unloading phase ($f(x) = \frac{a}{b}(e^{bx} - 1)$) in every cycle. The curvefit function, obtained from SciPy (V 0.18.0, The Scipy community), was used to perform a non-linear least squares approach to determine best fits for $f(x)$. Further, the first derivative was calculated analytically to compute the tangent of the obtained exponential fit (see straight colored lines in in figure 3.9-A). This tangent was used as the tensile modulus of each corresponding cycle and to illustrate the evolution of the tensile modulus with increasing cycle numbers (see figure 3.9-B).

Although the presented loading protocols enable a more detailed mechanical characterization, a reliable evaluation from a single experiment is still challenging.

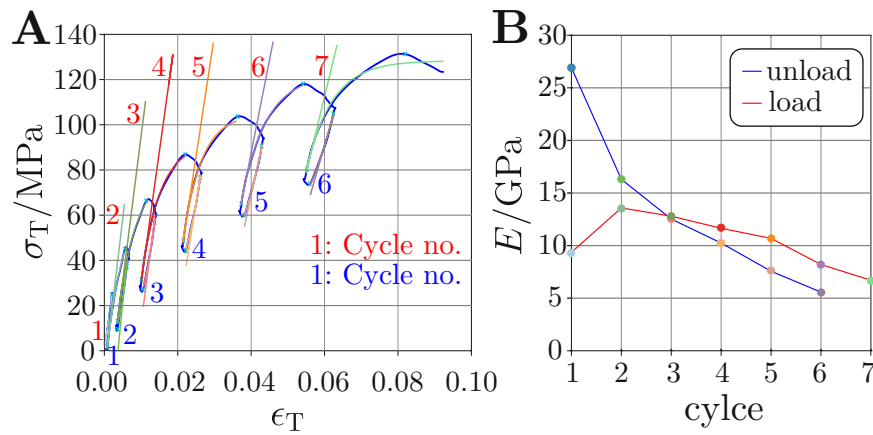


Figure 3.9: Determination of tensile modulus evolution in cyclic tensile testing. **A:** True stress-strain curve with fitted exponential functions and the tangent in every loading and unloading cycle. **B:** Corresponding tensile moduli (dots are color coded) for the loading and unloading cycles illustrates the evolution over cycle number.

One possibility is to determine each mechanical property separately, with curve fitting approaches. This procedure is rather time consuming and inherently has the drawback of splitting measurement data apart, e.g. into the envelope curve, the hold/relaxation part for the viscosity and the loading/unloading parts. A more elegant way to determine all material parameters at once would be the usage of a rheological model, as outlined in the next section.

3.2.2 Cyclic testing - envelope curve-fitting

Evaluation of the apparent mechanical properties was performed for cyclic tensile tests on the envelope curve (see figure 3.10), in the same way as described in section 3.1.3 “Determination of apparent mechanical parameters” (for monotonic loading). Hereby, the first loading cycle was used to determine the yield point with a linear regression in the same way as described previously. Next, the yield point, the turn points (x in figure 3.10) at the end of the loading cycles and the point of failure were used to determine the post-yield envelope curve as an exponential fit using Scipy (V 0.18.0, The Scipy community). An exemplary determination of the apparent elastic modulus (\hat{E}), apparent yield stress ($\hat{\sigma}_y$) and strain ($\hat{\epsilon}_y$), apparent hardening coefficient (\hat{p}), apparent hardening stress (\hat{R}), apparent ultimate stress

($\hat{\sigma}_u$), apparent ultimate strain ($\hat{\epsilon}_u$), apparent elastic work (\hat{W}_{el}), and apparent post-yield work (\hat{W}_{py}) is illustrated in figure 3.10.

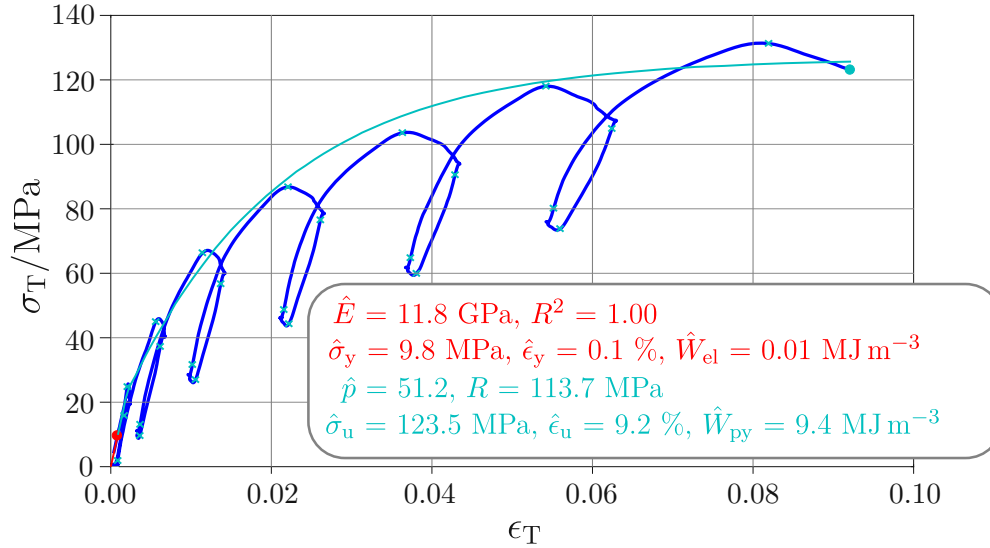


Figure 3.10: Determination of apparent mechanical properties by curve-fitting on the envelope curve. The cyclic tensile stress-strain curve is shown with the **linear fit**, for determination of the apparent elastic modulus and the apparent yield point (denoted as \bullet). The computed **envelope curve** describes the post-yield region, until the point of failure (denoted as \bullet). Apparent elastic modulus (\hat{E}), apparent yield stress ($\hat{\sigma}_y$) and strain ($\hat{\epsilon}_y$), apparent hardening coefficient (\hat{p}), apparent hardening stress (\hat{R}), apparent ultimate stress ($\hat{\sigma}_u$), apparent ultimate strain ($\hat{\epsilon}_u$), apparent elastic work (\hat{W}_{el}), and apparent post-yield work (\hat{W}_{py}).

3.3 Elasto-visco-plastic rheological modeling of trabecular bone tissue

3.3.1 Related publications and declaration of contributions

Partial results of the presented work (text, tables and figures) have been *published* in “Biomechanics and Modeling in Mechanobiology” in 2020, entitled “A 2-Layer Elasto-Visco-Plastic Rheological Model for the Material Parameter Identification of Bone Tissue”. This paper was written by Andreas G. Reisinger and co-authored

by *Martin Frank*, Philipp J. Thurner and Dieter H. Pahr.

Author contributions: *Andreas G. Reisinger* designed the study, developed the rheological model and implemented the optimization procedure. The second author, *Martin Frank*, who is the author of the current thesis, assisted *Andreas G. Reisinger* in the study design and carried out the mechanical experiments and data processing. *Philipp J. Thurner* and *Dieter H. Pahr* supervised the work of *Andreas G. Reisinger* and *Martin Frank*, took part in the study design and supported the interpretation of the results.

Since the rheological model was only applied in the current thesis, but not developed, this section focuses on the description and usage of the model. Thus, only the methodological part is presented here and the interested reader is referred to the original publication [224] for the actual investigation.

3.3.2 The 2-Layer elasto-visco-plastic rheological model

The model consists of a Prandtl-layer and a Maxwell model (see figure 3.11), arranged in parallel. The equations are formulated for geometric linear problems and thus, engineering stress and strain are used. The total stress σ_{mod} is calculated as the sum of the stresses in the two layers:

$$\sigma_{\text{mod}} = \sigma_{\text{pr}} + \sigma_{\text{mx}} \quad (3.10)$$

Prandtl-Layer: This layer is composed of an elastic spring, with elastic modulus E_{pr} , in series with a plastic slider. Thus, the strain of the Prandtl-layer (ϵ) can be split into an elastic and a plastic part (ϵ_{p}). The stress in this layer (σ_{pr}) is calculated as:

$$\sigma_{\text{pr}} = E_{\text{pr}} (\epsilon - \epsilon_{\text{p}}) \quad (3.11)$$

The plastic slider is defined by a yield condition (f), whose yield limit is expanding exponentially with equivalent plastic strain (α) [220]:

$$f(\sigma_{\text{pr}}, \alpha) = |\sigma_{\text{pr}}| - [\sigma_y + (\sigma_u - \sigma_y)(1 - e^{-\alpha p})] \quad (3.12)$$

Here, σ_y denotes the yield stress, σ_u the ultimate/failure stress and p the exponential hardening coefficient. Based on the evolutionary equation, the flow rule, the plastic flow direction and the consistency condition the final equation for the slip rate (γ) is obtained as:

$$\gamma = \begin{cases} \text{sign}(\sigma_{\text{pr}}) \frac{E_{\text{pr}} \dot{\epsilon}}{E_{\text{pr}} + (\sigma_u - \sigma_y) p e^{-p \alpha}} & , \text{ if } f(\sigma_{\text{pr}}, \alpha) = 0 \\ 0 & , \text{ if } f(\sigma_{\text{pr}}, \alpha) < 0 \end{cases} \quad (3.13)$$

Maxwell Layer: This layer is composed of an elastic spring, with the Maxwell/dynamic modulus (E_{mx}), in series with a viscous damper, with the coefficient of viscosity (η). The governing equation is formulated as [225]:

$$\dot{\sigma}_{\text{mx}} + \frac{E_{\text{mx}}}{\eta} \sigma_{\text{mx}} = E_{\text{mx}} \dot{\epsilon} \quad (3.14)$$

Further, the strain in the damper (ϵ_v) is calculated as:

$$\epsilon_v = \epsilon - \frac{\sigma_{\text{mx}}}{E_{\text{mx}}} \quad (3.15)$$

Solving of differential equations: The strain (ϵ) is used as a time (t) dependent input variable for the 2-layer model. Thus, the stress response in the Prandtl-layer (σ_{pr}) and in the Maxwell-layer (σ_{mx}) can be determined independently and added up to the total stress (σ_{mod} , see equation 3.10). Both layers can be solved by using ODE solvers in the time domain.

Dynamic mechanical analysis (DMA): The pure visco-elastic properties of the 2-layer model can be described by DMA, for comparison with other studies. Hence, the storage modulus (E'), the loss modulus (E'') and the loss tangent ($\tan(\delta)$) are derived.

$$E'(\omega) = \frac{\frac{\eta}{E_{\text{mx}}} \frac{\eta(E_{\text{pr}}+E_{\text{mx}})}{E_{\text{mx}}} \omega^2 + E_{\text{pr}}}{\left(\frac{\eta}{E_{\text{mx}}}\right)^2 \omega^2 + 1} \quad (3.16)$$

$$E''(\omega) = \frac{\frac{\eta(E_{\text{pr}}+E_{\text{mx}})}{E_{\text{mx}}} \omega^2 - \frac{\eta}{E_{\text{mx}}} E_{\text{pr}} \omega}{\left(\frac{\eta}{E_{\text{mx}}}\right)^2 \omega^2 + 1} \quad (3.17)$$

Based on equation 3.16 and 3.17 the loss tangent, which is the tangent of the phase shift δ , between strain excitation and stress response is calculated as:

$$\tan(\delta) = \frac{E''}{E'} = \frac{\frac{\eta(E_{\text{pr}}+E_{\text{mx}})}{E_{\text{mx}}} \omega^2 - \frac{\eta}{E_{\text{mx}}} E_{\text{pr}} \omega}{\frac{\eta}{E_{\text{mx}}} \frac{\eta(E_{\text{pr}}+E_{\text{mx}})}{E_{\text{mx}}} \omega^2 + E_{\text{pr}}} \quad (3.18)$$

Long-term and instantaneous elastic modulus: Depending on the applied strain rate ($\dot{\epsilon}$) the 2-layer model shows different responses. If the model is loaded quasi-statically the Maxwell-layer has no stress contribution ($\sigma_{\text{mx}} = 0$). The same response is obtained if the deformation state is hold constant until the viscous stress contribution is decayed. Sequentially, the total elastic modulus is solely determined by the elastic spring in the Prandtl-layer (E_{pr}). Thus, this value can be referred as the long term elastic modulus (E_{∞}). In contrast, application of a Heaviside step function causes a response in both layers. The total model elastic modulus is the the sum of (E_{pr}) and (E_{mx}), the instantaneous elastic modulus (E_0). These two values determine the lower and upper boundary for the elastic modulus obtained at any finite strain rate.

Ultimate stress (σ_u) is the maximum stress level, which is reached in the Prandtl-layer during plastic deformation. However, this stress is usually not reached in the experiments, likely because of material voids or inhomogeneities. Interestingly, also the theoretical apparent elastic modulus (\hat{E} , see section 3.1.3 “Determination of apparent mechanical parameters”), which is simply determined as the tangent modulus of the envelope curve, is sometimes larger than the instantaneous modulus (E_0). This might be related to usage of true vs. engineering stress or experimental issues.

Material parameter identification

In principle, a set of material parameters $\underline{q} = [E_{pr}, \sigma_y, \sigma_u, p, E_{mx}, \eta]$ has to be identified, requiring a minimal deviation between the stress response of the 2-layer model (σ_{mod}) and the measured stress in the experiment (σ_{exp}). σ_{mod} is determined at discrete time points of σ_{exp} and hence, both time series are synchronized. Sequentially, the goodness of fit can be expressed in terms of the weighted root mean square error (RMSE_w), which is evaluated at the time points (t_i) of the time series (with $i = 1 \dots n$ and n being the total number of time points, as shown in figure 3.11-A).

$$RMSE_w(\underline{q}) = \sqrt{\frac{1}{n} \sum_{i=1}^n w_i (\sigma_{mod}(\underline{q}, \epsilon, t_i) - \sigma_{exp}(t_i))^2} \quad (3.19)$$

In order to perform a robust and reliable optimization, the weighting factor w_i was determined in pre-tests as 1.0 at highlighted points in figure 3.12-A (and 0 otherwise). Equation 3.19 is used as the objective function for the optimization process, such that the RMSE_w is minimized for \underline{q} . In short, a reliable start parameter set \underline{q} (determined in pre-trials) is selected and a multi-start method is initialized to determine the optimized material parameter set \underline{q}^* .

An exemplary evaluation of a cyclic loading experiment with optically measured strain (see section 3.1.3) and determined stress is demonstrated in figure 3.12. The effects of neglecting different elements of the 2-layer model is demonstrated in figure 3.13. Omitting plasticity results in a steady increase of stress, whereas neglecting post-yield hardening keeps stress constant after yielding. Neglecting the Maxwell-layer causes loss of energy storage and dissipation. Switching to a linear hardening law causes a deviation from the actual curve shape (Root Mean Square Error (RMSE) increases from 2.17 MPa to 5.67 MPa for the shown example).

In summary, the applied 2-layer elasto-visco-plastic rheological model can reproduce the stress response of individual trabeculae in uni-axial cyclic loading at a high accuracy. Elastic, viscous, yield, post-yield hardening and failure material properties are identified in an inverse approach. The proposed model inherits a minimal amount

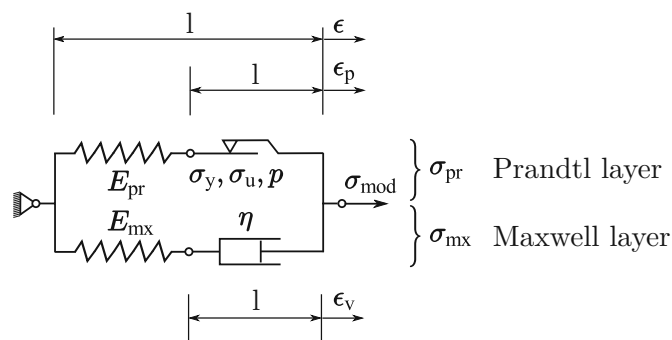


Figure 3.11: 2-layer rheological model. Total stress (σ_{mod}) consists of stress in the Prandtl-layer (σ_{pr}) and the Maxwell-layer (σ_{mx}). The Prandtl-layer is composed of a spring (with elastic modulus (E_{pr})) and a slider (with yield stress (σ_y), ultimate stress (σ_u), and hardening coefficient (p)). The Maxwell-layer is composed of a spring (with elastic modulus (E_{mx})) and a damper (with viscosity (η)). The strain in the slider is denoted as ϵ_p the one in the damper as ϵ_v and global strain as ϵ . Image modified from Reisinger et al. [224].

of rheological elements and is able to quantify multiple constitutive effects based on a single mechanical experiment.

3.4 Microdamage formation in individual trabeculae during fatigue tests

3.4.1 Related publications and declaration of contributions

Partial results of the presented work (text, tables and figures) have been *published* in “Journal of Biomechanics”, entitled “Microdamage formation in individual bovine trabeculae during fatigue testing” and co-authored by Julia-Theresa Fischer and Philipp J. Thurner. This work is further based on the Diploma thesis of *Julia-Theresa Fischer*, entitled “Quantification of microdamage formation during fatigue testing of individual trabeculae”, which was co-supervised and assisted by *Martin Frank*.

Author contributions: *Martin Frank*, who is the author of the current the-

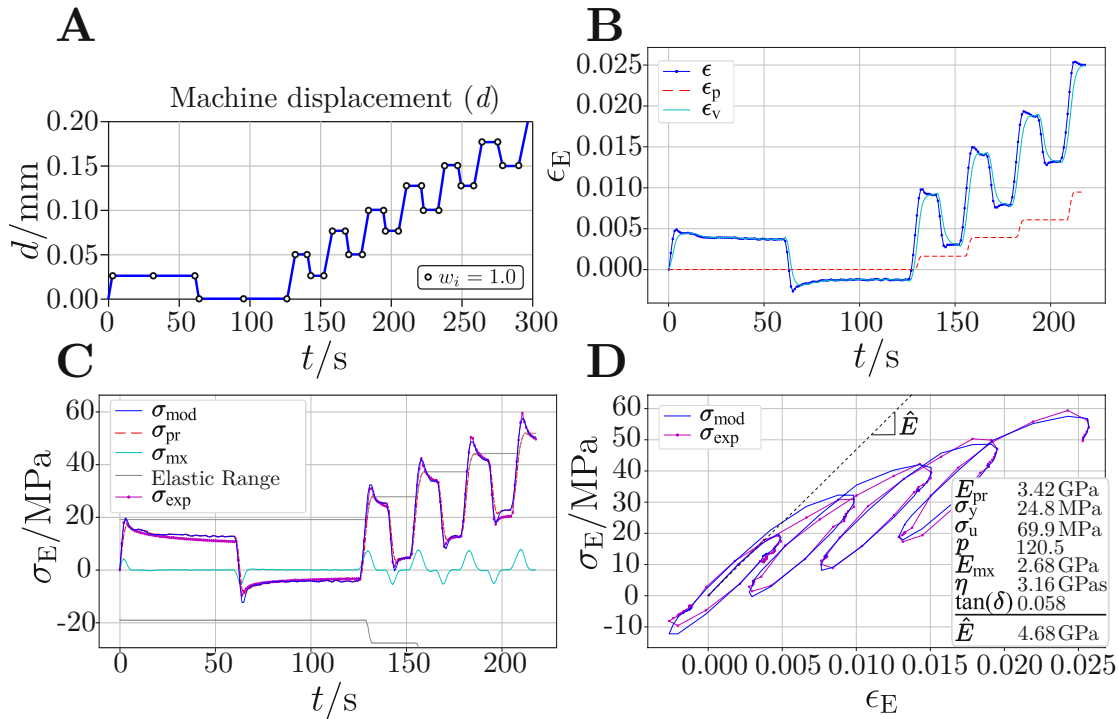


Figure 3.12: **A**: Loading profile with controlled machine displacement (d) over time (t). \circ illustrate the positions of the RMSE weighting factor ($w_i = 1.0$, which is 0 at all other positions). **B**: Input strain signal (ϵ), measured experimentally, split into plastic strain (ϵ_p) and viscous strain (ϵ_v). **C**: Experimentally determined stress (σ_{exp}) and optimized output stress (σ_{mod}) from the 2-layer model, which is further split into stress in the Prandtl-layer (σ_{pr}) and in the Maxwell-layer (σ_{mx}). **D**: Stress-strain diagram for the experimental (σ_{exp}) and simulation based evaluation (σ_{mod}). Identified material parameters (q^*) after optimization, are indicated in the box. Image modified from Reisinger et al. [224].

sis, contributed to the study design, performed mechanical data processing, data interpretation, assisted in the modification process of the fatigue test set-up, co-supervised the work of Julia-Theresa Fischer, and wrote the manuscript. The joint first author, *Julia-Theresa Fischer*, developed the fatigue test procedure, performed the specimen preparation, the mechanical tests, introduced the microdamage labeling technique, performed sample microscopy and did the microdamage evaluation. *Philipp J. Thurner* performed the study design, co-supervised the work of Julia-Theresa Fischer and supported the interpretation of the results.

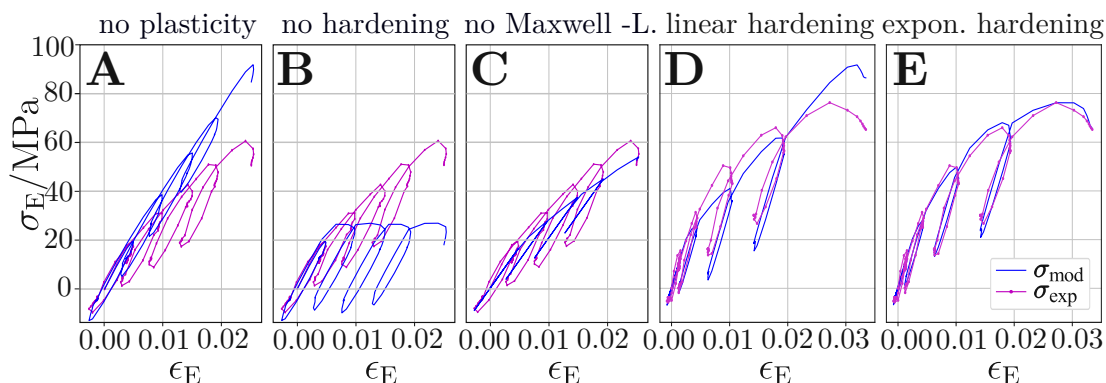


Figure 3.13: Effects of neglecting different elements of the 2-layer model. **A:** No plasticity ($\sigma_y = \text{inf}$). **B:** No hardening ($\sigma_u = \sigma_y$). **C:** No Maxwell-layer ($E_{\text{mx}} = 0$, $\eta = 0$). **D:** Linear hardening. **E:** Exponential hardening, model including all elements. Image modified from Reisinger et al. [224].

The presented work is intended to be used as a basis for microdamage induction in individual trabeculae. However, because of time issues, a modified form of microdamage induction (see section 3.2) was used in the study of chapter 6 “Changes of material properties with anti-resorptive treatment”.

To overcome this time issues, improvements were made in course of the subsequent Diploma thesis of *Omar Kabbani*, entitled “Quantification of microdamage formation during fatigue testing of individual trabeculae”, which was also co-supervised by *Martin Frank*, and are described in section 3.4.5 Limitations, improvements, and outlook.

3.4.2 Introduction

In daily activities, such as walking, bone is subjected to fatigue loading, leading to the formation of microdamage [50] (see section 2.3). Hereby, linear microcracks, which have a preferential orientation, can be distinguished from diffuse damage, which has no orientation in any direction [50]. In healthy bone, linear microcracks are removed during the remodeling process [87], whereas diffuse damage is repaired independently from it [88, 89]. However, aging and disease may slow down repair mechanism and eventually result in stress fractures [91].

In osteoporosis, bisphosphonates (BPs) are the first line medication to increase overall bone mass [25]. BPs reduce the resorptive phase of bone remodeling by reducing the amount of osteoclasts [226], the cells responsible for bone removal (see section 2.4). Moreover, bone mineralization is increased, but at the cost of a reduced energy absorption during mechanical loading, eventually leading to an accumulation of microdamage [226]. This effect has been linked to an increased risk of so called atypical fractures, like in the femoral strut [54].

Sequentially, knowledge about microdamage formation, detection and repair mechanism is of great medical interest. So far, most studies dealt with microdamage in cortical bone [227–230], although most fragility fractures occur in regions rich of trabecular bone [7]. The chemical composition of cortical and trabecular bone is similar, but they are macroscopically and microscopically different [231]. Thus, microdamage formation was further investigated in trabecular bone [84, 232, 233]. Trabecular bone is a highly hierarchical material (see section 2.1) and information about microdamage was only gained at the structural level so far. Hereby, only a few large microdamage sites in the central, interstitial bone were responsible for the decrease of stiffness in fatigue tests [234]. However, like in *in vivo* loading, statements about the actual load acting on individual trabeculae are almost impossible because of a large variation of trabecular orientation. Further, in bending experiments of cortical bone it has been demonstrated that mainly diffuse damage forms in tensile areas, whereas linear microcracks were dominant in compression areas [90, 235, 236]. Interestingly, this has not been investigated for trabecular bone tissue, yet. As a result, the goal of the current study was to develop a fatigue tensile test protocol to investigate microdamage formation at the tissue level.

This approach enables induction of microdamage at a defined tensile stress state, independently from potential structural influences, like deterioration of trabecular bone morphology in aged or osteoporotic bone. In that way the morphology, location and growth of microdamage in individual trabeculae in solely uniaxial tension could be investigated. According to previous tests on cortical and trabecular bone it was hypothesized that (1) diffuse damage is dominantly formed and (2) only in

a few, large sites in the central region of trabeculae. As this is the first study of microdamage formation in individual trabeculae, also adaptations of microdamage classifications had to be performed, based on previous studies of cortical [89, 229] and trabecular bone [232, 233]. The presented classification might serve as a basis for comparison of microdamage at the tissue/material (individual trabeculae or osteons) and meso (trabecular or cortical bone) scale.

3.4.3 Materials and methods

The second phalanx of a 16-month-old bull was used to obtain individual trabeculae. Sample preparation and testing was done in HBSS at $\text{pH} = 7.4$. Between preparations steps, samples were stored at $-18\text{ }^{\circ}\text{C}$, wrapped in tissue soaked with HBSS ($\text{pH} = 7.4$).

Sample preparation

Sample preparation was done as described in section 3.1.3 “Sample preparation”. Measurement of trabecular geometry and volume was performed with μCT (see section “Micro computed tomography (μCT) and image processing”) and with a light microscope (Zeiss Axio Imager, Carl Zeiss AG, Germany). Individual trabeculae were divided into *large* or *small* samples, based if they were smaller or larger than the mean trabecular volume of $1.5 \times 10^7\ \mu\text{m}^3$. This approach was used to account for size differences when applying the pre-load (see following section).

Fatigue testing and mechanical data analysis

Mechanical testing was performed displacement controlled with a sine wave of 0.05 mm amplitude at a frequency of 1 Hz (see inset in figure 3.14) on top of a pre-stress of about 40 MPa until damage formation, but with avoiding failure of samples. In pre-trials it was determined that selection of this pre-stress allows a more consistent start value than selection of strain, because of small deviations in the relation of trabecular length to total sample length. It was aimed to get a strain amplitude of about 0.5 %, as this value was previously reported in tensile tests of cortical bone to cause sample failure after $\tilde{1}0^4$ cycles [237]. Different approaches were examined for their feasibility as a stop criterion for fatigue loading. Finally,

the Number of Cycles (NoC) was used, but differences in the sample size required a consideration of that issue. Thus, the pre-load was set depending on the size of the samples. A pre-load of 1.0 N was applied for *large* trabeculae and 0.8 N was applied for *small* ones. After setting the pre-load, the position was hold constant for 60 s to allow sample alignment and viscous relaxation. Then, the sine wave was applied for 1000 cycles. Since viscous effects were still present in the specimens consisting of epoxy and bone, the load decreased over time, making it necessary to increase the load by 0.1 N after every 1000 cycles. The largest NoC was chosen as 3000, since trabeculae fractured slightly above 3000 cycles, as determined in pre-trials. 1500 cycles were found to correspond approximately to the beginning of microdamage formation and thus, were used as the lowest NoC. In order to show the progress of microdamage formation, 2100 cycles were used as an intermediate step.

Stress-strain determination was done as described previously (see section 3.1.3 “Determination of apparent mechanical parameters”). At the beginning and end of each 1000 cycle subset 100 cycles were recorded with a video camera to perform an optical strain measurement (see section 3.1.3 “Displacement and strain determination”). The force measurement was done continuously and converted to engineering stress, based on an assumed elliptical cross-sectional area (for details see section 3.1.3 “Force and stress determination”). Elastic modulus, and stress and strain amplitude were determined for each cycle and monitored over NoC. A selected stress-strain diagram for 14 cycles can be seen in figure 3.14.

Fluorochrome labeling, preparation and microscopy of microdamage

Labeling of microdamage was done with fluorochromes. Trabeculae were stained before fatigue testing, to monitor pre-existing damage (in red), and after testing to label induced microdamage (in green), according to a previously established protocol for subsequent microdamage staining [228]. Trabeculae were stained in $5 \times 10^{-4} \text{ mol dm}^{-3}$ Alizarin Red S (0.1711 g in 1 L distilled water; Sigma-Aldrich, MO, USA) for 4 h in a vacuum desiccator. After that, samples were washed three times in distilled water for 3 min. Then, trabeculae were subjected to fatigue

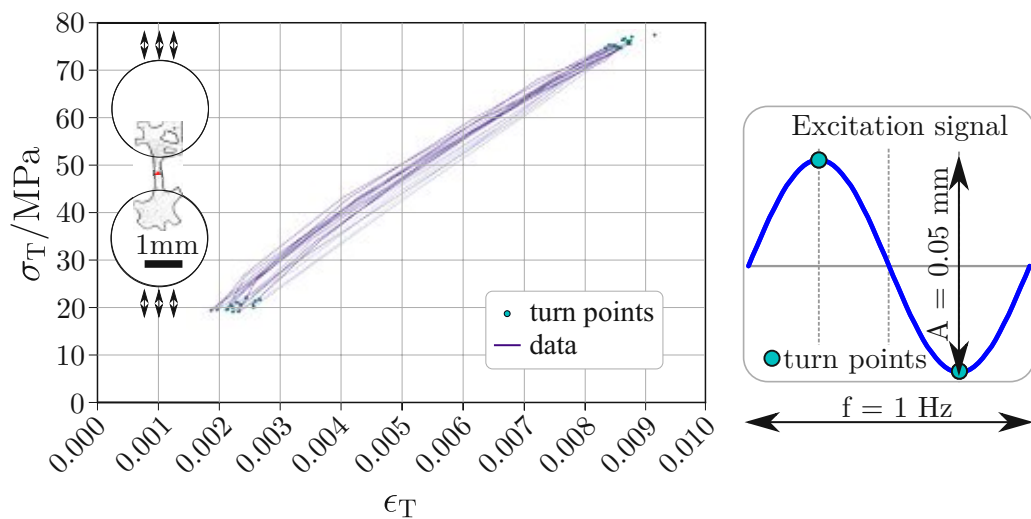


Figure 3.14: Left: Stress-strain diagram for fatigue loading, shown for 14 cycles. The violet color fades out with increasing cycle number, to better indicate different cycles. Right: Sine wave as excitation signal. • marks the turn-points and hence, illustrate the minimum and maximum stress-strain values of each cycle.

loading. Directly after testing, samples were put in $5 \times 10^{-4} \text{ mol dm}^{-3}$ Calcein (0.312 g in 1 L distilled water; Sigma-Aldrich, MO, USA) for 4 h in a vacuum desiccator. Next, samples were washed three times in distilled water for 3 min. Samples were dried in air with a paper tissue and fixed on microscopy glass slides with epoxy glue (UHU Endfest 300, UHU, Germany). Specimens were left at ambient conditions (in a black box to protect the fluorochromes from light) for 16 h to allow the epoxy to harden. Hardened samples were then put on an ultra-miller (Leica SP2600, Leica, Germany) and milled to a smooth surface for high quality images. Since ultra-milling induced some scratches, specimens were additionally polished to provide a flat, even surface.

Visual inspection of microdamage was done with Confocal Laser Scanning Microscopy (CLSM). A confocal Zeiss Axiolab microscope was used, equipped with a laser and operated with Zeiss ZEN Black software (Carl Zeiss AG, Germany). Samples were first visualized with a $10\times$ and a $20\times$ objective (EC Plan-Neouar 20x/0.50 M27), to detect sample orientation and potential microdamage. A more detailed inspection was done with a $100\times$ objective to distinguish damage and

cracks from lacunae and other micro-structures of bone. After that, images were taken with the 20× objective (resolution x-y: 0.6 μm, z: 3.0 μm) to perform the actual microcrack analysis.

Image data analysis

Image data analysis (taken with the 20× objective) was done with ImageJ (1.45 s, National Institutes of Health, USA). Analysis was done in 3D confocal images and in selected 2D images, for comparison to literature (as most studies only report data for 2D-analysis). In 3D-analysis image sequences were split into z-stacks to analyze 2D-planes individually and to combine analysis results to 3D data. For 2D analysis the first slice, where microdamage was present, was selected, together with a randomly selected one. As the actual microdamage analysis was done in 2D slices, this procedure is described for both, 2D and 3D analysis, in the following section.

First, the bone area (BA) was determined as the Region of Interest (ROI) using the polygon tool in ImageJ (see figure 3.15-A). Here, the boundary of the curvature was determined as the onset point by drawing tangents (shown in blue) on the trabecular strut and the residual bone. This was done in the first and last image of the image sequence and added to the ROI-Manager. The ROI-Manager was used to interpolate the ROIs in-between those slices. Microdamage was determined only in the green channel (as no microdamage was seen in the red channel). Images were segmented using the triangle threshold method [238], as implemented in ImageJ. The amount of microdamage was subsequently determined by calculating the number of segmented pixels and converted to the damage area ($Dx.Ar$) for each slice, as pixel size was known from CLSM. Next, the damaged volume (V_{tot}) was calculated, as the height of the z-stacks was known for each z-stack from CLSM. Microdamage was further categorized either as linear microcracks or as diffuse damage. Linear microcracks are typically much smaller (~ 2 orders of magnitude) in one direction, compared to the other two directions. Diffuse damage is simply any damage, which has no preferred orientation [50]. If no linear cracks were observed in one sample, than all damage was accounted as diffuse damage

volume (V_{diff}). Otherwise, the damage volume of linear microcracks (V_{lin}) was determined by fitting an ellipse in each slice containing a linear microcrack (see figure 3.15-B). Microcrack length was measured as the major axis of the ellipse and the width as the minor axis, using the *straight line* tool in every visible slice in ImageJ. In contrast, diffuse damage volume was determined by subtraction of linear microcrack volume from total damaged volume (V_{tot} , see figure 3.15-C for marked diffuse damage). The damaged volumes were put in relation the trabecular volume (V_{trab} , which was calculated as the elliptical cross-sectional area times trabecular length) to determine the damage densities (damage density (Dx.Dn), linear microcrack density (Cr.Dn), and diffuse damage density (Df.Dx.Dn)).

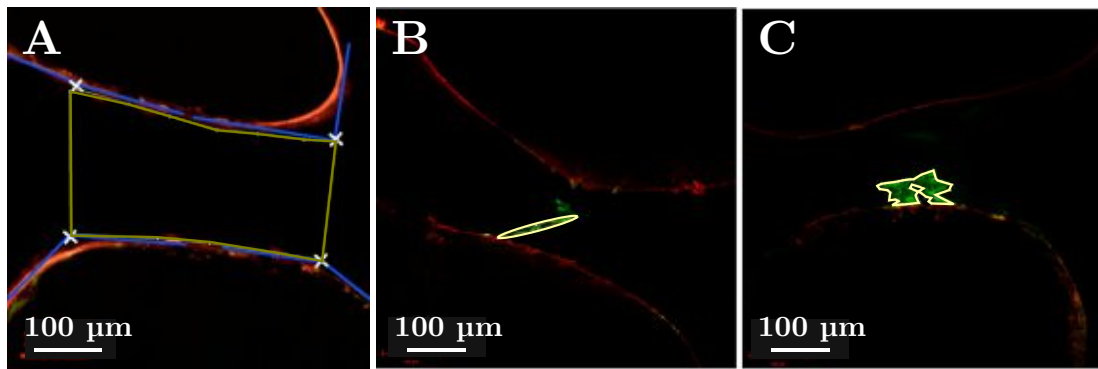


Figure 3.15: Determination of damage area. **A**: Determination of trabecular area with onset points (tangents in blue) for boundary lines (in yellow). **B**: Measurement of linear microcracks with an ellipse. **C**: Marked diffuse damage area with a polygon. Note that determination of diffuse damage was done by subtraction of linear damage from total damage.

Statistical analysis

Statistical analysis was done in SPSS (Version 26, IBM, US). Normality of data was analyzed using a Shapiro-Wilk-Test and found to be not normal distributed. Sequentially, a Kruskal-Wallis-Test for N variables (3D analysis) and a Mann-Whitney-U-Test for two variables (2D analysis) was used. The significance level (α) was set to 0.05. Additionally, the effect size (d) was calculated to predict the effect of found significant differences.

3.4.4 Results

In total 21 samples were tested successfully in fatigue loading. Seven samples were stopped after 1500 cycles, six after 2100 cycles and eight after 3000 cycles. The average mean strain of samples tested for 3000 cycles was (0.38 ± 0.27) % with a strain amplitude of (0.23 ± 0.11) %. The corresponding mean stress was (56.4 ± 29.4) MPa with a amplitude of (37.6 ± 12.4) MPa. Interestingly, larger stress amplitudes were not associated with larger amounts of microdamage, in the range studied here. Two samples could not be included in the microdamage evaluation (one of 1500 cycles and one of 3000 cycles) because of issues with the sample preparation after testing.

Two samples had to be excluded from data analysis (one from 1500 cycles and one from 3000 cycles) because of issues with sample preparation and staining. In addition, four non-tested trabeculae were analyzed for microdamage in the same way as trabeculae tested in fatigue loading. This procedure verified that microdamage was only induced during the fatigue loading process and not already present before or induced during sample preparation. However, to completely exclude pre-existing damage, all samples were also stained before fatigue loading in red. In course of the present study no pre-existing microdamage was observed in any trabeculae. Figure 3.16 illustrates representative samples for 1500, 2100 and 3000 cycles.

3D microdamage analysis

Almost no microdamage was visible in trabeculae tested for 1500 cycles. In more detail, no microdamage at all was visible in four samples, and two samples indicated microdamage initiation. In each of those two samples one linear microcrack and one diffuse damage area were observed. Compared to measurements of larger number of cycles (2100 and 3000), geometric measurements, like crack length and damage area, were small. Four samples tested for 2100 showed microdamage, but two samples illustrated no microdamage at all. Three out of those four samples indicated a larger number of linear microcracks, compared to the number of diffuse damage areas. The other sample did not show any linear microcrack. All samples

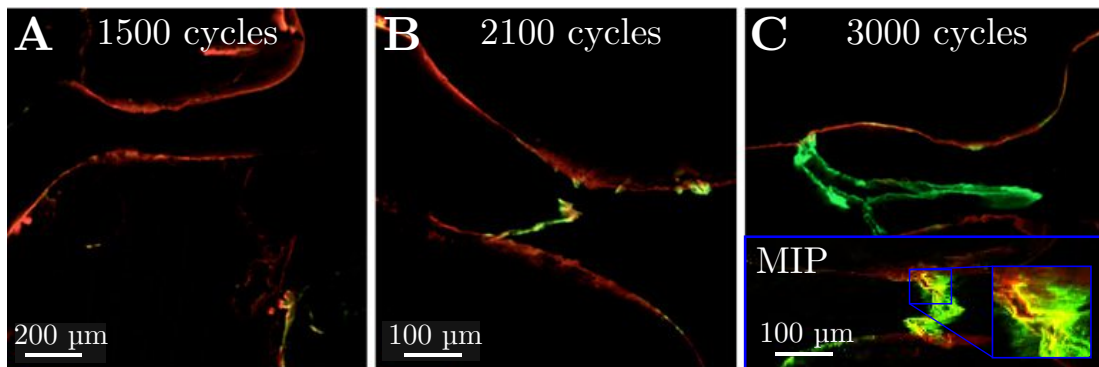


Figure 3.16: Microdamage formation shown for different cycle numbers. Pre-existing damage is labeled in red, induced microdamage in green. **A:** At 1500 cycles almost no microdamage is visible. **B:** At 2100 cycles microdamage is evolved locally. **C:** At 3000 cycles microdamage is enlarging so much that trabeculae are usually close to the point of fracture. Bottom: Maximum intensity projection (MIP) of a different sample with magnified area of crack opening at the trabecular surface.

that were tested for 3000 cycles demonstrated microdamage formation, whereby two samples indicated linear microcracks and five diffuse damage only. On average, linear microcracks were measured 100 μm in length and 9 μm in width in the present study. In contrast, diffuse damage was always wider than 30 μm .

Figure 3.17-A demonstrates the development of microdamage with increasing number of test cycles for 3D analysis. However, the linear microcrack density increases from 1500 to 2100 cycles, but decreases from 2100 to 3000 cycles (not significant, $p = 0.507$). In contrast, diffuse damage density increases continuously from 1500 to 2100 to 3000 cycles ($p = 0.076$). Diffuse damage density is larger than linear microcrack density in all cycles, but this difference is only significant at 3000 cycles ($p = 0.001$). Interestingly, all microdamage sites were connected with small straight cracks to the trabecular surface. Especially at 3000 cycles crack opening was visible at the trabecular surface, while the majority of diffuse damage was located in the central region of the trabeculae (see inset in Figure 3.16–C).

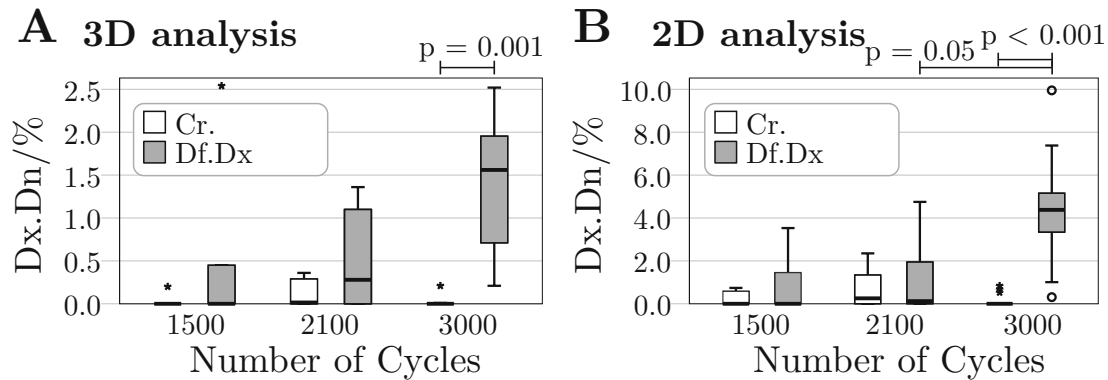


Figure 3.17: Damage density (Dx.Dn), dependent on the number of fatigue cycles. **A:** 3D analysis. Diffuse damage (Df.Dx) density is increasing with number of cycles. Linear microcracks (Cr.) increase from 1500 to 2100 cycles, but decrease again to 3000 cycles. **B:** 2D analysis. Diffuse damage and linear microcracks show the same behavior as in 3D analysis. However, relative damage densities are much larger (factor 3-4) than in 3D analysis. Significant differences ($p < 0.05$) are marked with bars and actual p-values are provided on top. Illustration of used boxplot styles (symbols and outliers) is given in figure 2.9.

2D microdamage analysis

Although 3D analysis is preferable, since information about the whole trabeculae is included, 2D analysis was performed additionally as it is more common in literature. In principle, the same effects as seen in 3D microdamage analysis were observed in 2D analysis. Figure 3.17-B demonstrates that there is a significant increase in diffuse damage density with increasing number of cycles ($p \leq 0.001$). As seen in 3D analysis, linear crack damage density increases from 1500 to 2100 cycles but decreases again at 3000 cycles ($p = 0.092$). Compared to 3D analysis, damage densities appear larger in 2D analysis, but differences were only significant for diffuse damage at 3000 cycles ($p = 0.003$).

3.4.5 Discussion

A fatigue tensile test approach for induction of microdamage in individual trabeculae, close to a physiologic environment, was successfully developed. A maximum strain of $(0.61 \pm 0.37) \%$ was determined on average, with a corresponding maximum stress of $(93.9 \pm 40.4) \text{ MPa}$ for 3000 cycles. Previously, tensile fatigue tests on corti-

cal bone reported 0.5 % for 10 000 cycles [237], 68 MPa for 1000 cycles and 51 MPa for 10 000 cycles [239] until failure. In literature, creep was determined as an important failure mechanism in cortical [240] and trabecular bone [51,241–243], especially if stress is high and number of cycles low [239,244]. However, in the present study recorded strain indicated even a slow decrease ($(1.7 \times 10^{-6} \pm 8.2 \times 10^{-6}) \text{ s}^{-1}$) and the contribution of creep to microdamage accumulation may be negligible [242,245].

As expected from a theoretical point of view [50] fatigue loading caused a moderate induction of microdamage for low number of cycles (1500 to 2100), but resulted in a rapid increase of microdamage density close before fracture (3000 cycles). Figure 3.17 illustrates the damage density evaluated in 2D and 3D image data. It becomes obvious that diffuse damage is the major type of microdamage. In contrast, linear microcracks show the largest density at 2100 cycles, both in 2D and 3D analysis. This might be related to the rapid increase of diffuse damage at 3000 cycles, which could mask linear cracks, if diffuse damage occurs nearby. A significant increase of total damage in 2D-analysis ($p \leq 0.001$) but not for 3D ($p = 0.09$) was seen from 2100 to 3000 cycles. The increase in microdamage from 1500 to 2100 cycles was not significant in 2D- and 3D-analysis and might be caused by the plateau-phase of microdamage development, as described previously [50]. However, a direct comparison of obtained values for microdamage densities in individual trabeculae is limited, since this is the first study that performed such measurements. Nevertheless, values can be compared to studies where trabecular networks or cortical bones were tested.

In literature, most studies performed compression tests on cancellous bone cores [232, 234] or cortical bone [227–230] for microdamage induction. In compression loads linear microcracks were found to be the dominant type of microdamage, whereas diffuse damage was dominant in tensile loaded cortical bone areas [90]. Similarly, mainly diffuse damage was observed in the present tensile fatigue loading test. Diffuse damage density was significantly larger at 3000 cycles ($p = 0.001$ in 2D and 3D) than linear microcrack density. In the current study microdamage was mostly concentrated in one to three large regions in the trabecular center of samples loaded for 3000 cycles, as previously reported in cancellous bone [234]. Surprisingly, all

damage sites were connected to the trabecular surface with small straight cracks (see Figure 3.16-C). The diffuse damage area increased significantly from 2100 to 3000 cycles, without initiation of new damage sites (occurred only in one sample). Thus, it was speculated that initiation of damage started at the trabecular surface mainly with straight cracks and grew towards the central region, where mainly diffuse damage was accumulated. However, this has to be verified with sequential staining techniques as reported for cortical bone [228].

Given the small size of individual trabeculae, the amount of induced microdamage was rather small, compared to whole trabecular networks or even compact bone. Sequentially, conventional evaluation of microdamage proved to be hardly possible for individual trabeculae. For instance, linear microcrack density (Cr.Dn in $\#/mm^2$) is frequently reported in literature [85, 227, 229, 230, 232]. However, microcrack number (Cr.N in $\#$) was usually one or two in the current study per trabeculae (average area of 0.08 mm^2), resulting in non comparable values of Cr.Dn of (10 to 30) $\#/mm^2$, compared to (0.1 to 0.5) $\#/mm^2$ [229]. In the present study it was intended to induce at least one crack per trabeculae, whereas cracks are more heterogeneously distributed over several trabeculae in bone cores. Further, the exact definition how to measure a *linear microcrack* was so far not well established in literature. Linear microcracks were simply measured from tip to tip [85, 227, 229], assuming to have sharp borders and a straight orientation. In reality, linear cracks can be shaped straight, curved, or mixed-shaped [93]. Thus, the tip to tip method is only feasible for straight linear cracks. Further, the width of linear microcracks is usually neglected. Hence, Taylor et al. made an effort to establish a 3D measuring technique for linear cracks by fitting an ellipse on cracks [246]. Based on the findings from Taylor et al. [246] and Fazzalari et al. [93] an attempt was made in the present study to unify measurements. Linear microcracks were measured with ellipses (in all confocal planes) from tip to tip, if they appeared perfectly straight, but with a number of short ellipses following the run of the crack if they appeared curved.

Using this approach, linear microcracks were on average $93\text{ }\mu\text{m}$ long and $9\text{ }\mu\text{m}$ wide. In comparison linear microcrack length was reported as $80\text{ }\mu\text{m}$ [83], $50\text{ }\mu\text{m}$ [84], and $71\text{ }\mu\text{m}$ for young and $90\text{ }\mu\text{m}$ for old bone [85]. Surprisingly, reported values are in

the range of (50 to 100) μm , despite of being not well defined and determined with potentially different measurement techniques. Possibly, most linear microcracks were indeed straight, resulting in the same outcome if different measurement techniques were applied. Nevertheless, the proposed elliptical fitting method should be used to ensure comparable results, especially if cracks are curved.

Determination of diffuse damage density (Df.Dx.Dn) has been first described by Vashishth et al. as the percentage of damaged area in relation to bone area [233]. Further studies used similar approaches to report diffuse damage density either in percentage or as absolute values (diffuse damage area in relation to bone area: $\text{Df.Dx.Dn} = \text{Df.Dx.Ar}/\text{BA}$ in $\text{mm}^2 \text{mm}^{-2}$ or %) [87, 247, 248]. However, a detailed description of the actual measurement of the damage area or the bone area is lacking. Sequentially, an attempt to measure diffuse damage area with polygons was first suggested in the present study. However, as only linear cracks and diffuse damage were present, it was found to be more convenient to first measure linear microcracks with ellipses and sequentially subtract those areas from total damaged area. This approach can be also applied if cross-hatch damage is present, as this can be measured using the polygon approach and finally subtracted from total damage. Taken together, a more detailed reporting of actual measuring approaches would ease comparison between different histological microdamage evaluation studies. The methods presented in the current study can serve as a reference, as these are also valid for individual trabeculae and thus, small areas, which are more sensitive to imprecise area determination.

Interestingly, also the diffuse damage density was smaller ($\text{Df.Dx.Dn} = 4.43\%$ for 2D at 3000 cycles), compared to previous studies. Vashishth et al. reported 15.0 % diffuse damaged area for males and 10.0 % for females in vertebral bone [233]. Parsamian et al. determined diffuse damage area in the range of (4.0 to 9.0) % in human vertebral cancellous bone [247]. Diffuse damaged area in rat ulnae was determined as 4.9 % for 3000 cycles and 7.1 % for 4500 cycles [87]. Sequentially, determined values in the present study occur at the lower range of previously reported values for diffuse damage density. Possible discrepancies are the different scale (individual trabeculae vs. trabecular networks), fatigue test induced microdamage

vs. *in vivo* formation and different histological methods. The major influence might be that only the trabecular strut was evaluated in the current study (as stress is assumed to be homogeneous in that region), neglecting the curved regions, which are included in the analysis of trabecular networks. Especially at the curved transition from the trabecular strut towards neighboring bone stress might be locally elevated, causing microdamage formation.

A direct comparison of 2D- and 3D-analysis demonstrated that the overall trend of damage density, dependent on the number of cycles, is very similar. However, more linear cracks were counted in 2D-analysis than in 3D. Cracks might appear as linear in 2D images, but could develop into diffuse damage if the whole damage area is observed in 3D. This effect was indeed recognized in some cracks in course of the present study (see figure 3.18). This highlights the need to perform microdamage classification in 3D confocal images, as already suggested previously [93,249]. Especially, Fazzalari et al. pointed out the advantages of a volumetric analysis [93], but the majority of microdamage evaluation was and is done in 2D sections. Confocal light microscopy is a powerful tool to determine 3D microdamage, but also inherits some drawbacks. Specific fluorochromes have to be used to be excited with a laser. Further, the sample surface has to be extremely flat, as rough surfaces cause irritations (scattering and reflection) of the excitation and emission light. Last but not least, confocal images are usually analyzed as 2D-stacks, since the vertical resolution is almost one order of magnitude lower, than the horizontal one (several μm compared to $\sim 0.1\mu\text{m}$). 3D-analysis of microdamage has also been performed with barium-sulphate labeled bone in μCT measurements, at a resolution of $10\mu\text{m}$ [250]. This technique enables *in situ* volumetric analysis, but at the cost of a reduced resolution. Thus, discrimination between actual microdamage, diffuse or linear and other porous structures might be challenging.

Limitations, improvements, and outlook

Several limitations were encountered during this study. First, only 21 trabeculae could be tested in tensile fatigue loading. Especially a rather long test time of

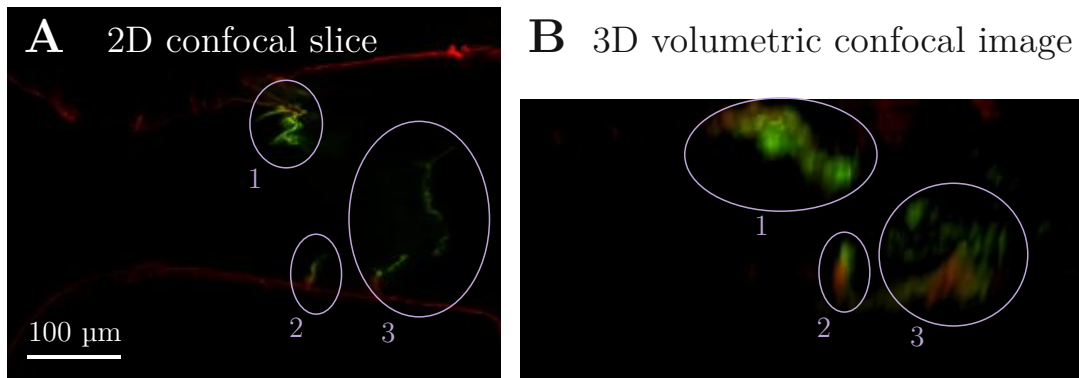


Figure 3.18: Confocal images of microdamage in 2D and 3D images. **A:** 2D confocal slice of a sample tested for 2100 cycles. Representative areas are marked with 1, 2 and 3. **B:** 3D volumetric confocal image obtained from the same sample as in A. Corresponding areas are also marked with 1, 2 and 3. Area 1 indicates diffuse damage, area 2 a linear microcrack, and area 3 appeared as multiple linear cracks in 2D, but was determined as one linear crack and mainly diffuse damage in 3D.

4 h per sample was the limiting factor. In a subsequent study, issues in sample relaxation were identified to cause a drop in force that caused pausing after 1000 cycles and the need to manually increase the pre-load, to avoid a further decrease of force. In this follow-up study it was determined that the position obtained after applying the pre-load should be hold constant for 1 h to ensure complete relaxation. Sequentially, sample testing could be performed continuously for 50 min, without the need to increase the force every 1000 cycles. In that way, also the number of tested samples could be increased. Second, in the current study no clear correlation between a decrease of the tissue elastic modulus, and increasing microdamage could be observed, as proposed previously [50]. Nevertheless, half of the samples showed a decrease of the elastic modulus in the current study. Especially difficulties in strain measurement, because of the low strain amplitudes, could be responsible for these discrepancies. Third, the stop criterion could be defined more objectively, if a specific decrease of the elastic modulus could be used instead. An attempt to perform a more sample specific loading was done in a subsequent study. Here, the applied load amplitude was based on the cross-sectional area of each trabeculae. A linear regression was used to convert the displacement driven loading to pseudo-stress based loading. Viscous effects of the epoxy-bone specimens (see figure 3.19)

caused a drop of force over time. Thus, after every 1000 cycles new displacement limits were extrapolated in that study, to ensure that the load stayed within the desired boundary (here (0.4 to 1.2) N). To avoid these necessary adaptations of force in total, a new approach was developed (see figure 3.20). Here, the sample was hold constant at the maximum displacement value for 1 h to get rid of relaxation.

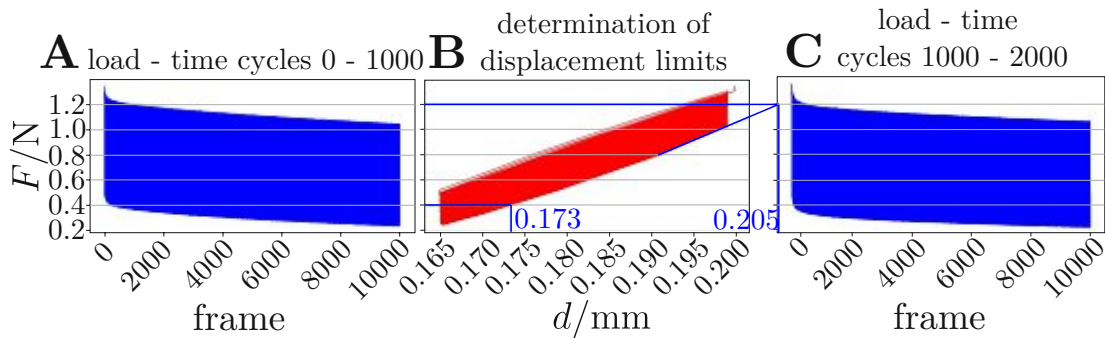


Figure 3.19: Adjustment of displacement in fatigue tests. **A**: The load signal decreases over time because of relaxation. **B**: New displacement limits for the desired (0.4 to 1.2) N load amplitude are extrapolated in the corresponding load-displacement diagram. **C**: In the next cycles (1000 to 2000) the newly determined displacement limits are chosen, but the load decreases again.

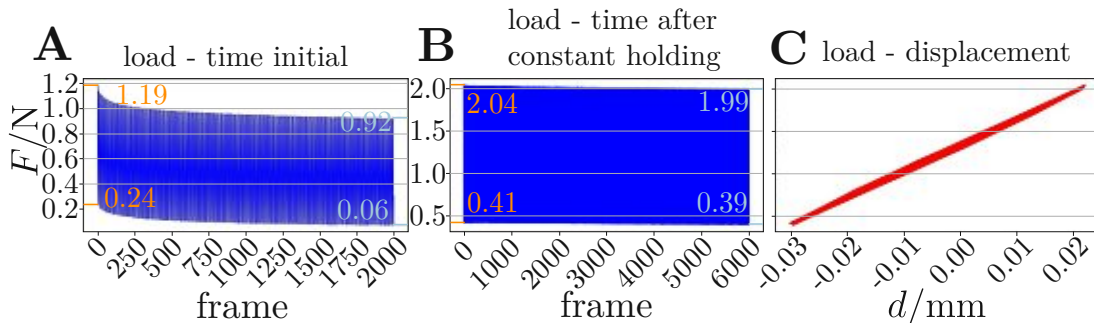


Figure 3.20: Constant holding ahead of testing in fatigue tests. **A**: The load signal decreases over time because of relaxation. **B**: After constant holding of the sample at the upper displacement limit for 1 h almost no relaxation was present anymore. **C**: The corresponding load-displacement diagram illustrates a very stable behavior over 1000 cycles.

As a further stop criterion also a visible formation of microdamage, seen as whitening of the bone, could be used. Here, young and healthy bovine trabeculae were tested, which might react differently than human osteoporotic samples. However,

3. METHODS DEVELOPMENT AND DATA ANALYSIS APPROACHES

the overall goal was the development of the fatigue test approach and obtained microdamage parameters are in accordance with previously reported values.

Taken together, a novel test procedure was successfully developed to determine microdamage formation in individual trabeculae in tension. Mainly diffuse damage was induced with increasing number of cycles. Further, only a few microdamage areas were generated in individual trabeculae that grew with increasing cycle number, instead of inducing new sites. Although 2D- and 3D-analysis yielded similar results, 3D-analysis is preferable to reliably discriminate the different types of microdamage. The presented microdamage classification might serve as a reference method in upcoming studies not only at the tissue/material level, but also at the meso-scale. In future, potential changes of the fatigue behavior of aged, osteoporotic or BP treated trabecular bone at the tissue/material level, independent of structural effects are now accessible.

Dehydration causes transition from ductile to quasi-brittle failure mode

“The University of Nebraska says that elderly people that drink beer and wine at least four times a week have the highest bone density. They need it - they’re the ones falling down the most”

Jay Leno

4.1 Related publications and declaration of contributions

Partial results of the presented work (text, tables and figures) have been *published* in the “Journal of the Mechanical Behavior of Biomedical Materials” in 2018, entitled “Dehydration of individual bovine trabeculae causes transition from ductile to quasi-brittle failure mode” and co-authored by Dorothee Marx, Vedran Nedelkovski, Julia-Theresa Fischer, Dieter H. Pahr and Philipp J. Thurner.

Author contributions: The first author and author of the current thesis, *Martin*

Frank, wrote the manuscript, performed the development and refinement of the test set-up, all mechanical tests, data processing and data interpretation. *Dorothee Marx* developed the original test set-up, for tensile tests of cortical bone, close to a physiologic environment, which was further modified by Martin Frank for tensile tests of individual trabeculae. *Vedran Nedelkovski* took the electron microscopy images for fracture surface analysis and contributed in the data interpretation of fracture surfaces. *Julia-Theresa Fischer* contributed in optimization of the test set-up and the sample preparation. *Dieter H. Pahr* and *Philipp J. Thurner* designed the study, supervised the work of Martin Frank and supported the interpretation of the results.

4.2 Introduction

Bone is a highly hierarchical material, whose mechanical characterization is important at all levels, as already outlined in section 2.7. Age [31, 251, 252], disease [9, 61, 252] and treatment [29, 122, 253] cause changes of bone at different levels, compared to the healthy state. Hereby, it is known that bone is altered at the structural [254–257] as well as at the sub-tissue level [31, 61, 256]. However, there is not much known about possible changes at the tissue scale, the level of individual trabeculae. Here it is of great interest to determine the mechanical properties of healthy and altered trabeculae, to link the observed changes at the structural level to the sub-tissue scale.

So far, determination of mechanical properties of individual trabeculae has been mostly performed in a dry environment (air), because of easier sample testing. For example, three-point bending [18, 119, 171–176], tensile [18, 36, 162, 171, 177–179], buckling [66, 180] and four-point bending [181] tests have been performed on individual trabeculae (see section 2.7.3). But, in its natural state bone is encompassed by body fluid [258], which is mainly composed of water. Further, also trabecular bone tissue itself is composed of 27% water [62]. Sequentially, known mechanical properties of individual trabeculae were mainly obtained from a non-physiologic test environment, so far. This leads to the assumption, that reported material and apparent mechanical properties might deviate from true, physiologic values. Indeed,

Townsend et al. have already shown that tissue elastic modulus of individual trabeculae increases significantly in dehydrated samples [66]. Similarly, at the sub-tissue scale the elastic modulus of lamellae, measured with nanoindentation, has also been reported to increase significantly in dried specimens [16,17]. At the scale of trabecular bone cores dehydration caused a significant increase in apparent elastic modulus, accompanied by significant shrinkage [65].

Taken together, there is a clear need to determine mechanical properties of individual trabeculae in a wet, physiologic environment. Previous studies focused mainly on the elastic tissue properties, like the elastic modulus. This value is especially important for numerical simulations, such as FE analysis. In contrast, post-yield properties, such as stress and strain at failure and post-yield work are more relevant in clinics, as these values quantify the ability of the trabecula to resist fracture. So far, only a few studies determined the point of failure in individual trabeculae [18,36,171]. Hereby, tensile experiments are superior to other tests, such as three-point bending or compression, because of a defined, homogeneous stress state, ideal for material characterization (see section 2.7.5). In previous micro-tensile tests two major limitations were identified. First, because of the small scale, sample handling is difficult and results in damaging of samples during preparation and testing [12,184]. Second, it is known that there is a large biological variation of obtained material and apparent mechanical properties [259]. Thus, it is essential to measure a large amount of individual trabeculae to obtain a sufficient amount of reliable values of mechanical properties.

Aim of the current study was to determine the mechanical properties of individual trabeculae in tension, close to a physiologic environment and in air (for comparison). Hereby, a sufficient throughput of tested samples was necessary because of the large biological variation. It has been hypothesized that dehydration causes a different failure mechanism because of differences in microdamage accumulation.

4.3 Material and methods

4.3.1 Sample selection

The second phalanx of a 16-month-old bull was obtained from a local butcher within 1 h after death, wrapped in tissue soaked with HBSS and stored immediately at $-20\text{ }^{\circ}\text{C}$. Individual trabeculae were randomly assigned to the *wet* or *dry* group. In total, 40 samples were prepared for tensile testing (20 for each group).

4.3.2 Sample preparation and mechanical testing

Sample preparation of individual trabeculae was performed according to section 3.1.3 “Sample preparation”. Tensile testing and strain determination were done as reported in sections 3.1.3 “Tensile test” and 3.1.3 “Displacement and strain determination”.

Tensile tests were done displacement controlled (displacement rate of 0.01 mm s^{-1}), with a linear ramp until fracture. As mentioned in section 3.1.3 “Tensile test”, a pre-load of 0.08 N was applied to facilitate sample alignment. After verification with the video camera, the actual tensile test was started and stopped after sample fracture.

4.3.3 Determination of mechanical properties and TMD

Determination of sample geometry was done with μCT measurements, as described in section 3.1.3 “Micro computed tomography (μCT) and image processing”. Hereby, the mid cross-sectional area A_{mid} was used to calculate true stress σ_{T} , according to section 3.1.3 “Force and stress determination”. Subsequently, determination of apparent mechanical properties was performed as described in section 3.2.2. TMD was determined as mentioned in section 3.1.3 “Determination of Tissue Mineral Density (TMD)”.

4.3.4 Full field strain determination

Full field strain maps were determined with GOM Correlate (GOM GmbH, Germany). Vertical (y) strain was calculated using a facet size of 25 and an overlap

of 13. The region used for full field strain maps was confined to the top and bottom borders obtained from optical strain tracking with trackpy (see section 3.1.3 “Displacement and strain determination”). Obtained strain maps were illustrated by applying the GOM-6-color map. To exclude outliers in the display, a 3-sigma filter scale was used. In principle, data that lied within three standard deviations ($\sim 99.7\%$) was shown. Additionally, the average strain (ϵ_{avg}) and the standard deviation of the strain map (ϵ_{std}) were displayed, together with the corresponding histogram. It has to be noted that obtained values for ϵ_{avg} were mostly lower than the corresponding global strains (ϵ_{T}), determined with the point tracking algorithm, because of losing of facets in full field strain tracking at large strains ($\epsilon > 10\%$). The local point in the strain maps, where the trabecula is going to fail, was further labeled manually as ϵ_{fract} . In those cases, where facets, containing the region of failure, were lost, the closest point to this region was labeled instead.

4.3.5 Whitening

The whitening effect has been first linked to microdamage formation in trabecular bone by Thurner et al. [260] and was further analyzed in subsequent studies [167, 172, 174, 175]. In the present study, the bone area was partly masked by the applied speckle pattern. Hence, the speckled area had to be excluded from data analysis, to only analyze the visible bone area. Further, because of large strains at failure ($\epsilon_{\text{u}} \sim 10\%$), the visible bone area increased with increasing strain. Sequentially, the originally suggested algorithm for whitening detection [260] had to be replaced by a new procedure that accounts for these issues. A custom written python script was used to perform image processing and detection of whitening (see figure 4.1 as operation chart).

First, the mean position of the top and bottom particles, which were used for strain tracking (see section 3.1.3 “Displacement and strain determination”), was loaded. Then, the original images were cropped according to the top and bottom positions used for strain tracking for each frame, respectively (see figure 4.1-A). Then, a mask was applied on each image to consider bone only. As such, images were segmented using the *Otsu* method in python [261], for each image individually.

4. DEHYDRATION CAUSES TRANSITION FROM DUCTILE TO QUASI-BRITTLE FAILURE MODE

Next, the histogram was determined for each image, considering only the masked area (see figure 4.1-B). The histograms are illustrated for the first (left) and last (right) frame for the masked, trabecular area (green in A) and the dark speckle pattern. As mentioned above, only the masked area was considered for further analysis, as these regions were capable of increasing the gray value, in contrast to the dark speckle pattern (which gray value stayed almost unchanged). The python script determined a Gaussian fit for the masked histogram for each frame. With increasing strain, the histogram was shifted towards the right, because of increasing gray values, caused by the whitening effect. The Gaussian fit of the first and the last frame were combined in the central image to determine the whitening threshold, the intersection between both distributions. The basic concept was that in the first frame no whitened areas were present, whereas the last frame represented the maximum amount of whitened area. These two populations were considered as being different and thus, their intersection was used as the threshold. A small amount of pixels in the first frame had a gray value larger than the whitening threshold. Sequentially, the number of whitened pixels in the first frame was subtracted from all subsequent images.

The corresponding diagrams of whitened area (A_W), depending on frame number and true strain (ϵ_T) are shown in figure 4.1-C. Here, also the first frame is shown with no marked whitened area on the left and with marked whitened area in the last frame on the right. The onset of whitening strain ($\epsilon_{W_{on}}$) was determined as the point after that the whitened area A_W increased monotonously. In more detail, $\epsilon_{W_{on}}$ is the last point where the derivative of A_W is negative. The maximum increase in whitened area ($A_{W_{max}}$) is the difference between the maximum of A_W and A_W at the onset point.

4.3.6 Fracture surface analysis

Fracture surface analysis was done on four wet and four dry fractured trabeculae using scanning electron microscopy (SEM) and on three wet and three dry samples using μ CT. Imaging of fractured samples with μ CT was done in the same way as described in section 3.1.3 “Micro computed tomography (μ CT) and image

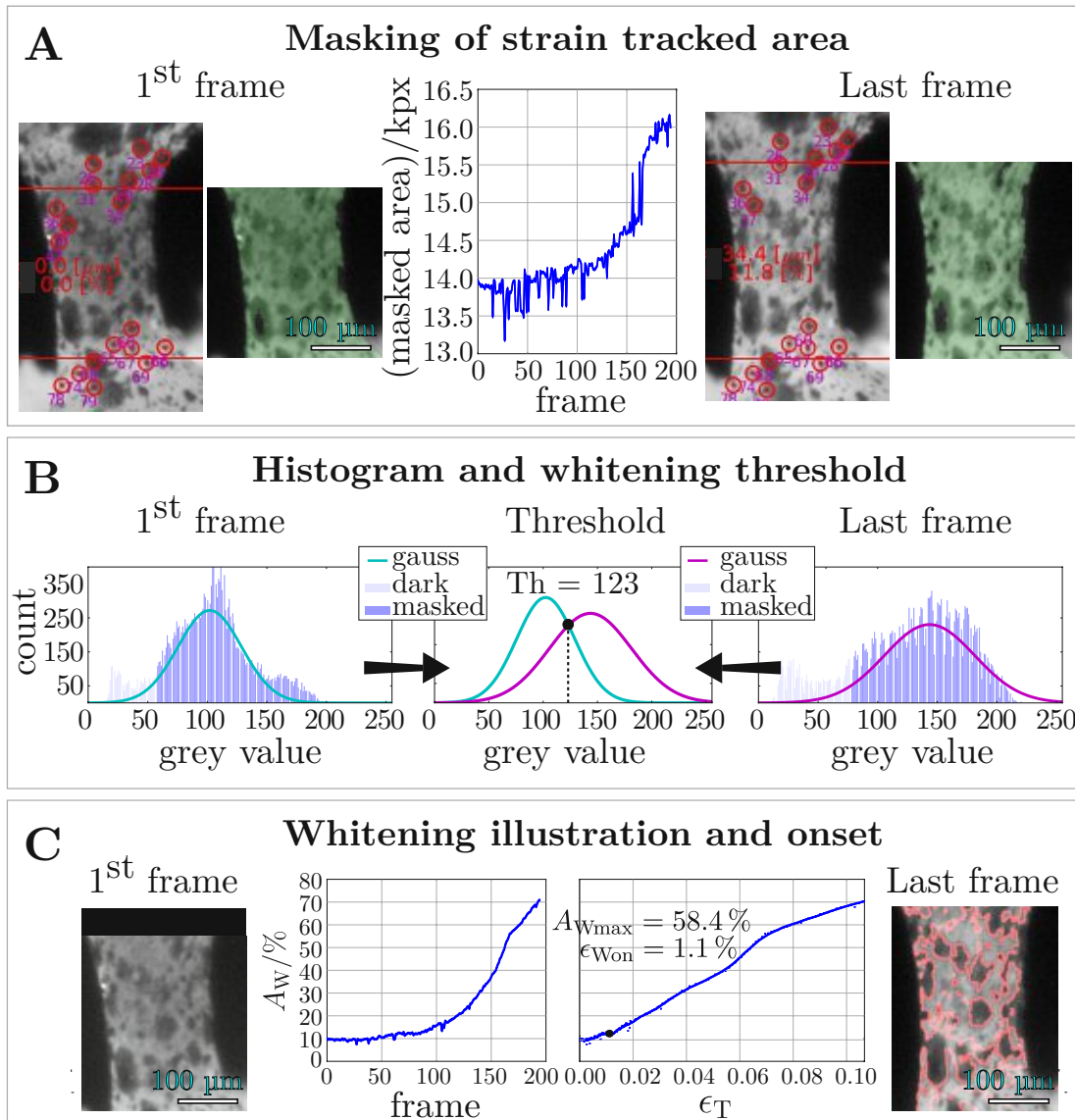


Figure 4.1: Operation chart for whitening detection in speckle-patterned trabeculae. **A:** The known top and bottom mean particle position from strain tracking (see red lines) was used to crop the original images to this area (illustrated for the 1st and last frame). The trabecular area, excluding dark speckle pattern areas, is **masked** and considered for histogram based whitening detection. Because of increasing displacement, the masked area increased (see diagram in the center). **B:** Histograms are shown for the 1st (left) and last (right) frame. Here, the considered, masked trabecular area (without the speckle pattern) is noted as **masked**, the speckle pattern as **dark**. The Gaussian fitting curve is also shown for the considered, masked trabecular area in the histogram of the 1st and last image. A clear shift of the Gaussian distribution towards larger gray values is seen in the last frame. The central image illustrates the Gaussian fits of the 1st and last image. The intersection between those two curves is used as the threshold. **C:** The left diagram demonstrates the increase of the whitened area (A_W) with increasing frame number. The right diagram shows A_W in dependence of true strain (ϵ_T) and the marked onset of whitening onset strain (ϵ_{Won}) and the maximum whitened area (A_{Wmax}). The right image illustrates the last frame, whereby gray values larger than $Th = 123$ are **marked** (whitened areas).

4. DEHYDRATION CAUSES TRANSITION FROM DUCTILE TO QUASI-BRITTLE FAILURE MODE

processing”. Additionally, SEM was used to perform a more detailed analysis of sub-tissue scale features of fracture surfaces. For SEM analysis samples were glued onto a SEM pin mount using silver-paint and sputtered with a gold-palladium (60:40) layer of about 5 nm thickness at 30 mA for 30 s (Sputter Coater Quorum Q150T S, Quorum Technologies Ltd, Great Britain). SEM was performed with a Quanta 200 3D DualBeam-FIB, operated in secondary electron mode (5 kV, \times 1500 magnification, 0.18 nA).

4.3.7 Statistical analysis

Statistical analysis was done in SPSS (Version 23, IBM, US). Data was first inspected using histograms and Q-Q plots. Further, apparent mechanical properties of wet and dry samples indicated significant differences in equality of variances, using a Levene’s test. Several of those variables (yield strain, exponential hardening coefficient, elastic and post-yield work) were also not normally distributed, as seen in a Kolmogorov-Smirnov test. In contrast, the variables determining the geometry and local strain behavior proved to be normally distributed. As the Mann-Whitney-U non-parametric test is stricter in rejection of the null-hypothesis, compared to the independent t-test for comparison of means, this test was used for all further analysis. The significance level α was set to 0.05 and p-values < 0.05 were considered as significant. Because of the non normally distributed data, the Spearman’s rank correlation coefficient was used for data correlation. Since a single outlier was present in the correlation between yield strain and the whitening onset in the wet group, this data point had to be excluded, whereby outlier identification was performed using the 1.5 times Inter Quartile Range (IQR) criterion.

4.4 Results

31 individual trabeculae were successfully tested and analyzed. Five dry trabeculae failed during the preparation and mounting procedure, likely because of the brittle behavior of dehydrated bone. Issues in the alignment and mounting process during tensile testing caused a further loss of three wet and one dry trabeculae. In total, 17 wet and 14 dry samples, out of initial 20 specimens per group, were tested

and analyzed. Geometry measurements, determined in μ CT images, displayed an average trabecular strut length of (550 ± 170) μm for dry samples and (470 ± 150) μm for wet samples. The average trabecular diameter was (120 ± 30) μm for both groups. No significant difference in any geometric parameter was found.

4.4.1 Stress strain behavior

Dehydration of individual trabeculae resulted in a significant different stress-strain behavior (see figure 4.2). Dehydrated trabeculae indicated a significantly larger apparent elastic modulus (\hat{E}), yield stress ($\hat{\sigma}_y$ and $\hat{\sigma}_{y0.2}$), ultimate stress ($\hat{\sigma}_u$) and hardening exponent (p). In contrast, ultimate strain ($\hat{\epsilon}_u$) and post-yield work (\hat{W}_{py}) were significantly lower in dry samples (see table 4.1). Boxplots of all mentioned apparent mechanical properties are shown in figure 4.3.

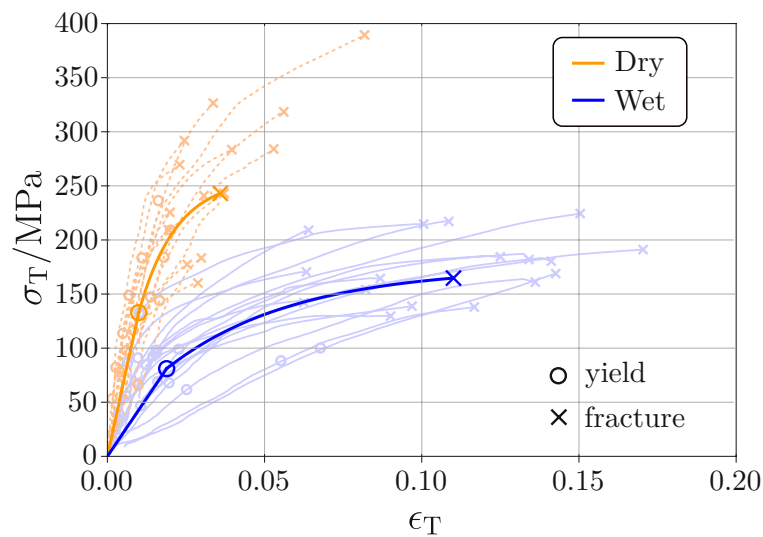


Figure 4.2: True stress-strain (σ_T - ϵ_T) curves for **wet** and **dry** trabeculae; experimental curves (light) and calculated average curves (**bold**), according to equations 3.8 and 3.9. Yield points are marked as \circ , point of fracture as \times .

4.4.2 Strain localization

Full field strain maps were determined to highlight local strain elevation in the trabeculae (see figure 4.4 for a representative dry and wet sample). Maps are shown for three distinct strain points: (1) The center of the elastic region, (2) the yield

4. DEHYDRATION CAUSES TRANSITION FROM DUCTILE TO QUASI-BRITTLE FAILURE MODE

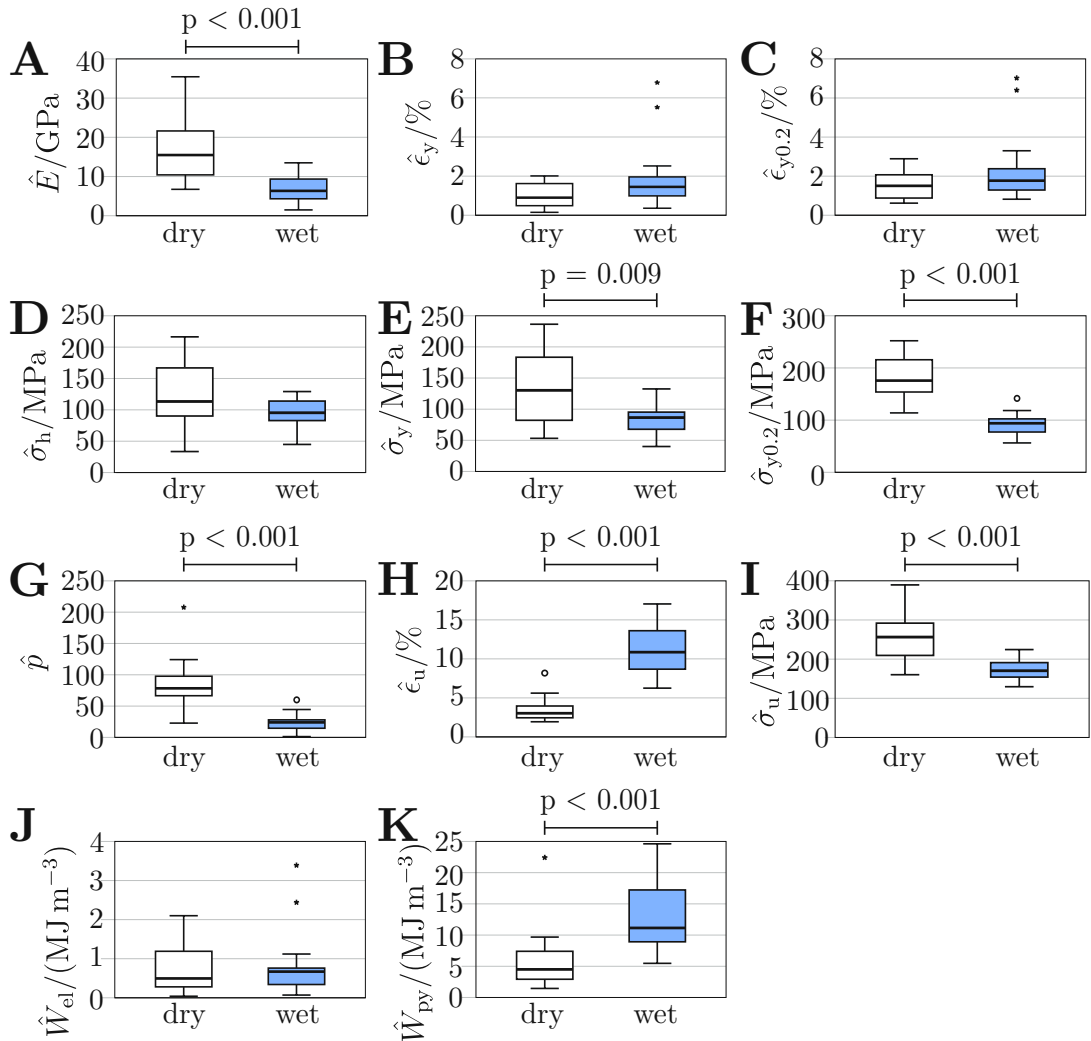


Figure 4.3: Apparent mechanical properties of wet and dry trabeculae, as defined in equations 3.8 and 3.9. Variables are denoted with $\hat{\cdot}$ to indicate their determination based on curve fitting, in contrast to values determined with the rheological model. **A:** Elastic modulus \hat{E} . **B:** Yield strain $\hat{\epsilon}_y$. **C:** 0.2% Yield strain $\hat{\epsilon}_{y0.2}$. **D:** Ultimate strain $\hat{\epsilon}_u$. **E:** Hardening stress $\hat{\sigma}_h$. **F:** Yield stress $\hat{\sigma}_y$. **G:** 0.2% Yield stress $\hat{\sigma}_{y0.2}$. **H:** Ultimate stress $\hat{\sigma}_u$. **I:** Hardening exponent \hat{p} . **J:** Elastic work \hat{E}_{el} . **K:** Post-yield work \hat{E}_{py} . Significant ($p < 0.05$) differences are marked with bars and displayed with actual p-values. Illustration of used boxplot styles (symbols and outliers) is given in figure 2.9.

Parameter	dry		wet		p-value
\hat{E}/GPa	17.1 ±	8.4	6.5 ±	3.7	< 0.001
$\hat{\epsilon}_y/\%$	1.0 ±	0.6	1.9 ±	1.7	0.109
$\hat{\epsilon}_{y0.2}/\%$	1.5 ±	0.7	2.3 ±	1.8	0.230
$\hat{\epsilon}_u/\%$	3.6 ±	1.7	11.0 ±	3.3	< 0.001
$\hat{\sigma}_h/\text{MPa}$	125 ±	29	94 ±	25	0.161
$\hat{\sigma}_y/\text{MPa}$	133 ±	56	81 ±	23	0.009
$\hat{\sigma}_{y0.2}/\text{MPa}$	181 ±	40	93 ±	21	< 0.001
$\hat{\sigma}_u/\text{MPa}$	257 ±	64	175 ±	30	< 0.001
\hat{p}	83 ±	45	25 ±	14	< 0.001
$\hat{W}_{el}/(\text{MJ m}^{-3})$	0.8 ±	0.7	0.8 ±	0.8	0.830
$\hat{W}_{py}/(\text{MJ m}^{-3})$	6.0 ±	5.3	13.3 ±	5.7	< 0.001

Table 4.1: Apparent mechanical properties of **dry** and **wet** trabeculae. Mean values are indicated \pm standard deviation. Explanation of variable names and corresponding box-plots are illustrated in figure 4.3. **Bold** p-values indicate a significant ($p < 0.05$) difference.

point and (3) the point of failure. The corresponding stress-strain diagrams are also shown to link the already mentioned different apparent stress-strain behavior to local strains. In the elastic region, strain maps indicated a homogeneous, narrow distribution. Mean ($\epsilon_{\text{avg}} \pm$ standard deviation (ϵ_{std}) for all samples was (1.6 ± 0.8) % for wet and (2.1 ± 1.2) % for dry trabeculae. However, at the yield point, dry trabeculae exhibited a more inhomogeneous strain distribution with locally elevated strains ((2.8 ± 1.5) %), compared to a homogeneous distribution in wet samples ((2.1 ± 1.1) %), without being significantly different. At the point of fracture, strain distribution was significantly ($p < 0.05$) different between wet and dry trabeculae. The Coefficient of Variation ($CV = \frac{\epsilon_{\text{std}}}{\epsilon_{\text{avg}}}$) was significantly lower in wet (1.0 ± 0.4), compared to dry samples (1.6 ± 0.7). The larger Coefficient of Variation (CV) in dehydrated samples can be interpreted as being caused by a more heterogeneous strain distribution with a skew towards higher strains, related to a small amount of locally elevated strains. It has to be noted that the CV is a relative value. Additionally, the absolute values of the local strain, where the trabecula is going to fail, was labeled for each sample specifically as ϵ_{fract} in figure 4.4. This local failure strain was significantly ($p < 0.01$) larger at the point

4. DEHYDRATION CAUSES TRANSITION FROM DUCTILE TO QUASI-BRITTLE FAILURE MODE

of failure ($\hat{\epsilon}_u$) in wet trabeculae ($(27.4 \pm 12.8) \%$), compared to dry ones ($(16.4 \pm 9.9) \%$). Sequentially, wet trabeculae showed a larger, more homogeneous region of elevated strains and larger absolute numbers of strain, compared to dehydrated samples.

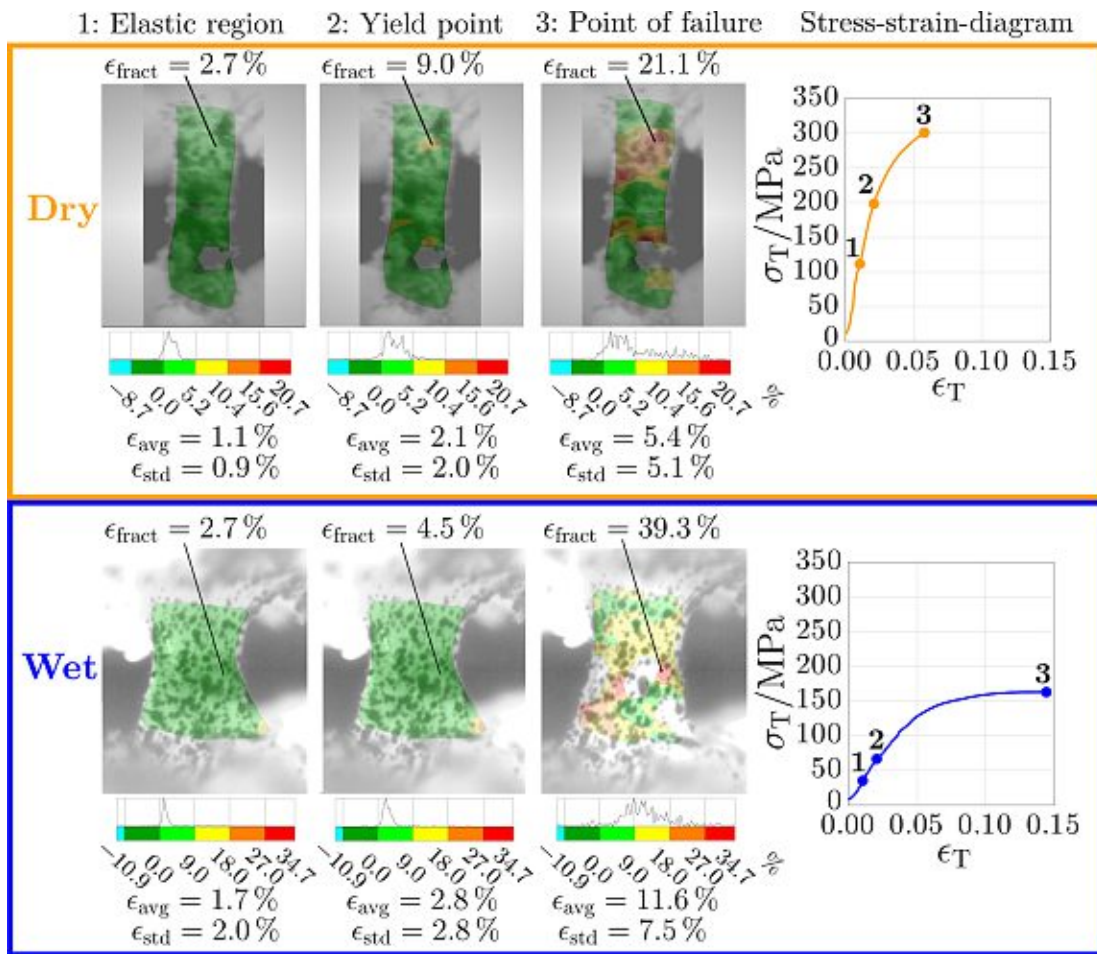


Figure 4.4: Full field strain maps of a selected **dry** (top) and **wet** (bottom) trabecula. Full field strain maps are shown for the elastic region (1), the yield point (2) and the point of failure (3), with corresponding true stress-strain diagrams on the right. In full-field strain maps, the strain at the point where the sample is going to fail is marked as ϵ_{fract} . Additionally, the histogram of the full field strain maps is shown below each image, with denoted values for average strain (ϵ_{avg}) and standard deviation of strain (ϵ_{std}).

4.4.3 Larger toughness of hydrated bone is caused by increased damage accumulation

Observed local differences in strain maps were further investigated using the whitening effect. Figure 4.5 illustrates exemplary differences in the accumulation of the damaged (whitened) area in wet and dry trabeculae. As supposed in full field strain maps, dry trabeculae indicated a significant ($p < 0.001$) smaller visible whitened area (A_W) at the point of failure, compared to wet specimens ($(26.5 \pm 15.6) \%$ in dry and $(52.9 \pm 13.9) \%$ in wet samples). Interestingly, there was no significant difference in the strain at whitening onset (ϵ_{won}) between wet ($1.7 \pm 1.1) \%$) and dry ($1.0 \pm 0.6) \%$) samples. Figure 4.6 displays the correlation chart of strain at whitening onset (ϵ_{won}) with yield strain (ϵ_y). Hydrated samples indicated a significant ($p < 0.01$) correlation ($r_s = 0.82$), whereas dried samples remained close to a significant ($p = 0.08$) correlation ($r_s = 0.55$).

4.4.4 Dehydration causes transition from ductile to quasi-brittle failure mode

Fracture surface images, determined with SEM and μCT , demonstrated that hydrated trabeculae exhibited a rugged fracture surface, as commonly known in ductile failure modes, whereas dehydrated samples illustrated a much more blunt fracture surface, typically for a quasi-brittle failure mode (see figure 4.7). In SEM images, fibrous features on fracture surfaces were visible in wet samples, which might be related to delamination of mineralized collagen fibrils and might act as an important failure and energy dissipation mechanism. On the other hand, dried samples demonstrated flat homogeneous fracture surfaces because of fiber pull-out and brittle rupture of mineralized collagen fibrils. At the trabecular scale, fracture surfaces of wet samples were much larger than those of dried ones. This is in accordance to a larger energy dissipation (larger W_{py}) in wet samples and might be enabled by shearing of adjacent surfaces, such as lamellae.

4. DEHYDRATION CAUSES TRANSITION FROM DUCTILE TO QUASI-BRITTLE FAILURE MODE

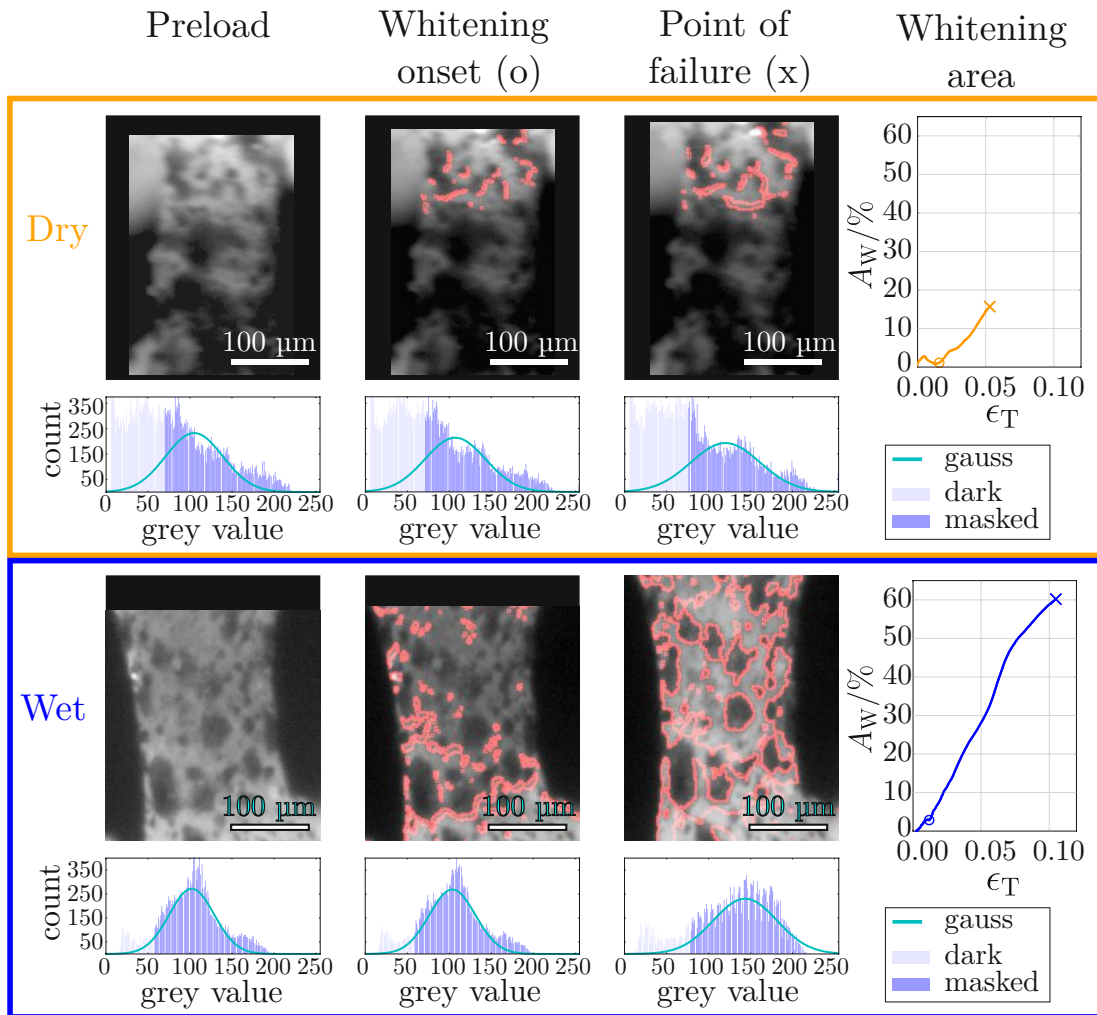


Figure 4.5: Whitening of a selected **wet** (bottom) and **dry** (top) trabecula. Images with **marked** whitening area are illustrated at pre-load (left), whitening onset (o, middle) and the point of failure (x, right). The corresponding whitening area (A_W) vs. true strain (ϵ_T) diagrams are shown on the right. The histograms of each image are shown below the corresponding images. The considered, masked trabecular area (without the speckle pattern) is noted as **masked**, the speckle pattern as **dark**. The **Gaussian fitting curve** is also shown for the considered, masked trabecular area and indicates a shift to larger gray values with increasing strain. In dry trabeculae the whitening area increased only moderately after the onset of whitening. In contrast, there was a rapid increase of the whitening area to larger relative values for A_W in wet trabeculae.

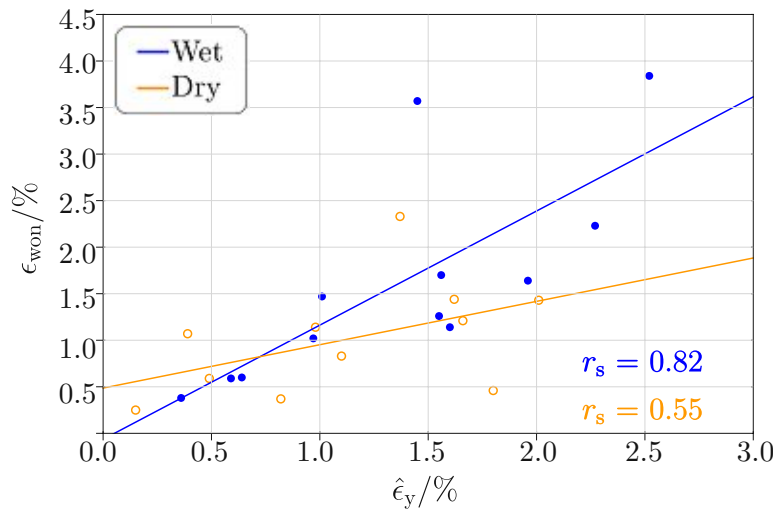


Figure 4.6: Correlation of strain at whitening onset (ϵ_{won}) with apparent yield strain ($\hat{\epsilon}_y$), shown for **wet** and **dry** trabeculae. Corresponding Spearman's rank correlation coefficients are illustrated at the bottom right corner.

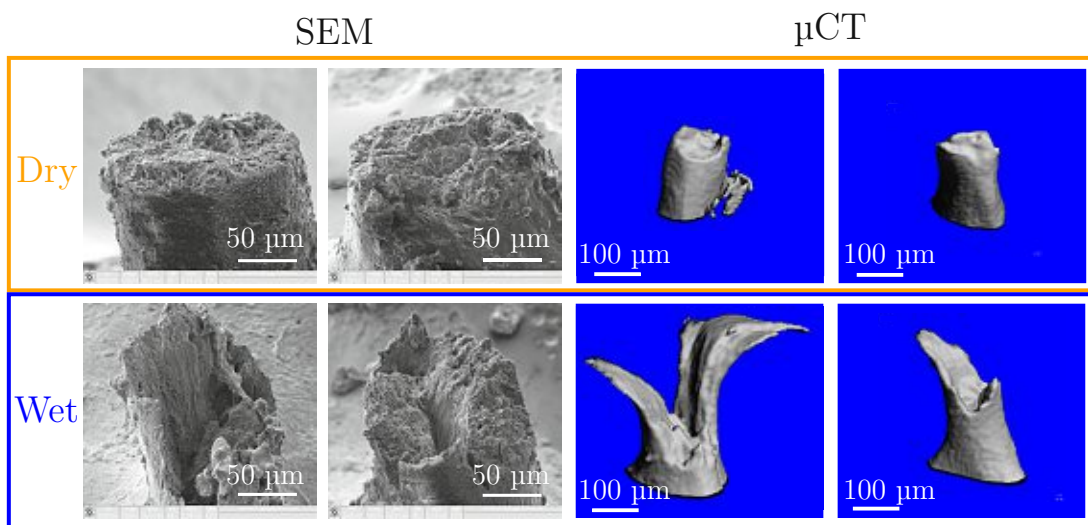


Figure 4.7: Fracture surface analysis of **dry** (top) and **wet** (bottom) trabeculae. SEM images are shown on the left, 3D rendered μCT images on the right. Dry trabeculae show blunt fracture surfaces, with a much smaller fracture surface area, compared to larger, ragged surfaces in wet samples.

4.5 Discussion

Dehydration of individual trabeculae resulted in an approximately two-fold increase of apparent elastic modulus, yield stress, and failure stress in uniaxial tension. On the contrary, failure strain and post-yield work decreased by a factor of three and two, respectively. Sequentially, the hypothesis that the mechanical properties of individual trabeculae are dependent on the hydration state could be verified. So far, only one study quantified the effect of dehydration on individual trabeculae. Townsend et al. determined a elastic modulus of 11.4 GPa for hydrated and a value of 14.1 GPa for dehydrated trabeculae in buckling tests [66]. However, buckling tests might be erroneous because of end artifacts and an undefined stress state (see section 2.7.3).

The elastic modulus of trabecular tissue has also been determined in nanoindentation experiments on hydrated and dehydrated samples [15,16,212]. All these studies also reported a significant increase of the elastic modulus in dehydrated samples. However, the effect of dehydration on the change of elastic modulus is larger in the current study, than reported previously. For example, Wolfram et al. reported a decrease of 29 % in re-hydrated human trabeculae, compared to dehydrated samples [212]. In contrast, in the current study a decrease of 62 % in apparent elastic modulus of hydrated trabeculae was determined. Several issues might explain this observed deviation. First, bone tissue is investigated at the lamellar level in nanoindentation, whereas trabecular tensile experiments determine the homogenized mechanical behavior at a larger scale. Hereby, included structures, like cement lines (the regions between trabecular packets, see section 2.1) are potentially more affected by hydration than bone lamellae [262]. Second, trabecular tissue is tested mainly in compression in nanoindentation, whereas trabeculae were tested in tension in the current study. Third, a different drying regime was used here, compared to previous nanoindentation experiments. This might have caused disparities in the amount of bound water. According to Nyman et al. water associated with collagen is first removed and water associated with the mineral phase only evaporates at higher temperatures [263]. In the current study, trabeculae were dehydrated at 37 °C, meaning that water should be mainly removed from the

collagen phase. This assumption is based on the observation that the yield stress of bone is larger after dehydration of the collagen phase, whereas dehydration of the mineral phase results in a decrease of yield stress [263]. As yield stress increased after dehydration in the current study, water was indeed removed from the collagen phase only. Wolfram et al. dehydrated their samples at room temperature [212], hence, it is assumed that water was also removed only from the collagen phase. However, as room temperature is well below 37 °C less water might have been removed than in the current study. This would be in accordance to the less pronounced effect of dehydration on the elastic modulus, compared to the present study.

Previously reported values for elastic modulus from tensile experiments of individual trabeculae lie in-between the values determined in the present study ((17.1 ± 8.4) GPa for dry and (6.5 ± 3.7) GPa for wet samples). In more detail, elastic modulus was determined in the range of 11.5 GPa [179] to 16.2 GPa [18]. However, also very low values of elastic modulus, such as 1.4 GPa [184] and 0.8 GPa [178] have been reported. In the course of the present study, also damaged trabeculae were tested and obtained elastic moduli were in the range of 1 GPa. Thus, it is assumed that also previously reported values of that magnitude might be caused by pre-damage, shear forces, improper deformation measurement or improperly aligned samples. In fact, it was determined that a tilt of only 10° of the trabecular strut causes a reduction of the elastic modulus of almost 50 % if bending occurs (one end fixed while the other is able to move; see section 3.1.3 “Influence of trabecular tilt angle on determined stiffness and strength”).

In addition to the elastic properties, also the yield and post-yield behavior of individual trabeculae have been classified. Yield stress was increased significantly ($p < 0.001$) in dehydrated trabeculae ((133 ± 56) MPa), compared to hydrated samples ((81 ± 23) MPa). Interestingly, no significant changes in yield strain were observed ((1.9 ± 1.7) % for wet and (1.0 ± 0.6) % for dry samples). Nevertheless, variation of yield strain was high and a trend ($p = 0.1$) towards higher yield strain in wet samples was recognized. As previous studies performed tensile tests on dehydrated samples, yield strains can only be compared for dry samples. Here, previously determined yield strains were 0.7 % for bovine [171] and human [18] tra-

4. DEHYDRATION CAUSES TRANSITION FROM DUCTILE TO QUASI-BRITTLE FAILURE MODE

beculae, similar to the reported (1.0 ± 0.6) % in the present study. In contrast, yield strains back-calculated from non-linear FE analysis of hydrated (human) cancellous bone samples were reported to be as low as 0.4 % [201]. This value is surprisingly lower than the determined (1.9 ± 1.7) % for wet trabeculae. However, given that this value is also lower than the previously determined 0.7 % for bovine [171] and human [18] trabeculae, it is assumed that major differences between micro-tensile experiments and back-calculation from FE analysis caused this deviation. The applied constitutive model in Bayraktar et al. [201], differences in the anatomic site, and averaging over a larger non-homogeneous volume might explain this deviation. Only rod-shaped trabeculae are used in micro-tensile experiments, whereas cylindrical trabecular bone cores, used for FE analysis, contain a network of rod- and plate-shaped trabeculae. Further, tensile testes of these bone cores cause undefined loading states of individual trabeculae, compared to a homogeneous tensile stress in micro-tensile experiments. Keaveny et al. determined the yield strain of bone cores as 0.5 % in wet bovine samples [264]. Sequentially, individual trabeculae might deform much more elastically (1.9 % on average according to the present findings) than the entire trabecular network. Actually, Keaveny et al. mentioned that yielding of bone cores might be caused by fracturing of individual trabeculae, which naturally occurs after yielding.

Yield strain was significantly ($p < 0.01$) correlated with onset of whitening (associated with damage initiation [260]) for wet ($r_s = 0.82$) but not for dry ($r_s = 0.55$, $p = 0.08$, close to significance) trabeculae. As a result, microdamage initiation seems to be closely related to yielding. This finding is in agreement with previous studies, where whitening was linked to elevated tensile strains in three-point bending test of individual trabeculae [167, 172]. The onset of whitening occurred at (1.0 ± 0.6) % in dry samples and at (1.7 ± 1.1) % in wet samples, indicating no significant difference. So far, whitening determination in individual trabeculae has only been performed in three-point bending experiments, in a wet environment. Jungmann et al. reported a whitening onset of 1.6 % [172] and Szabo et al. determined 1.95 % [167] (for low strain rates), indicating a good agreement to the determined (1.7 ± 1.1) % for wet trabeculae.

The whitened area at the point of failure was significantly larger ($p < 0.001$) in wet ($(53 \pm 14) \%$) than in dry samples ($(27 \pm 16) \%$). Sequentially, microdamage is constrained to a significantly smaller region in dehydrated samples. This finding is in accordance to determined full-field strain maps. Here, dehydrated samples indicated a more pronounced localization of elevated strains, in contrast to hydrated trabeculae (see figure 4.4). Hence, observed differences in the global stress-strain behavior between wet and dry samples can be explained by differences in damage accumulation, linked to elevated strains.

Two different effects have been observed. First, in wet samples the region of fracture sustained significantly ($p < 0.01$) larger local strains ($(27 \pm 13) \%$) than dry specimens ($(16 \pm 10) \%$). Second, also the area of elevated strains was larger in the post-yield region. This effect can be best related to the significantly larger post-yield work with $(13.3 \pm 5.7) \text{ MJ m}^{-3}$ in wet samples, compared to $(6.0 \pm 5.3) \text{ MJ m}^{-3}$ in dry ones.

So far, only a few studies have determined post-yield properties of individual trabeculae [18, 36, 171], but only Hernandez et al. performed tests in a quasi wet environment by adding droplets of HBSS onto their samples during testing [36]. In that study, only ultimate strain was determined and reported as 8.8% on average for human samples. On the contrary, Carretta et al. determined 5.1% for young bovine trabeculae [171]. In the present study ultimate strain was determined as $(3.6 \pm 1.7) \%$ for dried samples and $(11.0 \pm 3.3) \%$ for wet ones. As a result, previously reported values of ultimate strain might have been obtained from not completely hydrated or dehydrated samples, as these values lie in-between the currently reported values.

As a consequence of the aforementioned differences, also the failure mode was significantly different between hydrated and dehydrated trabeculae. Essentially, dehydration resulted in a transition from a ductile to a quasi-brittle failure mode. This assumption was further strengthened with fracture surface analysis (see figure 4.7). Hereby, almost blunt fracture surfaces confirmed the assumed quasi-brittle failure mode in dehydrated samples. Townsend et al. already supposed this transi-

tion in buckling tests of individual trabeculae, based on the observed stress-strain behavior [66].

Compared to previous studies [18, 171, 179, 184] the present test set-up enabled a high throughput (20 samples per group) while maintaining a high reproducibility (see section 3.1.3 “Validation of tensile test set-up”). This is of great importance, as those studies also reported a high intra-group variation. Luccinetti et al. already highlighted the necessity of a high throughput for reliable average mechanical properties [12]. Even more importantly, the presented set-up allows determination of elastic and post-yield properties of individual trabeculae in a wet, close to physiologic environment.

4.5.1 Limitations

While this study delivered important findings and insights into the mechanical behavior of trabecular bone tissue also some limitations were encountered. Sample handling proved to be difficult, as also reported previously in other micro-mechanical studies [18, 36, 171, 184]. Some samples (6 dry and 3 wet ones out of 40 samples in total) fractured during sample preparation, similar to a reported rejection rate of 3 out of 24 samples in Carretta et al. [18]. Despite of large efforts to control sample alignment and hydration, intra-group variability was still high; e.g. the CV was in the range of 0.3 (wet samples) to 0.5 (dry samples). However, previous studies, like Carretta et al. [171] and Hernandez et al. [36], reported similarly high variations. Hereby, especially differences in the sample geometry might be contributing a lot to these deviations. For instance, Busse et al. determined a significant correlation between elastic modulus and trabecular thickness in three-point bending experiments [119]. Accordingly, also determined apparent mechanical properties of the current study showed a dependency on geometric variables. For example, ultimate strain and ultimate stress were significantly correlated with trabecular major ($r_s = -0.76$) and minor axis ($r_s = -0.75$) in dehydrated samples ($p < 0.01$). Thus, thinner trabeculae sustained larger strains and stresses before fracture, compared to thicker samples. Further, elastic modulus ($r_s = 0.75$), yield strain ($r_s = 0.77$) and 0.2% offset yield strain ($r_s = 0.74$) were

significantly correlated with trabecular length. The three curves in figure 4.2 that indicate the lowest elastic moduli were obtained from very short trabeculae ($\leq 200 \mu\text{m}$). Moreover, also the TMD of these three trabeculae was lower, compared to the other samples. Indeed, TMD proved to be significantly ($p < 0.01$) correlated with apparent elastic modulus ($r_s = 0.70$) and trabecular minor axis ($r_s = 0.66$) in wet samples. Taken together, these short trabeculae are possibly younger, less mineralized and sequentially less stiff, than more mature specimens. Further, small strains (up to yield) indicated a low SNR, resulting in error-prone strains. The speckle pattern that was used for optical strain tracking was interfering with whitening detecting. However, using the newly developed whitening detection approach (see section 4.3.5) overcame this issue. In the present study, young bovine bone was used to investigate the effect of dehydration. Hereby, the observed large variation of TMD values indicated that this bone did not reach full maturity, which might also contribute to the obtained large variation of apparent mechanical properties. Sequentially, bone from older animals should be preferentially used in future studies. Moreover, investigation of human trabeculae is important to use obtained values for fracture risk assessment of bone with FE analysis. As Carretta et al. determined similar values for mechanical properties of dry bovine and human trabeculae in the same test set-up [18, 171] it is assumed that the effect of hydration of human bone will be similar to bovine one, but this remains to be shown. TMD determination with μCT also inherits some limitations, such as underestimation of true mineralization and a larger deviation from true TMD at larger values. However, TMD determination was used to compare its effect on the apparent mechanical properties of wet and dry samples and not to obtain absolute TMD values.

4.6 Conclusions

The present study presented a reliable high-throughput tensile test set-up for the mechanical characterization of individual trabeculae, close to a wet, almost physiologic environment. Hereby, the necessity has been highlighted to perform mechanical characterization of bone tissue in a wet, physiologic environment. Dehydration of samples may simplify preparation and testing protocols but results

4. DEHYDRATION CAUSES TRANSITION FROM DUCTILE TO QUASI-BRITTLE FAILURE MODE

in an approximately two-fold increased apparent elastic modulus, yield stress, and failure stress, whereas failure strain and post-yield work decrease by a factor of three and two, respectively. Further, dehydration resulted in a transition from a ductile failure mode to a quasi-brittle failure behavior. Sequentially, only material parameters obtained in a wet, close to physiologic environment should be used as input parameters for computational simulations, like FE analysis.

Osteoporosis affects mainly morphometry not material properties in femoral head

“But I was losing so much bone density that I would have been in grave danger. And I mean grave danger. If I had let it go just a few more years I could have broken my hip or spine just picking up my granddaughter.”

Sally Field

5.1 Related publications and declaration of contributions

Partial results of the presented work (text, tables and figures) have been *conditionally accepted* in the “Journal of Bone and Mineral Research - Plus”, entitled “Effects of osteoporosis on bone morphometry and material properties of individual human trabeculae in the femoral head” and co-authored by Andreas G. Reisinger, Dieter H. Pahr and Philipp J. Thurner.

Author contributions: The first author and author of the current thesis, *Martin Frank*, contributed to the study design, performed the mechanical tests, data processing, data evaluation, and interpretation, and wrote the manuscript. *Andreas G. Reisinger* developed the rheological model and performed the data evaluation with that model. *Dieter H. Pahr* and *Philipp J. Thurner* designed the study, supervised the work of Martin Frank and supported the interpretation of the results.

5.2 Introduction

Osteoporosis is the most common bone disease and causes a decrease of total bone mass (see section 2.5 for more details). It is classified as a decrease in areal bone mineral density (aBMD) by more than 2.5 standard deviations, compared to healthy controls [1, 5]. Measurement of aBMD is performed via DEXA at the femoral neck and the lumbar spine [6] (see figure 2.5). Although patients are screened with this approach to determine need for treatment, only 60 % of people that will suffer an osteoporotic fracture are correctly diagnosed [1]. Accordingly, additional factors rather than aBMD alone are currently incorporated in the diagnoses of osteoporosis, such as age, BMI, fracture history, cortisol treatment, epidemiologic information and other factors to calculate a 10-year fracture risk probability, the Fracture Risk Assessment Tool (FRAX) score [6]. This score enables a more reliable risk prediction, but the underlying changes in osteoporosis, beside a decrease in aBMD, remain largely unknown. Specifically, aBMD only reflects a combination of changes in bone mass and global mineralization, without accounting for bone quality. Bone quality can be determined by bone morphometry and material/tissue properties, such as mechanical properties, material composition, and microdamage [265].

While there is a common agreement that osteoporosis causes a change of bone morphometry [9, 119, 254, 255], conflicting results exist regarding changes in the material and apparent mechanical properties [9, 10]. Some studies determined a significant change of material and apparent mechanical properties in osteoporosis (decrease in elastic modulus [119], increase in elastic modulus [120, 121], decrease in ultimate strain and post-yield work [18]), while no change was observed in ovariectomized animal models [266, 267]. Interestingly, opposing effects of osteoporosis on

TMD were reported. In several studies a decrease of TMD was observed [116–118], while in others an increase was detected [119–121]. Further no change in bone mineralization was also reported, but accompanied with an increased heterogeneity of tissue mineralization in osteoporosis [122].

Possible discrepancies in mechanical tests are differences in species, anatomical site, small donor and/or sample number, definition and/or severity of osteoporosis, different test methods, and focusing on elastic behavior only. The current study aimed to address several of these issues to perform a defined and thorough characterization of trabecular bone material and apparent mechanical properties in combination with bone morphometry. A previously established tensile test approach (see section 3.1) was used to test 200 individual trabeculae, oriented along and normal to trajectories, from human femoral heads (20 donors in total). Samples were tested cyclically in tension, in a wet, close to physiologic test environment. Additionally, bone morphometry was determined at the exact locations of trabecular dissection points to determine a potential correlation of morphometry with material properties. Osteoporosis was defined as a low trauma fracture of the femoral neck and, as a second classification, traditionally by a T-score smaller than -2.5 . Determination of material properties was based on a rheological model (see section 3.3, to get elastic, viscous, yield, and failure properties, and loss tangent). The first hypothesis was that there is a significant change of tissue mineralization and material properties in osteoporosis, which might be directly correlated to the known change in bone morphometry. The second hypothesis was that there is a change of material and apparent mechanical properties and bone morphometry with increasing age, independently from osteoporosis.

5.3 Material and methods

5.3.1 Study design

The main goal of this descriptive study was to determine if there is a significant difference in the apparent mechanical or material properties between osteoporotic and control trabeculae. As such, six individual trabeculae obtained from a donor

5. OSTEOPOROSIS AFFECTS MAINLY MORPHOMETRY NOT MATERIAL PROPERTIES IN FEMORAL HEAD

with a low trauma (osteoporotic) fracture (female, 77 years old) and six from a control cadaveric donor (male, 64 years old) were tested and evaluated in a pilot study in the same way as described for the actual study. Based on the obtained results, sample size was estimated with a power-analysis at a significance level of 95 % (Type I error: 0.05) and a power of 80 % (Type II error: 0.20). The required total number of samples (both groups) was 14 for apparent elastic modulus and 62 for apparent post-yield work. Since a large biological and inter-donor variation of the material and apparent mechanical properties is known from previous studies [13,14,259], it was aimed to test 200 individual trabeculae in total, obtained from 20 donors (10 per group).

5.3.2 Human bone samples and clinical data

Human femoral head samples, together with clinical data (age, sex, BMI, aBMD, T-score, and FRAX score), were obtained from a previous study [268] and collected from two groups: osteoporotic fracture group (10 samples) and cadaveric control group (10 samples). Osteoporotic samples were obtained from patients undergoing hip arthroplasty at University Hospital Southampton NHS Foundation Trust (UHS) after a low trauma intra-capsular fracture of the femoral neck. Sequentially, those patients suffered of an actual osteoporotic fracture (which would not have occurred in healthy patients) and ensures bad bone quality. Cadaveric control samples were provided by Innoved Institute LLC (Besenville, IL, USA). These donors had no known history of fracture or bone disease. In an additional second classification, grouping was based on T-score, to avoid overlooking of osteoporotic, but non fractured donors. T-score was measured at the proximal femoral neck *in vivo* for fracture patients and with a modified approach for explanted cadaveric control specimens, as described previously [268]. In this second approach, six donors were classified as osteoporotic ($T < -2.5$), six as osteopenic ($-1.0 < T < -2.5$) and eight as healthy controls ($T > -1.0$).

Full IRB and ethics approvals were obtained for the study (LREC 194/99/1; 210/01; 12/SC/0325) from Southampton and South West Hampshire Research Ethics Committee.

5.3.3 Sample preparation and mechanical testing

Sample preparation of individual trabeculae was performed according to section 3.1.3 “Sample preparation” of femoral heads in the frontal plane (see figure 5.1–A). As the femoral head shows a typical arrangement of trabecular orientation (with tensile and compressive areas [269]), half of individual trabeculae were selected from the compressive, longitudinal trajectories (see figure 5.1–B, green) and half from the arcuate, transversal trabecular system (red). Final test specimens, including trabeculae embedded in epoxy glue are shown in figure 5.1–D). Average gauge length was $(687 \pm 166) \mu\text{m}$. Tensile testing and strain determination were done as reported in sections 3.1.3 “Tensile test” and 3.1.3 “Displacement and strain determination”.

Tensile tests were done displacement controlled at a displacement rate of 0.01 mm s^{-1} . A cyclic loading-hold-unloading protocol was chosen, as illustrated in figure 3.8–A. As mentioned in section 3.1.3 “Tensile test”, a pre-load of 0.08 N was applied to facilitate sample alignment. Verification was done with the video camera and the actual tensile test was started, and stopped after sample fracture. This cyclic loading protocol was chosen to enable a thorough mechanical characterization of the bone tissue in one single experiment, as outlined in section 3.2.

5.3.4 Determination of apparent mechanical and material properties, and TMD

Determination of sample geometry was done with μCT measurements, as described in section 3.1.3 “Micro computed tomography (μCT) and image processing”. Hereby, the mean cross-sectional area (A_{mean}) was used to calculate true stress (σ_{T}), according to section 3.1.3 “Force and stress determination”.

Evaluation of stress-strain diagrams (see figure 5.1–F) was performed with three approaches. First, the elasto-visco-plastic rheological model (see section 3.3 and figure 5.1–H) was used to determine the following material properties: Long-term modulus (E_{∞}), Maxwell/dynamic modulus (E_{mx}), yield stress (σ_{y}), hardening

5. OSTEOPOROSIS AFFECTS MAINLY MORPHOMETRY NOT MATERIAL PROPERTIES IN FEMORAL HEAD

coefficient (p), hardening stress (R), ultimate stress (σ_u), viscosity (η) and loss tangent ($\tan(\delta)$). Second, the envelope curve of the experimental data was evaluated to determine the following apparent mechanical properties: Apparent yield strain ($\hat{\epsilon}_y$), apparent ultimate strain ($\hat{\epsilon}_u$), apparent elastic work (\hat{W}_{el}) and apparent post-yield work (\hat{W}_{py}) (see section 3.2.2). It has to be noted that evaluations done with the rheological model are based on engineering stress and strain, because of assuming geometric linearity. In contrast, evaluations based on the envelope curve are based on true stress and strain, as ultimate strains were in the range of 10%. The third evaluation was the determination of the tensile modulus in each loading and unloading cycle (see figure 5.1-G), as described in section 3.2.1.

Tissue mineral density was determined as described in section 3.1.3 “Determination of Tissue Mineral Density (TMD)”. Hereby, TMD was determined in whole individual trabeculae and in the fracture zone of the trabecular struts. The exact locations of the fracture zone were known from the video recording because of the appeared whitening effect (which is related to microdamage accumulation, see section 4.3.5 and hence, marks fractured areas). As such, an overlay of the μ CT scanned trabeculae was performed with the optical images taken during testing. In more detail, the trabecular struts elongated during the test and the initial frame had to be used for correlation of whitened area for cropping the μ CT image (as scanning was done ahead of sample testing). Thus, the speckle pattern was used to estimate the boundaries of the whitened area in the last image (the image at sample fracture) and was translated to the first image (at test start). Next, the start video frame and the μ CT image were loaded into 3DSlicer (v4.1.0r19886, Slicer Community) and the μ CT image was cropped to the known boundaries of whitened area (see figure 5.6-A & B). The mean normalized histograms, (number of voxels divided by total number of non-zero voxels) were determined on μ CT images, which were masked with corresponding segmented images in medtool (4.3, Dr. Pahr Ingenieure e.U., Austria) to only consider voxels inside the trabeculae (see Figure 5.7). Further, mean \pm standard deviation of TMD (see table 5.5) and heat-plots of TMD were determined with python scripts (see Figure 5.6-A & B). Mean intensity profiles across the cross-sectional mass centroid axes at the center of the fracture zone were computed too (see Figure 5.6-D - F)). Here, length position

was normalized by trabecular thickness.

5.3.5 μ CT-derived bone morphometry

Ahead of bone dissection, the femoral head was scanned with a μ CT-100 (Scanco Medical AG, Switzerland) at 70 kVp, 114 μ A, integration time 200 ms, average data 3, 1500 projections, nominal resolution of 16 μ m and aluminum filter 0.5 mm. Image processing and determination of bone morphometry was done using medtool 4.3 (Dr. Pahr Ingenieure e.U., Austria). The obtained images were segmented using a Gaussian filter ($\sigma = 1$, support = 1) and a single level threshold of 490 mg cm⁻³ HA. Sequentially, spheres with a diameter of 5 mm were cropped at the exact positions, where individual trabeculae were dissected (see figure 5.1-C). This procedure enabled a direct comparison of the obtained material and apparent mechanical data with the local bone morphometry. Bone Volume to Total Volume (BV/TV), Bone Surface (BS), Degree of Anisotropy (DA), Trabecular Thickness (Tb.Th), Trabecular Number (Tb.N) and Trabecular Separation (Tb.Sp) were determined, according to [270,271].

5.3.6 Statistical analysis

Statistical data analysis was done in SPSS (Version 26, IBM, US). First, data distribution was investigated with histograms, boxplots and Q-Q plots, before selecting appropriate statistical tests, as suggested by Lix et al. [272]. Normality of data was further analyzed using a Kolmogorov-Smirnov-Test. Age, BMI, R , σ_y , σ_u , aBMD, length, BS and Tb.N were normally distributed, whereas all other variables showed a non-normal distribution. Thus, a Mann-Whitney-U non-parametric test was used for comparison of means for the fracture based classification (2 groups). Similarly, a non-parametric Kruskal-Wallis-test (K.W.) was used for comparison of means for the T-score based classification (3 groups) and for the analysis of the tensile modulus in each loading and unloading cycle (further referred as tensile modulus evolution, figure 5.3; 4 groups: osteoporotic loading and unloading, control loading and unloading). In addition, a general linear model was used to determine if age is a contributing covariate in determining the apparent mechanical or material properties, with fracture grouping or T-score grouping as independent variable.

5. OSTEOPOROSIS AFFECTS MAINLY MORPHOMETRY NOT MATERIAL PROPERTIES IN FEMORAL HEAD

Correlation was determined using the Spearman's rank correlation coefficient. Significance was accepted as $p < 0.05$ and a Bonferroni correction was applied for multiple testing.

As determination of material properties using the rheological model resulted in some non-physiologic values, an IQR test was performed to detect outliers. First, this approach was applied on the pooled RMSE of the calculated stress signal, to remove bad fittings. Next, only curves that showed at least three cycles before fracture were used for further analysis (in accordance with Reisinger et al. [224]). Then, all material parameters underwent an IQR test separately for each variable to remove non-physiologic values. The variable based IQR test was also used for detection and removal of outliers in bone morphometry data and cyclic loading tensile moduli.

Comparison between inter- and intra-donor variability of data was performed both, with a Kruskal-Wallis-test and a one-way ANOVA, as data showed similar distributions, but deviated from a normal distribution. This procedure was performed to ensure that there is no influence from the assumed data distributions on the statistical outcome. As such, it was estimated if there is a larger variation of given parameters between individual donors, compared to the variation inside a single donor.

5.4 Results

In total, 179 individual trabeculae were successfully tested in cyclic tensile mode (89.5%, control: 90, fracture: 89, $T > -1.0$: 70, $-1.0 > T > -2.5$: 54, $T < -2.5$: 55). Clinical baseline characteristics is shown in table 5.1 and figure 5.2. Both grouping classifications indicated no significant difference in age and BMI. Patients that suffered from a low trauma fracture or with $T < -2.5$ had a significantly lower aBMD, T-score and FRAX score. No significant difference of the clinical, material, apparent mechanical properties, or the bone morphometry was detectable between male and female donors (except a higher FRAX score and yield strain in females, data not shown).

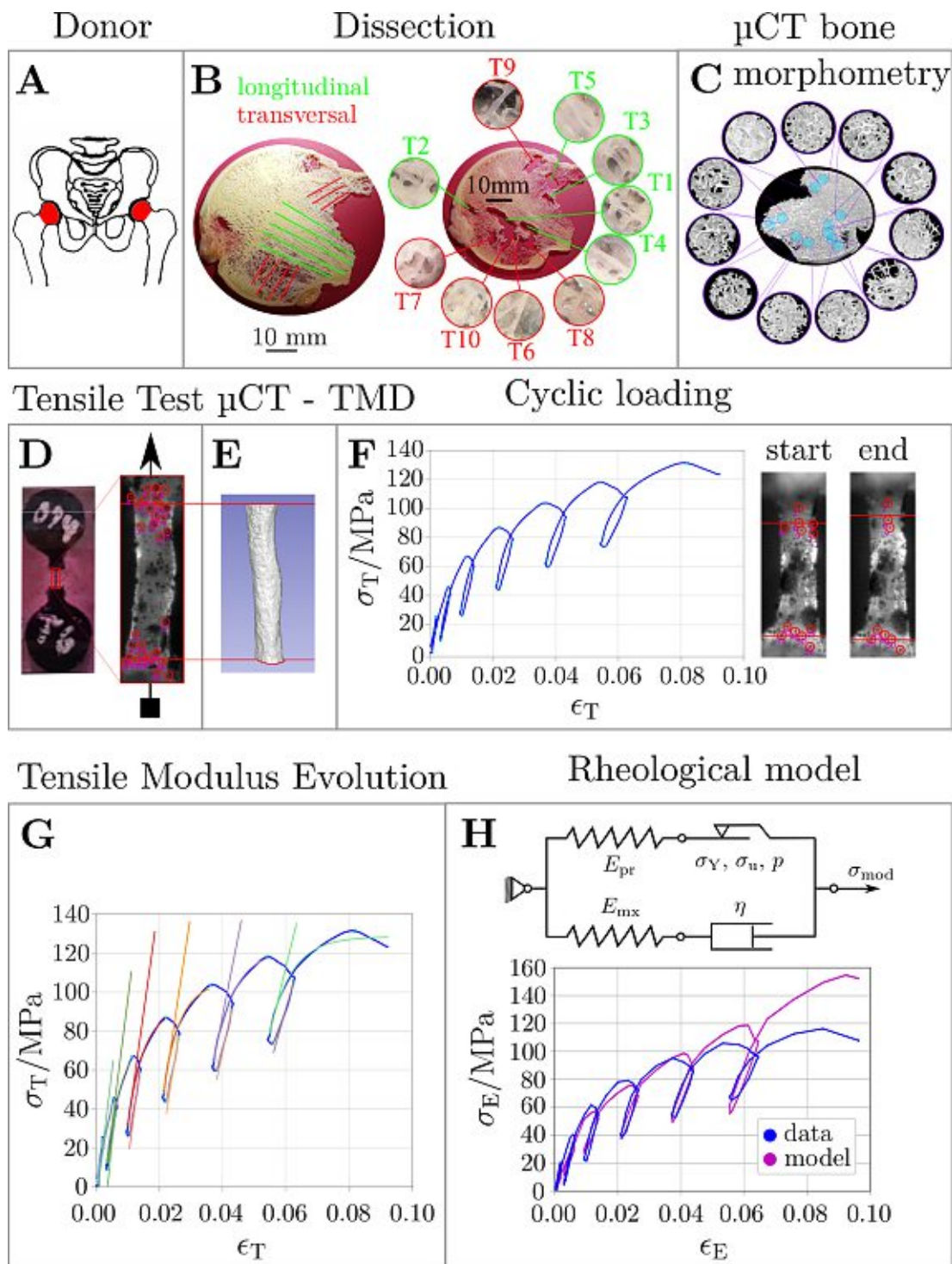


Figure 5.1: Operation chart: **A:** Femoral head as sampling location from donors. **B:** Dissection of individual trabeculae in longitudinal (green) and transversal (red) direction. **C:** μ CT-derived bone morphometry on the same locations, where individual trabeculae were dissected. **D:** Tensile test sample (left, embedded in circular epoxy end pieces) and optical strain tracking (right, black speckle pattern). **E:** μ CT scanning of individual trabeculae to obtain geometry and TMD, with respect to the optically tracked region in the experiment. **F:** True stress-strain curve, obtained from cyclic loading. Inset shows the trabecula at the start and end of the experiment. **G:** Tensile modulus evolution, determined with exponential fits in each loading and unloading cycle. **H:** Rheological model with determined engineering stress-strain curve.

5. OSTEOPOROSIS AFFECTS MAINLY MORPHOMETRY NOT MATERIAL PROPERTIES IN FEMORAL HEAD

Parameter	Fracture			T-score				
	CTRL	FRAC	p-value	> -1.0	-1.0 > T > -2.5	< -2.5	K.W.	
Age/years	69.5 ± 9.2	74.6 ± 11.0	0.307	68.1 ± 10.2	80.0 ± 7.5	71.3 ± 9.6	0.128	
BMI/kg m ⁻²	30.1 ± 9.2	26.1 ± 5.2	0.288	30.7 ± 9.5	29.4 ± 3.8	22.6 ± 3.2	0.068	
T-score	1.12 ± 2.94	-2.41 ± 0.83	0.002	1.70 ± 2.60	-2.14 ± 0.21	-2.92 ± 0.31*	< 0.001	
FRAX (excl. aBMD)/%	3.1 ± 3.4	13.9 ± 11.3	0.031	2.9 ± 3.6	13.2 ± 12.6	13.0 ± 10.8 *	0.033	

Table 5.1: Baseline clinical characteristics of osteoporotic and control patients. Data is shown based on the low trauma classification (fracture, left) and on the T-score classification (right). Significant p-values ($p < 0.05$) are marked **bold**. For T-score based classification p-values of the K.W. are noted and significant differences to $T > -1.0$ are marked with * in the corresponding column.

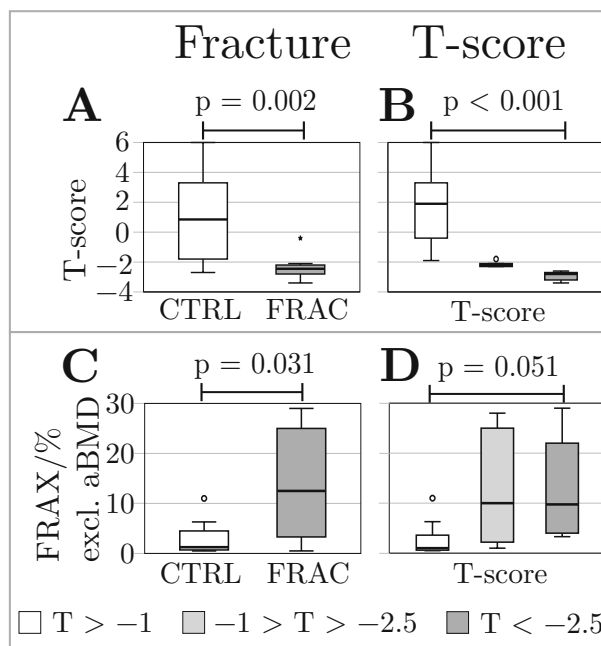


Figure 5.2: Clinical data is shown for grouping based on the fracture criterion (left, panels A & C) and on the T-score (right, panels B & D). **A, B**: T-score. **C, D**: FRAX (excl. aBMD). Significant differences ($p < 0.05$) are marked with bars and actual p-values are provided on top. Illustration of used boxplot styles (symbols and outliers) is given in figure 2.9.

5.4.1 Mechanical properties of trabecular bone tissue

Cyclic tensile modulus determination (see figure 5.1-G) is only shown for the low trauma fracture classification, as the T-score based grouping showed the same trends. Evaluation was successful for 162 curves in cycle 1 (86.0%, control: 76,

fracture: 78, $T > -1.0$: 59, $-1.0 > T > -2.5$: 45, $T < -2.5$: 50) and for 40 curves in cycle 7 (22.3%, control: 19, fracture: 21, $T > -1.0$: 13, $-1.0 > T > -2.5$: 21, $T < -2.5$: 6), since several samples fractured already after three cycles. The tensile modulus showed a significant difference between loading and unloading modulus in the first two cycles ($p < 0.001$, for fracture and control group), as illustrated in table 5.2 and in figure 5.3. However, no significant difference between the control and fracture group was detectable in any cycle. In the control group there was a significant decrease of the unloading modulus from cycle 1 to 3 ($p < 0.001$) and 2 to 3 ($p = 0.05$). Likewise, the unloading modulus decreased significantly from cycle 1 to 3 ($p = 0.011$) in the fracture group. After cycle 3, no significant changes in the tensile moduli were detectable.

Cycle	$E_{\text{load}}/\text{GPa}$		$E_{\text{unload}}/\text{GPa}$		p CTRL	p FRAC
	CTRL	FRAC	CTRL	FRAC		
1	7.4 ± 4.2	7.9 ± 4.7	21.4 ± 12.3	18.8 ± 13.4	< 0.001	< 0.001
2	8.4 ± 4.6	8.9 ± 5.6	15.1 ± 8.5	13.3 ± 8.2	< 0.001	0.001
3	9.8 ± 5.2	9.5 ± 5.2	10.7 ± 5.2	10.9 ± 5.4		0.282

Table 5.2: Tensile loading and unloading modulus of the first three cycles of osteoporotic (FRAC) and control (CTRL) trabeculae, based on the fracture criterion. Significant p-values ($p < 0.05$) are marked **bold**.

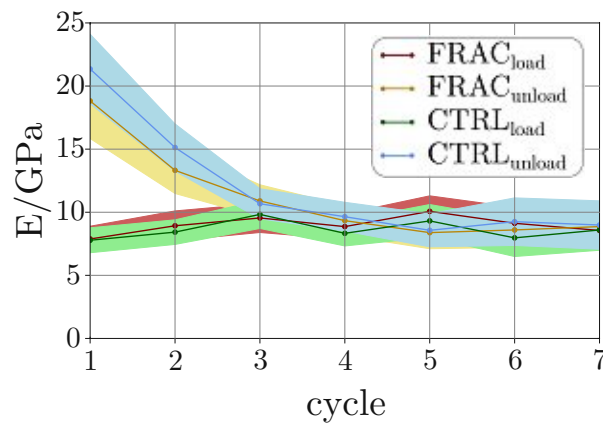


Figure 5.3: Tensile modulus evolution of osteoporotic (FRAC) and control (CTRL) trabeculae, based on the fracture criterion. Mean is shown with the 95% confidence interval. Tensile modulus is determined in each cycle as shown in figure 5.1-G.

5. OSTEOPOROSIS AFFECTS MAINLY MORPHOMETRY NOT MATERIAL PROPERTIES IN FEMORAL HEAD

Determination of material properties using the rheological model was successfully in 107 curves (58.1 %, control: 53, fracture: 54, $T > -1.0$: 43, $-1.0 > T > -2.5$: 32, $T < -2.5$: 32). As mentioned in section 5.3.6 “Statistical analysis” and in section 3.3 a strict selection regime was applied to only use reliable values. 10 curves (5.6 %) were omitted because of the IQR test on the RMSE, 57 curves (31.8 %) because of less than 4 successful test cycles and 14 values (7.8 %; on average for all determined parameters) because of the variable specific IQR test. No significant change in any material property could be detected for both classifications (see table 5.3-top, figure 5.4-A-H, and figure 5.5-A-H), except a significantly larger apparent yield strain and elastic work between $-1.0 > T > -2.5$ and $T < -2.5$. Even the general linear model (with age as a covariate) did not change the statistical outcome, except for apparent yield stress in T-score grouping. Further, selection of donor number as grouping variable indicated that long-term modulus ($p = 0.065$) and ultimate stress ($p = 0.049$) have a larger variability between individual donors, compared to intra-donor variability.

Parameter	Fracture			T-score				K.W.
	CTRL	FRAC	p-value	> -1.0	$-1.0 > T > -2.5$	< -2.5		
E_{∞}/GPa	5.0 ± 2.7	4.9 ± 2.5	0.872	4.9 ± 2.7	5.5 ± 2.9	4.5 ± 2.1	0.438	
E_{mx}/GPa	2.4 ± 1.3	2.6 ± 1.5	0.474	2.3 ± 1.3	2.8 ± 1.5	2.6 ± 1.5	0.351	
σ_y/MPa	30.8 ± 18.2	31.9 ± 19.8	0.813	30.8 ± 19.3	35.5 ± 20.6	28.1 ± 16.3	0.359	
p	62.7 ± 58.5	63.3 ± 66.2	0.991	59.5 ± 61.6	69.3 ± 63.9	61.0 ± 63.4	0.654	
R/MPa	59.4 ± 30.0	61.0 ± 26.9	0.517	62.7 ± 35.5	59.4 ± 20.7	57.9 ± 26.2	0.997	
σ_u/MPa	84.3 ± 29.4	93.8 ± 38.6	0.133	84.2 ± 34.1	93.4 ± 29.6	90.3 ± 39.7	0.343	
$\eta/\text{GPa}\cdot\text{s}$	4.8 ± 3.8	4.3 ± 3.2	0.665	5.4 ± 3.9	4.4 ± 3.6	3.7 ± 2.5	0.193	
$\tan(\delta)$	0.017 ± 0.011	0.021 ± 0.013	0.087	0.019 ± 0.011	0.019 ± 0.012	0.020 ± 0.014	0.948	
\hat{E}/GPa	8.5 ± 5.1	7.7 ± 4.4	0.408	7.5 ± 4.3	9.9 ± 5.7 ⁺	7.1 ± 4.0	0.020	
$\hat{\epsilon}_y/\%$	0.22 ± 0.16	0.27 ± 0.21	0.280	0.23 ± 0.17	0.19 ± 0.17 ⁺	0.31 ± 0.21	0.002	
$\hat{\epsilon}_u/\%$	5.0 ± 2.2	5.5 ± 2.4	0.159	5.1 ± 2.2	5.2 ± 2.6	5.4 ± 2.2	0.615	
$\hat{W}_{\text{py}}/(\text{MJ}\cdot\text{m}^{-3})$	3.0 ± 1.9	3.4 ± 1.9	0.157	3.0 ± 1.8	3.3 ± 2.0	3.6 ± 2.0	0.215	
$\hat{W}_{\text{el}}/(\text{MJ}\cdot\text{m}^{-3})$	0.018 ± 0.017	0.023 ± 0.022	0.274	0.019 ± 0.019	0.014 ± 0.019 ⁺	0.027 ± 0.022	0.001	

Table 5.3: Material properties determined with the rheological model and apparent mechanical properties determined with curve fitting on the envelope curve of osteoporotic and control trabeculae. Mean values are indicated ± standard deviation, σ_y and σ_u are corrected for the applied pre-load. The left part indicates the low trauma classification (Fracture), the right part the T-score based one. K.W. denotes the p-value obtained with the Kruskal-Wallis test. Significant p-values ($p < 0.05$) are highlighted **bold**. ⁺ illustrates a significant ($p < 0.05$) difference to $T < -2.5$.

The envelope curves of true stress-strain data were also evaluated, as described in sec-

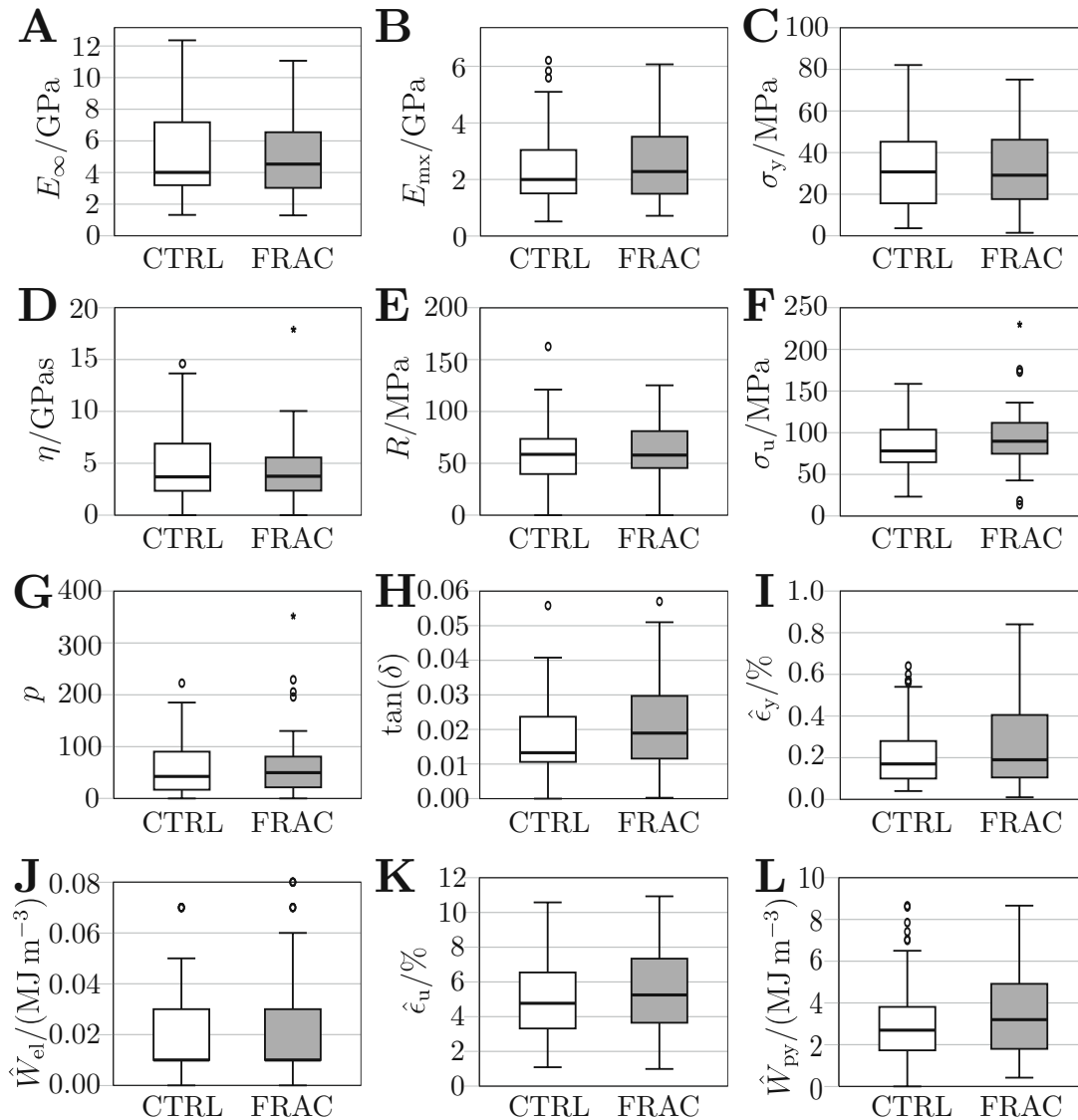


Figure 5.4: Material parameters determined with the rheological model and apparent mechanical properties determined with curve fitting of osteoporotic (FRAC) and control (CTRL) trabeculae, based on the fracture criterion. **A**: Long term modulus (E_∞), **B**: Maxwell/dynamic modulus (E_{mx}), **C**: Yield stress (σ_y), **D**: Viscosity (η), **E**: Hardening stress (R), **F**: Ultimate stress (σ_u), **G**: Hardening exponent (p), **H**: Loss tangent ($\tan(\delta)$). **I**: Apparent yield strain ($\hat{\epsilon}_y$), **J**: Apparent elastic work (\hat{W}_{el}), **K**: Apparent ultimate strain ($\hat{\epsilon}_u$), **L**: Apparent post-yield work (\hat{W}_{py}). Illustration of used boxplot styles (symbols and outliers) is given in figure 2.9.

5. OSTEOPOROSIS AFFECTS MAINLY MORPHOMETRY NOT MATERIAL PROPERTIES IN FEMORAL HEAD

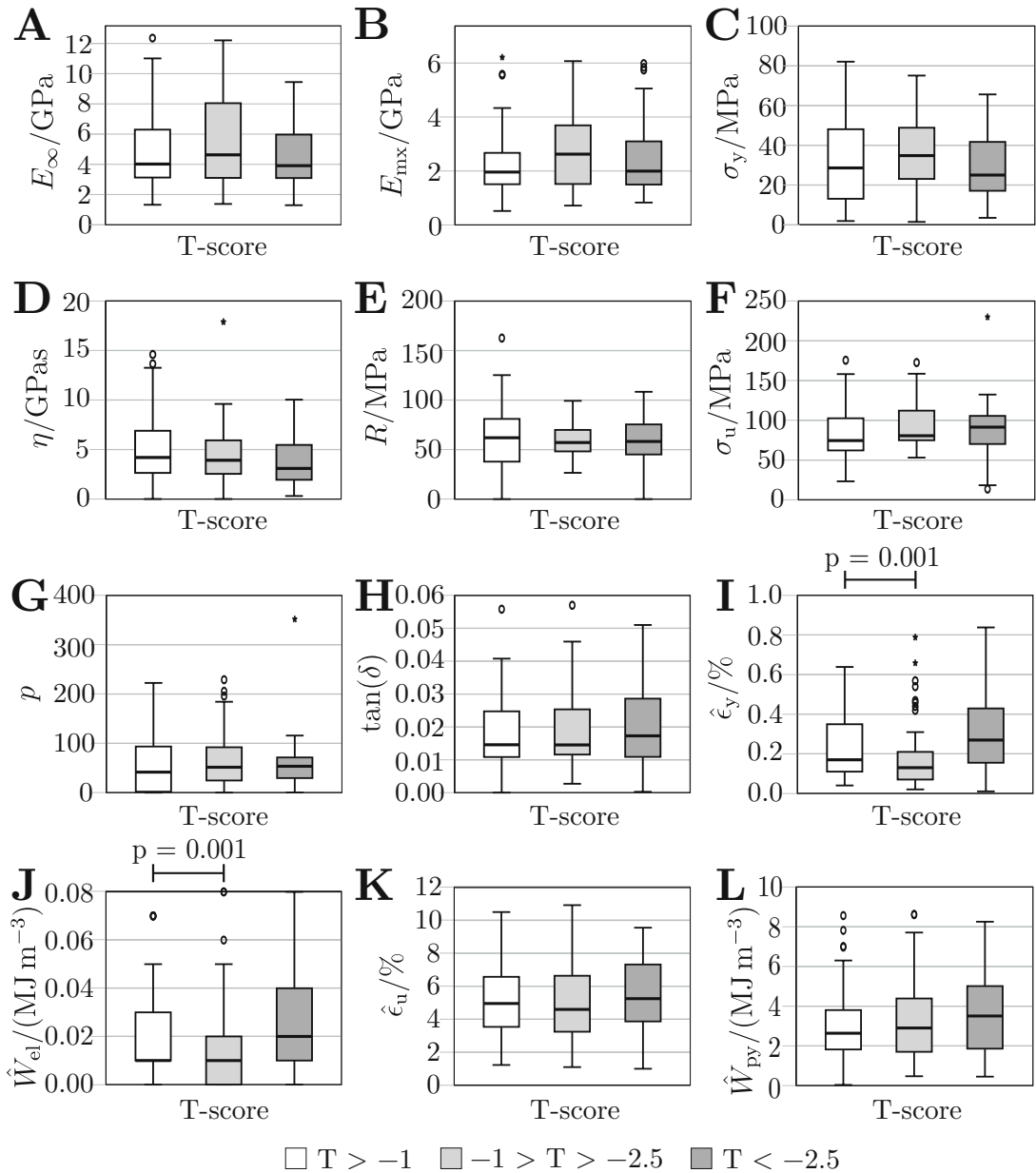


Figure 5.5: Material parameters determined with the rheological model and apparent mechanical properties determined with curve fitting of osteoporotic and control trabeculae, based on the T-score (legend at bottom). **A**: Long term modulus (E_∞), **B**: Maxwell/dynamic modulus (E_{mx}), **C**: Yield stress (σ_y), **D**: Viscosity (η), **E**: Hardening stress (R), **F**: Ultimate stress (σ_u), **G**: Hardening exponent (p), **H**: Loss tangent ($\tan(\delta)$). **I**: Apparent yield strain ($\hat{\epsilon}_y$), **J**: Apparent elastic work (\hat{W}_{el}), **K**: Apparent ultimate strain ($\hat{\epsilon}_u$), **L**: Apparent post-yield work (\hat{W}_{py}). Significant differences ($p < 0.05$) are marked with bars and actual p-values are provided on top. Illustration of used boxplot styles (symbols and outliers) is given in figure 2.9.

tion 3.2.2. Here, 171 curves (95.5 %) were successfully evaluated. Table 5.3-bottom and figures 5.4 and 5.5-I-L illustrate obtained apparent mechanical properties. In the fracture based classification, no significant change in any material or apparent mechanical property was observed. In contrast, there was a significant increase in yield strain and elastic work between $-1.0 > T > -2.5$ and $T < -2.5$.

Additionally, samples were grouped according to their orientation along the trajectories (longitudinal vs. transversal, see figure 5.1-B and table 5.4). No significant difference in any material or apparent mechanical property could be determined with respect to trabecular orientation, except apparent yield strain ($\hat{\epsilon}_y$) and apparent elastic work (\hat{W}_{el}). Splitting of samples into trabecular orientation and osteoporotic fracture (four groups) showed the same behavior as in pooled data shown in table 5.4. Average cross sectional area of pooled transverse trabeculae was significantly smaller than longitudinal ones ($(0.016 \pm 0.007) \text{ mm}^2$ vs. $(0.022 \pm 0.010) \text{ mm}^2$, $p < 0.001$) and thus indicated that the smaller, transversal trabeculae yield at larger strains.

5.4.2 Tissue mineral density (TMD)

TMD did not differ significantly in the fracture zone in both classifications ($p = 0.172$, see Table 5.5 and Figure 5.6). However, in T-score based grouping TMD of whole trabeculae was significantly larger in the group $-1.0 > T > -2.5$, compared to $T > -1.0$ and $T < -2.5$ (see Figure 5.7). Similarly, longitudinal trabeculae exhibited a significantly larger TMD than transversal samples. The mean intensity profile of all samples is illustrated in Figure 5.6 for fracture (D), T-score (E) and trabecular orientation (C) based classification. Here, no relevant differences could be detected across different groups.

Mean TMD was lower in the fracture zone, in comparison to the non-fractured part of corresponding whole individual trabeculae, (see Figure Figure 5.6-C, $p < 0.001$ for pooled data). TMD showed a significant positive correlation with long term modulus (E_∞ , $r_s = 0.42$, $p = 0.002$ for control samples and $r_s = 0.30$, $p = 0.002$ for pooled data, see Figure 5.8-A) and with all tensile moduli (cycle 2 to

5. OSTEOPOROSIS AFFECTS MAINLY MORPHOMETRY NOT MATERIAL PROPERTIES IN FEMORAL HEAD

Parameter	transversal	longitudinal	p-value
E_{∞}/GPa	4.9 ± 2.5	5.0 ± 2.7	0.929
E_{mx}/GPa	2.5 ± 1.6	2.5 ± 1.2	0.750
σ_y/MPa	31.6 ± 19.3	31.2 ± 18.7	0.942
p	66.8 ± 66.9	59.6 ± 58.4	0.572
R/MPa	57.7 ± 30.6	62.3 ± 26.5	0.717
σ_u/MPa	85.8 ± 38.9	91.8 ± 30.5	0.335
$\eta/\text{GPa s}$	4.7 ± 3.4	4.4 ± 3.5	0.717
$\tan(\delta)$	0.018 ± 0.011	0.020 ± 0.013	0.672
\hat{E}/GPa	8.0 ± 5.0	8.2 ± 4.7	0.648
$\hat{\epsilon}_y/\%$	0.28 ± 0.20	0.21 ± 0.17	0.012
$\hat{\epsilon}_u/\%$	5.1 ± 2.1	5.3 ± 2.5	0.958
$\hat{W}_{\text{py}}/(\text{MJ m}^{-3})$	3.2 ± 1.9	3.3 ± 2.0	0.865
$\hat{W}_{\text{el}}/(\text{MJ m}^{-3})$	0.024 ± 0.022	0.016 ± 0.017	0.003

Table 5.4: Material properties determined with the rheological model (top) and apparent mechanical properties determined with curve fitting on the envelope curve (bottom) of transversal and longitudinal trabeculae. Mean values are indicated ± standard deviation, σ_y and σ_u are corrected for the applied pre-load. Samples were pooled from osteoporotic and control donors. Significant p-values ($p < 0.05$) are highlighted **bold**.

7, loading and unloading). Ultimate strain ($r_s = -0.33$, $p < 0.001$, Figure 5.8-C) and post yield work ($r_s = -0.29$, $p < 0.001$, see Figure 5.8-B) were significantly negatively correlated with TMD, based on pooled data.

Parameter	Fracture			T-score				
	CTRL	FRAC	p-value	> -1.0	-1.0 > T	> -2.5	< -2.5	K.W.
Fr-zo	951 ± 74	954 ± 73	0.172	953 ± 75	956 ± 168		950 ± 77	0.172
Trab	958 ± 74	963 ± 73	0.066	960 ± 75	968 ± 167 ^{+,*}		955 ± 76	0.001

Table 5.5: TMD (in mg cm^{-3} HA) of osteoporotic and control trabeculae for fracture zone (Fr-zo) and whole trabecular struts (Trab). The left part indicates the low trauma classification (Fracture), the right part the T-score based one. Significant p-values ($p < 0.05$) are highlighted **bold**. K.W. denotes the p-value obtained with the Kruskal-Wallis test. ⁺ illustrates a significant ($p < 0.05$) difference to $T < -2.5$, ^{*} to $T > -1.0$.

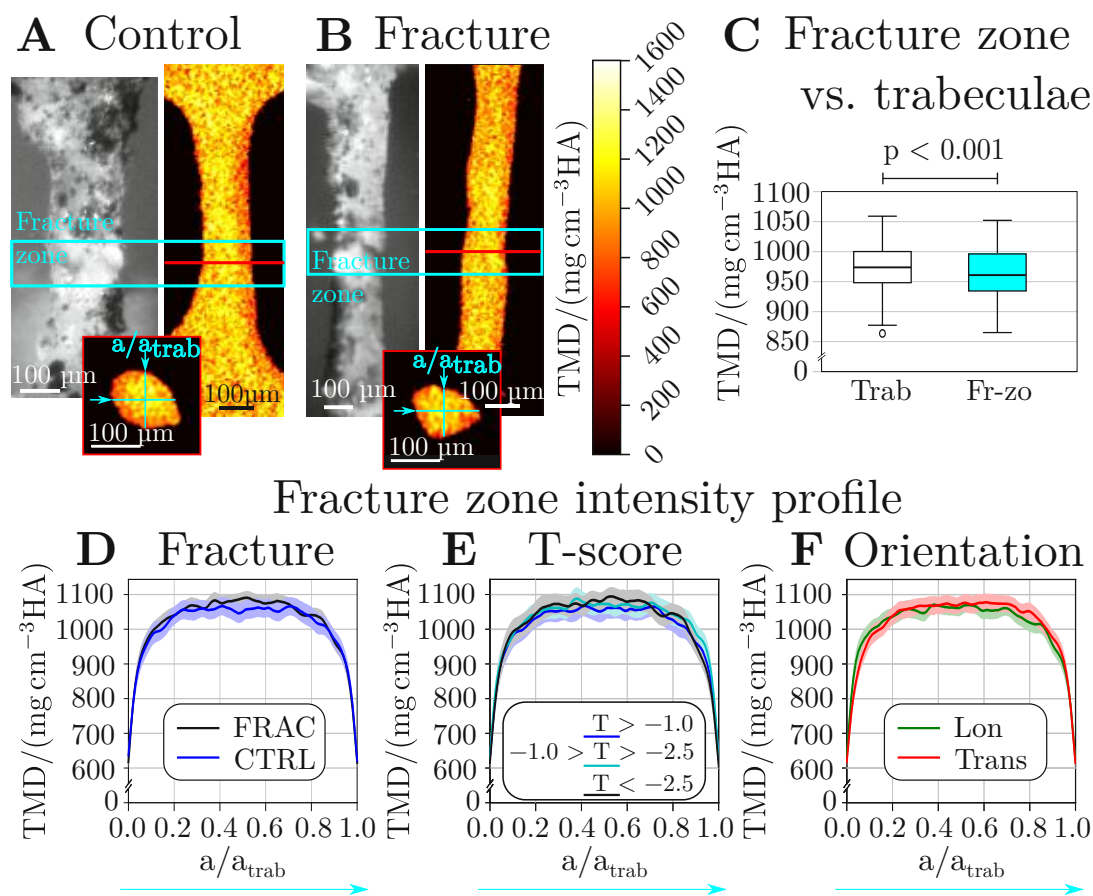


Figure 5.6: TMD distributions of individual trabeculae. **A & B**: Selected trabeculae, with optical tensile test recording at point of failure (left) and corresponding longitudinal TMD heat-plot (determined from μ CT-images, taken ahead of mechanical testing), at central plane (right). The fracture zone is highlighted in cyan. Small insets at the bottom show the cross sectional TMD heat-plot in the center of the fracture zone, as indicated in figures **A** & **B**. **C**: Boxplot of all pooled samples in the fracture zone (**Fr-zo**) and non-fractures areas of corresponding whole individual trabeculae (**Trab**; each value is the mean of each corresponding trabeculae and fracture zone, p -value determined with Wilcoxon signed rank test for pairwise samples). Illustration of used boxplot styles (symbols and outliers) is given in figure 2.9. Mean intensity profile for all samples based on fracture (**D**: Fracture (**FRAC**) and control (**blueCTRL**)), T-score (**E**) and trabecular orientation (**F**: Longitudinal (**Lon**) and transversal (**Trans**)). Mean in solid, 95% confidence interval shaded. The profile is set across the mass centroid axis (normalized), as illustrated in insets in subfigures **A** & **B**.

5. OSTEOPOROSIS AFFECTS MAINLY MORPHOMETRY NOT MATERIAL PROPERTIES IN FEMORAL HEAD

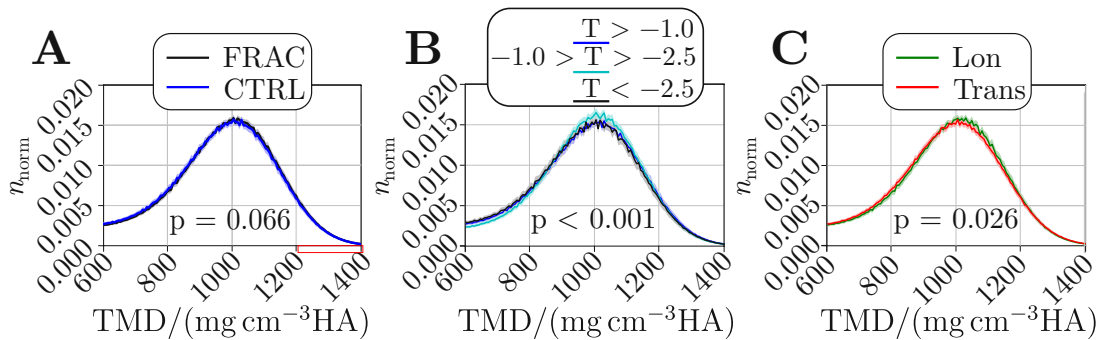


Figure 5.7: Normalized histograms of TMD distribution of all samples for classification based on fracture (**A**), T-score (**B**) and trabecular orientation (**C**). Mean solid, 95 % confidence interval shaded, of whole individual trabeculae (each value corresponds to one voxel obtained with μ CT). Actual p-values are stated in figures (see table 5.5 for details).

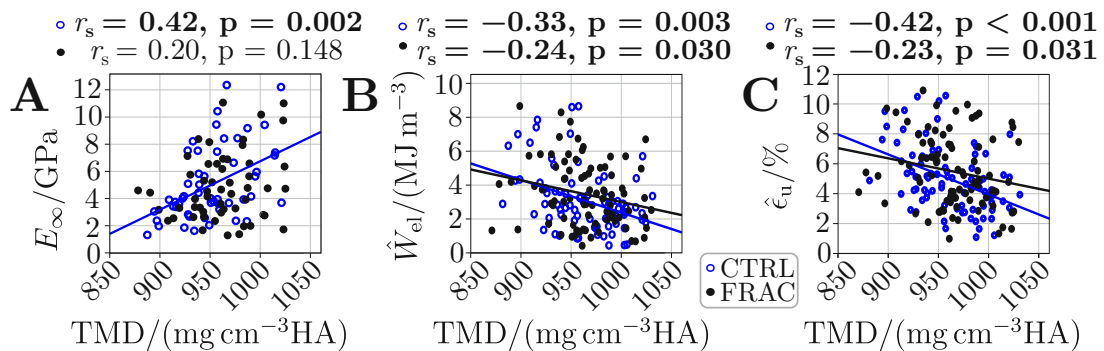


Figure 5.8: Correlation plots of mean TMD with apparent mechanical and material properties for fracture-based classification (control (**CTRL**) and fracture (**FRAC**)). **A**: Vs. long-term modulus (E_∞). **B**: Vs. apparent post-yield work (\hat{W}_{py}). **C**: Vs. apparent ultimate strain ($\hat{\epsilon}_u$). Spearman rank correlation coefficients (r_s) are given on top of each figure, together with corresponding p-values (significant values are labeled **bold**). Linear regression lines are provided for significant ($p < 0.05$) correlations.

5.4.3 μ CT-derived bone morphometry

The fracture based classification (see table 5.6-left and figure 5.9) indicated a significant difference with smaller values of BS and Tb.N for fracture samples. In contrast, BV/TV, Tb.Sp, Tb.Th and DA were not affected. Osteoporotic samples based on the T-score (see table 5.6, right and figure 5.10) showed significantly lower values of BV/TV, BS and Tb.N for osteoporotic and osteopenia samples, compared to $T > -1.0$. Further, Tb.Sp was significantly higher and DA and Tb.Th remained unaffected. Selected slices and spheres for bone morphometry determination are illustrated in figure 5.11.

Trabecular orientation did not result in a significant difference in bone morphometry, except DA (1.57 ± 0.25 vs. 1.64 ± 0.22 , transversal vs. longitudinal, $p = 0.046$). Bone morphometry showed no significant correlation with apparent mechanical but with material properties, namely for Tb.Sp vs. R ($r_s = 0.24$, $p = 0.034$), Tb.Sp vs. σ_u ($r_s = 0.24$, $p = 0.031$), and Tb.Th vs. σ_y ($r_s = 0.25$, $p = 0.011$) based on pooled data. Further, bone morphometry parameters indicated a significantly larger inter-donor variability, compared to intra-group variance (estimated with two-side ANOVA and Kruskal-Wallis-test, $p < 0.001$).

Parameter	Fracture			T-score			
	CTRL	FRAC	p-value	> -1.0	$-1.0 > T > -2.5$	< -2.5	K.W.
BS/mm ²	185.4 \pm 51.2	164.7 \pm 45.4	0.010	197.9 \pm 49.4	166.2 \pm 45.7 *	155.1 \pm 41.3 *	0.000
(BV/TV)%	16.8 \pm 7.0	15.5 \pm 6.7	0.186	18.4 \pm 7.0	16.0 \pm 6.4	13.5 \pm 6.2 *	0.000
Tb.N/mm ⁻¹	1.13 \pm 0.19	1.07 \pm 0.18	0.046	1.17 \pm 0.18	1.04 \pm 0.19*	1.07 \pm 0.18*	0.000
Tb.Sp/mm	0.72 \pm 0.15	0.77 \pm 0.16	0.128	0.69 \pm 0.14	0.78 \pm 0.16*	0.78 \pm 0.15*	0.001
Tb.Th/mm	0.17 \pm 0.03	0.17 \pm 0.03	0.466	0.17 \pm 0.03	0.17 \pm 0.03	0.17 \pm 0.04	0.311
DA	1.59 \pm 0.24	1.62 \pm 0.23	0.215	1.59 \pm 0.25	1.65 \pm 0.20	1.58 \pm 0.25	0.138

Table 5.6: μ CT-derived bone morphometry of osteoporotic and control trabeculae. The left part indicates the low trauma classification (Fracture), the right part the T-score based one. K.W. denotes the p-value obtained with the Kruskal-Wallis test. Significant p-values ($p < 0.05$) are highlighted **bold**. * illustrates a significant ($p < 0.05$) difference to $T > -1.0$.

5. OSTEOPOROSIS AFFECTS MAINLY MORPHOMETRY NOT MATERIAL PROPERTIES IN FEMORAL HEAD

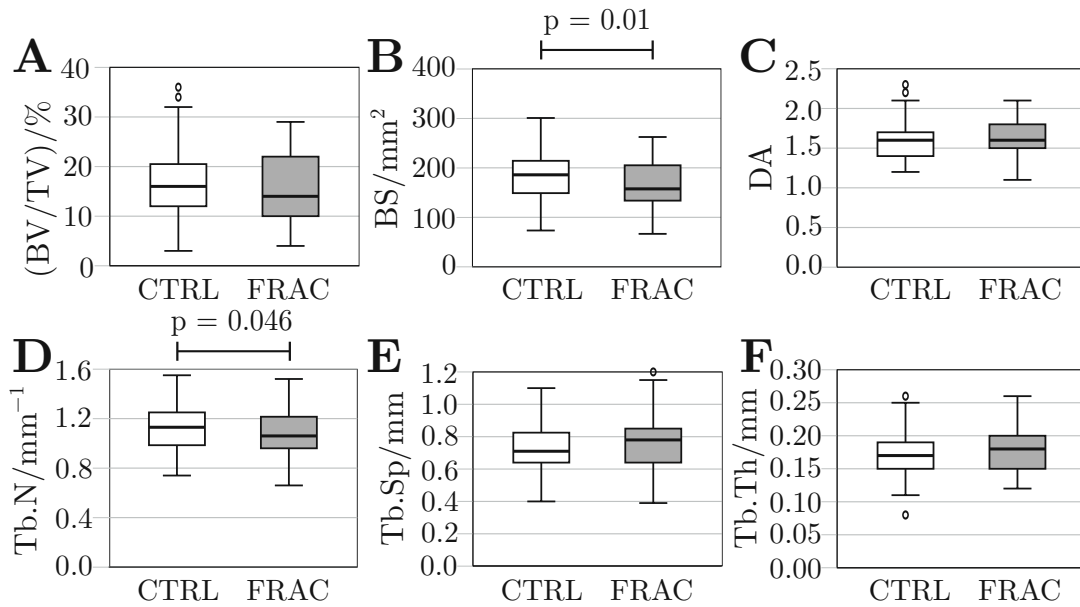


Figure 5.9: μ CT-derived bone morphometry, based on the fracture criterion (control (CTRL) and fracture (FRAC)). **A**: Bone volume to total volume (BV/TV). **B**: Bone surface (BS). **C**: Degree of anisotropy (DA). **D**: Trabecular number (Tb.N). **E**: Trabecular separation (Tb.Sp). **F**: Trabecular thickness (Tb.Th). Significant differences ($p < 0.05$) are marked with bars and actual p-values are provided on top. Illustration of used boxplot styles (symbols and outliers) is given in figure 2.9.

5.4.4 Age related changes

Age related changes of material and apparent mechanical properties and bone morphometry were determined both on pooled data (to check the influence of age together with osteoporosis) and on non-fractured samples (to determine the influence of aging independently of osteoporosis, see figure 5.12). For pooled data Tb.N ($r_s = -0.33$, $p < 0.001$), Tb.Sp ($r_s = 0.24$, $p = 0.002$), BV/TV ($r_s = -0.19$, $p = 0.012$), and BS ($r_s = -0.32$, $p < 0.001$) showed a significant dependency on age, whereas all other material and apparent mechanical properties (except exponential hardening coefficient p , $r_s = 0.22$, $p = 0.029$) did not correlate with age. Here, exponential hardening coefficient showed a moderate correlation ($r_s = 0.32$, $p = 0.023$) with age for fracture group, whereas control trabeculae were not correlated with age. In control trabeculae age was significantly correlated with Tb.N, Tb.Sp, and BV/TV. Interestingly, control trabeculae showed a moderate correlation with

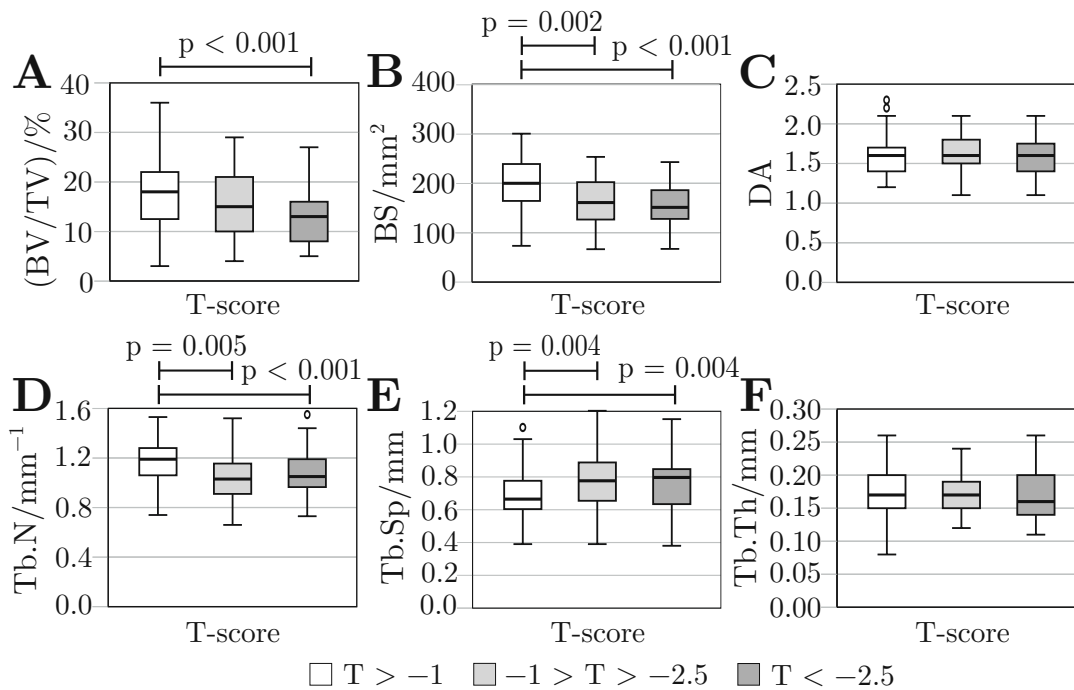


Figure 5.10: μ CT-derived bone morphometry, based on the T-score (legend at bottom). **A:** Bone volume to total volume (BV/TV). **B:** Bone surface (BS). **C:** Degree of anisotropy (DA). **D:** Trabecular number (Tb.N). **E:** Trabecular separation (Tb.Sp). **F:** Trabecular thickness (Tb.Th). Significant differences ($p < 0.05$) are marked with bars and actual p-values are provided on top. Illustration of used boxplot styles (symbols and outliers) is given in figure 2.9.

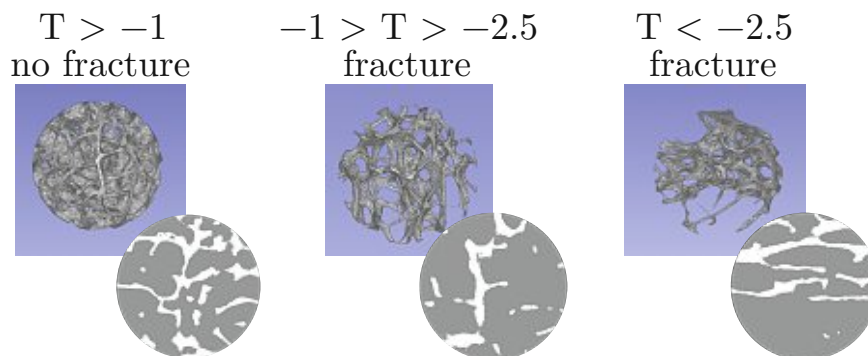


Figure 5.11: Representative cross-sectional slices of bone spheres, used for μ CT-derived bone morphometry. All spheres were oriented according to their three largest eigenvectors, to show the same orientation (all shown spheres were dissected from the trajectory, longitudinal group). **Left:** No fracture and $T > -1.0$. **Middle:** Fracture and $-1.0 > T > -2.5$. **Right:** Fracture and $T < -2.5$.

5. OSTEOPOROSIS AFFECTS MAINLY MORPHOMETRY NOT MATERIAL PROPERTIES IN FEMORAL HEAD

ultimate stress ($r_s = 0.38$, $p = 0.011$). Donor age was not correlated with TMD for pooled data and both grouping classifications.

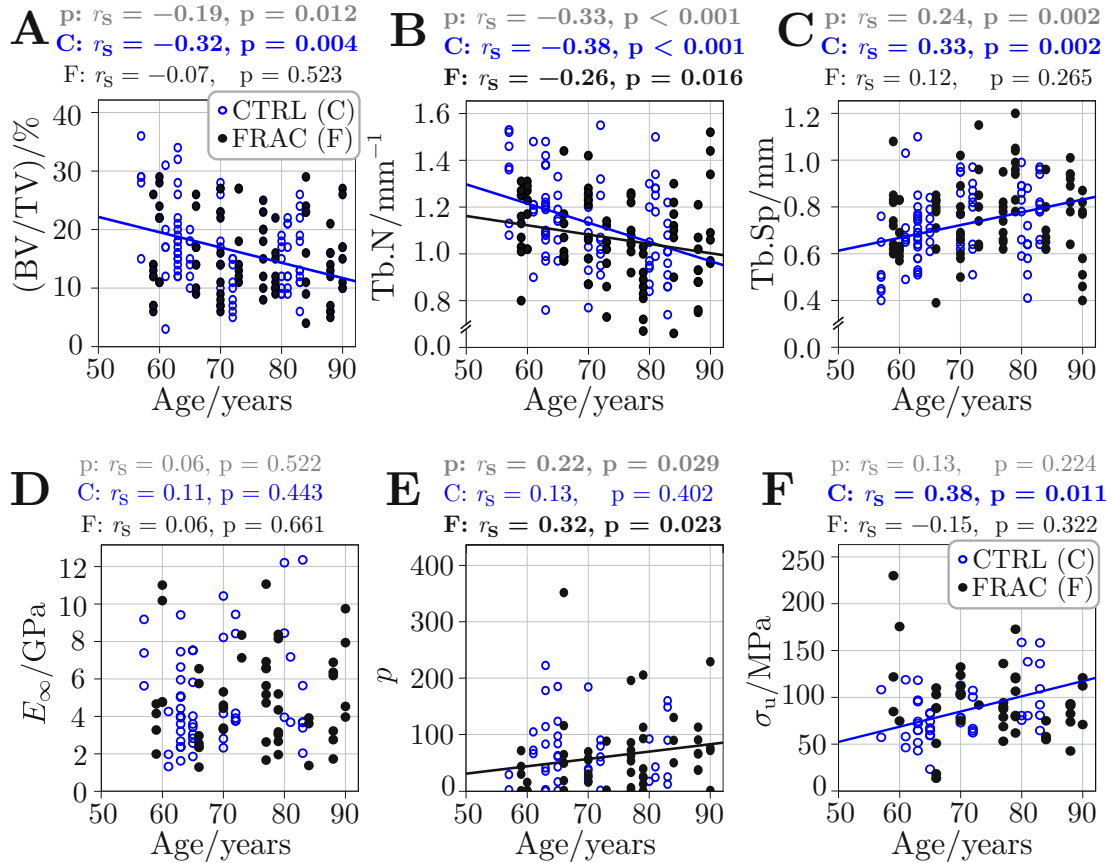


Figure 5.12: Correlation of μ CT-derived bone morphometry (top panels, A – C) and material properties (bottom panels, D – F) with age. p: pooled, **C**: Control, and **F**: Frac. **A**: Bone volume to total volume (BV/TV). **B**: Trabecular number (Tb.N). **C**: Trabecular separation (Tb.Sp). **D**: Long term modulus (E_∞). **E**: Hardening exponent (p). **F**: Ultimate stress (σ_u). Spearman rank correlation coefficients (r_s) are given on top of each panel, with actual p-values and highlighted **bold**, if significant. Linear regression lines are provided for significant correlations.

5.5 Discussion

This study demonstrates comprehensive apparent mechanical and material properties (elastic, viscous, and post yield) of individual osteoporotic and control trabeculae, loaded cyclically, in tension, in a wet, close to a physiologic environ-

ment. Inspired by work on micropillar compression on cortical bone [185]) the current study elucidates the significant difference between loading and unloading moduli for trabecular bone tissue. This difference can be explained with viscous effects and damage accumulation. Indeed, selection of different viscosities and holding periods in the rheological model could reproduce differences in the loading and unloading moduli (see figure 5.13).

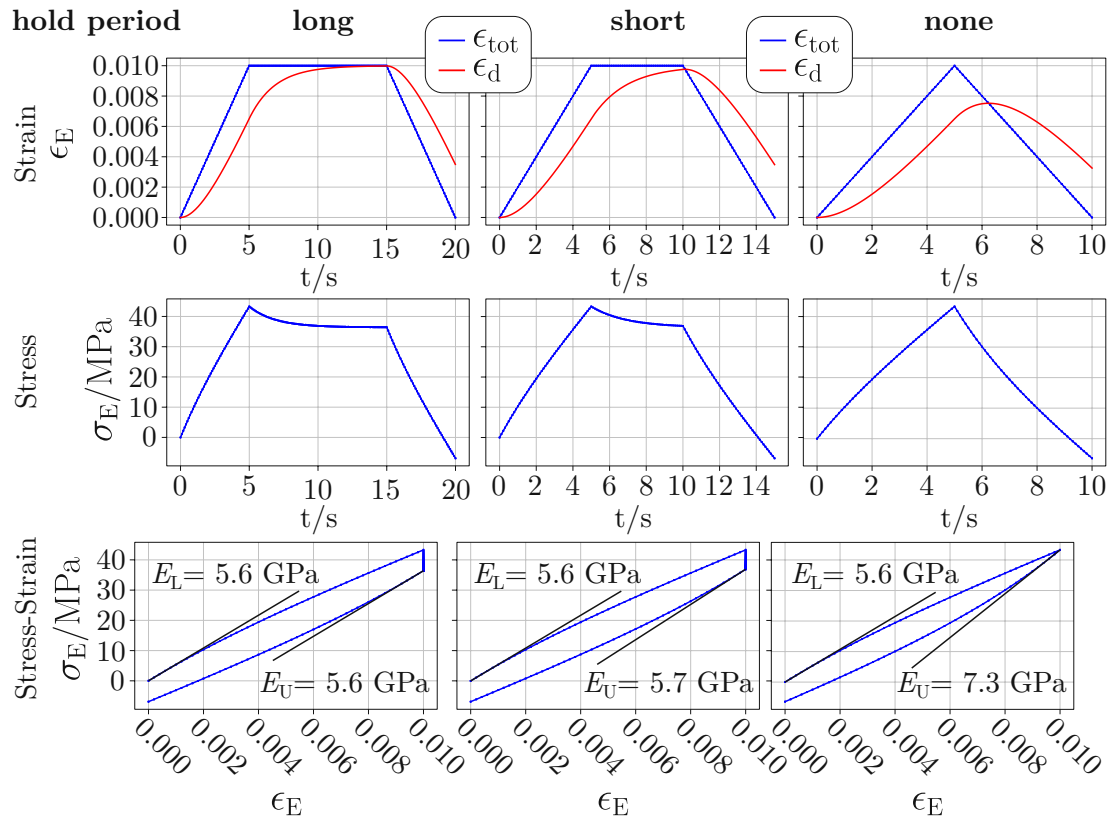


Figure 5.13: Effect of holding period on unloading modulus. **Left:** After long hold periods the damper has sufficient time for complete relaxation (damper strain (ϵ_d) approaches total strain (ϵ_{tot})). Hence, unloading modulus (E_U) equals loading modulus (E_L). **Middle:** After short hold periods the damper cannot relax completely and unloading modulus increases. **Right:** No hold period causes an even further increase of subsequent unloading modulus.

Further, it is speculated that damage initiation appears in the end phase of the second and third loading cycle, causing a drop of subsequent unloading modulus. According to the three-phase model of Fazzalari et al. [93] damage growth does not

5. OSTEOPOROSIS AFFECTS MAINLY MORPHOMETRY NOT MATERIAL PROPERTIES IN FEMORAL HEAD

cause a decrease of stiffness, which might explain why loading modulus (determined at the initial part of each loading cycle) stays almost constant. As only one to two damage sites are initiated per trabeculae [273] crack/damage growth might be dominant, instead of crack/damage initiation, explaining the constant unloading modulus in later cycles.

These findings highlight that human trabecular bone tissue is not linear-elastic by nature, as already observed in nanoindentation experiments [58, 189]. In fact, the present results shine some light on the discrepancy in material properties derived from nanoindentation and tests of individual trabeculae; nanoindentation looks at the unloading part whereas mechanical tests of individual trabeculae generally consider the loading part. Additionally, nanoindentation is most often performed on dry samples, which further increases the discrepancy. This puts forth the important question of how to deal with trabecular bone in computational models? For example, is a linear-elastic approach sensible enough? This will largely depend on what is being modeled, however it should be clear that such linear-elastic approaches can barely depict true mechanical behavior and do not deliver insight on actual material properties.

A main goal of the presented study was to perform a reliable characterization of osteoporotic trabeculae, in comparison to a healthy age-matched cohort. Trabeculae were taken from the longitudinal trajectories and from the transversal arcuate region, to discriminate potential differences in apparent mechanical and material properties. However, no significant difference in apparent mechanical or material properties was detected, except a higher apparent yield strain, apparent elastic work and a lower TMD ($p = 0.02$) in transversal trabeculae. Interestingly, Torres et al. mentioned that transversal oriented trabeculae serve as sacrificial elements and enhance fatigue life of cancellous bone [274] and this could be partly related to the increased elastic deformation of individual trabeculae, probably caused by decreased mineralization.

In total 179 trabeculae from 20 donors were successfully tested to ensure a good representation of actual apparent mechanical and material properties, as a large

biological variation [13, 14, 259], and technical difficulties in micro-mechanical testing [11] are known. Indeed, the CV was 0.54 and 0.46 for long-term and instantaneous tissue modulus, comparable to CV values of elastic moduli from previous studies on tensile tests of individual trabeculae ranging from 0.15 to 0.74 [18, 162, 179, 275, 276]. Reliability of the determined material properties, obtained with the rheological model, has already been demonstrated previously for healthy human trabeculae [224] (see section 3.3).

Taking this large variation into account, no significant differences in the material properties or mineralization were detected between osteoporotic trabeculae (in both classifications) compared to healthy control ones, even if age was considered as a covariate. However, apparent elastic modulus and TMD were significantly larger for donors with osteopenia ($-1.0 < T < -2.5$), whereas apparent yield strain and elastic work were significantly smaller, compared to osteoporotic donors ($T < -2.5$). For pooled data TMD was significantly negatively correlated with apparent yield strain ($r_s = -0.36$), elastic work ($r_s = -0.33$) and post-yield work ($r_s = -0.29$, $p < 0.001$) and positively with tensile modulus, long term modulus and Maxwell/dynamic modulus ($r_s = 0.30$ on average, $p = 0.002$). Apparently, increased TMD levels cause a stiffening of trabeculae, associated with a decrease of elastic work in patients with osteopenia. However, this effect is diminished in osteoporotic patients, since mechanical properties might depend on the duration of estrogen deficiency, as shown in ovariectomized sheep [116]. In the current study, average osteoporotic donor age was 74.6 years and prolonged estrogen deficiency might have diminished initial differences in elastic tissue properties of female donors. It has to be pointed out that trabeculae from donors with osteopenia had a significantly larger cross-sectional area compared to osteoporotic and control samples and only apparent (geometry dependent) mechanical properties (yield strain, elastic work and elastic modulus) were affected. In contrast, no actual material properties (determined with the rheological model) were significantly changed. A possible explanation might be that the apparent properties show a larger dependency on the geometry than the rheological model. The geometry dependency might further explain the large variation of previously reported values in literature and would favor the determination of material properties with models minimizing the influence

5. OSTEOPOROSIS AFFECTS MAINLY MORPHOMETRY NOT MATERIAL PROPERTIES IN FEMORAL HEAD

of sample geometry.

In literature, no consensus has been reached so far on the influence of age and disease on trabecular tissue properties [277]. On one hand no change of material properties of trabecular tissue of humans experiencing an osteoporotic fracture [211, 278], ovariectomized rats [267, 279] and post-menopausal women [208] was determined. On the other hand as well decreased mechanical properties in osteoporotic donors [119] and ovariectomized sheep [116, 280], as increased mechanical properties in ovariectomized rats [10, 120] were reported. Possible discrepancies might be related to differences between donors with osteopenia and osteoporosis, as observed in the present study at least for the elastic region. Further discrepancies are comparisons to not age-matched controls [119], reporting only apparent properties, testing on dried specimens, and different test procedures. The tensile test used in the present study enables a well-defined homogeneous stress state, in contrast to three-point bending, which has been shown to give different results than tensile tests for obtained material properties [171]. Further, small donor numbers might cause artificial differences between control and osteoporotic apparent mechanical and material properties, as variability between donors has already been reported as being much larger than inside a single donor [259], possible caused by differences in TMD and the remodeling state [11]. In the present study inter-donor variability was also significantly larger for ultimate stress ($p = 0.049$) and almost for long-term modulus ($p = 0.065$).

In contrast to previous studies [119, 122] no increased heterogeneity of mineralization of osteoporotic trabeculae could be detected. Only smaller TMD values at the trabecular surface, compared to the center, have been observed (as reported previously [122, 193]), without being different across groups. Previously, TMD was found to be increased [10, 120] or decreased [116–118, 281] in osteoporosis, but different measurement techniques were used (μ CT, qBEI, Fourier transform infrared microspectroscopy (FTIRM)), and different anatomical sites were investigated. Interestingly, mean TMD was significantly lower in the fracture zone in comparison to the non-fractured part of corresponding whole individual trabeculae ($p < 0.001$ for pairwise comparison for pooled data, see figure 5.6).

In general, TMD was always lower in the fracture zone, irrespective of grouping (see table 5.5). This finding agrees to Turunen et al. [282], where TMD was also significantly lower at crack locations, in comparison to surrounding trabecular bone. Hence, in a homogeneous stress state, these lower mineralized regions exhibit larger strains, because of the smaller local stiffness, and might thus be the initiation points of damage with elevated stress levels. It has to be mentioned that the found correlations of TMD with mechanical properties, although being similar to previously reported values for tissue elastic modulus [205, 275, 283, 284] and post-yield work [171], are only moderate ($r = 0.30$). This highlights that other factors, such as porosity (lacunae, microcracks) [119] and the collagen phase [88, 285, 286] play a relevant additional role in determination of apparent mechanical and material properties, which have not been assessed in the current study. The absence of changes of apparent mechanical and material properties and mineralization with aging is in accordance to previous findings about tissue elastic modulus [287], visco-elastic properties [288] and TMD [289]. However, also increased mineralization with increasing age was reported [116, 281, 290], possibly related to a slowed down bone turnover in the elderly [31]. As only rod-shaped trabeculae have been investigated in the present study, it might be that mineralization in plate-shaped trabeculae is more affected by aging, since mineralization is significantly different between these two trabecular shapes [291]. Only tissue strength was increased with increasing age in the present study for control trabeculae. In contrast to previous studies [116, 281, 290], no increased mineralization in the elderly has been detected, suggesting that other factors are additionally responsible for tissue stiffening, at least in the age range studied here. Interestingly, exponential hardening coefficient was increased with increasing age ($r_s = 0.32$, $p = 0.023$) for osteoporotic fracture donors only. Hence, aging may affect material properties differently between healthy and osteoporotic donors. Although all other apparent mechanical and material properties were independent of donor age, they might be dependent on tissue age [292, 293], which could be assessed in future studies, e.g. via qBEI.

In contrast, bone morphometry was significantly affected by osteoporosis and aging. Osteoporotic samples showed a significantly smaller BV/TV, BS and Tb.N, accompanied with a significantly larger Tb.Sp, without affecting Tb.Th. Accord-

5. OSTEOPOROSIS AFFECTS MAINLY MORPHOMETRY NOT MATERIAL PROPERTIES IN FEMORAL HEAD

ingly, a smaller BV/TV [119, 254, 294], Tb.N [119, 254, 294, 295], and a larger Tb.Sp [119, 254, 294, 295] has been reported in literature for osteoporotic trabecular bone. Tb.Th is reported controversial as being unaffected [119, 254] or larger [255]. Interestingly, only a few weak correlations were found ($r_s \leq 0.25$) of bone morphology parameters with material properties (for pooled data: Tb.Sp vs. R , Tb.Sp vs. σ_u and Tb.Th vs. σ_y), suggesting that bone structure only depends at most weakly on material properties. Although no significant differences of bone morphology parameters were observed between male and female donors, the large inter-donor variability might be partly caused by differences in the duration and intensity of metabolic changes in the female cohort. Prolonged estrogen deficiency has been reported to decrease BV/TV [296], Tb.N [297], Tb.Th [296], and increase Tb.Sp [296, 297] in the ovariectomized rat model. Additionally, BV/TV, BS, Tb.N and Tb.Sp indicated a significant dependency on age, as reported previously for BV/TV [8, 257, 294], Tb.Sp [8, 294], Tb.N [8, 257, 294], Tb.Th [256] and degree of anisotropy [256]. BV/TV between control and osteoporotic samples (fracture-grouping) was not significantly different, whereas T-score was. T-score was determined at the femoral neck and BV/TV was determined at the exact locations of trabecular dissections in the femoral head (see figure 5.1-C), which might explain this difference. Further, in the general linear model, with age as a covariate, BV/TV was also significantly lower in the fracture group. BV/TV was significantly correlated with age in the control group, but not for osteoporotic fractured samples. This data suggests that bone morphology changes differently between normal aging and osteoporosis. This finding is in agreement with Boskey et al. who stated that osteoporosis is associated with aging, but not a cause of aging [251].

5.5.1 Limitations

Micro-mechanical tests inherit several limitations, caused by the small, irregular sample geometry and difficulties in sample handling, as intensively reviewed in [12] and further mentioned in previous studies [119, 171, 184]. Thus, testing a large number of samples with an aspect ratio larger than three was performed to obtain a reasonable number of representative samples. Especially, misalignment of samples

causes shear stress [11] and obtained values might be erroneous. Sequentially, especial care was taken to align samples from two orthogonal planes under a z-stage equipped microscope. Further, heterogeneity in stresses might evolve from irregular shaped trabeculae and was minimized by selection of long cylindrical trabeculae.

Previously, compression loading of human femoral head plugs was found to result in compression and tensile strains [282]. Since the compression material properties could be potentially differently affected by osteoporosis, this issue should be investigated in future. Only rod shaped (likely “old”) trabeculae were tested. Plate-shaped (likely “younger” samples) might be affected differently, because of differences in the remodeling rate, similar to previously detected differences of TMD between longitudinal plate trabeculae and rod-shaped transversal samples [291].

Another limitation is the optical strain tracking, especially in the first cycle, as the signal to noise ratio is lower at low strains. Further, samples were tested in displacement control, because of technical limitations and a more efficient test procedure, whereas strain or stress control would enable a more uniform loading protocol. As trabecular length was not constant, the number of cycles until fracture differed, as small samples fractured already at three cycles (see section 3.3). Thus it is recommended to use a pseudo strain driven loading profile (the set displacement should be dependent on individual trabecular length) for future studies (see section 3.4.5). Addressing this issue would also increase the number of usable stress-strain curves for the rheological model (as samples would fracture at later cycles and as only samples that were tested for at least four cycles were included in this evaluation).

A further limitation was that potential changes of the collagen phase were not investigated in course of the present study. Previous studies highlighted the importance of collagen in determining bone mechanical properties [88, 285, 286] and this should also be evaluated in future studies for individual trabeculae. Determination of TMD with μ CT is known have a relatively good correlation with ash density, but also to underestimate true TMD values and to show a geometry dependency [298, 299]. μ CT-derived bone morphometry was determined at the exact points of trabecular

5. OSTEOPOROSIS AFFECTS MAINLY MORPHOMETRY NOT MATERIAL PROPERTIES IN FEMORAL HEAD

dissection, for correlation purposes with material and apparent mechanical properties. However, spheres were used to avoid misalignment of the ROI, whereas cubes are more common in bone morphometry. Still, comparable values for cubes of trabecular bone in the femoral head [300] were obtained and slightly smaller values for BV/TV and Tb.N are possibly caused by selection of regions with a low BV/TV, as they contain a larger amount of cylindrical trabeculae.

5.6 Conclusions

The observed weakening of the apparent mechanical behavior of trabecular bone in osteoporosis is likely largely caused by changes of the bone morphometry and to a lesser extent by weakening of the tissue itself, at least for the femoral head. Similarly, aging caused a deterioration of bone morphology, without affecting material properties, except an increase of tissue strength and exponential hardening coefficient. Since these two variables and BV/TV were differently affected between healthy and osteoporotic trabeculae, it is assumed that age-related changes are different in osteoporosis and healthy cohorts. The substantial variation of obtained material and apparent mechanical properties suggests that small differences between healthy and osteoporotic trabeculae could not be detected. Still, it is assumed that, if the effect of osteoporosis on the material properties of trabecular bone is indeed such small (compared to the large inter- and intra-donor variation), that it is not relevant for clinical discrimination. Detected differences in apparent yield strain and elastic work of donors with osteopenia might be related to differences at disease onset and the inherent geometrical dependency of apparent mechanical properties. The presented study is the first one that determined actual material (not only apparent) properties of healthy and osteoporotic trabeculae and highlighted that trabecular bone tissue is an elasto-visco-plastic material and cannot be described properly as being linear-elastic. This finding is important for computer simulations, like FE analysis or mechanistic approaches. Trabecular bone of the femoral head of healthy and osteoporotic patients can thus be modeled independently from age or osteoporosis, but as an elasto-visco-plastic material. Since only trabeculae from the femoral head were investigated in tensile mode here, further research is necessary focusing on different anatomical locations (e.g. spine and radius) and different

loading states (e.g. compression and bending) to verify these observations for cancellous bone in a more general manner.



Die approbierte gedruckte Originalversion dieser Dissertation ist an der TU Wien Bibliothek verfügbar.
The approved original version of this doctoral thesis is available in print at TU Wien Bibliothek.

Changes of material properties with anti-resorptive treatment

“The tendency of old age to the body, say the physiologists, is to form bone. It is as rare as it is pleasant to meet with an old man whose opinion is not ossified.”

Bob Wells

6.1 Related publications and declaration of contributions

Partial results of the presented work (text, tables and figures) have been *conditionally accepted* in “Bone”, entitled “Effects of anti-resorptive treatment on the material properties of individual canine trabeculae in cyclic tensile tests” and co authored by Andreas Grabos, Andreas G. Reisinger, David B. Burr, Dieter H. Pahr, Matthew R. Allen, and Philipp J. Thurner. This work is further based on the Diploma thesis of *Andreas Grabos*, entitled “Effect of anti-resorptive treatments on material properties and damage behavior of individual trabeculae of bone”, which was co-supervised and assisted by *Martin Frank*.

Author contributions: The first author and author of the current thesis, *Martin Frank*, contributed to the study design, assisted in establishing of the mechanical tests, performed the mechanical data processing, data interpretation, evaluation of the stress-strain behavior, TMD determination, co-supervised the work of *Andreas Grabos*, and wrote the manuscript. The joint first author, *Andreas Grabos*, performed the specimen preparation, the mechanical tests, the microdamage labeling, microscopy, and microdamage evaluation. *Andreas G. Reisinger* developed the rheological model and performed the data evaluation with this model. *Matthew R. Allen* supervised the microdamage labeling and provided the bone samples. *David B. Burr* contributed to the study design and supervision of the work. *Dieter H. Pahr* contributed to the development of the rheological model and supported the interpretation of the results. *Philipp J. Thurner* performed the study design, supervised the work of *Andreas Grabos* and *Martin Frank*, and supported the interpretation of the results.

6.2 Introduction

Medical treatment of osteoporosis is conventionally done with anti-resorptive drugs, such as bisphosphonates (BPs) or selective estrogen modulators (SERMs) [25] (see section 2.6 for further details). These drugs reduce bone resorption [301], increase the areal bone mineral density (aBMD) [148, 302] and thus reduce the probability of osteoporotic fractures [26]. However, an increase of aBMD alone cannot solely describe this phenomenon. For instance, it has been determined that only 4% of the observed vertebral fracture risk reduction in raloxifene treatment was associated with an increase of aBMD [27]. In animal models, the reduction of fracture risk has been linked to improved whole bone mechanics [265, 303], like increased elastic modulus and strength, both for BP and SERM treatment [53, 145, 304–307], whereas only raloxifene treatment increased bone toughness [305, 308]. As bone is a hierarchical structure (see section 2.1), its mechanical properties arise from bone architecture, bone mass and material properties [265]. The superior properties in BP treated bone have been linked to an improved or at least maintained trabecular architecture [309–311], accompanied with an increased bone mass [53, 304–306, 312].

However, effects on the material properties have been less conclusively reported [265] and seem to be differently affected by BP and SERM treatment [151]. Thus, it is essential to perform a thorough characterization of potential changes in the material properties after BP and SERM treatment. These findings will enhance our knowledge about the rationale of the observed superior whole bone mechanics. So far, most studies have focused on the elastic behavior of cortical bone specimens in nanoindentation [313–315], bone microindentation testing (BMT) [316] or in bending experiments [78, 253, 317]. Bone is a visco-elastic material [19, 318, 319] and especially characterization of physiologic relevant loading scenarios, such as fatigue and impact [21], would be favorable. Especially acquirement of mechanical properties of trabecular bone tissue is needed, since regions rich in trabecular bone are dominantly affected by falls [7].

Goal of the current study was to perform cyclic tensile tests of individual trabeculae close to failure and to use a previously established rheological model (see section 3.3) to determine elastic, viscous, yield, ultimate properties, and the loss tangent together with ultimate strain and toughness of individual trabeculae. Additionally, this test procedure allows induction of microdamage in a defined experimental set-up in-situ to compare potential differences in microdamage accumulation of alendronate, raloxifene and control specimens. These findings will shed more light on the potential changes of trabecular tissue/material properties during anti-resorptive treatment.

6.3 Material and methods

6.3.1 Sample selection

Thoracic (T8-T12) vertebrae were obtained from non-ovariectomized skeletally mature female beagle dogs (average age at beginning of treatment: (1.3 ± 0.2) years). These animals were treated orally for 12 months with clinically relevant doses of alendronate (ALN, $0.2 \text{ mg kg}^{-1} \text{ d}^{-1}$) or raloxifene (RAL, $0.5 \text{ mg kg}^{-1} \text{ d}^{-1}$) or saline (CON, $1.0 \text{ mL kg}^{-1} \text{ d}^{-1}$) in a previous study [305]. All experiments were approved by the Indiana University School of Medicine Institutional Animal Care

and Use Committee prior to initiating. Bone samples were wrapped in tissue soaked with HBSS (pH = 7.4) and stored at $-18\text{ }^{\circ}\text{C}$. In total, 24 trabeculae were harvested from CON animals, 28 specimens from RAL-treated animals and 30 trabeculae from ALN-treated animals.

6.3.2 Sample preparation and mechanical testing

Sample preparation of individual trabeculae was performed according to section 3.1.3 “Sample preparation”. It has to be noted that these dog trabeculae were much smaller than previous ones obtained from bulls (length $\sim 300\text{ }\mu\text{m}$, instead of (200 to 1000) μm) and thus hard to excise and handle, causing a large drop out rate during dissection. Further, the aspect ratio was in the range of 1 to 3, as almost all trabeculae showed a plate like, rectangular cross-section. Tensile testing and strain determination were done as reported in sections 3.1.3 “Tensile test” and 3.1.3 “Displacement and strain determination”.

Tensile tests were done displacement controlled at a displacement rate of 0.01 mm s^{-1} . A cyclic loading-hold-unloading protocol was chosen, as illustrated in figure 3.8-B. As mentioned in section 3.1.3 “Tensile test”, a pre-load of 0.08 N was applied to facilitate sample alignment. After verification with the video camera, the actual tensile test was started. Experiments were stopped as soon as trabeculae showed a clear, permanent whitening in the strut region that was still visible in the unloading phase (see figure 6.1 for more details). This behavior has been first described by Thurner et al. [260] and is further described in section 4.3.5 “Whitening”. However, whitening quantification was not performed further in the present study, as microdamage evaluation was done with basic fuchsin staining after mechanical testing (see section 6.3.4 “Microdamage labeling and evaluation”). In this way, permanent microdamage accumulation could be facilitated without necessarily fracturing the samples. The cyclic loading protocol was chosen to enable a thorough mechanical characterization of the bone tissue in one single experiment, as outlined in section 3.2.

6.3.3 Determination of apparent mechanical and material properties, and TMD

Determination of sample geometry was done with μ CT measurements, as described in section 3.1.3 “Micro computed tomography (μ CT) and image processing”. Hereby, the mid cross-sectional area (A_{mid}) was used to calculate true stress (σ_{T}), according to sections 3.1.3 “Force and stress determination”.

Evaluation of stress-strain diagrams was performed in two ways. First, the elasto-visco-plastic rheological model (see section 3.3) was used to determine the following material properties: Instantaneous modulus (E_0), long-term modulus (E_∞), yield stress (σ_y), hardening coefficient (p), hardening stress (R), ultimate stress (σ_u), viscosity (η), and loss tangent ($\tan(\delta)$). Additionally, the envelope curve of the experimental data was evaluated to determine the following apparent mechanical properties: Apparent elastic modulus (\hat{E}), apparent yield stress ($\hat{\sigma}_y$) and strain ($\hat{\epsilon}_y$), apparent hardening coefficient (\hat{p}), apparent hardening stress (\hat{R}), apparent maximum stress ($\hat{\sigma}_{\text{max}}$), apparent strain at maximum stress ($\hat{\epsilon}_{\text{max}}$), apparent elastic work (\hat{W}_{el}), and apparent post-yield work (\hat{W}_{py}) (see section 3.2.2). Hereby, the maximum stress and strain at maximum stress were chosen instead of ultimate stress and strain (the final point of the stopped experimental stress-strain curve), since the stop criterion caused some variations in the final point of the stress-strain data. Further, it was recognized that the stress-strain data showed a maximum stress with a monotonous decrease afterwards in most experiments. This indicates that, associated with the observed whitening effect, there was damage accumulation. Sequentially, the maximum stress is likely a better representation of the material’s strength than the ultimate stress.

It has to be noted that evaluations done with the rheological model are based on engineering stress and strain, because of assuming geometric linearity. In contrast, evaluations done with the envelope curve are based on true stress and strain, as ultimate strains were in the range of 10 %.

Tissue mineral density was determined as described in section 3.1.3 “Determi-

nation of Tissue Mineral Density (TMD)”.

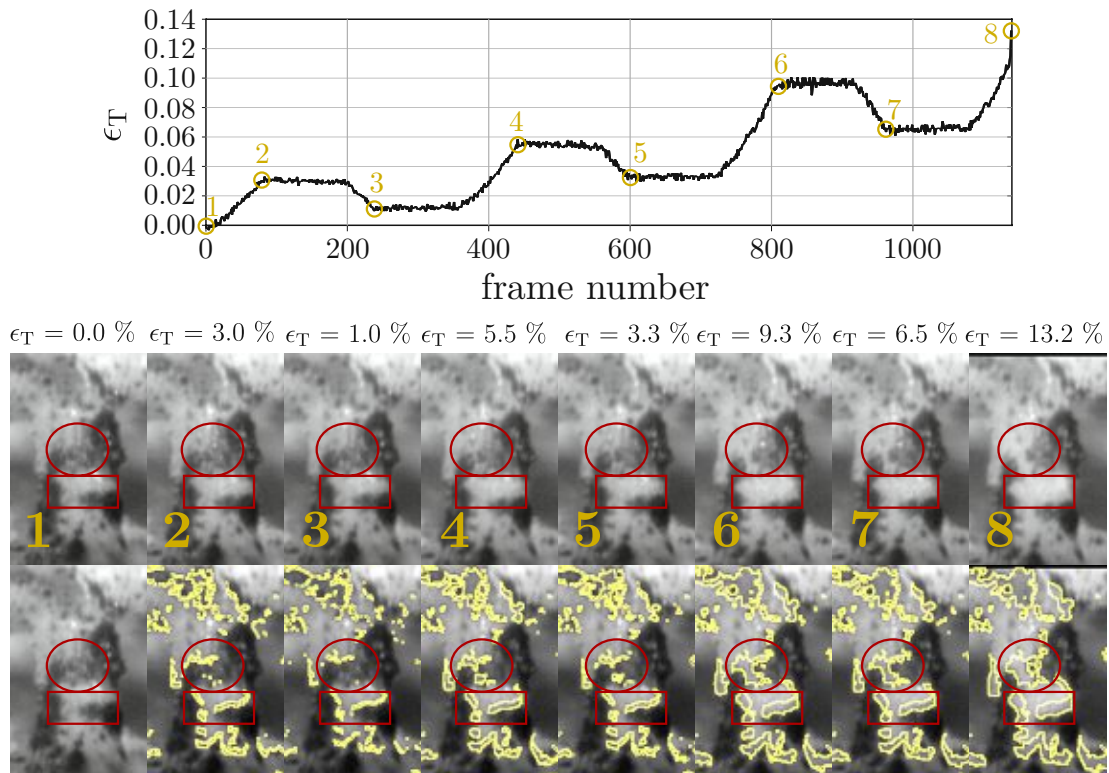


Figure 6.1: Determination of whitening as stop criterion shown for a selected sample. The true strain-frame curve is shown at the top with indicated points (dark yellow) at the start point (1) and at the end of each loading and unloading cycle. Below, the corresponding images of the trabecula are shown in original on the top row and with marked whitened regions (yellow) below. Additionally, the circle illustrates a region, where whitening appears at point 4, but disappears after unloading in point 5. However, in unloading point 7 the whitened area is still present and facilitated a stop in the subsequent loading phase at point 8. The rectangle indicates an area, which shows a similar behavior of increasing and decreasing whitened area with increasing loading/unloading cycles.

6.3.4 Microdamage labeling and evaluation

Microdamage labeling was done with en-bloc staining with basic fuchsin, as described previously [320]. In brief, specimens were put into 70% ethanol (EtOH) for at least 48 h after mechanical testing. Then, samples were stained with basic fuchsin (J.T. Baker, USA) in a graded series of increasing EtOH concentrations

(80 %, 95 %, and 100 % EtOH) under a 20-psi vacuum. The samples were stained for 1 h in each solution. Afterwards, samples were put twice into pure 100 % EtOH for 30 min under a 20-psi vacuum to remove residual fuchsin stain. Finally, samples were stored in 70 % EtOH at room temperature.

Stained samples were put onto glass microscopy slides and embedded in epoxy glue (UHU Endfest 300, UHU, Germany). As trabeculae were mounted on 2 mm thick epoxy circular end pieces (previously used for mechanical testing, see section 3.1.3 “Sample preparation”) the trabecular strut was located around 1 mm below the surface, in the center. Thus, a hand-held miller (Dremel 400, Dremel, Germany) was used to remove excessive epoxy until the trabecular strut was almost visible, verified under a stereo microscope (SZX10, Olympus Corporation, Japan). Next, samples were ground in two steps using sandpapers with grit numbers of 80 and 240 until the trabecula was reached. Then, sandpapers with grit numbers of 800, 1500, and 2400 were used each for 2 min to ensure an even, smooth surface for microscopy.

Microdamage visualization was done with a confocal laser scanning microscope (Zeiss Axiolab, Germany), operated by the Zeiss ZEN Black software for fluorescent materials. Unfortunately, the thickness of the trabeculae, including the epoxy underneath, was around 1 mm and caused, together with trapped air bubbles in the epoxy, a lot of interference of the light (especially scattering). As such, 3D confocal images were not usable and only the surface was accessible for 2D microdamage analysis. Images were taken with a 20× epi-fluorescent objective (EC Plan-Neouar 20x/0.50 M27) at an excitation wavelength of 555 nm and using an rhod-reflector (image pixel size: 1.25 μm).

Image analysis was done with ImageJ (1.45s, NIH, USA), as described in section 3.4.3 “Image data analysis”. In brief, the ROI was set to only contain the trabecular strut (corresponding to the boundaries of the strain tracking area). No linear cracks were visible at all, so only diffuse damage was present (except one cross-hatching area). Sequentially, each image was segmented using the triangle threshold method [238], as implemented in ImageJ. Then, the damage area (Dx.Ar)

was determined as the number of white pixels and put in relation to the total bone area (BA) to determine the damage density (Dx.Dn).

6.3.5 Statistical Analysis

Statistical analyses was done in SPSS (Version 26, IBM, USA). First, results were tested for normality with both, a Kolmogorov-Smirnov test combined with a Lilliefors Significance Correction and a Shapiro-Wilk test. Since most data was not normally distributed, a non-parametric Independent-Samples Kruskal-Wallis Test (K.W.) was used to check for significant differences between the different groups and pairwise comparisons were made calculating asymptotic significance (2-sided tests) with a significance level of $\alpha = 0.05$. Significance values were adjusted by the Bonferroni correction for multiple tests.

Determination of the material properties with the rheological model might result in non-physically meaningful values. Thus, an outlier removal strategy, based on the IQR test was performed on all three combined testing groups in two successive ways (as also described in chapter 5). First, the IQR-test was applied on the RMSE of the fitting curve to remove overall bad computational fits. Second, the IQR-test was also applied on each obtained material variables individually to remove non-physically meaningful values.

6.4 Results

In total 71 tests were performed that showed a reliable deformation behavior during video recording (27 ALN, 22 CON, 22 RAL). However, this number also includes seven (3 ALN, 4 CON) repeated experiments that were done because of sample sliding in the initial test. Here, the stress-strain diagrams of the second trial were checked for a reliable behavior and obtained mechanical properties remained in a reasonable range, minimizing the risk that samples were pre-damaged in the first trial. Sequentially, only the second trials were included and the first experiments were omitted. Visual inspection of obtained stress-strain diagrams resulted in a further drop out of ten tests (5 ALN, 2 CON, 3 RAL), mainly because of issues

in optical strain tracking. Sequentially, 54 out of 71 experiments (76.1%) could be used for determination of apparent mechanical properties (curve-fitting on the envelope curve). As the rheological model fitting should rely on similar experimental tests, only experiments that contained more than one loading and unloading cycle, were included as model input. This resulted in a further removal of five data sets (3 ALN, 2 RAL), leaving 49 stress-strain curves for model fitting. As already described in the previous section, overall bad model fittings were removed (eight in total), resulting in 41 remaining curves (57.7%) that were successfully evaluated with the rheological model (16 ALN, 13 CON, 12 RAL).

Exemplary stress-strain diagrams of experiments and superimposed ones obtained with the rheological model are illustrated in figure 6.2. The obtained material properties and apparent mechanical properties, obtained with the envelope curve, are reported in table 6.1 and displayed as boxplots in figure 6.3. A significant increase in the long-term (E_∞) and apparent elastic modulus (\hat{E}) was seen in the alendronate group, compared to control specimens (and a trend compared to raloxifene treated ones). Although not being significant, there was also the trend of increased hardening stress (R , K.W. $p = 0.07$) and ultimate stress (σ_u , K.W. $p = 0.129$) in the alendronate group. The statistically non-significant outcome is most likely attributed to two extreme outliers in the control group that could not be excluded because this would have caused multiple outlier testing. Moreover, in the classical evaluation the maximum apparent stress ($\hat{\sigma}_{max}$) showed also a trend of being increased in the alendronate ($p = 0.10$) and raloxifene ($p = 0.08$) group, compared to control. Strain at maximum stress ($\hat{\epsilon}_{max}$) and post-yield work (\hat{W}_{py}) were significantly larger in the raloxifene group, compared to control ($p = 0.03$ and 0.002 , respectively). Yield stress (σ_y and $\hat{\sigma}_y$), apparent yield strain ($\hat{\epsilon}_y$), apparent elastic work (\hat{W}_{el}), Maxwell/dynamic modulus (E_{mx}), viscosity (η), hardening coefficient (p), and loss tangent ($\tan(\delta)$) were not statistically different between the subgroups.

The mean TMD was increased in the alendronate treatment group, significantly ($p = 0.01$) compared to raloxifene and showed a trend towards increase in comparison to control ($p = 0.068$, see figure 6.4-A). TMD was significantly correlated with

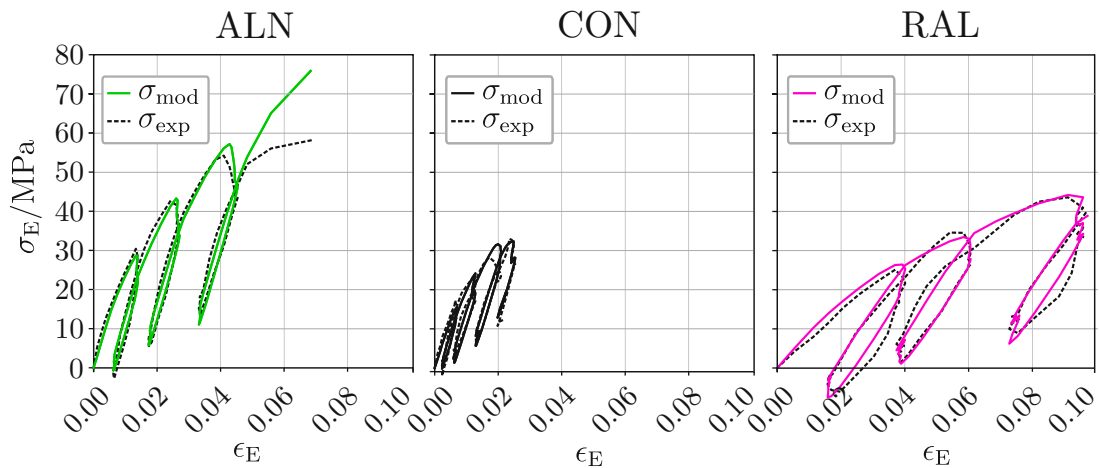


Figure 6.2: Selected stress-strain curves of alendronate (ALN), control (CON) and raloxifene (RAL) treated specimens. Experimentally obtained curves are shown with dashed lines (black), model fittings are colored in solid. In general, alendronate treatment resulted in an increased tissue elastic modulus and strength, whereas raloxifene treatment increased maximum strain and post-yield work.

long-term modulus (E_∞ , $r_s = 0.59$, $p = 0.045$) only for raloxifene treated trabeculae, but not for control or alendronate treated ones. In contrast, TMD was significantly correlated with Maxwell/dynamic modulus (E_{mx} , $r_s = 0.83$, $p = 0.001$) only for alendronate treated trabeculae, but not for control or raloxifene treated ones (see figure 6.4-B). Mean values \pm standard deviations of TMD are shown in the top part of table 6.2.

Figure 6.5 demonstrates selected basic fuchsin stained images to illustrate microdamage accumulation. No significant difference was observed in the damage area (Dx.Ar) or the damage density (Dx.Dn). However, there was a significant ($p = 0.022$) increased total bone area (BA) in the alendronate group, compared to raloxifene. Mean values \pm standard deviations of microdamage parameters are shown in the bottom part of table 6.2.

6.5 Discussion

Individual trabeculae showed an increased elastic modulus and maximum stress after one year treatment with alendronate, while yield stress, elastic and post-yield

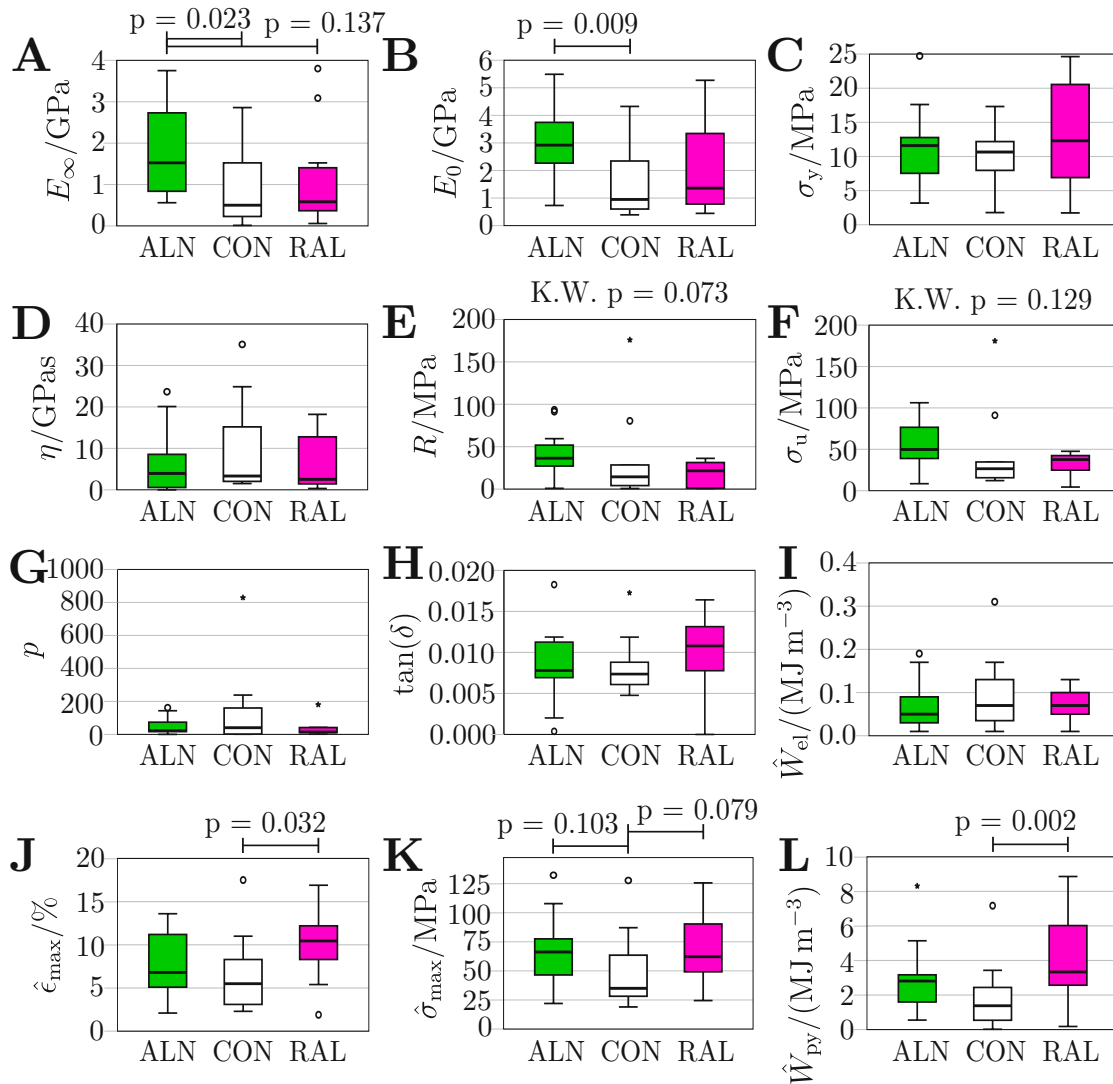


Figure 6.3: Boxplots of material properties determined with the rheological model and apparent mechanical properties, determined with curve fitting, of alendronate (ALN), control (CON), and raloxifene (RAL) treated specimens. **A:** Long-term tissue modulus (E_∞). **B:** Instantaneous tissue modulus (E_0). **C:** Yield stress (σ_y). **D:** Viscosity (η). **E:** Hardening stress (R). **F:** Ultimate stress (σ_u). **G:** Hardening coefficient (p). **H:** Loss tangent ($\tan(\delta)$). **I:** Elastic work (\hat{W}_{el}). **J:** Strain at maximum stress ($\hat{\epsilon}_{max}$). **K:** Maximum stress ($\hat{\sigma}_{max}$). **L:** Post-yield work (\hat{W}_{py}). Significant ($p < 0.05$) and close to significant ($p \sim 0.1$) differences are marked with bars and displayed with actual p-values. Further, close to significant ($p \sim 0.1$) differences for the Kruskal-Wallis test are shown on top of the boxplots as K.W.. Illustration of used boxplot styles (symbols and outliers) is given in figure 2.9.

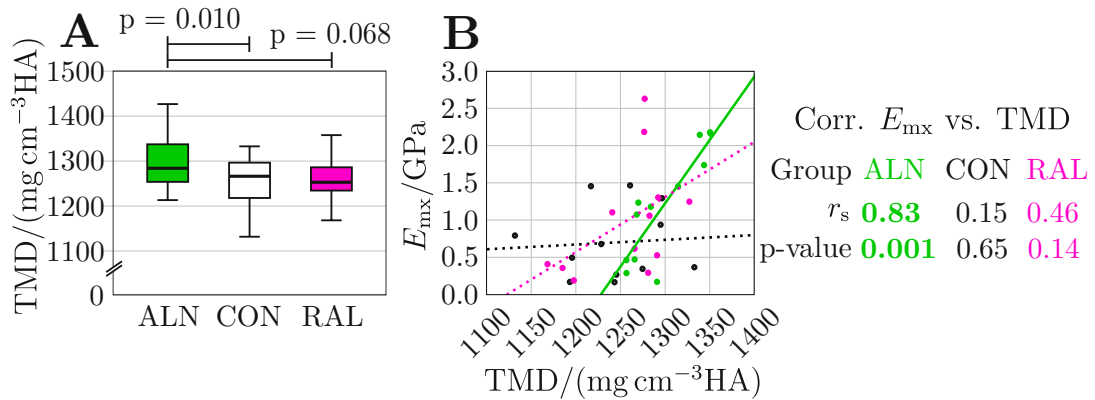


Figure 6.4: Tissue mineral density and its correlation with dynamic modulus of alendronate (ALN), control (CON), and raloxifene (RAL) treated specimens. **A**: Boxplot of mean TMD. **B**: Correlation of TMD with dynamic modulus (E_{mx}). Trend lines of significant correlations are shown solid, non-significant ones dashed. Spearman rank correlation coefficients (r_s) are shown with corresponding p-values on the right for all subgroups. Illustration of used boxplot styles (symbols and outliers) is given in figure 2.9.

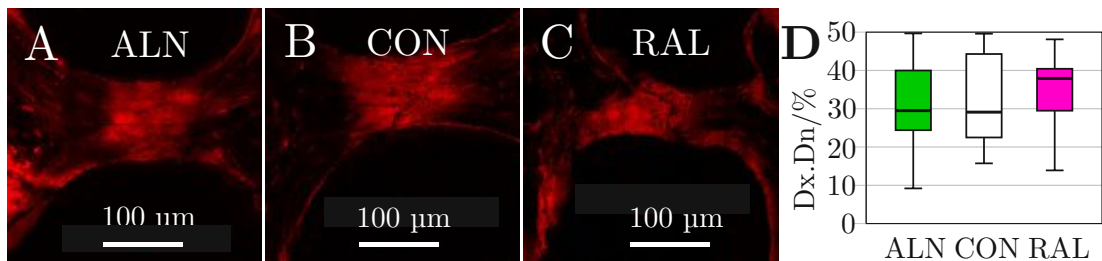


Figure 6.5: Selected microscopy images stained with basic fuchsin for microdamage and boxplot of damage density of alendronate (ALN), control (CON), and raloxifene (RAL) treated specimens. **A**, **B** and **C**: Basic fuchsin stained trabeculae, indicating diffuse damage through the trabecular strut, but most densely in the central region. Trabeculae already show black large cracks in the center, demonstrating that samples were close to fracture. **D**: Damage density (Dx.Dn in %). Illustration of used boxplot styles (symbols and outliers) is given in figure 2.9.

Parameter	ALN		CON		RAL		K.W.	A-C	A-R	C-R	
E_{∞}/GPa	1.8	± 1.1	^a	0.8	± 0.9	1.1	± 1.2	0.018	0.023	0.137	1.000
$E_{\text{max}}/\text{GPa}$	1.2	± 0.7		0.7	± 0.5	1.0	± 0.8	0.171			
E_0/GPa	2.9	± 1.3	^a	1.4	± 1.2	2.1	± 1.7	0.011	0.009	0.270	0.650
σ_y/MPa	11	± 5		10	± 5	13	± 8	0.627			
p	48	± 51		128	± 236	37	± 56	0.781			
R/MPa	41	± 28		35	± 55	20	± 15	0.073			
σ_u/MPa	55	± 31		45	± 53	32	± 14	0.129			
$\eta/\text{GPa}\cdot\text{s}$	6.6	± 7.5		9.3	± 11.2	6.1	± 6.6	0.645			
$\tan(\delta)$	0.009	± 0.005		0.008	± 0.003	0.009	± 0.003	0.467			
\hat{E}/GPa	2.4	± 1.2	^a	1.2	± 0.8	1.6	± 1.3	0.010	0.012	0.089	1.000
$\hat{\epsilon}_y/\%$	7	± 8		17	± 7	16	± 8	0.805			
$\hat{\sigma}_y/\text{GPa}$	0.9	± 0.6		1.6	± 1.4	1.5	± 1.1	0.194			
$\hat{\epsilon}_{\text{max}}/\%$	7.7	± 3.7		6.6	± 4.2	10.3	± 4.0	^a 0.032	1.000	0.246	0.032
$\hat{\epsilon}_u/\%$	8.4	± 3.7		8.5	± 5.5	11.5	± 4.7	0.083			
$\hat{\sigma}_{\text{max}}/\text{MPa}$	67	± 28		48	± 32	70	± 30	0.049	0.103	1.000	0.079
$\hat{\sigma}_u/\text{MPa}$	63	± 32	^a	37	± 28	64	± 31	0.007	0.024	1.000	0.014
$\hat{W}_{\text{el}}/(\text{MJ m}^{-3})$	0.07	± 0.05		0.10	± 0.09	0.07	± 0.04	0.776			
$\hat{W}_{\text{py}}/(\text{MJ m}^{-3})$	2.9	± 1.8		1.8	± 1.8	4.4	± 2.7	^a 0.003	0.171	0.411	0.002

Table 6.1: Material properties determined with the rheological model (top) and apparent mechanical properties determined with curve fitting on the envelope curve (bottom) of alendronate (A, ALN), control (C, CON), and raloxifene (R, RAL) treated specimens. Mean values are indicated \pm standard deviation, σ_y and σ_u are corrected for the applied pre-load. K.W. denotes the p-value obtained with the Kruskal-Wallis test. If K.W. shows a p-value < 0.05 then the actual p-values for group wise comparisons are shown on the right (corrected for multiple testing). ^a illustrates a significant ($p < 0.05$) difference to CON.

Parameter	ALN		CON		RAL		K.W.	A-C	A-R	C-R	
$TMD/(\text{mg cm}^{-3} \text{ HA})$	1294	± 53	^c	1260	± 47	1256	± 41	0.008	0.068	0.010	1.000
BA/ μm^2	36 526	$\pm 12 874$	^c	31 273	$\pm 10 601$	26 863	$\pm 11 801$	0.028	0.653	0.022	0.711
Dx.Ar/ μm^2	11 368	± 5682		9827	± 4773	9190	± 4452	0.394			
Dx.Dn/ $\%$	32	± 11		33	± 12	35	± 8	0.491			

Table 6.2: Mean TMD obtained with μCT and variables obtained with microdamage assessment (bone area (BA), damage area (Dx.Ar), and damage density (Dx.Dn)) for alendronate (A, ALN), control (C, CTRL), and raloxifene (R, RAL) treated specimens. Mean values are indicated \pm standard deviation. K.W. denotes the p-value obtained with the Kruskal-Wallis test. If K.W. shows a p-value < 0.05 then the actual p-values for group wise comparisons are shown on the right (corrected for multiple testing). ^c illustrates a significant ($p < 0.05$) difference to RAL.

work, viscosity, and loss tangent were not affected. In contrast, raloxifene treatment

resulted in a significant increase of post-yield work and strain at maximum stress, while elastic modulus, yield stress, elastic work, viscosity, and loss tangent were not affected.

6.5.1 Alendronate treatment increases elastic tissue modulus and strength

Apparent elastic modulus (\hat{E}) was increased significantly ($p = 0.012$) in alendronate treated samples, compared to control. This increase is potentially related to an increase in long-term modulus (E_∞), dynamic modulus (E_{mx}) or viscosity (η). The rheological model allowed to discriminate those effects, indicating that long-term modulus (E_∞) was significantly increased ($p = 0.023$), whereas dynamic modulus (E_{mx}) remained non significantly increased (K.W. $p = 0.171$). Instantaneous modulus is calculated as: $E_0 = E_\infty + E_{mx}$, and gives the resistance to an instant deformation. This property was also significantly increased in alendronate treated samples ($p = 0.009$), while viscosity was not significantly affected.

This finding is in agreement with the model predictions of Siegmund et al. [151] and an observed increase in indentation modulus of human iliac crest bone with increasing BP treatment duration [315]. On the contrary, the majority of previous studies found no significant change in tissue modulus, neither in bending [28, 313, 317, 321] nor in nanoindentation experiments [313, 314]. In one study, indentation modulus was even lower in alendronate treated women with osteoporosis [322]. However, indentation and bending experiments cause undefined loading modes, mainly a mixture of compression, tension, and partly shear. Tensile experiments allow a more defined, homogeneous stress state, depending on the sample geometry and alignment. Moreover, Carretta et al. have already shown that obtained material properties of individual trabeculae were significantly different between three-point bending and tensile tests [171]. The increased tissue elastic modulus and strength could be potentially related to an increase in TMD [323, 324], but also to an increased amount of cross-links in the collagen matrix [77, 325].

Indeed, TMD was almost significantly increased (K.W. $p = 0.07$) with alendronate

treatment, in accordance to previous studies [28, 304, 305, 326]. Thus, it appeared likely that the increase in TMD is related to the increase in elastic modulus, as shown previously [284, 327]. Surprisingly, there was no significant correlation between TMD and long-term or instantaneous modulus, but only with dynamic modulus (E_{mx} , $r_s = 0.83$, $p = 0.001$). This rather high correlation of TMD and dynamic modulus could only be determined because of the cyclic tensile tests, combined with the evaluation of the rheological model. Sequentially, only the elastic part that is activated with increasing strain-rates could be significantly correlated to tissue mineralization. As BP treatment increased the amount of non-enzymatic cross-links in the same beagle dog model [34] it is very likely that this effect also increased tissue strength and elastic modulus [77].

Stress at failure (σ_u) and maximum stress ($\hat{\sigma}_{\text{max}}$) showed a non-significant increase (K.W. $p = 0.129$ and 0.103) with alendronate treatment. Also bone tissue strength has been shown to be dependent on tissue mineralization [328]. However, all previous studies reported no significant change of tissue strength in bending experiments [28, 80, 313, 317, 321]. Similarly, indentation hardness was either decreased [322, 329], unaffected [313] or increased [314] with BP treatment. Hardness is a quantity that is effected by several different material properties, making it challenging to gain material properties [330]. At first sight, the found significant increased tissue elastic modulus and trend of increased strength contradicts most of the previous studies. Apparently, the potentially increased material behavior was counterbalance in those previous studies by alterations in the tissue, like accumulation of microdamage [265, 312]. As tissue strength is usually determined in bending experiments on mm sized cortical bone specimens, it is very likely that microdamage is present *in vivo* in those samples. In contrast, in the present study individual trabeculae were used for tissue testing (size $\sim (100 \text{ to } 300) \mu\text{m}$). As individual trabeculae that contain microcracks are very fragile, in comparison to undamaged samples, it is very likely that only intact, undamaged samples were tested here. Pre-damaged specimens would have been very likely destroyed during the dissection, embedding or unmounting procedures. Thus, it is assumed that the material/tissue indeed shows an increased elastic modulus and strength after BP treatment, but this effect is counterbalanced at larger scales because of present

microdamage.

In whole bone mechanics BP treatment resulted in a decrease of toughness [53, 145, 306, 331], which was linked to an increased brittleness at the tissue level in the non-linear model of Siegmund et al. [151]. Toughness is the material's ability to absorb energy before fracturing and can be split into elastic work and post-yield work. In the present study, both, elastic (\hat{W}_{el}) and post-yield work (\hat{W}_{py}), were not effected by alendronate treatment. This finding is in accordance to literature, where no change of elastic work and only a trend of decreased post-yield work was observed at the tissue scale [313, 321]. Similarly, Tang et al. found no significant change of post-yield work in alendronate or risedronate treatment at clinical doses, but only at thigh doses [80]. Decreased bone toughness has been linked to an accumulation of AGEs [332, 333]. As such, also the accumulation of AGEs has been reported to increase with BP treatment [34], but in some studies this effect was only significant in high dose regimes [35, 334]. Sequentially, the amount of AGEs in the current study could be only moderately increased, as only clinical doses of alendronate (0.2 mg kg^{-1}) were administered. As such, post-yield work could also stay unaffected. Similar results were obtained at the whole bone level, where toughness of BP treated bone was non significantly reduced at clinical doses [304, 305] and significantly reduced at high dose regimes [53, 145, 306].

In general, the trend of reduced toughness has been linked to an accumulation of microdamage [145, 304–306, 335]. In the present study it was aimed to induce microdamage in cyclic tensile tests with increasing amplitudes, similar as described previously [308]. However, neither a difference in accumulated damage density nor a difference in tensile modulus degradation (data not shown) was observed. Previously, stiffness loss was also reported to be unaffected by BP treatment [336], but the fatigue life was significantly reduced [336, 337]. As mentioned previously, it is feasible that toughness was unaffected by alendronate treatment in the present study because of a lack of pre-existing microdamage.

6.5.2 Raloxifene treatment increases tissue toughness

Tissue toughness of raloxifene treatment was increased because of a significant increase in the post-yield work (\hat{W}_{py} , $p = 0.002$), compared to control, while elastic work (\hat{W}_{el}) was not affected. The increase in post-yield work was mainly related to a significant increase in strain at maximum stress ($\hat{\epsilon}_{max}$, $p = 0.032$), whereas maximum stress only showed a trend towards increased values ($\hat{\sigma}_{max}$, $p = 0.079$). In contrast, yield strain ($\hat{\epsilon}_y$) was not changed with raloxifene treatment. These findings are in accordance with literature, where an increased tissue toughness was related to a significantly increased post-yield displacement, while pre-yield displacement was not affected [308]. Interestingly, also *ex vivo* exposure of canine and human cortical bone beams to raloxifene resulted in an increased post-yield work without affecting elastic work [338]. The authors related the increased toughness to an increase in matrix bound water. In course of the present thesis it has also been shown that hydrated individual trabeculae have an approximately 2-fold increased post-yield work, compared to dehydrated samples (see section 4.4.1 “Stress strain behavior”). Further, Siegmund et al. also predicted an increase of post-yield work, associated with an increased ultimate strain and stress in a non-linear model [151]. Although not being significant significant, maximum stress also tended to be increased in the current study, as already mentioned above (K.W. $p = 0.079$). However, ultimate stress (σ_u), determined with the rheological model, was even non-significantly decreased. Previous studies also did not found a significant change in ultimate stress [308, 338]. In the present study neither instantaneous modulus (E_0), nor long-term modulus (E_∞) or dynamic modulus (E_{mx}) were affected by raloxifene treatment. In literature, tissue elastic modulus has been reported as being unaffected [338], non-significantly increased [308, 339], or predicted as being decreased [151]. Thus, our findings coincidence with previous studies in the assumption that elastic modulus is not relevantly affected by raloxifene treatment.

Induction of microdamage with cyclic tensile testing raveled neither a significant difference in accumulated microdamage nor in the stiffness loss (data not shown), as mentioned previously [308]. However, it would have been assumed that an increased toughness should also increase the amount of accumulated microdamage

(see section 4.4.3 “Larger toughness of hydrated bone is caused by increased damage accumulation”). On the other hand, in a previous study, the damage density was also found to be unchanged *in vivo* after one year treatment with raloxifene in dog vertebrae [305]. In that study, only crack length was significantly increased, which has been assumed to be caused by an increase of length of previously present microcracks. In the current study no linear microcracks at all were identified in individual trabeculae. Instead, only diffuse damage was present in the current study, which has been determined as the major damage form after tensile loading [90] and is in accordance to our findings in the current thesis (see section 3.4.4 “Results”). As mentioned in previous paragraphs, individual trabeculae are unlikely to contain pre-existing microcracks (in relation to mm sized trabecular bone tissue), which might explain that damage accumulation was not affected, although toughness was increased.

TMD was not changed in the present study with raloxifene treatment, as reported previously [305,338]. As a result, the observed beneficial material properties are likely to be the main reason of observed increased whole bone strength, independently of bone mineralization (tissue mineralization and bone volume), as already pointed out by Allen et al. [305].

6.5.3 Limitations

Although micro-mechanical experiments of bone tissue enhance our understanding of changes at the material level, they also inherit several limitations, mainly related to the small size of bone specimens. First, since trabeculae were rather small ($\sim 300\ \mu\text{m}$ in length) several samples were damaged during dissection and could not be tested. Thus, there is a bias of selected trabeculae, in comparison to the whole population. It can be questioned how representative individual trabeculae are for trabecular bone tissue. However, testing a large number of samples should overcome this limitation. Further, as all samples were treated in the same way it is very unlikely that this bias was different among groups. Nevertheless, it cannot be solely excluded that e.g. more brittle trabeculae were damaged in the alendronate group. Given that material properties were found to be improved this possibility

does not seem very likely. Present trabeculae showed a plate like, rectangular cross-section with an aspect ratio of 1 - 3, meaning that stress was possibly not sufficiently homogeneous in the strut region to capture potential differences between control and raloxifene treated samples. Further, there is a large biological variation of the geometry and structure of individual trabeculae. Although tensile tests enable a good material characterization, differences in the aspect ratio and length of trabeculae still show an influence on the material properties and explains the large intra-group deviations. Thus, obtained material and apparent mechanical properties still inherit a structural influence, that might also differ among groups. As such, larger trabeculae in the alendronate group might be more mineralized because of their size. However, even if the effect of increased TMD in BP treatment is attributed to an increased trabecular thickness, the tissue elastic modulus and strength would be still improved at the trabecular scale.

6.6 Conclusions

The observed superior bone mechanics during anti-resorptive treatment is, besides changes in bone architecture and mass, related to an alteration of the bone tissue itself. Hereby, alendronate treatment causes an increase of tissue elastic modulus and strength, associated with an increase of tissue mineralization. In contrast, raloxifene treatment causes an increase of tissue toughness, pre-dominantly in the post-yield region. These findings highlight the different effects of both drugs on bone mechanics and the benefit of material/tissue testing to reveal material changes in the bone-matrix itself.



Die approbierte gedruckte Originalversion dieser Dissertation ist an der TU Wien Bibliothek verfügbar.
The approved original version of this doctoral thesis is available in print at TU Wien Bibliothek.

Influence of non-enzymatic glycation on the material properties

“Bones tell me the story of a persons life - how old they were, what their gender was, their ancestral background.”

Kathy Reichs

7.1 Related works and declaration of contributions

This chapter is intended as a first study to estimate the potential effects of non-enzymatic glycation on the apparent mechanical and material properties of individual trabeculae. The presented results shall serve as a basis for further investigation (testing a larger number of trabeculae), as currently published data is limited and inconclusive. The presented data is based on the project works of Masoud Chehrehazi and Patrick Karner and was co-supervised and assisted by the author of the current thesis, Martin Frank.

Study contributions: *Martin Frank*, contributed to the study design, co-supervised the study, performed the mechanical data evaluation, and interpretation. *Masoud Chehrehrazi* performed the initial study, however, data presented in this chapter was acquired by *Patrick Karner*, who performed the specimen preparation, the glycation, the mechanical tests, and the data evaluation. *Orestis G. Andriotis* designed the study. *Andreas G. Reisinger* developed the rheological model and performed the data evaluation with that model. *Dieter H. Pahr* and *Philipp J. Thurner* supervised the work of Martin Frank, took part in the study design and supported the interpretation of the results.

7.2 Introduction

Collagen is one of the two major constituents of bone (see section 2.1) and is partly cross-linked by enzymatic or non-enzymatic glycation (NEG). Hereby, enzymatic crosslinks make bone tougher, whereas non-enzymatic crosslinks have been shown to decrease bone toughness [31]. NEG forms adducts, which might further form inter- and intra-molecular collagen bonds, known as advanced glycation end-products (AGEs, see section 2.2). Accumulation of AGEs occurs naturally in bone with aging [32, 285, 340, 341], diabetes [71, 342] and after bisphosphonate treatment [34]. This accumulation of AGEs was predominately found in cortical bone [32] and might be related to a higher turnover rate in trabecular bone [31]. In contrast, a larger accumulation of AGEs in trabecular bone than in cortical bone was reported *in vitro* [76] and elevated levels of NEG were found in trabecular bone *in vivo* [343]. These discrepancies have been reviewed previously [344] and have to be investigated further, as huge differences in the glycation levels have been reported across previous studies.

Accumulation of AGEs has been linked to a decrease of strength and toughness in cortical bone [285], while secant modulus was increased [345]. Accordingly, apparent post-yield fracture properties of cancellous bone [35] and of individual trabeculae [35, 36] were decreased after induction of NEG by *in vitro* glycation. On the other hand, biomechanical properties of cancellous bone were not changed in adults suffering from type 2 diabetes [346]. Hereby, assessment of the mechanical properties of trabecular bone tissue is crucial, as these regions are often affected by

falls [7] and the accumulation of AGEs was associated with increased fracture risk of bones [30].

As outlined previously (see section 2.7) a thorough mechanical characterization of individual trabeculae is essential for linking changes at the sub-tissue scale to whole bone mechanics. Previously, only four-point bending experiments were performed on individual glycated trabeculae [35], which only describe their mechanical behavior poorly because of an irregular sample geometry and thus, an insufficiently defined loading state (see section 2.7.5). Hernandez et al. tested individual trabeculae in tension [36], however, they only determined ultimate strain as a sole mechanical parameter. Aim of the current study was to perform a thorough mechanical characterization of individual glycated trabeculae in cyclic tensile mode, combined with a rheological model (see section 3.3). It was hypothesized that an accumulation of AGEs causes a decline of the post-yield mechanical properties of individual trabeculae.

7.3 Material and methods

7.3.1 Sample selection

Individual trabeculae were obtained from the second phalanx of a 16-month-old bull, provided by a local butcher (Fleischerei Hödl, Vienna, Austria). The bone was cleaned from soft tissue with scalpels and scissors and stored at $-20\text{ }^{\circ}\text{C}$ within 1 h after death of the bull. 15 individual trabeculae were selected and divided into glycation (R, 8 samples) and control group (C, 7 samples).

7.3.2 Sample preparation and mechanical testing

Sample preparation of individual trabeculae was performed as described in section 3.1.3 “Sample preparation”. Trabeculae were selected for dissection if they were long ($\sim 500\text{ }\mu\text{m}$) and slender (aspect ratio ≥ 3) and appeared translucent in the microscope. Determination of sample geometry was done with μCT measurements, as described in section 3.1.3 “Micro computed tomography (μCT) and image

processing”. Hereby, the mean cross-sectional area (A_{mean}) was used to calculate true stress (σ_T), according to section 3.1.3 “Force and stress determination”. Next, trabeculae were embedded in epoxy glue and put in glycation or control treatment solution, respectively (see section 7.3.4).

Tensile testing and strain determination were done according to sections 3.1.3 “Tensile test” and 3.1.3 “Displacement and strain determination”. A cyclic loading profile (see figure 3.8-A), with alternating load-hold-unload ramps, was applied at a displacement rate of 0.01 mm s^{-1} until sample failure (see section 3.2). Hereby, a pre-load of 0.08 N was applied to facilitate sample alignment (see section 3.1.3 “Tensile test”), which was verified with the video camera.

7.3.3 Determination of material and apparent mechanical properties

Analysis of stress-strain diagrams was performed in different ways: Evaluation of material properties with the rheological model (see section 3.3, evaluation with curve fitting on the envelope curve (see section 3.2.2), evaluation of the tensile modulus in each loading and unloading cycle (see section 3.2.1), and evaluation of the secant modulus, as described below.

First, the elasto-visco-plastic rheological model (see section 3.3) was used to determine the following material properties: Instantaneous modulus (E_0), Maxwell/dynamic modulus (E_{mx}), long-term modulus (E_∞), yield stress (σ_y), hardening coefficient (p), hardening stress (R), ultimate stress (σ_u), viscosity (η), and loss tangent ($\tan(\delta)$). Additionally, the envelope curve of the experimental data was evaluated to determine the following apparent mechanical properties: Apparent elastic modulus (\hat{E}), apparent yield stress ($\hat{\sigma}_y$) and strain ($\hat{\epsilon}_y$), apparent hardening coefficient (\hat{p}), apparent hardening stress (\hat{R}), apparent ultimate stress ($\hat{\sigma}_u$), apparent ultimate strain ($\hat{\epsilon}_u$), apparent elastic work (\hat{W}_{el}), and apparent post-yield work (\hat{W}_{py} ; see section 3.2.2).

It has to be noted that evaluations done with the rheological model are based on

engineering stress and strain, because of assuming geometrical linearity. In contrast, evaluations done with the envelope curve are based on true stress and strain, as ultimate strains were in the range of 10%. As third method, evaluation of the tensile modulus in every loading and unloading cycle was performed as described in section 3.2.1.

Additionally, evaluation of the secant modulus (\hat{k}_{final}) was performed, as described previously [35, 345], to perform a comparison to those variables:

$$\hat{k}_{\text{final}} = \frac{\hat{\sigma}_{\text{u}}}{\hat{\epsilon}_{\text{u}}} \quad (7.1)$$

7.3.4 Induction of NEG with ribose

Glycation of bone was done to induce NEG *in vitro*, whereby one week treatment causes an approximate aging of 20 to 30 years [35]. The goal was to mimic an aging of 60 to 90 years, so glycation was performed for three weeks. HBSS was used as a basis to prepare the glycation and control solution, as described previously [35] (see table 7.1). The control solution is the same as the glycation solution, but lacks ribose. All components were mixed together on a magnet stirrer at a temperature of 37.4 °C and the pH-value was adjusted to 7.4. Samples were put in petri dishes containing the treatment solutions (see figure 7.1) and placed in an incubator at a constant a temperature of 37.4 °C. pH-value and temperature were controlled daily and the ph-value was adjusted to stay in the range of 7.3 to 7.6. After chemical treatment, trabeculae were removed from the solution and washed three times with HBSS. Samples were stored at −20 °C until mechanical testing. The progress of glycation was controlled with 11 trabecular bone disks (square of $\sim 1 \text{ cm} \times 1 \text{ cm}$), whereby one disc was removed every two days for later determination of the amount of AGEs (see figure 7.1).

7.3.5 Statistical Analysis

Statistical analyses was done in SPSS (Version 23, IBM, USA). First, data was explored and checked for normality with a Kolmogorov-Smirnov test combined with a Lilliefors Significance Correction. Since most data was not normally distributed,

7. INFLUENCE OF NON-ENZYMATIC GLYCATION ON THE MATERIAL PROPERTIES

Component	$c/(\text{mol L}^{-1})$	$M/(\text{g mol}^{-1})$	$\rho/(\text{g L}^{-1})$
Ribose	0.600	150.13	90.078
HEPES	0.030	238.30	7.149
ϵ -amino-n-caproic acid	0.025	297.26	7.432
Benzamidine	0.005	120.15	0.601
N-ethylmaleimide	0.010	125.13	1.251

Table 7.1: Components of glycation and control treatment solution. c : molar concentration; M : molar mass; ρ : mass concentration.



Figure 7.1: Induction of NEG with ribose. Left: Control treatment. Right: Glycation treatment. Bottom: Removed bone disks for control of progress of glycation.

a non-parametric Independent-Samples Wilcoxon-Mann-Whitney-U was used to check for significant differences between the two groups calculating asymptotic significance (2-sided tests) with a significance level of $\alpha = 0.05$. Additionally, the effect size (d) was calculated according to Cohen [347], for estimation of the relevance of determined differences in the material and apparent mechanical properties:

$$d = \frac{|\bar{x}_1 - \bar{x}_2|}{\sqrt{(s_1^2 + s_2^2)/2}} \quad (7.2)$$

, whereby s_i^2 denotes the estimated variance and \bar{x}_i the mean value, respectively. $d \geq 0.5$ is considered as a medium effect, $d \geq 0.8$ as a large one.

As mentioned in section 5.3.6, a strict outlier identification was performed based on the IQR-test to remove non-physiological values obtained from the rheological model.

7.4 Results

15 trabeculae were successfully tested in cyclic tensile mode (7 control, 8 glycated). One control and one glycated trabecula were removed from analysis with the rheological model because of a bad model fitting (IQR-test, RMSE > 10 MPa). Further, determined values for R and σ_u (whereby $\sigma_u = \sigma_y + R$) were excluded, as 4 out of 8 values were non-physiological ($R > 1000$ MPa). Instead, apparent properties (\hat{R} and $\hat{\sigma}_u$) are reported in table 7.2. Reliability of the other obtained parameters was verified with a comparison to values from previous studies (see section 3.3 and chapters 5 and 6), combined with a reasonable RMSE ((1.7 to 5.3) MPa).

Glycation of individual trabeculae caused no significant change neither of the material nor of the apparent mechanical properties, except of the hardening exponent (p , $p = 0.02$) and a non significant trend towards higher Maxwell modulus (E_{mx} , $p = 0.13$; see table 7.2). However, it has to be noted that there was a large variation of obtained parameters (average coefficient of variation was 0.64 for control and 0.73 for glycated samples). A qualitative comparison of two selected stress-strain curves is shown in figure 7.2. Evaluation of the evolution of the tensile modulus with increasing cycle number (see section 3.2.1) showed that there is a non-significant difference between the loading and unloading tensile modulus (see figure 7.3-A & B). The unloading modulus decreased from cycle 1 to 4 in the control and glycation group. In contrast, the loading modulus stayed almost constant,

although a large variation was visible. There was no significant difference between the tensile modulus of glycated and control samples in any cycle.

Parameter	Control	Glycated	p-value	Cohen d
E_{∞}/GPa	3.0 \pm 1.7	2.7 \pm 1.8	0.94	0.15
E_{mx}/GPa	1.6 \pm 0.8	2.8 \pm 1.6	0.13	0.93
E_0/GPa	4.6 \pm 2.2	4.4 \pm 1.8	0.93	0.11
σ_y/MPa	10 \pm 11	16 \pm 12	0.63	0.46
p	139 \pm 113	18 \pm 29	0.02	1.46
$\eta/\text{GPa s}$	6.8 \pm 3.3	7.6 \pm 5.3	0.84	0.19
$\tan(\delta)$	0.014 \pm 0.003	0.017 \pm 0.009	0.69	0.46
\hat{E}/GPa	5.3 \pm 3.3	6.6 \pm 4.4	0.63	0.32
$\hat{\sigma}_u/\text{MPa}$	88 \pm 43	87 \pm 31	0.84	0.39
$\hat{\epsilon}_u/\%$	7.9 \pm 3.0	6.3 \pm 2.9	0.53	0.55
$\hat{W}_{\text{el}}/(\text{MJ m}^{-3})$	0.008 \pm 0.008	0.006 \pm 0.008	0.53	0.28
$\hat{W}_{\text{py}}/(\text{MJ m}^{-3})$	4.9 \pm 3.0	3.8 \pm 2.5	0.63	0.14
$\hat{k}_{\text{final}}/\text{GPa}$	1.2 \pm 0.6	1.8 \pm 1.2	0.30	0.88

Table 7.2: Material properties determined with the rheological model (top) and apparent mechanical properties determined with curve fitting on the envelope curve (bottom) of control and glycated trabeculae. Mean values are indicated \pm standard deviation, actual p-values and Cohen d are shown on the right). P-values < 0.05 and Cohen $d > 0.8$ are highlighted **bold**.

7.5 Discussion

Induction of NEG with ribose did not cause a significant change neither in the material nor in the apparent mechanical properties, except a significant decrease of the hardening exponent (p) and a trend of increased Maxwell/dynamic modulus (E_{mx}). Hereby, a decrease of p causes a more linear increase of post-yield stress, as illustrated in figure 7.2. An increase of E_{mx} means that elastic modulus is only increased during fast deformations, whereas quasi-static deformations stay unaffected. Accordingly, previous studies also reported no effect on the quasi-static elastic modulus [35, 285, 345, 346], but the dynamic modulus has not been investigated yet, to the authors knowledge. However, the CV was large for $E_{\text{mx}}(\sim 0.5)$ in the current study, as well as for most other material and apparent mechanical properties.

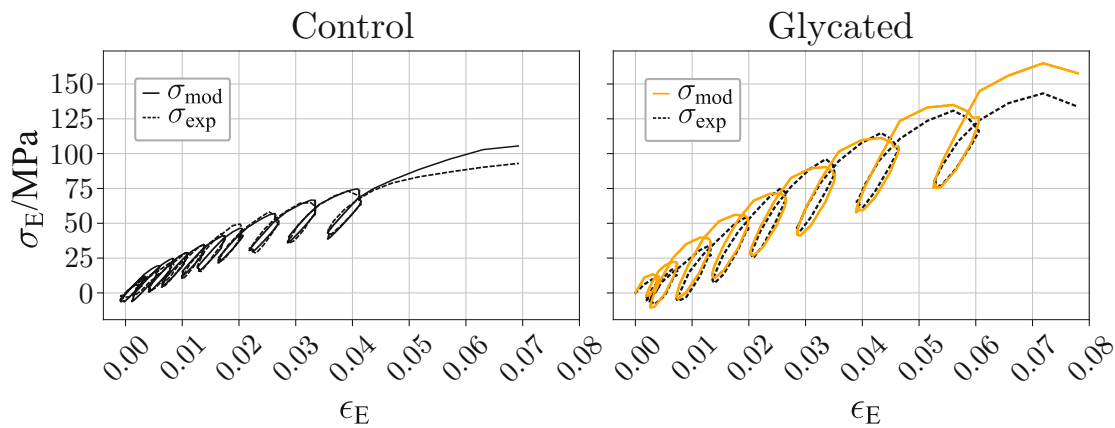


Figure 7.2: Selected stress-strain curves of control (left) and glycation (right) treated trabeculae. Control samples show a more curved post-yield hardening (hardening exponent (p) is larger), than glycated samples. It has to be noted that these are selected curves and that there is also a large intra-group variability of obtained material and apparent mechanical properties (see table 7.2).

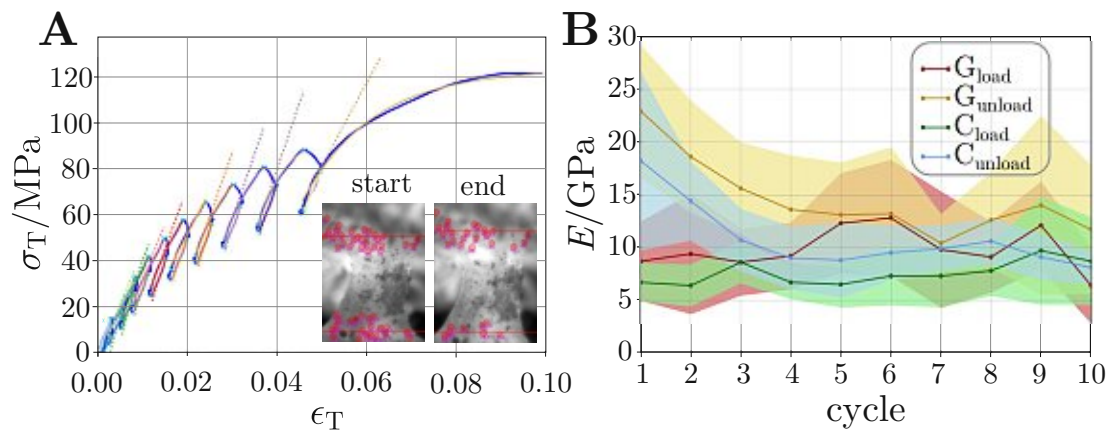


Figure 7.3: **A:** Selected cyclic stress-strain curve with fittings for tensile modulus in every loading and unloading cycle. **B:** Evolution of cyclic tensile modulus for control (C) and glycation (G) treated samples, with increasing number of tensile cycles. Lines indicate the mean values, shaded areas the 95 % confidence interval.

Interestingly, determination of Cohen d highlighted a large effect size for E_{mx} ($d = 0.93$) and p ($d = 1.46$). Hereby, these values indicate that the difference of the means is large, in comparison to their variance. Similarly, also final secant modulus (\hat{k}_{final}) was increased non-significantly ($p = 0.30$), but indicated a large effect size ($d = 0.88$). In accordance, secant modulus was significantly increased in glycated cortical bone [345], while it remained unaffected in four-point bending experiments of individual trabeculae [35]. An increased secant modulus is related to the fact that the point of failure is shifted towards lower ultimate strains (ϵ_u) and agrees with a decrease in the exponential hardening coefficient (p). Indeed, ϵ_u showed a trend of moderate correlation with p ($r_s = 0.50$, $p = 0.101$ for pooled data). Although secant modulus was almost significantly correlated with ϵ_u ($r_s = -0.48$, $p = 0.070$ for pooled data), no correlations were found for elastic work, post-yield work or total work to failure, questioning if the secant modulus is a representative parameter for describing material toughness. Interestingly, the decrease in ϵ_u was far from being significant ($p = 0.53$, $d = 0.55$) and thus, no relevant effect on the post-yield or total work was observed in the present study. In contrast, a decrease of post-yield work has been reported for cancellous bone cores [35] and cortical bone [345], previously. Similarly, in tensile tests of individual trabeculae an increased pentosidine concentration (a marker for AGEs) was weakly correlated with a decrease of ultimate strain [36].

Taken together, the presented data suggests that there might be indeed a relevant effect of glycation on some of the material and apparent mechanical properties. Since the effect of glycation might be small, in comparison to the large biological and methodological variation, a much larger number of trabeculae has to be tested in subsequent studies to enable a reliable determination of these potential changes. Further, the pentosidine concentration should be determined in the bone discs to assess the amount of AGEs, especially with increasing incubation time.

In summary, the current study demonstrated, that it is essential to continue the investigation of bone tissue glycation. Especially, a focus on the post-yield behavior and microdamage formation would be very interesting, as these properties have been shown to be mainly determined by the collagen phase [285, 286, 348].

Vashishth et al. demonstrated that an accumulation of AGEs causes a stiffening of the organic matrix and this might be one of the mechanisms of AGE-induced bone fragility [345]. Moreover, type 2 diabetes seems to have an effect on the biomechanical properties of bone [344,346], but effects on the trabecular tissue level remain unknown. In cortical bone, AGEs were accumulated with increasing age and were correlated with a decrease of strength and toughness [285]. The effects of aging on the mechanical properties of human individual trabeculae are demonstrated in section 5.4.4.

7.6 Conclusions

Accumulation of AGEs might have an influence on the dynamic and post-yield mechanical properties of individual trabeculae. However, this effect is likely to be small in comparison to sample variation and thus, requires a large amount of samples to be tested. Further, evaluation of the amount of AGEs is essential in future studies and has to be compared to human *in vivo* levels. In that way, it can be verified, if potential mechanical changes are also relevant in clinics, like in diabetic or aged patients.



Die approbierte gedruckte Originalversion dieser Dissertation ist an der TU Wien Bibliothek verfügbar.
The approved original version of this doctoral thesis is available in print at TU Wien Bibliothek.

Synthesis and outlook

The main goal of this thesis was to perform a thorough mechanical characterization of individual trabeculae in a wet, close to a physiologic environment and to determine the effect of aging, osteoporosis, treatment and glycation on the material properties. As such, the first part consisted of the development of a defined tensile test set-up, together with different data analysis approaches for determination of material and apparent mechanical properties of trabecular bone tissue (see chapter 3). In more detail, the apparent mechanical behavior of individual trabeculae was determined in monotonic (see section 3.1), cyclic (see section 3.2) and fatigue tensile tests (see section 3.4). Additionally, a previously developed rheological model (see section 3.3) was applied to determine the elastic, viscous, plastic, and failure properties of trabeculae in a single cyclic tensile experiment. In the second part, these developed and applied approaches were successfully used to determine the material properties of trabecular bone tissue in dependency on hydration state, osteoporosis, aging, anti-resorptive treatment and glycation. The main findings of the current thesis are:

- *Trabecular bone tissue should be characterized as an elasto-visco-plastic material.* A previously developed 2-layer rheological model was successfully applied to describe the full mechanical behavior with only four rheological elements (see section 3.3). This analysis procedure highlighted that trabecular bone

tissue is not linear-elastic at all. It shows a strain-rate dependency, because of a viscous element and indicates a large plastic deformation before failure.

- *Unloading modulus of individual trabeculae is significantly larger than loading modulus and decreases with increasing damage accumulation.* Cyclic tensile and fatigue tests revealed that individual trabeculae show an accumulation of microdamage with increasing load cycles (see sections 3.2 and 3.4). Interestingly, the unloading modulus was significantly larger than the loading modulus (see chapters 5 and 7) and only the unloading modulus decreased significantly with damage accumulation. Differences in reported values of elastic moduli from micro-mechanical and nanoindentation experiments could thus be related to reporting either loading or the unloading moduli, respectively.
- *Dehydration of trabeculae causes a transition from a ductile to a quasi-brittle failure mode (see chapter 4).* As such, material properties of individual trabeculae can only be reliably determined in a wet, close to a physiologic environment. Previously determined material and apparent mechanical properties in air cannot be used for numerical simulations, as e.g. elastic modulus was increased 2-fold, compared to hydrated trabeculae. Additionally, hydrated trabeculae showed a larger amount of microdamage accumulation, caused by an 3-fold increased strain at failure and post-yield work.
- *Osteoporosis mainly changes bone morphometry without relevantly affecting material properties of individual trabeculae in the human femoral head (see chapter 5).* In accordance to previous studies, it has been demonstrated that osteoporosis causes an increase of trabecular separation and a decrease of trabecular number. In contrast, neither apparent mechanical, nor material properties, or TMD were significantly affected in the femoral head by this disease. However, in patients with osteopenia apparent yield strain and elastic work were significantly decreased, accompanied with an increased TMD. Hence, there might be initial differences at disease onset, but they likely diminish with disease duration. Sequentially, material properties used for numerical analysis of fracture risk prediction can be selected independently of osteoporosis.

- *Aging causes a deterioration of the trabecular network and shows only minor effects on the material properties of individual trabeculae in the femoral head* (see chapter 5). Interestingly, aging indicated significant differences on bone morphology and a few material properties, highlighting that osteoporosis does not have the same effect as normal aging, at least in the studied age range (57 - 90 years).
- *Anti-resorptive treatment changes the material and apparent mechanical properties of individual trabeculae in the lumbar spine of dogs* (see chapter 6). Treatment of beagle dogs with clinical relevant doses of alendronate caused a significant increase of tensile modulus and strength, accompanied by an increase of TMD. On the contrary, treatment with raloxifene increased tissue (post-yield) toughness significantly. Taken together, both treatment regimens indicated beneficial material properties of trabecular bone tissue and thus partly explain the observed superior mechanical behavior of whole bones after anti-resorptive treatment.
- *Glycation tends to increase dynamic and secant modulus of individual trabeculae. In vitro glycation of bovine trabeculae illustrated a trend of increased Maxwell/dynamic modulus and the secant modulus at the point of failure. Thus, the accumulation of AGEs with aging or diabetes might also alter the material properties in the dynamic and post-yield range.*

8.1 Conclusion

In conclusion, the current thesis demonstrated the necessity of a thorough mechanical characterization of trabecular bone at the level of individual trabeculae for a better understanding of whole bone mechanics. The increased fracture risk in osteoporosis and aging, at least in the femoral head, is not relevantly caused by alterations at the material level, but instead by changes of bone morphometry. In contrast, the reduced fracture risk after anti-resorptive treatment seems to be at least partly caused by improved material properties. Accumulation of AGEs might cause a decline of the post-yield behavior and an increased dynamic modulus, but this remains to be demonstrated with a larger amount of samples.

8.2 Outlook

The characterization of the material and apparent mechanical properties of individual trabeculae was performed with tensile tests, as reasoned out in section 2.7.5. As three-point bending experiments resulted in significantly different material properties than tensile tests in previous studies [18,171] it would be beneficial to also use different loading scenarios, like bending and compression (see appendices B and C), for a full mechanical characterization of trabecular bone tissue. This would also enable an audit of previously found decreases of material properties of osteoporotic trabeculae in three-point bending experiments [119].

The large biological variation demonstrated the necessity to test a large amount of individual trabeculae for detecting potential differences in the material properties (see chapters 5 and 6). Thus, a larger amount of glycated and control trabeculae should be tested to verify the trend of an altered post-yield and dynamic behavior after glycation. Further, especially human samples from different anatomical locations (which are also commonly affected in low-trauma fractures, such as spine and radius) should be analyzed for potential changes with accumulation of AGEs, during aging and osteoporosis.

Last but not least also some technical improvements should be considered. Analysis of small strains ($< 0.5\%$) showed a low signal to noise ratio because of limitations of the optical camera system. An increased resolution would facilitate an improved strain tracking accuracy, especially in fatigue tests. Usage of a pseudo-stress or strain-driven sample specific loading profile would reduce the rather large variation of obtained material parameters by minimizing differences of obtained stress and strain values caused by the variation of sample geometry (see section 3.4.5 “Limitations, improvements, and outlook”). Lastly, the rheological model should be extended with a strain-amplitude-dependent elastic modulus (for the spring in the Prandtl-layer) to mimic the observed degradation of tensile moduli with damage accumulation.

These improvements and extensions of the characterization of the apparent me-

chanical and material properties will further enrich our understanding of causes of increased fracture risk in our aging society. Further, this knowledge will improve the prediction of fracture risk in computer simulations, that rely on reliable material properties as input parameters. Similarly, also monitoring of treatment success in osteoporosis might benefit from a better understanding of the causes of decreased fracture risk after anti-resorptive treatment.



Die approbierte gedruckte Originalversion dieser Dissertation ist an der TU Wien Bibliothek verfügbar.
The approved original version of this doctoral thesis is available in print at TU Wien Bibliothek.

Bibliography

- [1] World Health Organization. Who Scientific Group on the Assessment of Osteoporosis At Primary Health, 2004.
- [2] E. M. Lewiecki, J. D. Ortendahl, J. Vanderpuye-Orgle, A. Grauer, J. Arellano, J. Lemay, A. L. Harmon, M. S. Broder, and A. J. Singer. Healthcare Policy Changes in Osteoporosis Can Improve Outcomes and Reduce Costs in the United States. *JBMR Plus*, 3(9):e10192, 2019.
- [3] P. D. Miller. Underdiagnoses and undertreatment of osteoporosis: The battle to be won. *Journal of Clinical Endocrinology and Metabolism*, 101(3):852–859, 2016.
- [4] M. F. Delaney. Strategies for the prevention and treatment of osteoporosis during early postmenopause. *American Journal of Obstetrics and Gynecology*, 194(2 SUPPL.):1–4, 2006.
- [5] J. A. Kanis, L. J. Melton, C. Christiansen, C. C. Johnston, and N. Khaltaev. The diagnosis of osteoporosis. *Journal of Bone and Mineral Research*, 9(8):1137–1141, 1994.
- [6] J. A. Kanis, P. Delmas, P. Burckhardt, C. Cooper, and D. Torgerson. Guidelines for Diagnosis and Management of Osteoporosis. *Osteoporosis International*, 7:390–406, 1997.
- [7] A. H. Warriner, N. M. Patkar, J. R. Curtis, E. Delzell, L. Gary, M. Kilgore, and K. Saag. Which fractures are most attributable to osteoporosis? *Journal of Clinical Epidemiology*, 64(1):46–53, 2011.

- [8] D. Chappard, M. F. Baslé, E. Legrand, and M. Audran. Trabecular bone microarchitecture: A review. *Morphologie*, 92(299):162–170, 2008.
- [9] G. Osterhoff, E. F. Morgan, S. J. Shefelbine, L. Karim, L. M. McNamara, and P. Augat. Bone mechanical properties and changes with osteoporosis. *Injury*, 47(Supplement 2):S11—S20, 2016.
- [10] L. M. McNamara. Perspective on post-menopausal osteoporosis: Establishing an interdisciplinary understanding of the sequence of events from the molecular level to whole bone fractures. *Journal of the Royal Society Interface*, 7(44):353–372, 2010.
- [11] D. Wu, P. Isaksson, S. J. Ferguson, and C. Persson. Young’s modulus of trabecular bone at the tissue level: A review. *Acta Biomaterialia*, 78(August):1–12, 2018.
- [12] E. Lucchinetti, D. Thomann, and G. Danuser. Micromechanical testing of bone trabeculae-potentials and limitations. *Journal of Materials Science*, 35(24):6057–6064, 2000.
- [13] M. J. Jaasma, H. H. Bayraktar, G. L. Niebur, and T. M. Keaveny. Biomechanical effects of intraspecimen variations in tissue modulus for trabecular bone. *Journal of Biomechanics*, 35(2):237–246, 2002.
- [14] D.-g. Kim, Y.-h. Jeong, E. Kosel, A. M. Agnew, D. W. McComb, K. Bodnyk, R. T. Hart, M. Kyung, S. Yeun, and W. M. Johnston. Regional variation of bone tissue properties at the human mandibular condyle. *Bone*, 77:98–106, 2015.
- [15] R. Akhtar, S. J. Eichhorn, and P. M. Mummery. Microstructure-based Finite Element Modelling and Characterisation of Bovine Trabecular Bone. *Journal of Bionic Engineering*, 3(1):3–9, 2006.
- [16] S. Hengsbarger, A. Kulik, and P. H. Zysset. Nanoindentation Discriminates the Elastic Properties of Individual Human Bone Lamellae Under Dry and Physiological Conditions. *Bone*, 30(1):178–184, 2002.

- [17] U. Wolfram, H. J. Wilke, and P. K. Zysset. Rehydration of vertebral trabecular bone: Influences on its anisotropy, its stiffness and the indentation work with a view to age, gender and vertebral level. *Bone*, 46(2):348–354, 2010.
- [18] R. Carretta, E. Stüssi, R. Müller, and S. Lorenzetti. Within subject heterogeneity in tissue-level post-yield mechanical and material properties in human trabecular bone. *Journal of the Mechanical Behavior of Biomedical Materials*, 24:64–73, 2013.
- [19] R. S. Lakes, J. L. Katz, and S. S. Sternstein. Viscoelastic properties of wet cortical bone-I. Torsional and biaxial studies. *Journal of Biomechanics*, 12(9), 1979.
- [20] A. N. Natali, E. L. Carniel, and P. G. Pavan. Constitutive modelling of inelastic behaviour of cortical bone. *Medical Engineering and Physics*, 30(7):905–912, 2008.
- [21] M. R. Allen and D. B. Burr. Bisphosphonate effects on bone turnover, microdamage, and mechanical properties: What we think we know and what we know that we don't know. *Bone*, 49(1):56–65, 2011.
- [22] P. Varga, D. H. Pahr, S. Baumbach, and P. K. Zysset. HR-pQCT based FE analysis of the most distal radius section provides an improved prediction of Colles' fracture load in vitro. *Bone*, 47(5):982–988, 2010.
- [23] Y. Chevalier, D. Pahr, H. Allmer, M. Charlebois, and P. Zysset. Validation of a voxel-based FE method for prediction of the uniaxial apparent modulus of human trabecular bone using macroscopic mechanical tests and nanoindentation. *Journal of Biomechanics*, 40(15):3333–3340, 2007.
- [24] P. K. Zysset, E. Dall'Ara, P. Varga, and D. H. Pahr. Finite element analysis for prediction of bone strength. *BoneKEY Reports*, 2(June):1–9, 2013.
- [25] R. Eastell, C. J. Rosen, D. M. Black, A. M. Cheung, M. H. Murad, and D. Shoback. Pharmacological management of osteoporosis in postmenopausal women: An endocrine society clinical practice guideline. *Journal of Clinical Endocrinology and Metabolism*, 104(5):1595–1622, 2019.

- [26] P. D. Miller. Bone density and markers of bone turnover in predicting fracture risk and how changes in these measures predict fracture risk reduction. *Current osteoporosis reports*, 3(3):103–110, 2005.
- [27] S. Sarkar, B. H. Mitlak, M. Wong, J. L. Stock, D. M. Black, and K. D. Harper. Relationships between bone mineral density and incident vertebral fracture risk with raloxifene therapy. *Journal of Bone and Mineral Research*, 17(1):1–10, 2002.
- [28] M. Krause, M. Soltau, E. A. Zimmermann, M. Hahn, J. Kornet, A. Hapfelmeier, S. Breer, M. Morlock, B. Wulff, K. Püschel, C. C. Glueer, M. Amling, and B. Busse. Effects of long-term alendronate treatment on bone mineralisation, resorption parameters and biomechanics of single human vertebral trabeculae. *European Cells and Materials*, 28:152–165, 2014.
- [29] M. R. Allen. Recent Advances in Understanding Bisphosphonate Effects on Bone Mechanical Properties. *Current Osteoporosis Reports*, 16(2):198–204, 2018.
- [30] A. V. Schwartz, P. Garnero, T. A. Hillier, D. E. Sellmeyer, E. S. Strotmeyer, K. R. Feingold, H. E. Resnick, F. A. Tylavsky, D. M. Black, S. R. Cummings, T. B. Harris, and D. C. Bauer. Pentosidine and Increased Fracture Risk in Older Adults with Type 2 Diabetes. *Journal of Clinical Endocrinology and Metabolism*, 94(July 2009):2380–2386, 2009.
- [31] D. B. Burr. Changes in bone matrix properties with aging. *Bone*, 120, 2019.
- [32] P. Odetti, S. Rossi, F. Monacelli, A. Poggi, M. Cirnigliaro, M. Federici, and A. Federici. Advanced glycation end products and bone loss during aging. *Annals of the New York Academy of Sciences*, 1043:710–717, 2005.
- [33] L. Knott and A. J. Bailey. Collagen cross-links in mineralizing tissues: A review of their chemistry, function, and clinical relevance. *Bone*, 22(3):181–187, 1998.

- [34] M. R. Allen, E. Gineyts, and D. B. Burr. Bisphosphonates alter trabecular bone collagen cross-linking and isomerization in beagle dog vertebra. *Osteoporosis International*, 19(3):329–37, 2008.
- [35] S. Tang, U. Zeenath, and D. Vashishth. Effects of non-enzymatic glycation on cancellous bone fragility. *Bone*, 40(4):1144–1151, 2007.
- [36] C. J. Hernandez, S. Y. Tang, B. M. Baumbach, P. B. Hwu, A. N. Sakkee, F. van Der Ham, J. DeGroot, R. A. Bank, and T. M. Keaveny. Trabecular microfracture and the influence of pyridinium and non-enzymatic glycation-mediated collagen cross-links. *Bone*, 37(6):825–832, 2005.
- [37] S. Weiner, W. Traub, and H. D. Wagner. Lamellar bone: Structure-function relations. *Journal of Structural Biology*, 126(3):241–255, 1999.
- [38] J. D. Currey. The structure and mechanics of bone. *Journal of Materials Science*, 47(1):41–54, 2012.
- [39] S. Weiner and H. D. Wagner. The material bone: Structure-mechanical function relations. *Annual Review of Materials Science*, 28(1):271–298, 1998.
- [40] J. Y. Rho, L. Kuhn-Spearing, and P. Zioupos. Mechanical properties and the hierarchical structure of bone. *Medical Engineering and Physics*, 20(2):92–102, 1998.
- [41] J. D. Currey. *Bones : structure and mechanics*, volume 2. Princeton Univ. Pr., Princeton, NJ, 2002.
- [42] B. Clarke. Normal bone anatomy and physiology. *Clinical journal of the American Society of Nephrology : CJASN*, 3 Suppl 3:131–139, 2008.
- [43] R. A. Brand. The classic: On the significance of the architecture of the spongy substance for the question of bone growth: A preliminary publication. *Clinical Orthopaedics and Related Research*, 469(11):3077–3078, 2011.
- [44] R. A. Brand. The classic: The architecture of the trabecular bone (tenth contribution on the mechanics of the human skeletal framework). *Clinical Orthopaedics and Related Research*, 469(11):3079–3084, 2011.

- [45] P. Fratzl, H. S. Gupta, E. P. Paschalis, and P. Roschger. Structure and mechanical quality of the collagen-mineral nano-composite in bone. *Journal of Materials Chemistry*, 14(14):2115–2123, 2004.
- [46] E. F. Eriksen. Cellular mechanisms of bone remodeling. *Reviews in Endocrine and Metabolic Disorders*, 11(4):219–227, 2010.
- [47] T. D. Rachner, S. Khosla, and L. C. Hofbauer. Osteoporosis: Now and the future. *The Lancet*, 377(9773):1276–1287, 2011.
- [48] H. M. Frost. Tetracycline-based histological analysis of bone remodeling. *Calcified Tissue Research*, 3(1):211–237, 1969.
- [49] R. Florencio-Silva, G. R. D. S. Sasso, E. Sasso-Cerri, M. J. Simões, and P. S. Cerri. Biology of Bone Tissue: Structure, Function, and Factors That Influence Bone Cells. *BioMed Research International*, 2015, 2015.
- [50] Z. Seref-Ferlengez, O. D. Kennedy, and M. B. Schaffler. Bone microdamage, remodeling and bone fragility: how much damage is too much damage? *BoneKEY Reports*, 4(December 2014):1–7, 2015.
- [51] F. M. Lambers, A. R. Bouman, C. M. Rimnac, and C. J. Hernandez. Microdamage caused by fatigue loading in human cancellous bone: Relationship to reductions in bone biomechanical performance. *PLoS ONE*, 8(12):1–9, 2013.
- [52] T. C. Lee, A. Staines, and D. Taylor. Bone adaptation to load: Microdamage as a stimulus for bone remodelling. *Journal of Anatomy*, 201(6):437–446, 2002.
- [53] T. Mashiba, C. H. Turner, T. Hirano, M. R. Forwood, C. C. Johnston, and D. B. Burr. Effects of suppressed bone turnover by bisphosphonates on microdamage accumulation and biomechanical properties in clinically relevant skeletal sites in beagles. *Bone*, 28(5):524–531, 2001.
- [54] J. Schilcher, K. Michaëlsson, and P. Aspenberg. Bisphosphonate Use and Atypical Fractures of the Femoral Shaft. *The new england journal of medicine*, 364:1728–1738, 2011.

- [55] S. Weiner and W. Traub. Bone structure : from angstroms to microns. *The FASEB Journal*, 6:879–885, 1992.
- [56] N. Sasaki, A. Tagami, T. Goto, M. Taniguchi, M. Nakata, and K. Hikichi. Atomic force microscopic studies on the structure of bovine femoral cortical bone at the collagen fibril-mineral level. *Journal of Materials Science: Materials in Medicine*, 13(3):333–337, 2002.
- [57] K. S. Probst and S. Lees. Visualization of crystal-matrix structure. In situ demineralization of mineralized turkey leg tendon and bone. *Calcified Tissue International*, 59(6):474–479, 1996.
- [58] P. J. Thurner. Atomic force microscopy and indentation force measurement of bone. *Wiley Interdisciplinary Reviews: Nanomedicine and Nanobiotechnology*, 1(6):624–649, 2009.
- [59] P. J. Thurner, S. Lam, J. C. Weaver, D. E. Morse, and P. K. Hansma. Localization of phosphorylated serine, osteopontin, and bone sialoprotein on bone fracture surfaces. *Journal of Adhesion*, 85(8):526–545, 2009.
- [60] V. M. Monnier, D. R. Sell, F. W. Abdul-Karim, and S. N. Emancipator. Collagen Browning and Cross-Linking Are Increased in Chronic Experimental Hyperglycemia: Relevance to Diabetes and Aging. *Diabetes*, 37(7):867–872, 1988.
- [61] D. B. Burr, M. R. Forwood, D. P. Fyhrie, R. B. Martin, M. B. Schaffler, and C. H. Turner. Bone Microdamage and Skeletal Fragility in Osteoporotic and Stress Fractures. *Journal of Bone and Mineral Research*, 12(1):6–15, 1997.
- [62] J. K. Gong, J. S. Arnold, and S. H. Cohn. Composition of trabecular and cortical bone. *The Anatomical Record*, 149(3):325–331, 1964.
- [63] R. Oftadeh, M. Perez-Viloria, J. C. Villa-Camacho, A. Vaziri, and A. Nazarian. Biomechanics and Mechanobiology of Trabecular Bone: A Review. *Journal of Biomechanical Engineering*, 137(1):1–15, 2015.
- [64] A. L. Boskey. Bone composition: relationship to bone fragility and antiosteoporotic drug effects. *BoneKEy Reports*, 2(September):1–11, 2013.

- [65] W. B. Liewers, A. S. Poljsak, S. D. Waldman, and A. K. Pilkey. Effects of dehydration-induced structural and material changes on the apparent modulus of cancellous bone. *Medical Engineering and Physics*, 32(8):921–925, 2010.
- [66] P. R. Townsend, R. M. Rose, and E. L. Radin. Buckling studies of single human trabeculae. *Journal of Biomechanics*, 8:199–201, 1975.
- [67] M. Georgiadis, R. Müller, and P. Schneider. Techniques to assess bone ultrastructure organization: Orientation and arrangement of mineralized collagen fibrils. *Journal of the Royal Society Interface*, 13(119), 2016.
- [68] J. H. Kindt, P. J. Thurner, M. E. Lauer, B. L. Bosma, G. Schitter, G. E. Fantner, M. Izumi, J. C. Weaver, D. E. Morse, and P. K. Hansma. In situ observation of fluoride-ion-induced hydroxyapatite-collagen detachment on bone fracture surfaces by atomic force microscopy. *Nanotechnology*, 18(13), 2007.
- [69] N. Verzijl, J. Degroot, E. Oldehinkel, R. A. Bank, S. R. Thorpe, J. W. Baynes, M. T. Bayliss, J. W. J. Bijlsma, F. P. J. G. Lafeber, and J. M. Tekoppele. Age-related accumulation of Maillard reaction products in human articular cartilage collagen. *Biochemical Journal*, 350:381–387, 2000.
- [70] D. Vashishth. Advanced glycation end-products and bone fractures. *IBMS BoneKEy*, 6(8):268–278, 2009.
- [71] J. J. Tomasek, S. W. Meyers, J. B. Basinger, D. T. Green, and R. L. Shew. Diabetic and age-related enhancement of collagen-linked fluorescence in cortical bones of rats. *Life Science*, 55(11):855–861, 1994.
- [72] S. R. Thorpe and J. W. Baynes. Maillard reaction products in tissue proteins: New products and new perspectives. *Amino Acids*, 25(3-4):275–281, 2003.
- [73] A. Gautieri, F. S. Passini, U. Silván, M. Guizar-Sicairos, G. Carimati, P. Volpi, M. Moretti, H. Schoenhuber, A. Redaelli, M. Berli, and J. G. Snedeker. Advanced glycation end-products: Mechanics of aged collagen from molecule to tissue. *Matrix Biology*, 59(September 2016):95–108, 2017.

- [74] A. J. Bailey, R. G. Paul, and L. Knott. Mechanisms of maturation and ageing of collagen. *Mechanisms of ageing and development*, 106(1-2):1–56, 1998.
- [75] C. J. Thomas, T. P. Cleland, G. E. Sroga, and D. Vashishth. Accumulation of carboxymethyl-lysine (CML) in human cortical bone. *Bone*, 110:128–133, 2018.
- [76] L. Karim, S. Y. Tang, G. E. Sroga, and D. Vashishth. Differences in Non-Enzymatic Glycation and Collagen Crosslinks between Human Cortical and Cancellous Bone. *Osteoporosis International*, 24(9):2441–2447, 2013.
- [77] X. Banse, T. J. Sims, and A. J. Bailey. Mechanical properties of adult vertebral cancellous bone: Correlation with collagen intermolecular cross-links. *Journal of Bone and Mineral Research*, 17(9):1621–1628, 2002.
- [78] E. A. Zimmermann, E. Schaible, H. Bale, H. D. Barth, S. Y. Tang, P. Reichert, B. Busse, T. Alliston, J. W. Ager, and R. O. Ritchie. Age-related changes in the plasticity and toughness of human cortical bone at multiple length scales. *Proceedings of the National Academy of Sciences of the United States of America*, 108(35):14416–14421, 2011.
- [79] M. Saito, K. Fujii, S. Soshi, and T. Tanaka. Reductions in degree of mineralization and enzymatic collagen cross-links and increases in glycation-induced pentosidine in the femoral neck cortex in cases of femoral neck fracture. *Osteoporosis International*, 17(7):986–995, 2006.
- [80] S. Y. Tang, M. R. Allen, R. Phipps, D. B. Burr, and D. Vashishth. Changes in non-enzymatic glycation and its association with altered mechanical properties following 1-year treatment with risedronate or alendronate. *Osteoporosis International*, 20(6):887–894, 2009.
- [81] M. Alikhani, Z. Alikhani, C. Boyd, C. M. Maclellan, M. Raptis, R. Liu, N. Pischon, P. C. Trackman, L. Gerstenfeld, and T. G. Dana. Advanced Glycation Endproducts Stimulate Osteoblast Apoptosis Via the MAP Kinase and Cytosolic Apoptotic Pathways. *Bone*, 40(2):345–353, 2007.

- [82] N. L. Fazzalari, M. R. Forwood, K. Smith, B. A. Manthey, and P. Herreen. Assessment of cancellous bone quality in severe osteoarthritis: Bone mineral density, mechanics, and microdamage. *Bone*, 22(4):381–388, 1998.
- [83] T. E. Wenzel, M. B. Schaffler, and D. P. Fyhrie. In vivo trabecular microcracks in human vertebral bone. *Bone*, 19(2):89–95, 1996.
- [84] T. L. Moore, F. J. O'Brien, and L. J. Gibson. Creep does not contribute to fatigue in bovine trabecular bone. *Journal of Biomechanical Engineering*, 126(3):321–329, 2004.
- [85] S. Mori, R. Harruff, W. Ambrosius, and D. B. Burr. Trabecular bone volume and microdamage accumulation in the femoral heads of women with and without femoral neck fractures. *Bone*, 21(6):521–526, 1997.
- [86] T. Diab, K. W. Condon, D. B. Burr, and D. Vashishth. Age-related change in the damage morphology of human cortical bone and its role in bone fragility. *Bone*, 38(3):427–431, 2006.
- [87] B. C. Herman, L. Cardoso, R. J. Majeska, K. J. Jepsen, and M. B. Schaffler. Activation of Bone Remodeling after Fatigue: Differential Response to Linear Microcracks and Diffuse Damage. *Bone*, 47(4):766–772, 2010.
- [88] D. B. Burr. Repair mechanisms for microdamage in bone. *Journal of Bone and Mineral Research*, 29(12):2534–2536, 2014.
- [89] Z. Seref-Ferlengez, J. Basta-Pljakic, O. D. Kennedy, C. J. Philemon, M. B. Schaffler, Z. S. Ferlengez, J. B. Pljakic, O. D. Kennedy, C. J. Philemon, M. B. Schaf, Z. Seref-Ferlengez, J. Basta-Pljakic, O. D. Kennedy, C. J. Philemon, and M. B. Schaffler. Structural and Mechanical Repair of Diffuse Damage in Cortical Bone In Vivo. *Journal of Bone and Mineral Research*, 29(12):2537–2544, 2014.
- [90] T. M. Boyce, D. P. Fyhrie, M. C. Glotkowski, E. L. Radin, and M. B. Schaffler. Damage type and strain mode associations in human compact bone bending fatigue. *Journal of Orthopaedic Research*, 16(3):322–329, 1998.

- [91] D. Taylor, J. G. Hazenberg, and T. C. Lee. Living with cracks: Damage and repair in human bone. *Nature Materials*, 6(4):263–268, 2007.
- [92] B. Martin. Mathematical model for repair of fatigue damage and stress fracture in osteonal bone. *Journal of Orthopaedic Research*, 13(3):309–316, 1995.
- [93] N. L. Fazzalari, M. R. Forwood, B. A. Manthey, K. Smith, and P. Kolesik. Three-dimensional confocal images of microdamage in cancellous bone. *Bone*, 23(4):373–378, 1998.
- [94] F. Loi, L. A. Córdova, J. Pajarinen, T. hua Lin, Z. Yao, and S. B. Goodman. Inflammation, fracture and bone repair. *Bone*, 86:119–130, 2016.
- [95] C. H. Turner. Three rules for bone adaptation to mechanical stimuli. *Bone*, 23(5):399–407, 1998.
- [96] J. Marshall, E. Lloyd, J. Rundo, J. Linocki, G. Marotti, C. Mays, H. Sissons, and W. Snyder. Alkaline Earth Metabolism in Adult Man. *Health Physics*, 24(2):125–221, 1972.
- [97] S. Khosla, J. J. Westendorf, and U. I. Mödder. Concise review: Insights from normal bone remodeling and stem cell-based therapies for bone repair. *Stem Cells*, 28(12):2124–2128, 2010.
- [98] G. Karsenty. Transcriptional Control of Skeletogenesis. *Annual Review of Genomics and Human Genetics*, 9(1):183–196, 2008.
- [99] M. Capulli, R. Paone, and N. Rucci. Osteoblast and osteocyte: Games without frontiers. *Archives of Biochemistry and Biophysics*, 561:3–12, 2014.
- [100] T. A. Franz-Odenaal, B. K. Hall, and P. E. Witten. Buried alive: How osteoblasts become osteocytes. *Developmental Dynamics*, 235(1):176–190, 2006.
- [101] L. F. Bonewald and M. L. Johnson. Osteocytes, mechanosensing and Wnt signaling. *Bone*, 42(4):606–615, 2008.

- [102] T. Bellido. Osteocyte-driven bone remodeling. *Calcified Tissue International*, 94(1):25–34, 2014.
- [103] L. J. Raggatt and N. C. Partridge. Cellular and molecular mechanisms of bone remodeling. *Journal of Biological Chemistry*, 285(33):25103–25108, 2010.
- [104] N. K. Lee. Molecular Understanding of Osteoclast Differentiation and Physiology. *Endocrinology and Metabolism*, 25(4):264, 2010.
- [105] B. F. Boyce and L. Xing. Functions of RANKL/RANK/OPG in bone modeling and remodeling. *Archives of Biochemistry and Biophysics*, 473(2):139–146, 2008.
- [106] M. E. Abdelgawad, J. M. Delaisse, M. Hinge, P. R. Jensen, R. W. Alnaimi, L. Rolighed, L. H. Engelholm, N. Marcussen, and T. L. Andersen. Early reversal cells in adult human bone remodeling: osteoblastic nature, catabolic functions and interactions with osteoclasts. *Histochemistry and Cell Biology*, 145(6):603–615, 2016.
- [107] J. S. Kenkre and J. H. Bassett. The bone remodelling cycle. *Annals of Clinical Biochemistry*, 55(3):308–327, 2018.
- [108] E. F. Eriksen, H. J. Gundersen, F. Melsen, and L. Mosekilde. Reconstruction of the formative site in iliac trabecular bone in 20 normal individuals employing a kinetic model for matrix and mineral apposition. *Metabolic Bone Disease and Related Research*, 5(5):243–252, 1984.
- [109] E. F. Eriksen, F. Melsen, and L. Mosekilde. Reconstruction of the resorptive site in iliac trabecular bone: A kinetic model for bone resorption in 20 normal individuals. *Metabolic Bone Disease and Related Research*, 5(5):235–242, 1984.
- [110] T. Sozen, L. Ozisik, and N. Calik Basaran. An overview and management of osteoporosis. *European Journal of Rheumatology*, 4(1):46–56, 2017.

- [111] J.-H. Yoo, S.-H. Moon, Y.-C. Ha, D. Y. Lee, H. S. Gong, S. Y. Park, and K. H. Yang. Osteoporotic Fracture: 2015 Position Statement of the Korean Society for Bone and Mineral Research. *Journal of Bone Metabolism*, 22(4):175, 2015.
- [112] J. A. Kanis, O. Johnell, A. Oden, H. Johansson, and E. McCloskey. FRAX™ and the assessment of fracture probability in men and women from the UK. *Osteoporosis International*, 19(4):385–397, 2008.
- [113] A. Unnanuntana, B. P. Gladnick, E. Donnelly, and J. M. Lane. The assessment of fracture risk. *Journal of Bone and Joint Surgery - Series A*, 92(3):743–753, 2010.
- [114] F. A. Trémollières, J. M. Pouillès, N. Drewniak, J. Laparra, C. A. Ribot, and P. Dargent-Molina. Fracture risk prediction using BMD and clinical risk factors in early postmenopausal women: Sensitivity of the WHO FRAX tool. *Journal of Bone and Mineral Research*, 25(5):1002–1009, 2010.
- [115] N. Li, X. M. Li, L. Xu, W. J. Sun, X. G. Cheng, and W. Tian. Comparison of QCT and DXA: Osteoporosis detection rates in postmenopausal women. *International Journal of Endocrinology*, 2013:5–10, 2013.
- [116] M. A. Brennan, J. P. Gleeson, F. J. O’Brien, and L. M. McNamara. Effects of ageing, prolonged estrogen deficiency and zoledronate on bone tissue mineral distribution. *Journal of the Mechanical Behavior of Biomedical Materials*, 29:161–170, 2014.
- [117] S. J. Gadeleta, A. L. Boskey, E. Paschalis, C. Carlson, F. Menschik, T. Baldini, M. Peterson, and C. M. Rimnac. A physical, chemical, and mechanical study of lumbar vertebrae from normal, ovariectomized, and nandrolone decanoate-treated cynomolgus monkeys (*macaca fascicularis*). *Bone*, 27(4):541–550, 2000.
- [118] P. Roschger, E. P. Paschalis, P. Fratzl, and K. Klaushofer. Bone mineralization density distribution in health and disease. *Bone*, 42(3):456–466, 2008.
- [119] B. Busse, M. Hahn, M. Soltau, J. Zustin, K. Püschel, G. N. Duda, and M. Amling. Increased calcium content and inhomogeneity of mineralization

render bone toughness in osteoporosis: Mineralization, morphology and biomechanics of human single trabeculae. *Bone*, 45(6):1034–1043, 2009.

- [120] L. M. McNamara, A. G. H. Ederveen, C. G. Lyons, C. Price, M. B. Schaffler, H. Weinans, and P. J. Prendergast. Strength of cancellous bone trabecular tissue from normal, ovariectomized and drug-treated rats over the course of ageing. *Bone*, 39(2):392–400, 2006.
- [121] L. M. McNamara, P. J. Prendergast, and M. B. Schaffler. Bone tissue material properties are altered during osteoporosis. *Journal of Musculoskeletal and Neuronal Interactions*, 5(4):342–343, 2005.
- [122] M. A. Brennan, J. P. Gleeson, M. Browne, F. J. O’Brien, P. J. Thurner, and L. M. McNamara. Site specific increase in heterogeneity of trabecular bone tissue mineral during oestrogen deficiency. *European Cells and Materials*, 21(353):396–406, 2011.
- [123] N. M. Chhipa and D. Jyoti Sen. Aminobiphosphonates in osteoporosis: A review. *International Journal of Drug Development and Research*, 5(3):120–132, 2013.
- [124] R. Marcus, D. W. Dempster, and M. L. Bouxsein. *The Nature of Osteoporosis*. Elsevier, fourth edi edition, 2013.
- [125] B. L. Riggs, H. W. Wahner, E. Seeman, K. P. Offord, W. L. Dunn, R. B. Mazess, K. A. Johnson, and L. J. Melton. Changes in bone mineral density of the proximal femur and spine with aging. Differences between the postmenopausal and senile osteoporosis syndromes. *Journal of Clinical Investigation*, 70(4):716–723, 1982.
- [126] J. E. South-Paul. Osteoporosis: Part I. Evaluation and assessment. *American Family Physician*, 63(5):897–904, 2001.
- [127] G. Duque and B. R. Troen. Understanding the mechanisms of senile osteoporosis: New facts for a major geriatric syndrome. *Journal of the American Geriatrics Society*, 56(5):935–941, 2008.

- [128] M.-X. Ji and Q. Yu. Primary osteoporosis in postmenopausal women. *Chronic Diseases and Translational Medicine*, 1(1):9–13, 2015.
- [129] E. Damien, J. S. Price, and L. E. Lanyon. The estrogen receptor’s involvement in osteoblasts’ adaptive response to mechanical strain. *Journal of Bone and Mineral Research*, 13(8):1275–1282, 1998.
- [130] A. Tomkinson, J. Reeve, R. W. Shaw, and B. S. Noble. The death of osteocytes via apoptosis accompanies estrogen withdrawal in human bone. *Journal of Clinical Endocrinology and Metabolism*, 82(9):3128–3135, 1997.
- [131] J. I. Aguirre, L. I. Plotkin, S. A. Stewart, R. S. Weinstein, A. M. Parfitt, S. C. Manolagas, and T. Bellido. Osteocyte apoptosis is induced by weightlessness in mice and precedes osteoclast recruitment and bone loss. *Journal of Bone and Mineral Research*, 21(4):605–615, 2006.
- [132] M. Almeida, L. Han, M. Martin-Millan, L. I. Plotkin, S. A. Stewart, P. K. Roberson, S. Kousteni, C. A. O’Brien, T. Bellido, A. M. Parfitt, R. S. Weinstein, R. L. Jilka, and S. C. Manolagas. Skeletal involution by age-associated oxidative stress and its acceleration by loss of sex steroids. *Journal of Biological Chemistry*, 282(37):27285–27297, 2007.
- [133] R. S. Weinstein, R. L. Jilka, A. Michael Parfitt, and S. C. Manolagas. Inhibition of osteoblastogenesis and promotion of apoptosis of osteoblasts and osteocytes by glucocorticoids potential mechanisms of their deleterious effects on bone. *Journal of Clinical Investigation*, 102(2):274–282, 1998.
- [134] M. E. Arlot, P. D. Delmas, D. Chappard, and P. J. Meunier. Trabecular and endocortical bone remodeling in postmenopausal osteoporosis: Comparison with normal postmenopausal women. *Osteoporosis International*, 1(1):41–49, 1990.
- [135] R. Civitelli, S. Gonnelli, F. Zacchei, S. Bigazzi, A. Vattimo, L. V. Avioli, and C. Gennari. Bone turnover in postmenopausal osteoporosis. Effect of calcitonin treatment. *Journal of Clinical Investigation*, 82(4):1268–1274, 1988.

- [136] G. Wheeler, M. Elshahaly, S. P. Tuck, H. K. Datta, and J. M. van Laar. The clinical utility of bone marker measurements in osteoporosis. *Journal of Translational Medicine*, 11(1), 2013.
- [137] F. Cosman, S. J. de Beur, M. S. LeBoff, E. M. Lewiecki, B. Tanner, S. Randall, and R. Lindsay. Clinician’s Guide to Prevention and Treatment of Osteoporosis. *Osteoporosis International*, 25(10):2359–2381, 2014.
- [138] P. M. Camacho, S. M. Petak, N. Binkley, B. L. Clarke, S. T. Harris, D. L. Hurley, M. Kleerekoper, E. M. Lewiecki, P. D. Miller, H. S. Narula, R. Pessah-Pollack, V. Tangpricha, S. J. Wimalawansa, and N. B. Watts. American association of clinical endocrinologists and American college of endocrinology clinical practice guidelines for the diagnosis and treatment of postmenopausal osteoporosis - 2016. *Endocrine Practice*, 22(September):1–42, 2016.
- [139] F. Milat and P. R. Ebeling. Osteoporosis treatment: A missed opportunity. *Medical Journal of Australia*, 205(4):185–190, 2016.
- [140] A. B. Hodsman, D. C. Bauer, D. W. Dempster, L. Dian, D. A. Hanley, S. T. Harris, D. L. Kendler, M. R. McClung, P. D. Miller, W. P. Olszynski, E. Orwoll, and K. Y. Chui. Parathyroid hormone and teriparatide for the treatment of osteoporosis: A review of the evidence and suggested guidelines for its use. *Endocrine Reviews*, 26(5):688–703, 2005.
- [141] E. Kućukalić-Selimovic, A. Valjevac, A. Hadžović-Džuvo, A. Skopljak-Beganović, R. Alimanovic-Alagić, and A. Brković. Evaluation of bone remodelling parameters after one year treatment with alendronate in postmenopausal women with osteoporosis. *Bosnian Journal of Basic Medical Sciences*, 11(1):41–45, 2011.
- [142] H. G. Bone, R. W. Downs, J. R. Tucci, S. T. Harris, R. S. Weinstein, A. A. Licata, M. R. McClung, D. B. Kimmel, B. J. Gertz, E. Hale, and W. J. Polvino. Dose-response relationships for alendronate treatment in osteoporotic elderly women. *Journal of Clinical Endocrinology and Metabolism*, 82(1):265–274, 1997.

- [143] D. M. Black, S. R. Cummings, D. B. Karpf, J. A. Cauley, D. E. Thompson, M. C. Nevitt, D. C. Bauer, H. K. Genant, W. L. Haskell, R. Marcus, S. M. Ott, J. C. Torner, S. A. Quandt, T. F. Reiss, and K. E. Ensrud. Randomised trial of effect of alendronate on risk of fracture in women with existing vertebral fractures. *The Lancet*, 348(9041):1535–1541, dec 1996.
- [144] C. V. Odvina, J. E. Zerwekh, D. S. Rao, N. Maalouf, F. A. Gottschalk, and C. Y. Pak. Severely suppressed bone turnover: A potential complication of alendronate therapy. *Journal of Clinical Endocrinology and Metabolism*, 90(3):1294–1301, 2005.
- [145] T. Mashiba, T. Hirano, C. H. Turner, M. R. Forwood, C. C. Johnston, and D. B. Burr. Suppressed Bone Turnover by Bisphosphonates Increases Microdamage Accumulation and Reduces Some Biomechanical Properties in Dog Rib. *Journal of Bone and Mineral Research*, 15(4):613–620, 2000.
- [146] S. Khosla, D. Burr, J. Cauley, D. W. Dempster, P. R. Ebeling, D. Felsenberg, R. F. Gagel, V. Gilsanz, T. Guise, S. Koka, L. K. McCauley, J. McGowan, M. D. McKee, S. Mohla, D. G. Pendrys, L. G. Raisz, S. L. Ruggiero, D. M. Shafer, L. Shum, S. L. Silverman, C. H. Van Poznak, N. Watts, S. B. Woo, and E. Shane. Bisphosphonate-associated osteonecrosis of the jaw: Report of a Task Force of the American Society for Bone and Mineral Research. *Journal of Bone and Mineral Research*, 22(10):1479–1491, 2007.
- [147] E. Shane, D. Burr, B. Abrahamsen, R. A. Adler, T. D. Brown, A. M. Cheung, F. Cosman, J. R. Curtis, R. Dell, D. W. Dempster, P. R. Ebeling, T. A. Einhorn, H. K. Genant, P. Geusens, K. Klaushofer, J. M. Lane, F. McKiernan, R. McKinney, A. Ng, J. Nieves, R. O’Keefe, S. Papapoulos, T. S. Howe, M. C. Van Der Meulen, R. S. Weinstein, and M. P. Whyte. Atypical subtrochanteric and diaphyseal femoral fractures: Second report of a task force of the American society for bone and mineral research. *Journal of Bone and Mineral Research*, 29(1):1–23, 2014.
- [148] B. Ettinger, B. H. Mitlalc, T. Nickelsen, H. K. Genant, C. Christiansen, J. R. Zanchetta, and J. Stakkestad. Reduction of Vertebral Fracture Risk in

Postmenopausal Women With Osteoporosis Treated With Raloxifene. *Jama*, 282(7):637–645, 1999.

- [149] J. A. Cauley, L. Norton, M. E. Lippman, S. Eckert, K. A. Krueger, D. W. Purdie, J. Farrerons, A. Karasik, D. Mellstrom, K. W. Ng, J. J. Stepan, T. J. Powles, M. Morrow, A. Costa, S. L. Silfen, E. L. Walls, H. Schmitt, D. B. Muchmore, and V. C. Jordan. Continued Breast Cancer Risk Reduction in Postmenopausal Women Treated with Raloxifene: 4-Year Results from the MORE Trial. *Breast Cancer Research and Treatment*, 65(2):125–134, 2001.
- [150] E. Barrett-Connor, L. Mosca, P. Collins, M. J. Geiger, D. Grady, M. Kornitzer, M. A. McNabb, and N. K. Wenger. Effects of Raloxifene on Cardiovascular Events and Breast Cancer in Postmenopausal Women. *New England Journal of Medicine*, 355(2):125–137, jul 2006.
- [151] T. Siegmund, M. R. Allen, and D. B. Burr. Can Deterministic Mechanical Size Effects Contribute to Fracture and Microdamage Accumulation in Trabecular Bone? *Journal of Theoretical Biology*, 265(2):202–210, 2010.
- [152] J. H. Cole and M. C. Van Der Meulen. Whole bone mechanics and bone quality. *Clinical Orthopaedics and Related Research*, 469(8):2139–2149, 2011.
- [153] T. M. Keaveny and W. C. Hayes. A 20-year perspective on the mechanical properties of trabecular bone. *Journal of Biomechanical Engineering*, 115(4):534–542, 1993.
- [154] B. van Rietbergen, H. Weinans, R. Huiskes, and A. Odgaard. A new method to determine trabecular bone elastic properties and loading using micromechanical finite-element models. *Journal of Biomechanics*, 28(1):69–81, 1995.
- [155] T. Hara, E. Tanck, J. Homminga, and R. Huiskes. The Influence of Micro-computed Tomography Threshold Variations on the Assessment of Structural and Mechanical Trabecular Bone Properties. *Bone*, 31(1):107–109, 2002.
- [156] T. N. Hangartner. Thresholding technique for accurate analysis of density and geometry in QCT , pQCT and ÌCT images. *Journal of Musculoskeletal and Neuronal Interactions*, 7(1):9–16, 2007.

- [157] E. Verhulp, B. V. Rietbergen, R. Müller, and R. Huiskes. Computer Methods in Biomechanics and Biomedical Engineering Micro-finite element simulation of trabecular-bone post-yield behaviour – effects of material model , element size and type. *Computer Methods in Biomechanics and Biomedical Engineering*, 11(4):389–395, 2008.
- [158] T. Topoli, A. Cicha, A. Mazurkiewicz, and K. Nowicki. The Relationship between Trabecular Bone Structure Modeling Methods and the Elastic Modulus as Calculated by FEM. *The scientific World Journal*, 2012:1–9, 2012.
- [159] D. Ulrich, B. van Rietbergen, H. Weinans, and P. Rügsegger. Finite element analysis of trabecular bone structure : a comparison of image-based meshing techniques. *Journal of Biomechanics*, 31:1187–1192, 1998.
- [160] J.-y. Rho. An ultrasonic method for measuring the elastic properties of human tibial cortical and cancellous bone. *Ultrasonics*, 34:777–783, 1996.
- [161] K. Hasegawa, C. H. Turner, R. R. Recker, E. Wu, and D. B. Burr. Elastic Properties of Osteoporotic Bone Measured by Scanning Acoustic Microscopy. *Bone*, 16(I):85–90, 1995.
- [162] J. Y. Rho, R. B. Ashman, and C. H. Turner. Young’s modulus of trabecular and cortical bone material: Ultrasonic and microtensile measurements. *Journal of Biomechanics*, 26(2):111–119, 1993.
- [163] R. B. Ashman. Elastic Modulus of Trabecular Bone Material. *Journal of Biomechanics*, 21(3):177–181, 1988.
- [164] P. H. F. Nicholson, X. G. Cheng, G. Lowet, S. Boonen, M. W. J. Davie, J. Dequeker, and G. Van Der Perre. Structural and material mechanical properties of human vertebral cancellous bone. *Medical Engineering and Physics*, 19(8):729–737, 1997.
- [165] C. H. Turner, J. Rho, Y. Takano, T. Y. Tsui, and G. M. Pharr. The elastic properties of trabecular and cortical bone tissues are similar : results from two microscopic measurement techniques. *Journal of Biomechanics*, 32:437–441, 1999.

- [166] J. D. Currey. The effects of strain rate, reconstruction and mineral content on some mechanical properties of bovine bone. *Journal of Biomechanics*, 8(1), 1975.
- [167] M. E. Szabó, M. Taylor, and P. J. Thurner. Mechanical properties of single bovine trabeculae are unaffected by strain rate. *Journal of Biomechanics*, 44(5):962–967, 2011.
- [168] S. Blouin, S. Puchegger, A. Roschger, A. Berzlanovich, P. Fratzl, K. Klaushofer, and P. Roschger. Mapping dynamical mechanical properties of osteonal bone by scanning acoustic microscopy in time-of-flight mode. *Microscopy and Microanalysis*, 20(3):924–936, 2014.
- [169] S. Blouin, N. Fratzl-Zelman, A. Roschger, W. A. Cabral, K. Klaushofer, J. C. Marini, P. Fratzl, and P. Roschger. Cortical bone properties in the Brtl/+ mouse model of Osteogenesis imperfecta as evidenced by acoustic transmission microscopy. *Journal of the Mechanical Behavior of Biomedical Materials*, 90(October 2018):125–132, 2019.
- [170] R. Carretta, S. Lorenzetti, and R. Müller. Automated displacement and strain tracking in single trabecula using fluorescent microspheres and time lapsed microscopy. *Proceedings of the 23rd Congress of the International Society of Biomechanics*, page 826, 2011.
- [171] R. Carretta, B. Luisier, D. Bernoulli, E. Stüssi, R. Müller, and S. Lorenzetti. Novel method to analyze post-yield mechanical properties at trabecular bone tissue level. *Journal of the Mechanical Behavior of Biomedical Materials*, 20:6–18, 2013.
- [172] R. Jungmann, M. E. Szabo, G. Schitter, R. Yue-Sing Tang, D. Vashishth, P. K. Hansma, and P. J. Thurner. Local strain and damage mapping in single trabeculae during three-point bending tests. *Journal of the Mechanical Behavior of Biomedical Materials*, 4(4):523–534, 2011.
- [173] J. L. Kuhn, S. A. Goldstein, K. Choi, M. London, L. A. Feldkamp, L. Matthews, and L. S. Kuhn, J. L.; Goldstein, S. A.; Choi, K.; London, M.;

Feldkamp, L. A.; Matthews. Comparison of the Trabecular and Cortical Tissue Moduli from Human Iliac Crests. *Journal of Orthopaedic Research*, 7:876–884, 1989.

- [174] H. Ridha and P. J. Thurner. Finite element prediction with experimental validation of damage distribution in single trabeculae during three-point bending tests. *Journal of the Mechanical Behavior of Biomedical Materials*, 27:94–106, 2013.
- [175] M. E. Szabó and P. J. Thurner. Anisotropy of bovine cortical bone tissue damage properties. *Journal of Biomechanics*, 46(1):2–6, 2013.
- [176] M. E. Szabó, J. Zekonyte, O. L. Katsamenis, M. Taylor, and P. J. Thurner. Similar damage initiation but different failure behavior in trabecular and cortical bone tissue. *Journal of the Mechanical Behavior of Biomedical Materials*, 4(8):1787–1796, 2011.
- [177] O. Jiroušek, J. Němeček, D. Kytýř, J. Kunecký, P. Zlámal, and T. Doktor. Nanoindentation of trabecular bone-comparison with uniaxial testing of single trabecula. *Chemické Listy*, 105(17), 2011.
- [178] S. D. Ryan and J. L. Williams. Tensile testing of rodlike trabeculae excised from bovine femoral bone. *Journal of Biomechanics*, 22(4):351–355, 1989.
- [179] S. Yamada, S. Tadano, and S. Fukuda. Nanostructure and elastic modulus of single trabecula in bovine cancellous bone. *Journal of Biomechanics*, 47(14):3482–3487, 2014.
- [180] J. C. Runkle and J. Pugh. The micro-mechanics of cancellous bone. II. Determination of the elastic modulus of individual trabeculae by a buckling analysis. *Bulletin of the Hospital for Joint Diseases*, 36(1):2–10, apr 1975.
- [181] K. Choi and S. A. Goldstein. A Comparison of the Fatigue Behavior of Human Trabecular and Cortical Bone Tissue. *Journal of Biomechanics*, 25(12):1371–1381, 1992.

- [182] J. Hong, H. Cha, Y. Park, S. Lee, G. Khang, and Y. Kim. Elastic moduli and poisson's ratios of microscopic human femoral trabeculae. *IFMBE Proceedings*, 16(1):274–277, 2007.
- [183] J. W. Pugh, R. M. Rose, and E. L. Radin. Elastic and Viscoelastic Properties of Trabecular Bone: Dependence on Structure. *Journal of Biomechanics*, 6:475–485, 1973.
- [184] F. Bini, A. Marinozzi, F. Marinozzi, and F. Patanè. Microtensile measurements of single trabeculae stiffness in human femur. *Journal of Biomechanics*, 35(11):1515–1519, 2002.
- [185] K. W. Luczynski, A. Steiger-Thirsfeld, J. Bernardi, J. Eberhardsteiner, and C. Hellmich. Extracellular bone matrix exhibits hardening elastoplasticity and more than double cortical strength : Evidence from homogeneous compression of non-tapered single micron-sized pillars welded to a rigid substrate. *Journal of the Mechanical Behavior of Biomedical Materials*, 52:51–62, 2015.
- [186] J. Schwiedrzik, R. Raghavan, A. Bürki, V. Lenader, U. Wolfram, J. Michler, and P. Zysset. In situ micropillar compression reveals superior strength and ductility but an absence of damage in lamellar bone. *Nature Materials*, 13(June):740–747, 2014.
- [187] L. M. McNamara, J. C. V. D. Linden, H. Weinans, and P. J. Prendergast. Stress-concentrating effect of resorption lacunae in trabecular bone. *Journal of Biomechanics*, 39:734–741, 2006.
- [188] S. Yamada, S. Tadano, and K. Fukasawa. Micro-cantilever bending for elastic modulus measurements of a single trabecula in cancellous bone. *Journal of Biomechanics*, 49(16):4124–4127, 2016.
- [189] P. K. Zysset. Indentation of bone tissue : a short review. *Osteoporosis International*, 20:1049–1055, 2009.
- [190] E. Mittra, S. Akella, and Y.-x. Qin. The effects of embedding material , loading rate and magnitude , and penetration depth in nanoindentation of trabecular bone. *Journal of Biomedical Materials Research*, 79A:86–93, 2006.

- [191] W. C. Oliver and G. M. Pharr. An improved technique for determining hardness and elastic modulus using load and displacement sensing indentation experiments. *Journal of Materials Research*, 7(6):1564–1583, 1992.
- [192] P. K. Zysset, X. Edward Guo, C. Edward Hoffler, K. E. Moore, and S. A. Goldstein. Elastic modulus and hardness of cortical and trabecular bone lamellae measured by nanoindentation in the human femur. *Journal of Biomechanics*, 32(10):1005–1012, 1999.
- [193] L. Mulder, J. H. Koolstra, J. M. den Toonder, and T. M. van Eijden. Intra-trabecular distribution of tissue stiffness and mineralization in developing trabecular bone. *Bone*, 41(2):256–265, 2007.
- [194] J. Y. Rho, T. Y. Tsui, and G. M. Pharr. Elastic properties of human cortical and trabecular lamellar bone measured by nanoindentation. *Biomaterials*, 18(20):1325–1330, 1997.
- [195] M. J. Silva, M. D. Brodt, Z. Fan, and J.-y. Rho. Nanoindentation and whole-bone bending estimates of material properties in bones from the senescence accelerated mouse SAMP6. *Journal of Biomechanics*, 37:1639–1646, 2004.
- [196] S. Hengsberger, J. Enstroem, F. Peyrin, and P. Zysset. How is the indentation modulus of bone tissue related to its macroscopic elastic response ? A validation study. *Journal of Biomechanics*, 36:1503–1509, 2003.
- [197] G. L. Niebur, M. J. Feldstein, J. C. Yuen, T. J. Chen, and T. M. Keaveny. High-resolution finite element models with tissue strength asymmetry accurately predict failure of trabecular bone. *Journal of Biomechanics*, 33(12):1575–1583, 2000.
- [198] H. Daoui, X. Cai, F. Boubenider, P. Laugier, and Q. Grimal. Assessment of trabecular bone tissue elasticity with resonant ultrasound spectroscopy. *Journal of the Mechanical Behavior of Biomedical Materials*, 74(May):106–110, 2017.
- [199] H. Isaksson, S. Nagao, M. Małkiewicz, P. Julkunen, R. Nowak, and J. S. Jurvelin. Precision of nanoindentation protocols for measurement of viscoelas-

ticity in cortical and trabecular bone. *Journal of Biomechanics*, 43(12):2410–2417, 2010.

- [200] X. J. Wang, X. B. Chen, P. D. Hodgson, and C. E. Wen. Elastic modulus and hardness of cortical and trabecular bovine bone measured by nanoindentation. *Transactions of Nonferrous Metals Society of China (English Edition)*, 16(SUPPL.), 2006.
- [201] H. H. Bayraktar, E. F. Morgan, G. L. Niebur, G. E. Morris, E. K. Wong, and T. M. Keaveny. Comparison of the elastic and yield properties of human femoral trabecular and cortical bone tissue. *Journal of Biomechanics*, 37(1):27–35, 2004.
- [202] J. S. Day, M. Ding, J. C. Van Der Linden, I. Hvid, D. R. Sumner, and H. Weinans. A decreased subchondral trabecular bone tissue elastic modulus is associated with pre-arthritic cartilage damage. *Journal of Orthopaedic Research*, 19(5):914–918, 2001.
- [203] F. J. Hou, S. M. Lang, S. J. Hoshaw, D. A. Reimann, and D. P. Fyhrie. Human vertebral body apparent and hard tissue stiffness. *Journal of Biomechanics*, 31(11):1009–1015, 1998.
- [204] A. J. Ladd, J. H. Kinney, D. L. Haupt, and S. A. Goldstein. Finite-element modeling of trabecular bone: Comparison with mechanical testing and determination of tissue modulus. *Journal of Orthopaedic Research*, 16(5):622–628, 1998.
- [205] K. Choi, J. L. Kuhn, M. J. Ciarelli, and S. A. Goldstein. The elastic moduli of human subchondral, trabecular, and cortical bone tissue and the size-dependency of cortical bone modulus. *Journal of Biomechanics*, 23(11):1103–1113, 1990.
- [206] H. Giambini, H. J. Wang, C. Zhao, Q. Chen, A. Nassr, and K. N. An. Anterior and posterior variations in mechanical properties of human vertebrae measured by nanoindentation. *Journal of Biomechanics*, 46(3):456–461, 2013.

- [207] C. E. Hoffer, K. E. Moore, K. Kozloff, P. K. Zysset, M. B. Brown, and S. A. Goldstein. Heterogeneity of bone lamellar-level elastic moduli. *Bone*, 26(6):603–609, 2000.
- [208] B. J. Polly, P. A. Yuya, M. P. Akhter, R. R. Recker, and J. A. Turner. Intrinsic material properties of trabecular bone by nanoindentation testing of biopsies taken from healthy women before and after menopause. *Calcified Tissue International*, 90(4):286–293, 2012.
- [209] J. Y. Rho, M. E. Roy, T. Y. Tsui, and G. M. Pharr. Elastic properties of microstructural components of human bone tissue as measured by nanoindentation. *Journal of Biomedical Materials Research*, 45(1):48–54, 1999.
- [210] L. J. Smith, J. P. Schirer, and N. L. Fazzalari. The role of mineral content in determining the micromechanical properties of discrete trabecular bone remodeling packets. *Journal of Biomechanics*, 43(16):3144–3149, 2010.
- [211] C. K. Tjhia, C. V. Odvina, D. S. Rao, S. M. Stover, X. Wang, and D. P. Fyhrie. Mechanical property and tissue mineral density differences among severely suppressed bone turnover (SSBT) patients, osteoporotic patients, and normal subjects. *Bone*, 49(6):1279–1289, 2011.
- [212] U. Wolfram, H. J. Wilke, and P. K. Zysset. Valid μ finite element models of vertebral trabecular bone can be obtained using tissue properties measured with nanoindentation under wet conditions. *Journal of Biomechanics*, 43(9):1731–1737, 2010.
- [213] T. Ridler and S. Calvard. Picture Thresholding Using. *IEEE Transactions on Systems, Man and Cybernetics*, smc-8(8):630–632, 1978.
- [214] M. A. Scanco. Bone Density Conversation, 2020.
- [215] P. Thévenaz, U. E. Ruttimann, and M. Unser. A pyramid approach to subpixel registration based on intensity. *IEEE Transactions on Image Processing*, 7(1):27–41, 1998.
- [216] D. Allan, T. Caswell, N. Keim, and C. van der Wel. Trackpy v0.3.2, aug 2016.

- [217] J. C. Crocker and D. G. Grier. Methods of digital video microscopy for colloidal studies. *Journal of Colloid and Interface Science*, 179(1):298–310, 1996.
- [218] T. Savin and P. S. Doyle. Static and dynamic errors in particle tracking microrheology. *Biophysical Journal*, 88(1):623–638, 2005.
- [219] M. M. Ashby and D. R. Jones. *Engineering Materials 1*. Butterworth Heinemann, 2012.
- [220] E. Voce. The relationship between stress and strain for homogeneous deformation. *Journal of the Institute of Metals*, 74:537–562, 1948.
- [221] A. Synek, Y. Chevalier, S. F. Baumbach, and D. H. Pahr. The influence of bone density and anisotropy in finite element models of distal radius fracture osteosynthesis: Evaluations and comparison to experiments. *Journal of Biomechanics*, 48(15):4116–4123, 2015.
- [222] R Core Team. R: A Language and Environment for Statistical Computing, 2013.
- [223] J. P. Bilezikian, L. G. Raisz, and T. J. Martin. *Principles of bone biology*. Academic press, 2008.
- [224] A. G. Reisinger, M. Frank, P. J. Thurner, and D. H. Pahr. A two - layer elasto - visco - plastic rheological model for the material parameter identification of bone tissue. *Biomechanics and Modeling in Mechanobiology*, 2020.
- [225] S. P. C. Marques and G. J. Creus. *Computational viscoelasticity*. Springer Science & Business Media, 2012.
- [226] M. Pazianas, S. van der Geest, and P. Miller. Bisphosphonates and bone quality. *BoneKEy Reports*, 3(529):1–8, 2014.
- [227] T. C. Lee, E. R. Myers, and W. C. Hayes. Fluorescence-aided detection of microdamage in compact bone. *Journal of Anatomy*, 193(2):179–184, 1998.

- [228] F. J. O'Brien, D. Taylor, and T. C. Lee. An improved labelling technique for monitoring microcrack growth in compact bone. *Journal of Biomechanics*, 35(4):523–526, 2002.
- [229] F. J. O'Brien, D. Taylor, and T. C. Lee. Microcrack accumulation at different intervals during fatigue testing of compact bone. *Journal of Biomechanics*, 36(7):973–980, 2003.
- [230] M. B. Schaffler, K. Choi, and C. Milgrom. Aging and matrix microdamage accumulation in human compact bone. *Bone*, 17(6):521–525, 1995.
- [231] D. J. Hadjidakis and I. I. Androulakis. Bone remodeling. *Annals of the New York Academy of Sciences*, 1092:385–396, 2006.
- [232] E. I. Waldorff, S. A. Goldstein, and B. R. McCreadie. Age-dependent microdamage removal following mechanically induced microdamage in trabecular bone in vivo. *Bone*, 40(2):425–432, 2007.
- [233] D. Vashishth, J. Koontz, S. J. Qiu, D. Lundin-Cannon, Y. N. Yeni, M. B. Schaffler, and D. P. Fyhrie. In vivo diffuse damage in human vertebral trabecular bone. *Bone*, 26(2):147–152, 2000.
- [234] M. G. Goff, F. M. Lambers, T. M. Nguyen, J. Sung, C. M. Rimnac, and C. J. Hernandez. Fatigue-induced microdamage in cancellous bone occurs distant from resorption cavities and trabecular surfaces. *Bone*, 79:8–14, 2015.
- [235] T. Diab and D. Vashishth. Effects of damage morphology on cortical bone fragility. *Bone*, 37:96–102, 2005.
- [236] G. C. Reilly and J. D. Currey. The development of microcracking and failure in bone depends on the loading mode to which it is adapted. *Journal of Experimental Biology*, 202(5):543–552, 1999.
- [237] D. R. Carter, W. E. Caler, D. M. Spengler, and V. H. Frankel. Fatigue behavior of adult cortical bone: the influence of mean strain and strain range. *Acta Orthopaedica*, 52(5):481–490, 1981.

- [238] G. W. Zack, W. E. Rogers, and S. A. Latt. Automatic measurement of sister chromatid exchange frequency. *The Journal of Histochemistry and Cytochemistry*, 25(7):741–753, 1977.
- [239] W. E. Caler and D. R. Carter. Bone creep-fatigue damage accumulation. *Journal of Biomechanics*, 22(6-7):625–635, 1989.
- [240] D. R. Carter and W. E. Caler. Cycles-dependent and time-dependent bone fracture with repeated loading. *Journal of Biomechanical Engineering*, 105(2):166–170, 1983.
- [241] S. M. Bowman, X. E. Guo, D. W. Cheng, T. M. Keaveny, L. J. Gibson, W. C. Hayes, and T. A. McMahon. Creep contributes to the fatigue behavior of bovine trabecular bone. *Journal of Biomechanical Engineering*, 120(5):647–654, 1998.
- [242] S. M. Haddock, O. C. Yeh, P. V. Mummaneni, W. S. Rosenberg, and T. M. Keaveny. Similarity in the fatigue behavior of trabecular bone across site and species. *Journal of Biomechanics*, 37(2):181–187, 2004.
- [243] E. Yamamoto, R. Paul Crawford, D. D. Chan, and T. M. Keaveny. Development of residual strains in human vertebral trabecular bone after prolonged static and cyclic loading at low load levels. *Journal of Biomechanics*, 39(10):1812–1818, 2006.
- [244] D. R. Carter and W. E. Caler. A cumulative damage model for bone fracture. *Journal of Orthopaedic Research*, 3(1):84–90, 1985.
- [245] T. L. Moore and L. J. Gibson. Fatigue of Bovine Trabecular Bone. *Journal of Biomechanical Engineering*, 125(6):761–768, 2003.
- [246] D. Taylor and T. C. Lee. Measuring the shape and size of microcracks in bone. *Journal of Biomechanics*, 31(12):1177–1180, 1998.
- [247] G. P. Parsamian and T. L. Norman. Diffuse damage accumulation in the fracture process zone of human cortical bone specimens and its influence on fracture toughness. *Journal of Materials Science: Materials in Medicine*, 12(9):779–783, 2001.

- [248] Y. N. Yeni, F. J. Hou, T. Ciarelli, D. Vashishth, and D. P. Fyhrie. Trabecular shear stresses predict in vivo linear microcrack density but not diffuse damage in human vertebral cancellous bone. *Annals of Biomedical Engineering*, 31(6):726–732, 2003.
- [249] P. Zioupos and J. D. Currey. The extent of microcracking and the morphology of microcracks in damaged bone. *Journal of Materials Science*, 29(4):978–986, 1994.
- [250] X. Wang, D. B. Masse, H. Leng, R. K. Roeder, and G. L. Niebur. Detection Of Trabecular Bone Microdamage by Micro-CT Imaging. *J Biomech*, 40(15):3397–3403, 2007.
- [251] A. L. Boskey and R. Coleman. Aging and Bone. *Critical Reviews in Oral Biology & Medicine*, 89(12):1333–1348, 2010.
- [252] J. C. Van Der Linden, J. S. Day, J. A. N. Verhaar, and H. Weinans. Altered tissue properties induce changes in cancellous bone architecture in aging and diseases. *Journal of Biomechanics*, 37(3):367–374, 2004.
- [253] S. Ma, E. L. Goh, A. Jin, R. Bhattacharya, O. R. Boughton, B. Patel, A. Karunaratne, N. T. Vo, R. Atwood, J. P. Cobb, U. Hansen, and R. L. Abel. Long-term effects of bisphosphonate therapy: Perforations, microcracks and mechanical properties. *Scientific Reports*, 7(November 2016):1–10, 2017.
- [254] T. E. Ciarelli, D. P. Fyhrie, M. B. Schaffler, and S. A. Goldstein. Variations in three-dimensional cancellous bone architecture of the proximal femur in female hip fractures and in controls. *Journal of Bone and Mineral Research*, 15(1):32–40, 2000.
- [255] M. Kleerekoper, A. R. Villanueva, J. Stanciu, D. S. Rao, and A. M. Parfitt. The role of three-dimensional trabecular microstructure in the pathogenesis of vertebral compression fractures. *Calcified Tissue International*, 37(6):594–597, 1985.
- [256] S. Nagaraja, A. S. P. Lin, and R. E. Guldborg. Age-related changes in trabecular bone microdamage initiation. *Bone*, 40(4):973–980, 2007.

- [257] P. Pietschmann, M. Skalicky, M. Kneissel, M. Rauner, G. Hofbauer, D. Stupphann, and A. Viidik. Bone structure and metabolism in a rodent model of male senile osteoporosis. *Experimental Gerontology*, 42(11):1099–1108, 2007.
- [258] G. Bhave and E. G. Neilson. Body fluid dynamics: Back to the future. *Journal of the American Society of Nephrology*, 22(12):2166–2181, 2011.
- [259] J. Norman, J. G. Shapter, K. Short, L. J. Smith, and N. L. Fazzalari. Micromechanical properties of human trabecular bone: A hierarchical investigation using nanoindentation. *Journal of Biomedical Materials Research - Part A*, 87(1):196–202, 2008.
- [260] P. J. Thurner, B. Erickson, R. Jungmann, Z. Schriock, J. C. Weaver, G. E. Fantner, G. Schitter, D. E. Morse, and P. K. Hansma. High-speed photography of compressed human trabecular bone correlates whitening to microscopic damage. *Engineering Fracture Mechanics*, 74(12):1928–1941, 2007.
- [261] N. Otsu. A Threshold Selection Method from Gray-Level Histograms. In *IEEE Transactions on Systems, Man, and Cybernetics*, volume 9, pages 62–66, 1979.
- [262] H. C. Park and R. S. Lakes. Cosserat micromechanics of human bone: Strain redistribution by a hydration sensitive constituent. *Journal of Biomechanics*, 19(5):385–397, 1986.
- [263] J. S. Nyman, A. Roy, X. Shen, R. L. Acuna, J. H. Tyler, and X. Wang. The influence of water removal on the strength and toughness of cortical bone. *Journal of Biomechanics*, 39(5):931–938, 2006.
- [264] T. M. Keaveny, X. E. Guo, E. F. Wachtel, T. A. McMahon, and W. C. Hayes. Trabecular bone exhibits fully linear elastic behavior and yields at low strains. *Journal of Biomechanics*, 27(9), 1994.
- [265] M. R. Allen and D. B. Burr. Mineralization , Microdamage , and Matrix : How Bisphosphonates Influence Material Properties of Bone. *BoneKEY-Osteovision*, 4(2):49–60, 2007.

- [266] O. Brennan, O. D. Kennedy, T. C. Lee, S. M. Rackard, F. J. O. Brien, and L. M. McNamara. The effects of estrogen deficiency and bisphosphonate treatment on tissue mineralisation and stiffness in an ovine model of osteoporosis. *Journal of Biomechanics*, 44(3):386–390, 2011.
- [267] X. E. Guo and A. Goldstein. Vertebral Trabecular Bone Microscopic Tissue Elastic Modulus and Hardness Do Not Change in Ovariectomized Rats. *Journal of Orthopaedic Research*, 18:333–336, 2000.
- [268] T. Jenkins, L. V. Coutts, S. D’Angelo, D. G. Dunlop, R. O. C. Oreffo, C. Cooper, N. C. Harvey, and P. J. Thurner. Site-Dependent Reference Point Microindentation Complements Clinical Measures for Improved Fracture Risk Assessment at the Human Femoral Neck. *Journal of Bone and Mineral Research*, 31(1):196–203, 2016.
- [269] M. Singh, A. R. Nagrath, P. S. Maini, and R. Haryana. Changes in Trabecular Pattern of the Upper End of the Femur as an Index of Osteoporosis. *The Journal of Bone*, 52-A(3):457–467, 1970.
- [270] M. L. Bouxsein, S. K. Boyd, B. A. Christiansen, R. E. Guldborg, K. J. Jepsen, and R. Müller. Guidelines for assessment of bone microstructure in rodents using micro-computed tomography, jul 2010.
- [271] D. W. Dempster, J. E. Compston, M. K. Drezner, F. H. Glorieux, J. A. Kanis, H. Malluche, P. J. Meunier, S. M. Ott, R. R. Recker, and A. M. Parfitt. Standardized nomenclature, symbols, and units for bone histomorphometry: A 2012 update of the report of the ASBMR Histomorphometry Nomenclature Committee, jan 2013.
- [272] L. M. Lix, J. C. Keselman, and H. J. Keselman. Consequences of assumption violations revisited: A quantitative review of alternatives to the one-way analysis of variance F test. *Review of Educational Research*, 66(4):579–619, 1996.
- [273] M. Frank, J.-T. Fischer, and P. J. Thurner. Microdamage formation in individual bovine trabeculae during fatigue testing. *Journal of Biomechanics*, 115(110131), 2020.

- [274] A. M. Torres, A. A. Trikanad, C. A. Aubin, F. M. Lambers, M. Luna, C. M. Rimnac, P. Zavattieri, and C. J. Hernandez. Bone-inspired microarchitectures achieve enhanced fatigue life. *Proceedings of the National Academy of Sciences of the United States of America*, 116(49):24457–24462, 2019.
- [275] M. Frank, D. Marx, D. H. Pahr, and P. J. Thurner. Mechanical properties of individual trabeculae in a physiological environment. *Proceedings of the 13th IASTED International Conference on Biomedical Engineering, BioMed 2017*, pages 141–146, 2017.
- [276] M. Frank, D. Marx, V. Nedelkovski, J. T. Fischer, D. H. Pahr, and P. J. Thurner. Dehydration of individual bovine trabeculae causes transition from ductile to quasi-brittle failure mode. *Journal of the Mechanical Behavior of Biomedical Materials*, 87(July):296–305, 2018.
- [277] E. F. Morgan, G. U. Unnikrisnan, and A. I. Hussein. Bone Mechanical Properties in Healthy and Diseased States. *Annual Review of Biomedical Engineering*, 20:119–143, 2018.
- [278] X. Wang, D. S. Rao, L. Ajdelsztajn, T. E. Ciarelli, E. J. Lavernia, and D. P. Fyhrie. Human Iliac Crest Cancellous Bone Elastic Modulus and Hardness Differ With Bone Formation Rate per Bone Surface But not by Existence of Prevalent Vertebral Fracture. *Journal of Biomedical Materials Research Part B: Applied Biomaterials*, 85B(1):68–77, 2008.
- [279] S. Hu, J. Li, L. Liu, R. Dai, Z. Sheng, X. Wu, X. Feng, X. Yao, E. Liao, E. Keller, and Y. Jiang. Micro / Nanostructures and Mechanical Properties of Trabecular Bone in Ovariectomized Rats. *International Journal of Endocrinology*, 2015, 2015.
- [280] O. Brennan, O. D. Kennedy, T. C. Lee, S. M. Rackard, and F. J. O’Brien. Biomechanical properties across trabeculae from the proximal femur of normal and ovariectomised sheep. *Journal of Biomechanics*, 42(4):498–503, 2009.
- [281] J. D. Currey, K. Brear, and P. Zioupos. The effects of ageing and changes in mineral content in degrading the toughness of human femora. *Journal of Biomechanics*, 29(2):257–260, 1996.

- [282] M. J. Turunen, S. Le Cann, E. Tudisco, G. Lovric, A. Patera, S. A. Hall, and H. Isaksson. Sub-trabecular strain evolution in human trabecular bone. *Scientific Reports*, 10(1):1–14, 2020.
- [283] J. D. Currey. The effect of porosity and mineral content on the Young’s modulus of elasticity of compact bone. *Journal of Biomechanics*, 21(2):131–139, 1988.
- [284] L. Mulder, J. H. Koolstra, J. M. J. den Toonder, and T. M. G. J. van Eijden. Relationship between tissue stiffness and degree of mineralization of developing trabecular bone. *Journal of Biomedical Materials Research Part A*, 84A:508–515, 2008.
- [285] X. Wang, X. Shen, X. Li, and C. M. Agrawal. Age-related Changes in the Collagen Network and Toughness of Bone. *Bone*, 31(1):1–7, 2002.
- [286] X. Wang, R. A. Bank, J. M. TeKoppele, and C. Mauli Agrawal. The role of collagen in determining bone mechanical properties. *Journal of Orthopaedic Research*, 19(6):1021–1026, 2001.
- [287] A. E. Peters, R. Akhtar, E. J. Comerford, and K. T. Bates. The effect of ageing and osteoarthritis on the mechanical properties of cartilage and bone in the human knee joint. *Scientific Reports*, 8(5931):1–13, 2018.
- [288] X. Ojanen, H. Isaksson, J. Töyräs, M. J. Turunen, M. K. H. Malo, A. Halvari, and J. S. Jurvelin. Relationships between tissue composition and viscoelastic properties in human trabecular bone. *Journal of Biomechanics*, 48(2):269–275, 2015.
- [289] R. D. Bloebaum, G. A. Lundeen, J. E. Shea, and E. L. Whitaker. Age-related mineralization heterogeneity changes in trabecular bone of the proximal femur. *Anatomical Record - Part A Discoveries in Molecular, Cellular, and Evolutionary Biology*, 281(2):1296–1302, 2004.
- [290] E. G. Vajda and R. D. Bloebaum. Age-related hypermineralization in the female proximal human femur. *Anatomical Record*, 255(2):202–211, 1999.

- [291] J. Wang, G. J. Kazakia, B. Zhou, X. T. Shi, and X. E. Guo. Distinct tissue mineral density in plate- and rod-like trabeculae of human trabecular bone. *Journal of Bone and Mineral Research*, 30(9):1641–1650, 2015.
- [292] R. Zhang, H. Gong, D. Zhu, R. Ma, J. Fang, and Y. Fan. Multi-level femoral morphology and mechanical properties of rats of different ages. *Bone*, 76:76–87, 2015.
- [293] J. S. Nyman, M. Granke, R. C. Singleton, and G. M. Pharr. Tissue-Level Mechanical Properties of Bone Contributing to Fracture Risk. *Current Osteoporosis Reports*, 14(4):138–150, 2016.
- [294] S. Majumdar, H. K. Genant, S. Grampp, D. C. Newitt, V. H. Truong, J. C. Lin, and A. Mathur. Correlation of trabecular bone structure with age, bone mineral density, and osteoporotic status: In vivo studies in the distal radius using high resolution magnetic resonance imaging. *Journal of Bone and Mineral Research*, 12(1):111–118, 1997.
- [295] N. Okazaki, A. J. Burghardt, K. Chiba, A. L. Schafer, and S. Majumdar. Bone microstructure in men assessed by HR-pQCT: Associations with risk factors and differences between men with normal, low, and osteoporosis-range areal BMD. *Bone Reports*, 5:312–319, 2016.
- [296] J. Yang, S. M. Pham, and D. L. Crabbe. High-Resolution Micro-CT Evaluation of Mid- to Long-Term Effects of Estrogen Deficiency on Rat Trabecular Bone 1. *Academic Radiology*, 10(10):1153–1158, 2003.
- [297] C. M. Bagi, P. Ammann, R. Rizzoli, and S. C. Miller. Effect of Estrogen Deficiency on Cancellous and Cortical Bone Structure and Strength of the Femoral Neck in Rats. *Calcified Tissue International*, 61:336–344, 1997.
- [298] A. J. Burghardt, G. J. Kazakia, A. Laib, and S. Majumdar. Quantitative Assessment of Bone Tissue Mineralization with Polychromatic Micro-Computed Tomography. *Calcified Tissue International*, 83(129):1–7, 2008.
- [299] G. J. Kazakia, A. J. Burghardt, S. Cheung, and S. Majumdar. Assessment of bone tissue mineralization by conventional x-ray microcomputed tomography:

Comparison with synchrotron radiation microcomputed tomography and ash measurements. *Medical Physics*, 35(7):3170–3179, 2008.

- [300] T. Hildebrand, A. Laib, R. Müller, J. Dequeker, and P. Rügsegger. Direct Three-Dimensional Morphometric Analysis of Human Cancellous Bone: Microstructural Data from Spine, Femur, Iliac Crest, and Calcaneus. *Journal of Bone and Mineral Research*, 14(7):1167 – 1174, 1999.
- [301] S. Epstein. The roles of bone mineral density, bone turnover, and other properties in reducing fracture risk during antiresorptive therapy. *Mayo Clinic Proceedings*, 80(3):379–388, 2005.
- [302] H. G. Bone, D. Hosking, J. P. Devogelaer, J. R. Tucci, R. D. Emkey, R. P. Tonino, J. A. Rodriguez-Portales, R. W. Downs, J. Gupta, A. C. Santora, and U. A. Liberman. Ten Years' Experience with Alendronate for Osteoporosis in Postmenopausal Women. *New England Journal of Medicine*, 350(12):1189–1199, 2004.
- [303] P. Kostenuik. *On the Evolution and Contemporary Roles of Bone Remodeling*. Elsevier, fourth edi edition, 2013.
- [304] M. R. Allen, K. Iwata, R. Phipps, and D. B. Burr. Alterations in canine vertebral bone turnover , microdamage accumulation , and biomechanical properties following 1-year treatment with clinical treatment doses of riser-dronate or alendronate. *Bone*, 39:872–879, 2006.
- [305] M. R. Allen, K. Iwata, M. Sato, and D. B. Burr. Raloxifene enhances vertebral mechanical properties independent of bone density. *Bone*, 39(5):1130–1135, 2006.
- [306] S. Komatsubara, S. Mori, T. Mashiba, M. Ito, J. Li, Y. Kaji, T. Akiyama, K. Miyamoto, Y. Cao, J. Kawanishi, and H. Norimatsu. Long-term treatment of incadronate disodium accumulates microdamage but improves the trabecular bone microarchitecture in dog vertebra. *Journal of Bone and Mineral Research*, 18(3):512–520, 2003.

- [307] S. Komatsubara, S. Mori, T. Mashiba, J. Li, K. Nonaka, Y. Kaji, T. Akiyama, K. Miyamoto, Y. Cao, J. Kawanishi, and H. Norimatsu. Suppressed bone turnover by long-term bisphosphonate treatment accumulates microdamage but maintains intrinsic material properties in cortical bone of dog rib. *Journal of Bone and Mineral Research*, 19(6):999–1005, 2004.
- [308] M. R. Allen, H. A. Hogan, W. A. Hobbs, A. S. Koivuniemi, M. C. Koivuniemi, and D. B. Burr. Raloxifene Enhances Material-Level Mechanical Properties of Femoral Cortical and Trabecular Bone. *Endocrinology*, 148(8):3908–3913, 2007.
- [309] B. Borah, T. E. Dufresne, P. A. Chmielewski, T. D. Johnson, A. Chines, and M. D. Manhart. Risedronate preserves bone architecture in postmenopausal women with osteoporosis as measured by three-dimensional microcomputed tomography. *Bone*, 34(4):736–746, 2004.
- [310] M. Ding, J. S. Day, D. B. Burr, T. Mashiba, T. Hirano, H. Weinans, D. R. Sumner, and I. Hvid. Canine cancellous bone microarchitecture after one year of high-dose bisphosphonates. *Calcified Tissue International*, 72(6):737–744, 2003.
- [311] R. Recker, P. Masarachia, A. Santora, T. Howard, P. Chavassieux, M. Arlot, G. Rodan, L. Wehren, and D. Kimmel. Trabecular bone microarchitecture after alendronate treatment of osteoporotic women. *Current Medical Research and Opinion*, 21(2):185–194, 2005.
- [312] J. S. Day, M. Ding, P. Bednarz, J. C. van der Linden, T. Mashiba, T. Hirano, C. C. Johnston, D. B. Burr, I. Hvid, D. R. Sumner, and H. Weinans. Bisphosphonate treatment affects trabecular bone apparent modulus through micro-architecture rather than matrix properties. *Journal of Orthopaedic Research*, 22(3):465–471, 2004.
- [313] C. Acevedo, H. Bale, B. Gludovatz, A. Wat, S. Y. Tang, M. Wang, B. Busse, E. A. Zimmermann, E. Schaible, M. R. Allen, D. B. Burr, and R. O. Ritchie. Alendronate treatment alters bone tissues at multiple structural levels in healthy canine cortical bone. *Bone*, 81:352–363, 2015.

- [314] A. A. Lloyd, B. Gludovatz, C. Riedel, E. A. Luengo, R. Saiyed, E. Marty, D. G. Lorich, J. M. Lane, R. O. Ritchie, B. Busse, and E. Donnelly. Atypical fracture with long-term bisphosphonate therapy is associated with altered cortical composition and reduced fracture resistance. *Proceedings of the National Academy of Sciences of the United States of America*, 114(33):8722–8727, 2017.
- [315] D. Pienkowski, C. L. Wood, and H. H. Malluche. Young’s modulus and hardness of human trabecular bone with bisphosphonate treatment durations up to 20 years. *Osteoporosis International*, 30(2):277–285, 2019.
- [316] R. C. Güerri-Fernández, X. Nogués, J. M. Quesada Gómez, E. Torres Del Pliego, L. Puig, N. García-Giralt, G. Yoskovitz, L. Mellibovsky, P. K. Hansma, and A. Díez-Pérez. Microindentation for in vivo measurement of bone tissue material properties in atypical femoral fracture patients and controls. *Journal of Bone and Mineral Research*, 28(1):162–168, 2013.
- [317] E. A. Zimmermann, E. Schaible, B. Gludovatz, F. N. Schmidt, C. Riedel, M. Krause, E. Vettorazzi, C. Acevedo, M. Hahn, K. Puschel, S. Tang, M. Amling, R. O. Ritchie, and B. Busse. Intrinsic mechanical behavior of femoral cortical bone in young, osteoporotic and bisphosphonate-treated individuals in low- and high energy fracture conditions. *Scientific Reports*, 6(February):1–12, 2016.
- [318] C. Cherraf-Schweyer, G. Maurice, M. Taghite, and K. Taous. An experimental and theoretical approach of elasticity and viscoelasticity of compact and spongy bone with periodic homogenization. *Computer Methods in Biomechanics and Biomedical Engineering*, 10(3):195–207, 2007.
- [319] R. S. Lakes and J. L. Katz. Interrelationships among the viscoelastic functions for anisotropic solids: application to calcified tissues and related systems. *Journal of Biomechanics*, 7:259–270, 1974.
- [320] T. C. Lee, S. Mohsin, D. Taylor, R. Parkesh, T. Gunnlaugsson, F. J. O. Brien, M. Giehl, and W. Gowin. Detecting microdamage in bone. *Journal of Anatomy*, 2050:161–172, 2003.

- [321] D. B. Burr, T. Diab, A. Koivunemi, M. Koivunemi, and M. R. Allen. Effects of one to three years treatment with alendronate on mechanical properties of the femoral shaft in a canine model: implications for subtrochanteric femoral fracture risk. *Journal of Orthopaedic Research*, 27(10):1288–1292, 2009.
- [322] Y. Bala, B. Depalle, D. Farlay, T. Douillard, S. Meille, H. Follet, R. Chapurlat, J. Chevalier, and G. Boivin. Bone micromechanical properties are compromised during long-term alendronate therapy independently of mineralization. *Journal of Bone and Mineral Research*, 27(4):825–834, 2012.
- [323] J. D. Currey. Tensile yield in compact bone is determined by strain, post-yield behaviour by mineral content. *Journal of Biomechanics*, 37(4):549–556, 2004.
- [324] J. Currey. Incompatible mechanical properties in compact bone. *Journal of Theoretical Biology*, 231(4):569–580, 2004.
- [325] P. Garnero. The contribution of collagen crosslinks to bone strength. *BoneKEY Reports*, 1(May):182, 2012.
- [326] P. Roschger, S. Rinnerthaler, J. Yates, G. A. Rodan, P. Fratzl, K. Klaushofer, and B. Samples. Alendronate Increases Degree and Uniformity of Mineralization in Cancellous Bone and Decreases the Porosity in Cortical Bone of Osteoporotic Women *. *Bone*, 29(2):185–191, 2001.
- [327] N. M. B. K. Willems and L. Mulder. The correlation between mineralization degree and bone tissue stiffness in the porcine mandibular condyle. *Journal of Bone and Mineral Metabolism*, 32:29–37, 2014.
- [328] H. Follet, G. Boivin, C. Rumelhart, and P. J. Meunier. The degree of mineralization is a determinant of bone strength : a study on human calcanei. *Bone*, 34:783–789, 2004.
- [329] Y. Bala, D. Farlay, R. D. Chapurlat, and G. Boivin. Modifications of bone material properties in postmenopausal osteoporotic women long-term treated with alendronate. *European Journal of Endocrinology*, 165(4):647–655, 2011.

- [330] D. P. Fyhrie and B. A. Christiansen. Bone Material Properties and Skeletal Fragility Bone Material Properties and Skeletal Fragility. *Calcified Tissue International*, 97:213–228, 2015.
- [331] M. R. Allen, S. Reinwald, and D. B. Burr. Alendronate reduces bone toughness of ribs without significantly increasing microdamage accumulation in dogs following three years of daily treatment. *Calcified Tissue International*, 82(5):354–360, 2008.
- [332] A. A. Poundarik, P.-C. Wu, Z. Evis, G. E. Sroga, A. Ural, M. Rubin, and D. Vashishth. A Direct Role of Collagen Glycation in Bone Fracture. *Journal of the Mechanical Behavior of Biomedical Materials*, 52:120–130, 2015.
- [333] S. Y. Tang and D. Vashishth. The relative contributions of non-enzymatic glycation and cortical porosity on the fracture toughness of aging bone. *Journal of Biomechanics*, 44:330–336, 2011.
- [334] M. Saito, S. Mori, and S. Komatsubara. Collagen maturity, glycation induced-pentosidine, and mineralization are increased following 3-year treatment with incadronate in dogs. *Osteoporosis International*, 19:1343–1354, 2008.
- [335] A. Jin, J. Cobb, U. Hansen, R. Bhattacharya, C. Reinhard, N. Vo, R. Atwood, J. Li, A. Karunaratne, C. Wiles, and R. Abel. The effect of long-term bisphosphonate therapy on trabecular bone strength and microcrack density. *Bone and Joint Research*, 6(10):602–609, 2017.
- [336] D. Bajaj, J. R. Geissler, M. R. Allen, D. B. Burr, and J. C. Fritton. The Resistance of Cortical Bone Tissue to Failure under Cyclic Loading is Reduced with Alendronate. *Bone*, 64:57–64, 2014.
- [337] G. R. Brock, J. T. Chen, A. R. Ingraffea, J. MacLeay, G. E. Pluhar, A. L. Boskey, and M. C. van der Meulen. The effect of osteoporosis treatments on fatigue properties of cortical bone tissue. *Bone Reports*, 2:8–13, 2015.
- [338] M. A. Gallant, D. M. Brown, M. Hammond, J. M. Wallace, J. Du, J. D. Almer, S. R. Stock, M. R. Allen, and B. David. Bone cell-independent benefits

of raloxifene on the skeleton: A novel mechanism for improving bone material properties. *Bone*, 61:191–200, 2015.

- [339] J. C. Burketa, D. J. Brooks, J. M. MacLeay, S. P. Baker, A. L. Boskey, and M. C. van der Meulen. Variations in nanomechanical properties and tissue composition within trabeculae from an ovine model of osteoporosis and treatment. *Bone*, 52(1):326–336, 2013.
- [340] J. S. Nyman, A. Roy, J. H. Tyler, R. L. Acuna, H. J. Gayle, and X. Wang. Age-related factors affecting the post-yield energy dissipation of human cortical bone. *Journal of Orthopaedic Research*, 25(5):646–655, 2007.
- [341] M. Takahashi, H. Hoshino, K. Kushida, and T. Inoue. Direct measurement of crosslinks, pyridinoline, deoxypyridinoline, and pentosidine, in the hydrolysate of tissues using high-performance liquid chromatography. *Analytical Biochemistry*, 232(2):158–162, 1995.
- [342] H. B. Hunt, A. M. Torres, P. M. Palomino, E. Marty, R. Saiyed, M. Cohn, J. Jo, S. Warner, G. E. Sroga, K. B. King, J. M. Lane, D. Vashishth, C. J. Hernandez, and E. Donnelly. Altered Tissue Composition, Microarchitecture, and Mechanical Performance in Cancellous Bone From Men With Type 2 Diabetes Mellitus. *Journal of Bone and Mineral Research*, 34(7):1191–1206, 2019.
- [343] L. Karim and D. Vashishth. Heterogeneous Glycation of Cancellous Bone and Its Association with Bone Quality and Fragility. *PLoS ONE*, 7(4):e35047, 2012.
- [344] L. Karim and M. L. Bouxsein. Effect of type 2 diabetes-related non-enzymatic glycation on bone biomechanical properties. *Bone*, 82:21–27, 2016.
- [345] D. Vashishth, G. J. Gibson, J. I. Khoury, M. B. Schaffler, J. Kimura, and D. P. Fyhrie. Influence of Nonenzymatic Glycation on Biomechanical Properties of Cortical Bone. *Bone*, 28(2):195–201, 2001.
- [346] L. Karim, J. Moulton, M. Van Vliet, K. Velie, A. Robbins, F. Malekipour, A. Abdeen, D. Ayres, and M. L. Bouxsein. Bone Microarchitecture, Biome-

chanical Properties, and Advanced Glycation End-Products in the Proximal Femur of Adults with Type 2 Diabetes. *Bone*, September(114):32–39, 2018.

- [347] J. Cohen. *Statistical Power Analysis for the Behavioral Sciences*. Lawrence Erlbaum Associates, New York, second edition, 1988.
- [348] D. B. Burr. The contribution of the organic matrix to bone’s material properties. *Bone*, 31(1):8–11, 2002.



Die approbierte gedruckte Originalversion dieser Dissertation ist an der TU Wien Bibliothek verfügbar.
The approved original version of this doctoral thesis is available in print at TU Wien Bibliothek.

Appendix A: List of publications and co-supervisions

Peer reviewed journal publications

M. Frank, D. Marx, V. Nedelkovski, J.-T. Fischer, D. H. Pahr, P. J. Thurner. Dehydration of individual bovine trabeculae causes transition from ductile to quasi-brittle failure mode. *Journal of the Mechanical Behavior of Biomedical Materials*, 87(July):296-305, 2018

A. G. Reisinger, M. Frank, P. J. Thurner, D. H. Pahr. A 2-layer elasto-viscoplastic rheological model for the material parameter identification of bone tissue. *Biomechanics and Modeling in Mechanobiology*, 19, 2149–2162 (2020)

M. Frank*, J.-T. Fischer*, P. J. Thurner. Microdamage formation in individual bovine trabeculae during fatigue testing. *Journal of Biomechanics*, 2021 Jan 22;115:110131

M. Frank, A. G. Reisinger, D. H. Pahr, P. J. Thurner. Effects of osteoporosis on bone morphometry and material properties of individual human trabeculae in the femoral head. **Conditionally accepted** in *Journal of Bone and Mineral Research - Plus*

M. Frank, A. Grabos, A. G. Reisinger, D. B. Burr, D. H. Pahr, M. R. Allen, P. J. Thurner. Effects of anti-resorptive treatment on the material properties of

individual canine trabeculae in cyclic tensile tests. **Conditionally accepted in**
Bone

In-proceedings

M. Frank, D. Marx, D. H. Pahr, P.J. Thurner. Mechanical Properties of Individual Trabeculae in a Physiological Environment. 13th IASTED International Conference on Biomedical Engineering, BioMed 2017, pages 141–146, 2017.

Non-related peer reviewed journal publications

L. Kain, O. G. Andriotis, P. Gruber, M. Frank, M. Markovic, D. Grech, V. Nedelkovski, M. Stolz, A. Ovsianikov, P. J. Thurner. Calibration of colloidal probes with atomic force microscopy for micromechanical assessment. *Journal of the Mechanical Behavior of Biomedical Materials*, 85: 225-236, 2018

C, J. Collins, M. Kozyrev, M. Frank, O. G. Andriotis, R. A. Byrne, H. P. Kiener, M. L. Pretterklieber, P. J. Thurner. The impact of age, mineralization, and collagen orientation on the mechanics of individual osteons from human femurs. *Materialia*, 9, 2020, 100573

Award

ESB student award, 2019 (finalist)

Book chapter

C. J. Collins, O. G. Andriotis, V. Nedelkovski, M. Frank, O. L. Katsamenis, P. J. Thurner. Bone Micro- and Nanomechanics. Encyclopedia of Biomedical Engineering, Volume 2: 22 - 44, 2019

224

International conference podium presentations (presented by author)

M. Frank, D. Marx, D. H. Pahr, P.J. Thurner. Measurement of the Mechanical Tissue Parameters of Individual Trabeculae in a Physiologic Environment. 22nd Congress of the European Society of Biomechanics, Lyon, 2016. Talk

M. Frank, D. Marx, D. H. Pahr, P.J. Thurner. Tissue Mechanical Properties of Bovine Trabeculae in Tension are Different in a Dry or Wet Environment. 23rd Congress of the European Society of Biomechanics, Sevilla, 2017. Talk

J.T. Fischer, M. Frank, P.J. Thurner. Quantification of microdamage formation during fatigue testing of individual trabeculae. 90th Annual Meeting of the International Association of Applied Mathematics and Mechanics, Vienna, 2019. Talk

P. Karner, M. Frank, O.G. Andriotis, A.G. Reisinger, P.J. Thurner. Influence of Non-Enzymatic Glycation on Tensile Mechanical Properties of Bovine Individual Trabeculae. 25th Congress of the European Society of Biomechanics, Vienna, 2019. Talk

M. Frank, A. G. Reisinger, D. H. Pahr, P.J. Thurner. Tensile Mechanical Properties of Human Individual Trabeculae of Non- and Osteoporotic Fracture Donors. 25th Congress of the European Society of Biomechanics, Vienna, 2019. Student award talk

National conference podium presentations

M. Frank. Hydration state of individual trabeculae results in brittle to ductile mechanical behavior. Austrian Cluster for Tissue Regeneration Annual Meeting 2017, Vienna. Talk

M. Frank. Micromechanics of individual trabeculae. Beiträge Österreichs zur

internationalen Forschung auf dem Gebiet der Theoretischen und Angewandten Mechanik. Vienna, 2018. Talk

Co-supervised diploma theses

J.T. Fischer. Quantification of microdamage formation during fatigue testing of individual trabeculae. Supervisor: P.J. Thurner, M. Frank, 2018

A. Grabos. Effect of anti-resorptive treatments on material properties and damage behavior of individual trabeculae of bone. Supervisor: P.J. Thurner, M. Frank, M. Allen. 2019

O. Kabbani. Quantification of microdamage formation during fatigue testing of individual trabeculae. Supervisor: P.J. Thurner, M. Frank. 2019

Co-supervised project works

C. Didier. Characterization of bone properties as a function of porosity. Supervisor: Supervisor: P.J. Thurner, M. Frank, 2017

S. Chehrehrazi. Effects of non-enzymatic glycation on mechanical properties of individual bovine trabeculae. Supervisor: P.J. Thurner, M. Frank, 2018

P. Karner. Effects of non-enzymatic glycation on mechanical properties of individual bovine trabeculae. Supervisor: P.J. Thurner, M. Frank, 2018

Appendix B: Compression tests of individual trabeculae

In course of the present thesis also cyclic compression tests have been performed, in the same way as described in section 3.2, but with an inverted displacement loading protocol. Compression tests were performed in two different ways: with and without an x-y table mounted between the load cell and the sample holder (see figure B1 and figure B2). This x-y table allowed movement of the top sample holder in the horizontal plane (see figure B1). Thus, tested trabeculae exhibited also a horizontal movement and shear failure. In contrast, testing without the x-y table caused only a vertical movement and impaction failure (figure B2). Depending on the trabecular architecture (dense vs. loose) and loading direction on the trabecular strut (central vs. inclined), both failure modes might occur *in vivo*.

Compression with x-y table

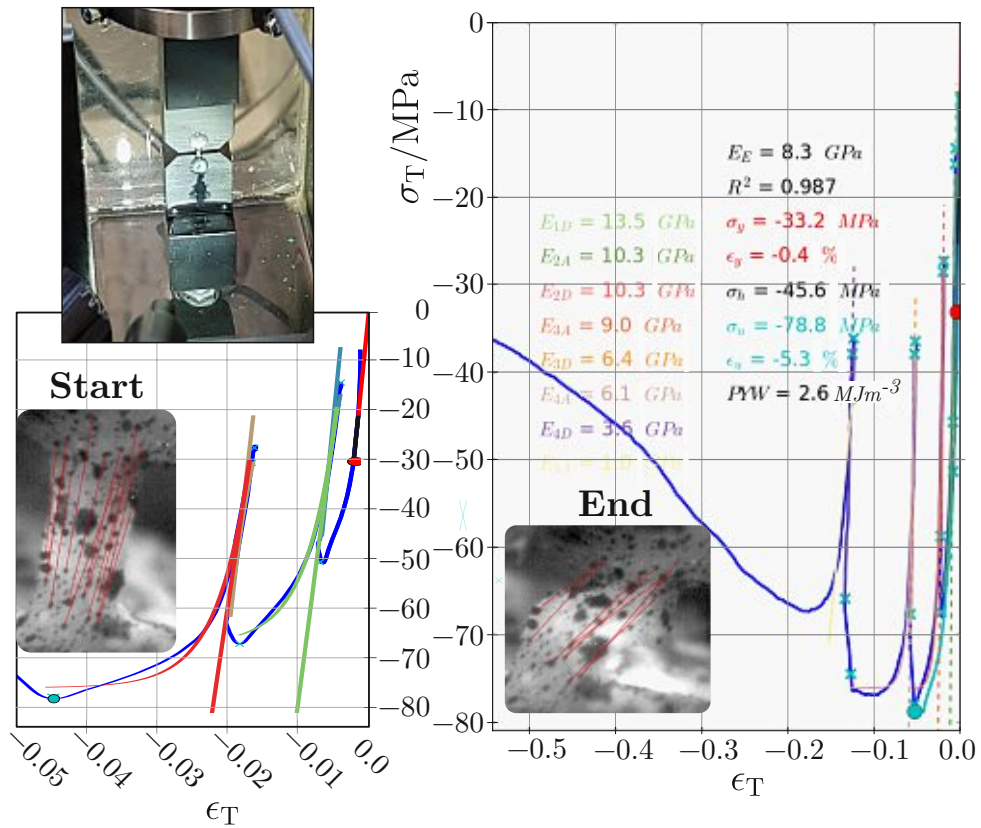


Figure B1: Compression tests of individual trabeculae - with x-y table to allow horizontal movement of the top part. Insets show the trabeculae at start and end of the compression tests. Corresponding true stress-strain curves are illustrated on the right. The left diagram displays the first region of the right diagram enlarged until -5% strain. Evaluation of loading/unloading modulus is described in section 3.2.1, evaluation of the envelope curve in section 3.2.2.

Compression **without** x-y table

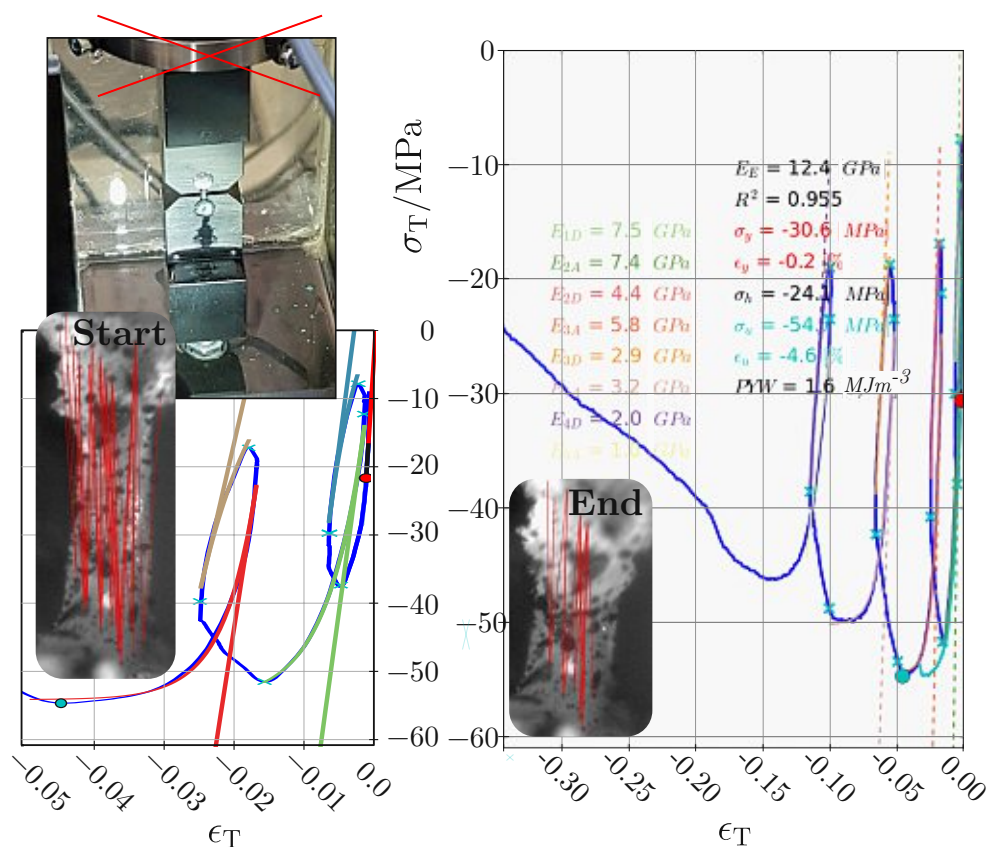


Figure B2: Compression tests of individual trabeculae - without x-y table to simulate pure vertical deformation. Insets show the trabeculae at start and end of the compression tests. Corresponding true stress-strain curves are illustrated on the right. The left diagram displays the first region of the right diagram enlarged until -5% strain. Evaluation of loading/unloading modulus is described in section 3.2.1, evaluation of the envelope curve in section 3.2.2.



Die approbierte gedruckte Originalversion dieser Dissertation ist an der TU Wien Bibliothek verfügbar.
The approved original version of this doctoral thesis is available in print at TU Wien Bibliothek.

Appendix C: Three-point bending tests of individual trabeculae

As a quick way of testing individual trabeculae, a three-point bending sample holder was manufactured. Here, three different span lengths ((700, 500, and 400) μm) were manufactured (see figure C1), as trabeculae show a large geometrical deviation. However, as tensile tests allow a more defined material characterization (see section 2.7.5) only preliminary tests were performed with the presented sample holder. Instead, the characterization of the mechanical behavior of individual trabeculae was performed with the novel tensile test approach (see section 3.1).

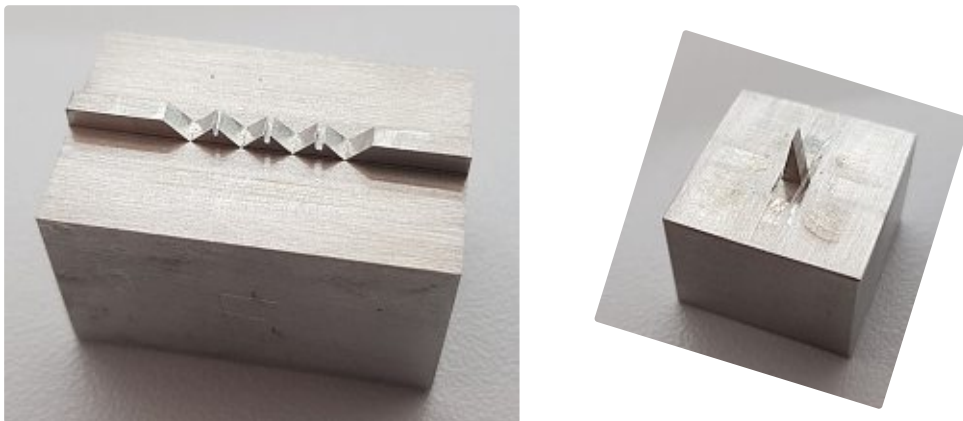


Figure C1: Three-point bending set-up for testing individual trabeculae. **Left:** The lower part of the sample holder has three different span lengths ((700, 500, and 400) μm). **Right:** The upper part consists of a sharp, long, rectangular tip.

ADDRESS: Aspangstraße 4/2/10, 1030 Vienna, Austria
 PHONE: +43 6991 4533953
 EMAIL: frankm@ilsb.tuwien.ac.at
 DATE OF BIRTH: 15.11.1987
 PLACE OF BIRTH: Vienna

EDUCATION

Enrolled in Doctoral Programme in Engineering Sciences, MECHANICAL ENGINEERING, University of Technology, Vienna	since APRIL 2015
Enrolled in Medicine Degree Programme, Medical University of Vienna, Vienna	since OCTOBER 2015
Master of Science in Biomedical Engineering, Graduation with honours, BIOMECHANICS & BIOMATERIALS, University of Technology, Vienna	MAY 2014
Bachelor of Science in Biomedical Engineering, Graduation with honours, CELL & TISSUE ENGINEERING, University of Applied Sciences (UAS) Technikum, Vienna	JUNE 2011
High School certificate and VET-Diploma, Graduation with honours, HIGH SCHOOL FOR MATERIALS ENGINEERING SPECIALISING IN POLYMER AND ENVIRONMENTAL ENGINEERING, Technologisches Gewerbemuseum (Technical College)	JUNE 2007

RESEARCH EXPERIENCE

Research Assistant (part-time), Biomechanics Department Anatomy and Biomechanics, Karl Landsteiner, Krems	JANUARY 2020 -PRESENT
University Assistant, Biomechanics Institute of Lightweight Design and Structural Biomechanics, TU Vienna	APRIL 2015 -APRIL 2020
Research Assistant, Neuroscience Vaziri Group, The Research Institute of Molecular Pathology, Vienna	SEPTEMBER 2014 -APRIL 2015
Intern, Neuroscience Hippenmeyer Group, Institute of Science and Technology, Klosterneuburg	JUNE 2014 -JULY 2014
Graduand, Biomathematical Modelling & Analysis Dept. Biomedical Systems, Austrian Institute of Technology, Vienna	APRIL 2013 -MARCH 2014
Research Assistant (part-time), Tissue Engineering Dept. Biochemical Engineering, UAS Technikum, Vienna	JULY 2010 -MARCH 2013
Bachelor Intern, Mechanisms Underlying Cell Migration Institute of Molecular Biotechnology, Vienna	FEBRUARY 2011 -AUGUST 2011

AWARDS AND SCHOLARSHIPS

Student award - finalist, 25th Congress of the European Society of Biomechanics, Vienna	JUNE 2019
Poster award, „Symposium Tissue Engineering & Regenerative Medicine“, UAS Technikum, Vienna	JUNE 2011
Scholarship for outstanding academic achievements, MUW, Vienna	2016-2018
Scholarship for outstanding academic achievements, TU Wien, Vienna	2011/2012
Scholarship for outstanding academic achievements, UAS Technikum, Vienna	2008-2010

PUBLICATIONS

4.1 Peer-reviewed journal articles

M. Frank*, J.-T. Fischer*, P. J. Thurner. „Microdamage formation in individual bovine trabeculae during fatigue testing“. *Journal of Biomechanics*, 2021 Jan 22;115:110131

A. G. Reisinger, M. Frank, P. J. Thurner, D. H. Pahr. „A two-layer elasto- visco-plastic rheological model for the material parameter identification of bone tissue“. *Biomechanics and Modeling in Mechanobiology*, 19, 2149–2162, 2020

M. Frank, D. Marx, V. Nedelkovski, J. Fischer, D. H. Pahr, P. J. Thurner. „Dehydration of individual bovine trabeculae causes transition from ductile to quasi-brittle failure mode“, *Journal of the Mechanical Behavior of Biomedical Materials*, 87(July):296–305, 2018

L. Kain, O. G. Andriotis, P. Gruber, M. Frank, M. Markovic, D. Grech, V. Nedelkovski, M. Stolz, A. Ovsianikov, P. J. Thurner. „Calibration of colloidal probes with atomic force microscopy for micromechanical assessment“, *Journal of the Mechanical Behavior of Biomedical Materials*, 85 (225-236), 2018

M. Frank, M. Bachler, S. Wassertheurer, C. Mayer, „Computational Aspects of Models for Minimizing the Effects of Ectopic Beats on Heart Rate Variability“, *Simulation Notes Europe*, 24 (3-4), 2014

4.2 Peer-reviewed conference papers

M. Bachler, M. Hoertenhuber, M. Frank, S. Wassertheurer, C. Mayer. „Simulation of Physiologic Ectopic Beats in Heartbeat Intervals to Validate Algorithms“. *Minisymposium, Mathmod 2015, Vienna*

M. Frank, D. Marx, D. H. Pahr, P.J. Thurner. „Mechanical Properties of Individual Trabeculae in a Physiological Environment“. *Proceedings of the 13th IASTED International Conference on Biomedical Engineering, BioMed 2017, Innsbruck*, pp. 141-146, 2017

4.3 Conference podium presentations

- M. Frank, A. G. Reisinger, D. H. Pahr, P.J. Thurner. „Tensile Mechanical Properties of Human Individual Trabeculae of Non- and Osteoporotic Fracture Donors“. 25th Congress of the European Society of Biomechanics, Vienna, Austria JUL 7 - 10, 2019
- P. Karner, M. Frank, O.G. Andriotis, A.G. Reisinger, P.J. Thurner. „Influence of Non-Enzymatic Glycation on Tensile Mechanical Properties of Bovine Individual Trabeculae“. 25th Congress of the European Society of Biomechanics, Vienna, Austria JUL 7 - 10, 2019
- J.T. Fischer, M. Frank, P.J. Thurner. „Quantification of microdamage formation during fatigue testing of individual trabeculae“. 90th Annual Meeting of the International Association of Applied Mathematics and Mechanics, Vienna, Austria FEB 18 - 22, 2019
- M. Frank, D. Marx, D. H. Pahr, P.J. Thurner. „Tissue Mechanical Properties of Bovine Trabeculae in Tension are Different in a Dry or Wet Environment“. 23rd Congress of the European Society of Biomechanics, Sevilla, Spain JUL 02 - 05, 2017
- M. Frank, D. Marx, D. H. Pahr, P.J. Thurner. „Measurement of the Mechanical Tissue Parameters of Individual Trabeculae in a Physiologic Environment“, 22nd Congress of the European Society of Biomechanics, Lyon, France JUL 10 - 13, 2016

4.4 Conference poster presentations

- M. Frank, J. Kollmitzer, H. Redl, D. Rünzler. „Shear Force Stimulation of Adipose-tissue Derived Stem Cells in a Novel Bioreactor“, Tissue Engineering & Regenerative Medicine International Society World Congress, Vienna SEPT 5 - 8, 2012
- M. Frank, M. Vinzenz, V. Small. „VASP-dependent Actin Filament Elongation in Cell Motility“, Symposium Tissue Engineering & Regenerative Medicine at UAS Technikum, Vienna JUNE 7, 2011

SUMMER SCHOOLS AND WORKSHOPS

- | | |
|------------------------------------------------------------------------------------|--------------------|
| Summer school , <i>Mein Hanusch-Krankenhaus</i> - Vienna, Austria | SEPT 16 - 18, 2019 |
| Summer school , <i>Bone Cell and Tissue Mechanics</i> - CISM, Udine, Italy | JUNE 22 - 26, 2015 |
| Summer school , <i>Arbeitsgemeinschaft Simulation</i> , Ljubljana, Slovenia | SEPT 14 - 19, 2013 |
| Workshop , <i>Expertissues Double-Workshop</i> , Vienna, Austria | JULY 20 - 22, 2010 |

LANGUAGES

German: Native

English: Fluent

IT SKILLS

OS: Windows, Linux

Programming: Python, Matlab

Image processing: 3DSlicer, Medtool, ImageJ

Office: MS Office, Latex

Numerics: Hypermesh, Abaqus



Martin Frank